Analytical and numerical studies for non-relativistic scalar field dark matter

Raquel Galazo García

université
PARIS-SACLAY

Analytical and numerical studies for non-relativistic scalar field dark matter

Études analytiques et numériques pour la matière noire scalaire non relativiste

Thèse de doctorat de l'Université Paris-Saclay

École doctorale n°564, Physique en Île-de-France (PIF)
Spécialité de doctorat : Physique
Graduate School : Physique. Référent : Faculté des sciences d'Orsay

Thèse préparée dans la unité de recherche **Institut de Physique Théorique, (Université Paris-Saclay, CNRS, CEA)**, sous la direction de **Philippe BRAX**, directeur de recherche, HDR et la co-direction de **Patrick VALAGEAS**, directeur de recherche, HDR.

Thèse présentée et soutenue à Paris-Saclay, le 22 Septembre 2023, par

Raquel Galazo-García

Composition du jury

Membres du jury avec voix délibérative

Michael JOYCE Proffeseur SU, HDR, Université Pierre et Marie Curie - Paris VI, LPNHE	Président
Massimo PIETRONI Proffeseur, HDR, Università di Parma	Rapporteur & Examinateur
Jean-Baptiste FOUVRY Chargé de recherche, HDR, CNRS, Institut d'Astrophysique de Paris	Rapporteur & Examinateur
Sandrine CODIS Chargée de recherche, LCEG, AIM, Université Paris-Saclay	Examinatrice

THESE DE DOCTORAT
NNT : 2023UPASP084

université PARIS-SACLAY

ÉCOLE DOCTORALE
Physique en Île-de-France (PIF)

Titre: Études analytiques et numériques pour la matière noire scalaire non relativiste
Mots clés: Matière noire, cosmologie, simulations numériques

Résumé: Le modèle le plus largement accepté pour décrire la matière noire (DM) de notre univers est le modèle de la matière noire froide (CDM), dans lequel le scénario des WIMPs est privilégié pour des raisons théoriques et expérimentales. Cependant, malgré de nombreuses expériences, les WIMPs n'ont toujours pas été détectés. De plus, plusieurs défis à petite échelle sont apparus au fur et à mesure que les observations et les simulations à l'échelle galactique se sont améliorées. Ces tensions pourraient être le signe d'une nouvelle physique nécessaire pour mieux comprendre notre univers. Dans ce contexte, des scénarios alternatifs ont émergé, y compris l'hypothèse que la DM pourrait être un champ scalaire (SFDM). Cette thèse développe de nouvelles études numériques et analytiques pour examiner les différents modèles de SFDM. A cette fin, nous analysons la DM aux petites échelles. Ici, la dynamique non-relativiste du système est gouvernée par le système non-linéaire de Schrödinger–Poisson (SP). Pour mieux comprendre cette dynamique, nous avons obtenu de nouvelles solutions auto-similaires par des méthodes semi-analytiques pour le modèle Fuzzy Dark Matter (FDM). Ces solutions auto-similaires diffèrent significativement de leurs homologues dans le modèle CDM. Contrairement à l'effondrement hiérarchique familier de ces dernières, elles correspondent à une explosion hiérarchique inverse. De plus, cette étude met en évidence le processus de refroidissement gravitationnel, qui permet au système d'éjecter l'énergie excédentaire par l'expulsion intermittente d'amas de matière sans dissipation. Ces comportements surprenants sont dus aux propriétés ondulatoires de l'équation de Schrödinger. En outre, nous avons réalisé de nouvelles études numériques pour résoudre la dynamique non linéaire du système SP, en étudiant la formation et l'évolution des solitons à l'intérieur de halos étendus pour des scénarios de matière noire à champ scalaire caractérisés par un potentiel d'interaction quartique ou borné. Les solitons sont des configurations d'équilibre du système SP et apparaissent dans ces modèles au centre des galaxies, ce qui pourrait améliorer l'accord avec les données. Nous nous concentrons sur le régime semi-classique où l'échelle des effets ondulatoires est typiquement beaucoup plus petite que l'échelle des auto-interactions. Nous présentons de nouvelles simulations numériques avec des conditions initiales où le halo est décrit par l'approximation WKB pour les coefficients de ses fonctions propres. Pour le potentiel quartique, nous constatons que lorsque la taille du système est de l'ordre de la longueur de Jeans associée aux auto-interactions, un soliton central se forme rapidement et représente environ 50% de la masse totale. Cependant, si le halo est dix fois plus grand que cette échelle d'auto-interaction, un soliton ne se forme rapidement que dans les halos où la densité centrale est suffisamment grande pour déclencher les auto-interactions. Si le halo a un profil plat, il faut plus de temps pour qu'un soliton apparaisse après que de petites fluctuations aléatoires sur la taille de la longueur d'onde de Broglie se soient accumulées pour atteindre une densité suffisamment importante. Dans certains cas, nous observons la coexistence de plusieurs pics de densité étroits à l'intérieur d'un soliton plus large soutenu par l'auto-interaction. Tous les solitons semblent robustes et croissent lentement à moins qu'ils ne représentent déjà 40% de la masse totale. Pour le potentiel borné, nous retrouvons les caractéristiques des systèmes FDM lorsque le potentiel est constant, tandis que nous retrouvons les résultats du potentiel quartique lorsqu'il est linéaire. Nous développons une théorie cinétique, valable pour un fond inhomogène, afin d'estimer le taux de croissance des solitons pour les faibles masses. Nos résultats devraient montrer que les halos cosmologiques montreraient une grande dispersion pour la masse de leur soliton, en fonction de l'histoire de leur processus de formation.

université PARIS-SACLAY | ÉCOLE DOCTORALE Physique en Île-de-France (PIF)

Title: Analytical and numerical studies for non-relativistic scalar field dark matter
Keywords: Dark matter, cosmology, numerical simulations

Abstract: The most widely accepted model to describe the dark matter (DM) of our Universe is the Cold Dark Matter model (CDM), where the weakly interacting massive particles (WIMPs) scenario is favoured for theoretical and experimental reasons. However, despite many experimental searches, WIMPs have still not been detected. Moreover, several small-scale challenges have emerged as observations and simulations at galactic scales have improved. These tensions could be signs of new physics needed to understand better our Universe. In this context, alternative scenarios have emerged, including the hypothesis that DM could be a scalar field (SFDM) with masses ranging from 10^{-22} eV to eV.

In this thesis we develop new numerical and analytical studies to examine different SFDM models. To this end, we analyze DM at small scales. Here, the non-relativistic dynamics of the system are governed by the non-linear Schrödinger – Poisson system (SP). In order to understand better the complex dynamics of the SP system, we have carried out new analytical studies. We have found new self-similar solutions for Fuzzy Dark Matter (FDM) by semi-analytical methods. Thanks to these explicit expressions, we have gained a much finer understanding of the dynamic processes. A novel result is that these self-similar solutions differ significantly of the usual CDM self-similar solutions. In contrast to the familiar hierarchical collapse of the current model for structure formation, they correspond to an inverse hierarchical explosion. Moreover, this study highlights the gravitational cooling process, which allows the system to eject excess energy through the intermittent expulsion of clumps of matter without dissipation. These surprising behaviours are due to the wave properties of the Schrödinger equation.

Furthermore, we have performed new numerical studies to solve the non-linear dynamics of the SP system, investigating the formation and evolution of solitons inside extended halos for scalar-field dark matter scenarios characterized by a quartic and bounded interaction potential. Solitons are equilibrium configurations of the SP system and appear in these models at the core of galaxies, which could improve the agreement with the data since they lead to a smooth density profile at the centre, solving one of the CDM tensions at galactic scales, the core–cusp problem.

We focus on the semiclassical regime where the scale of the wave-like effects is typically much smaller than the scale of the self-interactions. We present new numerical simulations with initial conditions where the halo is described by the WKB approximation for its eigenfunction coefficients. For the quartic potential, we find that when the size of the system is of the order of the Jeans length associated with the self-interactions, a central soliton quickly forms and makes about 50% of the total mass. However, if the halo is ten times greater than this self-interaction scale, a soliton only quickly forms in cuspy halos where the central density is large enough to trigger the self-interactions. If the halo has a flat core, it takes a longer time for a soliton to appear after small random fluctuations on the de Broglie wavelength size build up to reach a large enough density. In some cases, we observe the co-existence of several narrow density spikes inside the larger self-interaction-supported soliton. All solitons appear robust and slowly grow unless they already make up 40% of the total mass. For the bounded potential, we find features of FDM systems when the potential is constant, while we recover results for the quartic potential when it is linear. We develop a kinetic theory, valid for an inhomogeneous background, to estimate the soliton growth rate for low masses. Our results suggest that cosmological halos would show a large scatter for their soliton mass, depending on their assembly history.

Acknowledgements

First and foremost, I would like to express my deepest gratitude to my supervisors, Philippe and Patrick. Your mentorship, guidance, and dedicated time have been invaluable in shaping this project. I am also immensely grateful for the support you provided, especially during the challenging beginning amidst the pandemic. But in reality always. Thank you very much for your commitment in this thesis.

I would like to extend my heartfelt thanks to my PhD colleague, Alexis Boudon. Thank you very much for all your support during these years. It has been wonderful to have shared this time together.

A special thank you goes out to all the people at IPhT who have made our laboratory a warmest place. Thanks Natalie Hogg, Massimiliano M. Riva, Leong Khim Wong, Petter Taule, Pierre Fleury, and Filippo Vernizzi.

I would like to deeply thank my family for their unconditional love. To my sister Irene and my father Emilio, thank you for always supporting me. And, of course, to my mother Alicia, because I know that you are always by my side and you have always been my source of inspiration.

Finally, my warmest thanks go to Héctor. You have been my greatest support and the main source of happiness throughout these years. I genuinely could not have accomplished this without you and your love.

R.G.G. was supported by the CEA NUMERICS program, which has received funding from the European Union's Horizon 2020 research and innovation program under the Marie Sklodowska-Curie grant agreement No 800945.

Use of copyrighted material

Physical Review D

Contents

List of Figures

Preface

This dissertation is presented in partial fulfilment of the requirements for obtaining a *Philosophiae Doctor* degree from Paris Saclay University. The content of this thesis is based on three works that are the outcome of research conducted at the *Institut de Physique Theorique, CEA, CNRS* from October 2020 to July 2023 under the guidance of Dr. Philippe Brax and Dr. Patrick Valageas:

[1] *Self-similar solutions for fuzzy dark matter*, Raquel Galazo-García, Philippe Brax, and Patrick Valageas Phys. Rev. D 105, 123528 – Published 23 June 2022

[2] *Solitons and halos for self-interacting scalar dark matter*, Raquel Galazo-García, Philippe Brax, and Patrick Valageas, arXiv:2304.10221

[3] *Solitons and halos for truncated self-interacting scalar field dark matter*, Raquel Galazo-García, Philippe Brax, and Patrick Valageas (in preparation)

Outline

This thesis undertakes a comprehensive exploration of both numerical and analytical investigations concerning different scalar field dark matter models in the non-relativistic regime. The structure of this thesis is as follows:

In Chapter 1, we introduce the dark matter paradigm, provide an overview of the evidence supporting dark matter, and discuss the emergence of Cold Dark Matter. Additionally, we introduce Scalar Field Dark Matter as a compelling alternative to the Cold Dark Matter model. In Chapter 2, we explore how scalar fields can act as dark matter and examine the fundamental equations of the theory. Chapter 3 focuses on a comprehensive study of self-similar solutions for Fuzzy Dark Matter. In Chapter 4, we discuss in detail the numerical methods employed to compute the dynamics of scalar field dark matter clouds. In Chapter 5 our attention shifts to investigating the formation and evolution of solitons supported by repulsive self-interactions within extended halos focusing on the quartic model. In Chapter 6, we present and analyze the results pertaining to the formation and evolution of solitons in truncated potentials. Finally in Chapter 7 we conclude and summarize the key findings derived from this thesis.

Résumé

La nature de la matière noire (DM) est actuellement l'un des plus grands défis de la cosmologie, du point de vue de la relativité générale et du modèle standard de la physique des particules. La matière noire est une forme hypothétique de matière qui n'interagit pas avec la lumière ou d'autres formes de rayonnement électromagnétique, ce qui signifie qu'elle ne réfléchit pas, n'absorbe pas et n'émet pas de lumière, ce qui la rend invisible et difficile à détecter. C'est pourquoi on l'appelle "matière noire". Son existence est déduite de ses effets gravitationnels sur la matière visible et de la structure à grande échelle de l'Univers. Les mesures du rayonnement du fond diffus cosmologique (CMB), la rémanence du Big Bang, effectuées par les missions Planck (Planck Collaboration et al., 2020a) et WMAP (Bennett et al., 2013) ont fourni des preuves solides que la matière noire représente environ 85 % de la matière totale de l'Univers.

Le modèle standard de la physique des particules, qui décrit les particules élémentaires connues et leurs interactions, n'explique pas les propriétés de la matière noire. Les particules de matière noire, si elles existent, doivent être non baryoniques, c'est-à-dire qu'elles ne sont pas constituées des mêmes éléments que la matière ordinaire (protons, neutrons et électrons) (Del Popolo, 2014). Cela suggère qu'une extension du modèle standard est nécessaire pour inclure la matière noire.

La combinaison de la matière noire et de la constante cosmologique donne naissance au modèle ΛCDM, le modèle standard de la cosmologie (Weinberg, 2008). Ce cadre est le modèle cosmologique le plus largement accepté pour décrire l'évolution et les propriétés de notre Univers. Il repose sur la combinaison de la constante cosmologique (Λ) et de la matière noire froide (CDM). La constante cosmologique représente une forme d'énergie uniformément répartie dans l'espace et contribue à l'accélération de l'expansion de l'Univers. Elle a été introduite pour la première fois par Einstein (1986) et est souvent associée au concept d'énergie noire. La nature exacte de l'énergie noire reste inconnue, mais elle représente environ 68 % de l'énergie totale de l'univers (Planck Collaboration et al., 2020a). D'autre part, le CDM fait référence à un type de matière noire composé de particules non relativistes qui se déplacent lentement à l'échelle cosmique (Peebles, 1982; Bond et al., 1982). Elle est considérée comme "froide" car elle ne possède pas d'énergie cinétique significative. Le modèle standard de cosmologie a remarquablement réussi à simuler et à reproduire les caractéristiques observées de l'Univers. Il fournit un cadre complet qui correspond étroitement à nos observations.

Cependant, l'absence de signal DM dans les canaux les plus prometteurs (Schumann, 2019; Conrad, 2014; Arcadi et al., 2018) et les incohérences qui apparaissent au fur et à mesure que les observations et les simulations des échelles galactiques et subgalactiques s'améliorent (Weinberg et al., 2015), ouvrent une nouvelle fenêtre pour l'exploration de nouveaux modèles DM.

C'est pourquoi, dans cette thèse, nous nous aventurerons au-delà des modèles standard de la physique des particules et de la cosmologie. Nous explorerons différents aspects de la matière noire à champ scalaire (SFDM) (Hu et al., 2000; Goodman, 2000), une alternative intrigante au paradigme CDM conventionnel qui remet en question certaines des hypothèses sous-jacentes au modèle ΛCDM. En considérant cette alternative, nous visons à élargir notre compréhension et à explorer les possibilités au-delà du cadre établi.

Le point essentiel des modèles SFDM est qu'ils reproduisent les prédictions du CDM concernant la structure à grande échelle de l'univers (Shapiro et al., 2022) et qu'ils apportent une solution naturelle à la crise à petite échelle (Weinberg et al., 2015; Del Popolo & Delliou, 2016; Nakama et al., 2017; Di Luzio et al., 2020). En outre, ils expliquent l'absence de preuves de détection directe et sont bien étayés du point de vue de la physique des particules.

La principale hypothèse sous-jacente de la SFDM est que la masse associée au champ doit être extrêmement légère, de l'ordre de 10^{-22} eV (Hu et al., 2000; Hui et al., 2017). Cela correspond à une longueur d'onde de Broglie à l'échelle du kiloparsec,

$$\lambda_{dB} = \frac{2\pi}{mv} = 0.48\text{kpc}\left(\frac{10^{-22}\text{eV}}{\text{m}}\right)\left(\frac{250\text{km/s}}{\text{v}}\right). \tag{1}$$

Ainsi, à des échelles beaucoup plus petites que λ_{dB}, le champ présente un comportement ondulatoire conduisant à des interférences ondulatoires. Ces effets ondulatoires sont dus à un nouveau terme de pression qui apparaît dans l'équation des mouvements, également appelé *pression quantique*, provenant des gradients du champ scalaire. À ces échelles, lorsque cette pression quantique s'équilibre avec la gravité, une solution d'équilibre se forme. Ces solutions sont appelées solitons (Lee & Pang, 1992; Guth et al., 2015; Sikivie & Yang, 2009). Ils apparaissent au centre des halos et donnent lieu à un profil de densité radial plat au centre. Par conséquent, la formation de structures aux petites échelles est entravée par l'effet de cette pression quantique. La formation et l'évolution de ces solitons est l'un des objectifs de cette thèse. Nous nous demandons dans quelles conditions les potentiels quartiques et tronqués sont formés.

Sur des échelles beaucoup plus grandes que la longueur d'onde de Broglie, cependant, le comportement de la SFDM ne se distingue pas de celui de la CDM (Shapiro et al., 2022). Les simulations cosmologiques montrent que l'on retrouve la distribution des vides et des filaments lorsque l'on compare les deux résultats. Ainsi, la SFDM représente une solution reliée à la crise des petites échelles, tout en préservant les acquis du CDM aux plus grandes échelles (Ferreira, 2020; Hui, 2021).. La compréhension de la limite semi-classique reliant le modèle CDM aux modèles SFDM est un autre objectif de la thèse, en particulier nous explorons ce point avec le modèle FDM à travers des solutions auto-similaires.

Du point de vue de la physique des particules, l'idée d'un boson extrêmement léger trouve un soutien dans plusieurs scénarios de physique des particules. Un exemple notable est l'axion de la QCD, qui résout le problème CP fort (Peccei & Quinn, 1977). En tant que boson ultra-léger, le SFDM constitue un candidat viable pour la matière noire sans dépendre d'extensions supersymétriques du modèle standard.

Dans l'ensemble, la SFDM apparaît comme une alternative bien étayée au CDM, démontrant son potentiel pour résoudre les problèmes à petite échelle de ce dernier. En même temps, la convergence des prédictions du SFDM et du CDM aux échelles cosmologiques garantit que ce modèle est un candidat viable pour reproduire les observations dérivées des études sur la formation des structures cosmologiques.

En particulier, dans cette thèse, nous nous concentrons sur l'étude analytique et numérique de différents modèles de matière noire scalaire dans le régime non relativiste. Ce régime est pertinent pour les structures astrophysiques et à grande échelle. Par conséquent, les équations fondamentales avec lesquelles nous allons travailler sont les équations de Schrödinger–Poisson.

La dérivation de ces équations, ainsi que la façon dont les champs scalaires peuvent jouer le rôle de matière noire et les principales équations de la théorie sont présentées dans le Chapitre 2.

Dans le Chapitre 3, nous utilisons des techniques semi-analytiques pour calculer des solutions auto-similaires pour la matière noire fuzzy, (FDM) (Galazo-García et al., 2022). L'autosimilarité fait référence à la propriété de rester inchangé dans la forme et l'apparence sous des transformations d'échelle appropriées. En considérant des solutions auto-similaires, nous visons à étendre notre compréhension au-delà de l'équilibre hydrostatique présenté par les solitons. Cela nous permet d'explorer d'éventuelles solutions analytiques dépendant du temps, ce qui nous fournit un outil précieux pour mieux contrôler et comprendre la dynamique du modèle. Grâce à ces solutions auto-similaires, nous pouvons examiner les configurations dynamiques intégrées dans un arrière-plan cosmologique en expansion.

Une autre motivation de l'étude des solutions auto-similaires pour le FDM est d'établir un lien et de faciliter les comparaisons avec les solutions auto-similaires dans le cadre du CDM (Fillmore & Goldreich, 1984; Bertschinger, 1985; Teyssier et al., 1997). Dans le scénario CDM, les solutions auto-similaires présentent un modèle d'effondrement hiérarchique bien connu. Au départ, de petites perturbations linéaires de la densité apparaissent sur un fond homogène, leurs amplitudes décroissant comme une loi de puissance aux grands rayons. Au fur et à mesure que le temps passe, des coquilles de masse plus importante se retournent et s'effondrent. Pour des profils initiaux suffisamment abrupts, le noyau interne se stabilise en coordonnées physiques, conduisant à la formation d'un halo viralisé. Le profil de densité dans la région non linéaire suit une distribution en loi de puissance, augmentant en masse et en rayon au fur et à mesure que des coquilles plus éloignées se séparent du flux de Hubble et s'effondrent. Par conséquent, en explorant ces solutions, nous pouvons mieux comprendre les similitudes et les différences entre les modèles FDM et CDM.

L'étude des solutions autosimilaires nous aide également à comprendre la relation entre les modèles FDM et CDM dans la limite semi-classique. Cette limite nous permet d'étudier le comportement du FDM dans le régime où les effets quantiques sont significatifs, mais où la gravité classique reste la force dominante.

Nos résultats mettent en évidence la nature différente de ces solutions auto-similaires pour la FDM par rapport à leurs homologues pour la matière noire froide (CDM). Les solutions auto-similaires pour la CDM dans un univers perturbé d'Einstein-de Sitter décrivent un effondrement gravitationnel, avec un contraste de densité croissant dans le régime linéaire et une transition vers le régime non-linéaire où la forme du profil dans les régions intérieures est altérée par des effets non-linéaires.

Cependant, les solutions auto-similaires pour la FDM présentent des différences significatives. Elles ne présentent pas d'effondrement gravitationnel ; au lieu de cela, la matière est expulsée des pics centraux par des amas successifs, ce qui ressemble à un refroidissement gravitationnel. Ce comportement est attribué à la pression quantique et aux propriétés ondulatoires de l'équation de Schrödinger. Contrairement à la CDM, les coquilles extérieures de la FDM ne suivent pas la trajectoire de l'effondrement sphérique

en chute libre. La prédominance de la pression quantique sur la gravité conduit à des oscillations de type acoustique, facilitant le couplage entre petites et grandes échelles.

De plus, en comparant le profil du soliton avec le profil de la solution auto-similaire dans la limite asymptotique à haute densité, nous observons que le pic central du profil auto-similaire ne converge pas vers l'état d'équilibre du profil du soliton, malgré l'augmentation de la densité centrale. Cette divergence peut être attribuée à l'influence des effets cinétiques près de la limite du pic central.

En ce qui concerne la limite semi-classique, nous découvrons que les solutions autosimilaires FDM disparaissent à l'approche de la limite, devenant confinées dans un rayon de plus en plus petit. Cela indique que la limite semi-classique ne permet pas de retrouver la dynamique de la CDM dans le cas de la FDM. Cela souligne la nécessité de faire preuve de prudence et d'examiner attentivement la limite semiclassique, car les solutions auto-similaires standard du CDM ne sont retrouvées avec précision qu'à $\epsilon = 0$.

Au Chapitre 4, nous présentons le code pseudo-spectral conçu pour simuler l'évolution dynamique du système de Schrödinger–Poisson. Le code utilise une combinaison d'opérations dans le domaine de Fourier et d'évaluations dans l'espace des positions pour traiter les termes linéaires et non linéaires, respectivement. Cette approche élimine le bruit généralement associé aux méthodes de différences finies pour le calcul des dérivées spatiales (Pathria & Morris, 1990; Zhang & Hayee, 2008; Edwards et al., 2018). Bien que le code entraîne des coûts de calcul dus aux transformées de Fourier et de Fourier inverse, nous optimisons ces transformées à l'aide du logiciel efficace FFTW3 (Frigo & Johnson, 2005) et tirons parti des capacités de parallélisation offertes par OpenMP (OpenMP Architecture Review Board, 2005–*present*; Miguel Hermanns, 1997). La création de ce code est fortement motivée par les études numériques des chapitres suivants, dans lesquels la dynamique des halos de matière noire non relativistes est étudiée.

Dans le Chapitre 5, nous explorons la formation et l'évolution des solitons à l'intérieur de halos étendus dans le modèle quartique à la fois analytiquement et numériquement (Galazo García et al., 2023). Nous supposons que le halo est formé par l'instabilité de Jeans et nous cherchons à savoir si les solitons peuvent émerger dynamiquement de l'évolution de la matière noire dans le halo.

En considérant des conditions initiales spécifiques et en résolvant l'équation de Schrödinger non linéaire, nous observons l'émergence rapide de solitons centraux soutenus par des auto-interactions au sein de halos à l'échelle de la longueur d'auto-interaction. Ces solitons amortissent les fluctuations de densité initiales et représentent une fraction significative de la masse totale. Ce comportement est valable pour les profils de halos plats et cuspides, les halos cuspides présentant des pics supplémentaires de haute densité à l'intérieur du soliton.

Pour les halos plus grands que l'échelle des auto-interactions, il faut plus de temps pour que les solitons se forment, les profils de densité plats nécessitant beaucoup de temps jusqu'à ce que des pics à petite échelle se développent pour déclencher les auto-interactions. Les halos épais, en revanche, conduisent rapidement à la formation de solitons. Nous développons une théorie cinétique et un ansatz simplifié pour estimer les taux de croissance des solitons, qui montrent un accord raisonnable avec la croissance précoce pour les halos cuspides, mais ont des limites pour les grandes masses de solitons et les profils de halo plats.

Dans l'ensemble, nos résultats suggèrent que les solitons jouent un rôle crucial dans les scénarios de matière noire à champ scalaire avec des auto-interactions. Ils peuvent se

former dans des régions surdenses qui s'effondrent et persistent au fur et à mesure que les halos grandissent, augmentant progressivement leur masse par accrétion et fusions. La relation entre les masses du halo et du soliton est complexe, dépendant de l'histoire de l'assemblage du système et pouvant conduire à une grande dispersion des masses du soliton pour une masse donnée du halo.

Enfin, dans le Chapitre 6, nous étudions numériquement l'émergence et l'évolution des solitons dans deux modèles de matière noire de champ scalaire à potentiel tronqué. L'une des principales motivations est d'explorer les caractéristiques du modèle du cosinus. Bien que nous fassions une approximation de ce modèle et que nous complétions l'étude par l'incorporation d'un potentiel tronqué, les simulations fourniront des indications et des indices précieux sur le comportement et la phénoménologie de la résolution du potentiel réel. En étudiant le modèle simplifié du cosinus, nous pouvons acquérir une meilleure compréhension de la dynamique sous-jacente et potentiellement appliquer ces connaissances au potentiel réel plus complexe.

En plus, ce scénario offre la possibilité d'étudier de nouveaux phénomènes qui donnent lieu à des équilibres et des dynamiques inédits. Il est ainsi possible d'étudier les transitions de soliton et la manière dont elles se manifestent dans ce modèle. Ces résultats peuvent avoir des implications significatives pour la compréhension des systèmes astrophysiques. En particulier, dans le contexte des galaxies, les galaxies très massives peuvent être assimilées au régime FDM, tandis qu'en dessous d'un certain seuil, l'équilibre entre les auto-interactions et la gravité s'applique aux galaxies satellites. En revanche, les galaxies plus petites présentent un équilibre entre la pression quantique et la gravité. Ces simulations pourraient nous éclairer sur les mécanismes qui régissent leur équilibre et leur dynamique. Les comparaisons avec d'autres modèles de matière noire en considérant ce potentiel, nous visons à étendre notre compréhension au-delà du modèle quartique et de la matière noire floue. Ce faisant, nous pouvons établir un lien et faciliter les comparaisons avec d'autres modèles de matière noire, nous pouvons établir un lien et faciliter les comparaisons entre ces deux modèles.

Le modèle A est basé sur un potentiel de cosinus limité, tandis que le modèle B est le potentiel opposé. Nous examinons les halos formés à une échelle comparable à la longueur d'auto-interaction. Dans le modèle A, un soliton central soutenu par les auto-interactions se forme rapidement lorsque la densité critique est élevée. Ce soliton représente une fraction significative de la masse totale et réduit les fluctuations initiales de densité. Lorsque la densité critique est intermédiaire, un nouveau phénomène apparaît. On passe d'un soliton dominé par les auto-interactions qui s'effondre à un pic de matière noire dominé par la pression quantique. Aux faibles densités critiques, la formation du pic FDM est retardée mais se produit quand même, ce qui indique que la formation du pic FDM est plus efficace lorsque la condition initiale est un état cohérent.

Dans le modèle B, les solitons se forment rapidement lorsque la densité critique est petite et intermédiaire. Cependant, la forme du soliton dans ce dernier cas présente de légères variations par rapport aux autres cas. La chute de densité aux bords est plus rapide, ce qui peut être attribué à l'absence d'un potentiel d'auto-interaction, ce qui signifie qu'aucune force n'agit dans cette région. Aux grandes densités critiques, le système ne conduit pas à la formation de solitons. L'absence de formation de solitons à de grandes densités critiques s'aligne sur des études antérieures indiquant l'évaporation de solitons légers dans les halos FDM.

Nous étudions également des halos avec des tailles beaucoup plus grandes que l'échelle d'auto-interaction et nous trouvons que la formation de solitons prend un temps considérable dans des profils de densité plats pour les modèles A et B lorsque le potentiel ressemble au modèle quartique. Dans d'autres cas, un régime flou de matière noire est observé avec la signature d'un halo fluctuant.

Dans l'ensemble, ces résultats donnent un aperçu de la formation et de l'évolution des solitons dans les modèles scalaires de matière noire, en soulignant l'influence des auto-interactions et des conditions initiales sur l'émergence des solitons et des pics FDM.

Grâce à ces études, nous avons élargi l'étendue de nos connaissances dans les différents modèles scalaires de la matière noire. Nous avons pu mieux comprendre la frontière semi-classique entre les modèles CDM et SFDM, ainsi que la formation et l'évolution des solitons dans les halos de matière noire.

Chapter 1

Introduction

The nature of dark matter is currently one of the greatest challenges in Cosmology, from the perspective of General Relativity and the Standard Model of Particle Physics. Dark matter is a hypothetical form of matter that does not interact with light or other forms of electromagnetic radiation, meaning that it does not reflect, absorb and emit light, making it invisible and difficult to detect. This is why it is called *dark matter* (DM). Its existence is inferred from its gravitational effects on visible matter and the large-scale structure of the Universe. Measurements of the Cosmic Microwave Background (CMB) radiation, the afterglow of the Big Bang from the Planck (Planck Collaboration et al., 2020a) and WMAP (Bennett et al., 2013) missions have provided strong evidence that dark matter makes up about 85% of the total matter in the Universe.

The Standard Model of Particle Physics, which describes the known elementary particles and their interactions, does not explain the properties of dark matter. Dark matter particles, if they exist, must be non-baryonic, meaning that they are not made up of the same building blocks as ordinary matter (protons, neutrons and electrons) (Del Popolo, 2014). This suggests that an extension of the Standard Model is needed to include dark matter.

The combination of dark matter and the cosmological constant gives rise to the ΛCDM model (see eg. Weinberg (2008)) the Standard Model of Cosmology. This framework is the most widely accepted cosmological model describing the evolution and properties of our Universe. It is based on the combination of the cosmological constant (Λ) and cold dark matter (CDM). The cosmological constant, represents a form of energy that is uniformly distributed throughout space and contributes to the acceleration of the expansion of the Universe. It was first introduced by Einstein (1986) and is often associated with the concept of dark energy. The exact nature of dark energy remains unknown, but it contributes about 68% of the total energy in the Universe (Planck Collaboration et al., 2020a). On the other hand, CDM refers to Cold Dark Matter, a type of dark matter consisting of non-relativistic particles that move slowly on cosmic scales (Peebles, 1982; Bond et al., 1982). It is thought to be "cold" because it has no significant kinetic energy. The Standard Model of Cosmology has been remarkably successful in simulating and reproducing the observed features of the Universe. It provides a comprehensive framework that closely matches our observations.

However, the lack of DM signal in the most promising channels (Schumann, 2019; Conrad, 2014; Arcadi et al., 2018), and the inconsistencies that arise as observations and simulations of the galactic and subgalactic scales improve (Weinberg et al., 2015), open a

new window for exploring new DM models.

Therefore, in this thesis we will venture beyond the Standard Models of Particle Physics and Cosmology. We will explore different aspects of Scalar Field Dark Matter (SFDM) (Hu et al., 2000; Goodman, 2000), an intriguing alternative to the conventional CDM paradigm which challenges some of the assumptions underlying the ΛCDM model. By considering this alternative, we aim to broaden our understanding and explore the possibilities beyond the established framework.

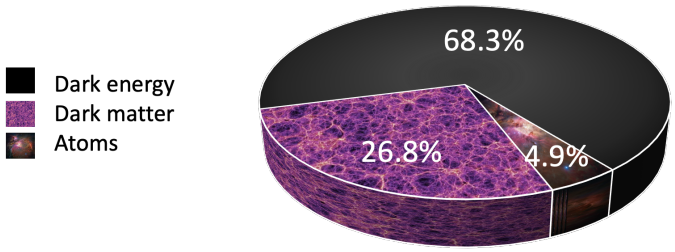

Figure 1.1. Energy content of the Universe

This chapter is organized as follows: In Section 1.1, we present the observational evidence that supports the existence of dark matter. Then, in Section 1.2, we provide an overview of the CDM paradigm and we discuss its success. Next, in Section 1.3, we examine the challenges faced by the CDM model. Finally, in Section Section 1.4, we introduce scalar field dark matter as an alternative to the CDM model.

1.1 Observational evidence

The existence of dark matter is supported by its gravitational influence on visible matter. These gravitational effects have been observed at different scales and are briefly described below.

1.1.1 Galaxy clusters

The first observational evidence for dark matter came in 1933, when the Swiss astronomer Fritz Zwicky suggested the existence of missing matter by studying the dynamics of the Coma cluster (Zwicky, 1933). He used spectral redshift to measure the radial velocities of 7 galaxies belonging to Coma and estimated the total dynamical mass of the cluster using the virial theorem. Then, he compared this dynamical mass with the luminous mass obtained from the rotation curve of some nearby galaxies and found a discrepancy between them by a factor of 400. This led him to conclude that the existence of invisible matter, which he called dark matter, had a significant effect on the dynamics of the Coma cluster. The work of Zwicky on the Coma cluster was followed up by Smith (1936) for the Virgo cluster. Once again, the velocities of its galaxies highlighted an unexpectedly high mass-to-light ratio.

1.1.2 Rotational curves

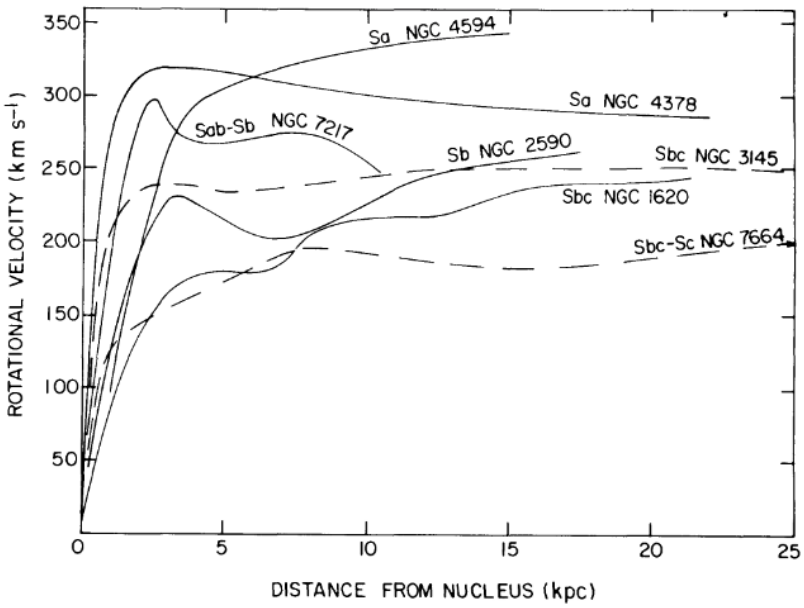

Figure 1.2. Figure from Rubin et al. (1978). Rotational velocities for seven galaxies as a function of distance from nucleus.

Vera Rubin and collaborators significantly advanced our understanding of spiral galaxies by making high-resolution measurements of their rotation curves (Rubin & Ford, 1970). She discovered that the rotation curves of these galaxies remain flat even at very large radii. This poses a challenge to Newtonian analysis, which suggests that the orbital velocity should decrease as one moves away from the galactic centre. The rotation, or circular velocity is given by,

$$v_c = \sqrt{\frac{GM(<r)}{r}}, \tag{1.1}$$

where $M(<r) = \int_0^r 4\pi r^2 \rho(r)$ is the mass enclosed by a radius r and $\rho(r)$ is the density profile. For large values of r, where the density profile ($\rho(r)$) is expected to be zero, the velocity $v_c \propto r^{-1/2}$ follows a Keplerian fall-off. However, the observed rotational speeds in spiral galaxies remain roughly constant at large r, as seen in Fig.1.2, indicating that $M(<r) \propto r$ and $\rho(r) \propto r^{-2}$. These results strongly suggest the presence of a spherical dark matter halo surrounding the luminous matter, which contributes significantly to the flat behaviour of the rotation curves through gravitational forces under the assumption of Newtonian gravity. Ostriker & Peebles (1973) further supported this idea with numerical simulations, showing that the galactic discs of spiral galaxies would be unstable if only baryonic matter were considered. However, the inclusion of a dark matter halo resolves the problem of disc instability.

1.1.3 Gravitational lensing

The existence of dark matter is further supported by gravitational lensing, a phenomenon predicted by General Relativity. Gravitational lensing occurs when the space-time is

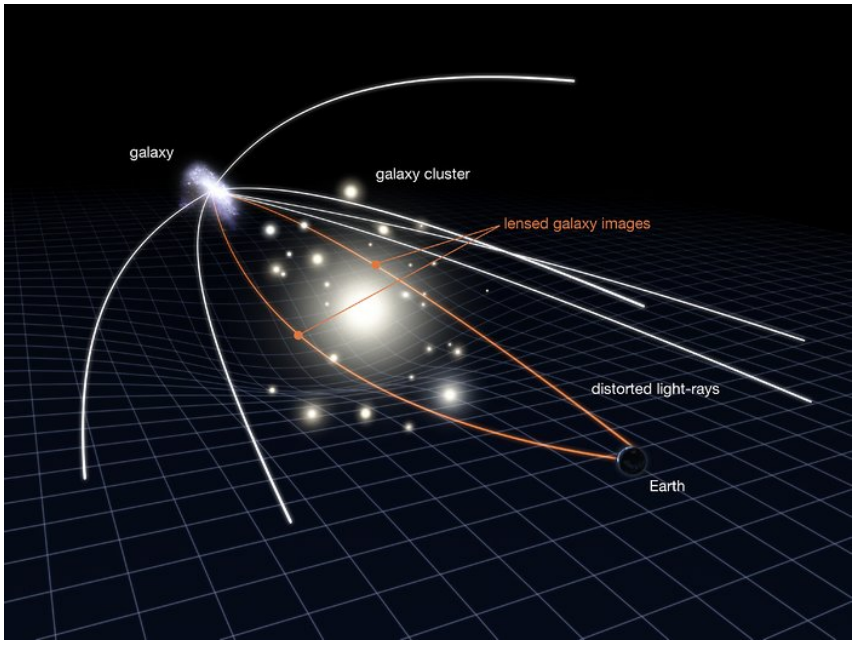

Figure 1.3. Illustration of gravitational lensing (Image: NASA, ESA & L. Calçada).

Figure 1.4. Gravitational lensing in Webb's First Deep Field taken by James Webb Space Telescope (2022). Galaxy cluster SMACS 0723 (Image credit: NASA, ESA, CSA, and STScI)

distorted by massive objects, causing the path of photons from a distant source to deviate based on irregularities in the mass distribution along the way (Einstein, 1936; Chwolson, 1924), as illustrated in Fig.1.3. As a result, the images of distant bright sources carry information about the cosmic structure.

Strong lensing occurs when extremely massive objects like galaxies or clusters of galaxies cause multiple images and distorted shapes of objects, as seen in Fig.1.4. From these images, we can reconstruct the total matter content and sometimes its distribution. This technique has revealed intriguing conclusions, such as the dominance of dark matter in galaxies and galaxy clusters (Massey et al., 2010; Limousin et al., 2022).

Weak lensing, also known as gravitational shear, refers to the collective gravitational lensing effect caused by the distribution of matter in the Universe. It causes subtle distortions in the images of distant galaxies. By studying gravitational weak-lensing maps of large clusters of galaxies, it has been observed that the gravitational potential does not align with the distribution of visible mass (Kaiser & Squires, 1993). This provides evidence that these structures are primarily influenced by dark matter. Another compelling evidence for dark matter is observed in the Bullet cluster Fig.1.5, formed by the collision

Figure 1.5. Bullet Cluster. The optical image from the Magellan and the Hubble Space Telescope shows galaxies in orange and white in the background. Hot gas, which contains the bulk of the normal matter in the cluster, is shown by the Chandra X-ray image, which showst the hot intracluster gas (pink). Gravitational lensing, the distortion of background images by mass in the cluster, reveals the mass of the cluster is dominated by dark matter (blue), an exotic form of matter abundant in the Universe, with very different properties compared to normal matter. Credit: NASA.

of two clusters. By mapping baryonic matter through X-ray observations and inferring gravitational mass through weak and strong lensing (Clowe et al., 2006), we observe the separation of baryonic and dark matter components.

1.1.4 Cosmic Microwave Background

After the Big Bang, a hot dense plasma of particles (mostly protons, neutrons, and electrons) and photons (light) filled space in the Universe. As the Universe expanded, the plasma and radiation gradually cooled and neutral atoms formed when electrons combined with protons, and the temperature was too low to separate them again. This allowed photons to travel freely without being absorbed by the neutral atoms, giving rise to the cosmic microwave background. Measurements of the CMB show that its temperature is nearly uniform across the sky. However, small variations in temperature contain valuable information about the Universe. In the early stages, ordinary matter was ionised and interacted with radiation through Thomson scattering, while dark matter interacted with radiation only weakly, if at all. As a result, the CMB was affected differently by dark matter compared to ordinary matter.

The discovery of the CMB (Penzias & Wilson, 1965) and subsequent measurements, such as COBE satellite (Smoot et al., 1992), the MAXIMA (Hanany et al., 2000) and BOOMERanG (Mauskopf et al., 2000) experiments and observations by WMAP (Hinshaw et al., 2013) and Planck (Planck Collaboration et al., 2020b), have provided further evidence for the existence of dark matter. These observations suggest that dark matter accounts for about 26% of the energy density of the Universe, while ordinary matter accounts for about 5%. The different behaviour of dark matter and ordinary matter is

expected to leave its mark on the CMB, providing a means of distinguishing between the two components through analysis of the CMB power spectrum. In particular, extensive studies have convincingly revealed a density field in the CMB that is dominated by dark matter (Dent et al., 2012; Chluba & Grin, 2013).

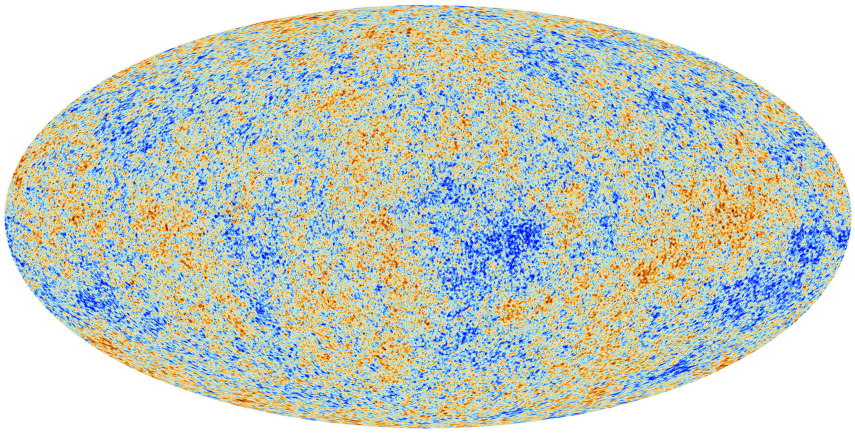

Figure 1.6. Planck CMB. Projection of sphere, where the colours represent deviations with respect to a homogenous distribution of temperature. The scale of the typical deviation is 10^5. Credit: ESA and the Planck Collaboration

1.2 CDM paradigm and success

The combined evidence from the dynamics of galaxies and galaxy clusters, gravitational lensing, and the anisotropies observed in the CMB strongly supports the existence of a significant dark component within the matter composition of the Universe as we have seen in Section 1.1. Observations consistently show that dark matter is massive, stable over long periods of time, largely collisionless, and interacts primarily gravitationally, while remaining distinct from baryonic matter. However, one of the major challenges in understanding dark matter is its lack of electromagnetic interaction, which limits our ability to constrain its specific properties. These properties provide important clues, and many dark matter candidates with a huge range of masses, as seen in Fig.1.7, have been proposed in recent decades. In this section, we briefly discuss some potential candidates for dark matter and explain why the CDM paradigm has become the dominant model in cosmology.

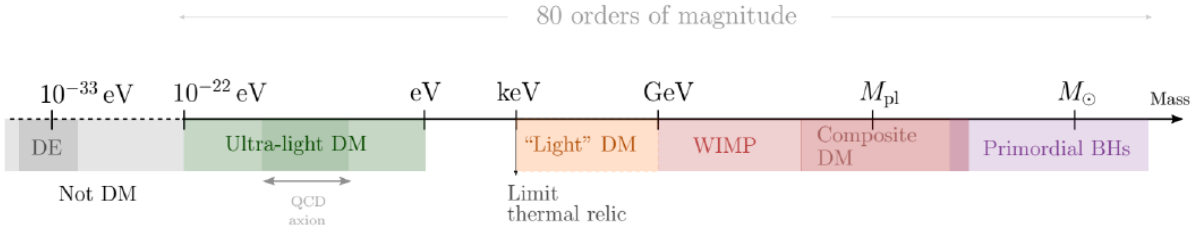

Figure 1.7. Figure from (Ferreira, 2020). Sketch (not to scale) of the huge range of possible DM models that have been conceived. They span many orders of magnitude in mass, with DM represented by very distinct phenomena, ranging from new elementary particles to black holes

Dark matter models can be categorized in different ways, such as astrophysical or particle origin. Examples of astrophysical dark matter include Massive Compact Halo Objects (MACHOs) (Alcock et al., 1993; Griest, 1996; Tisserand et al., 2007; Yoo et al., 2004) and primordial black holes (Bird et al., 2016; García-Bellido & Ruiz Morales, 2017; Sasaki et al., 2018). On the other hand, particle dark matter examples encompass axions (Peccei & Quinn, 1977; Kim, 1979; Graham et al., 2015; Svrcek & Witten, 2006; Bachlechner et al., 2019; Marsh, 2016), neutrinos (Dodelson & Widrow, 1994; Shi & Fuller, 1999; Kopp, 2021), or supersymmetric partners to Standard Model particles (Jungman et al., 1996; Drees et al., 2004; Steigman & Turner, 1985). These particle candidates for dark matter are often called Weakly Interacting Massive Particles (WIMPs) because they interact weakly through gravity and weak interactions while being non-electromagnetic.

Another important categorization of dark matter is its energy scale, which determines its characteristic velocities. Candidates can be classified as *hot, warm,* or *cold*, depending on their velocities. Neutrinos are an example of hot dark matter (HDM) as they travel at speeds close to the speed of light. In contrast, stable supersymmetric WIMP particles are considered CDM since they move much slower than light. There are also warm dark matter (WDM) candidates like light gravitinos (Steffen, 2006) that exhibit intermediate behaviour. Mapping of CMB anisotropies has provided increasingly stringent constraints on dark matter models (Galli et al., 2009, 2011; Planck Collaboration et al., 2020c,a) turning the CDM as the prevailing dark matter model.

The success of the CDM model can be attributed to several factors. First, as we see in Fig.1.8, it is consistent with detailed measurements of the CMB. Moreover, it it successfully predicts and explains the observed large-scale structure of the Universe, including the formation of galaxy clusters, filaments, and voids observed in galaxy surveys and it effectively reproduces the observed large-scale structure with N-body simulations (Jing et al., 1998; Coil, 2013; Springel et al., 2006) solving Vlasov or Collisionless Boltzmann equation as seen in Fig. 1.9.

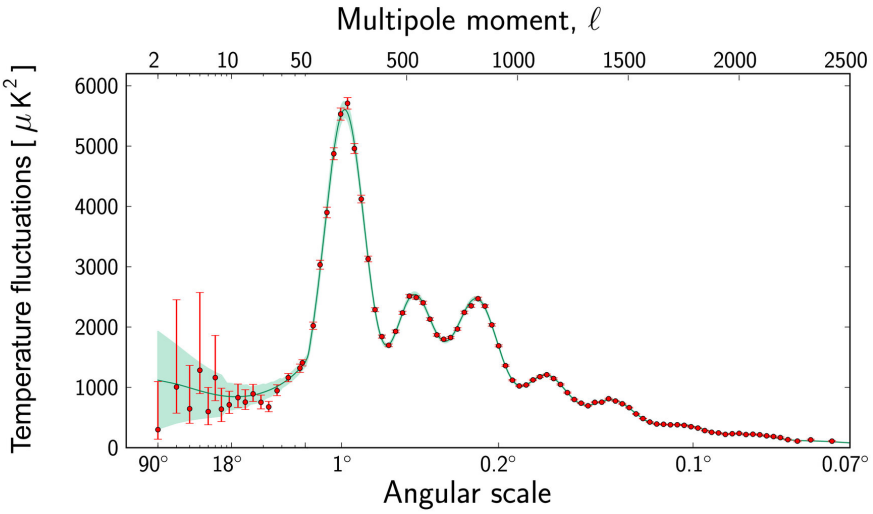

Figure 1.8. The temperature fluctuations in the CMB measured by Planck (red dots) at different angular scales on the sky. The green curve represents the best fit of the ΛCDM. Credit: ESA and the Planck Collaboration (Planck Collaboration et al., 2014)

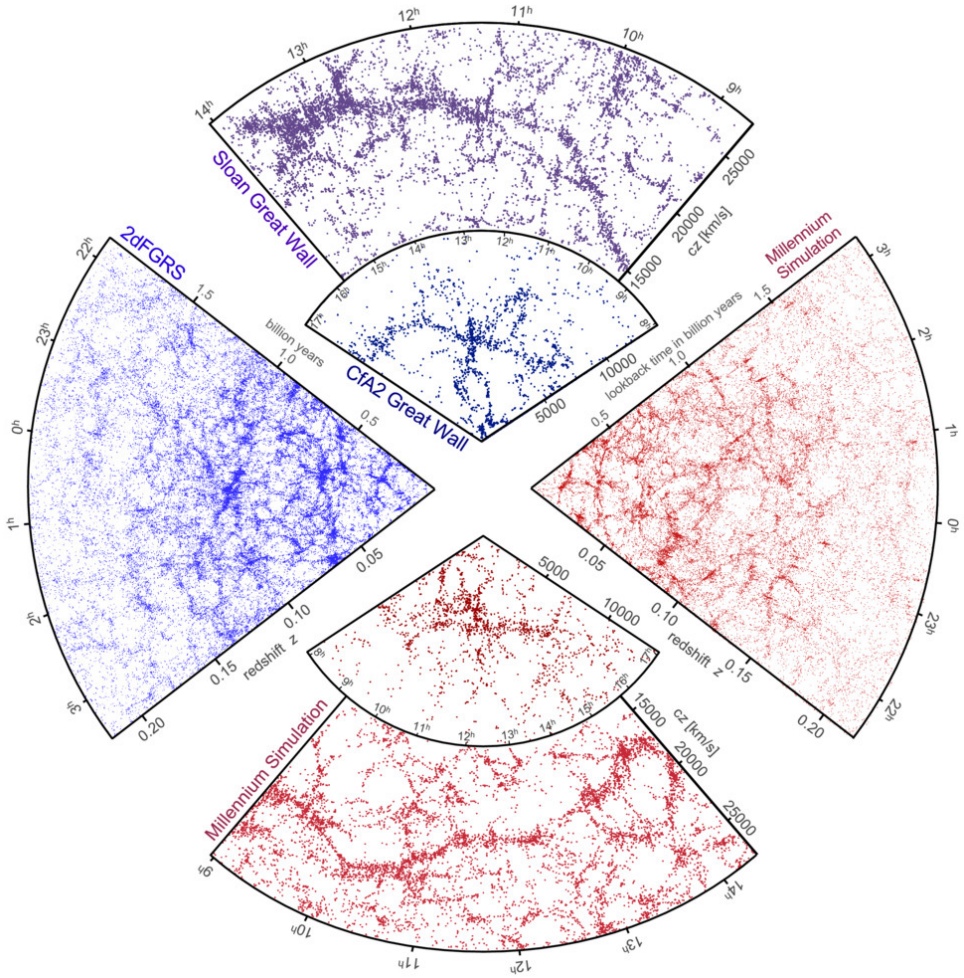

Figure 1.9. Figure from https://wwwmpa.mpa-garching.mpg.de/millennium/. Large scale structure of the Universe. In blue, observations by the 2dF Galaxy Redshift Survey (Colless et al., 2001) , the Sloan Digital Sky Survey (Gott et al., 2003) and the CfA Redshift Survey (Geller & Huchra, 1989). Each point represents a galaxy as a function of R.A. and redshift. The three redshift survey are accompanied by the corresponding N-body Millenium-II simulations considering the ΛCDM in red.

While different CDM candidates exist, supersymmetric partners to Standard Model particles are among the most popular. Specifically, models of supersymmetry where the lightest stable supersymmetric particle is a neutralino provide a natural WIMP dark matter candidate (Bednyakov et al., 1997). The appeal of this model arises because it conveniently predicts the correct relic abundance to account for dark matter, which has historically been referred to as the "WIMP Miracle". Moreover, the posibility of direct detection in experiments like the Large Hadron Collider (Giagu, 2019) and indirect detection with gamma ray-astronomy (Funk, 2015) have further bolstered the popularity. In summary, CDM has emerged as the favoured model for dark matter, with viable WIMP CDM candidates arising naturally from supersymmetric extensions to the Standard Model of particle physics.

1.3 CDM Tensions

The CDM paradigm is a powerful model that successfully explains the observed features of large-scale cosmological structures as we have seen in Section 1.2. However, as the observations and simulations of the galactic and subgalatic scales improve, a number of inconsistencies have emerged. These discrepancies are referred in the literature as small-scale tensions (Weinberg et al., 2015; Del Popolo & Delliou, 2016; Nakama et al., 2017) and the explanations are still under debate (Di Luzio et al., 2020).

1.3.1 Core-cusp

The core-cusp tension refers to the disagreement between simulations and observations of the halo density profile. In CDM-only simulations, the halo density profile typically forms a sharp cusp at the centre. This component is described by the Navarro-Frenk-White (NFW) profile (Navarro et al., 1996a). However, different observations of dwarf galaxies indicate a preference for cored density profiles (Moore, 1994; Flores & Primack, 1994). The relevance of considering these objects is that they provide excellent opportunities to study halo structure since they are dominated by DM throughout their halo. Because of this mismatch, there is ongoing discussion surrounding the core-cusp problem, and multiple solutions consistent with the CDM framework have been proposed. One of the most promising explanations highlights the importance of considering the impact of baryonic physics (Madau et al., 2014; Read et al., 2016; Dashyan et al., 2018). The latest hydrodynamical simulations suggest that baryonic feedback can smooth the inner cusps and produce core-like profiles like those observed for dwarf galaxies. However, not all simulations agree with this finding, and it is deeply complicated to model these physical processes as many parameters are introduced and sometimes are difficult to justify. Therefore, despite the suggested explanations, the core-cusp problem is still under debate. Thus, until a fully justified agreement is reached, alternatives such as modifying the properties of the DM or small-scale gravity dynamics (such as MOND) should be considered.

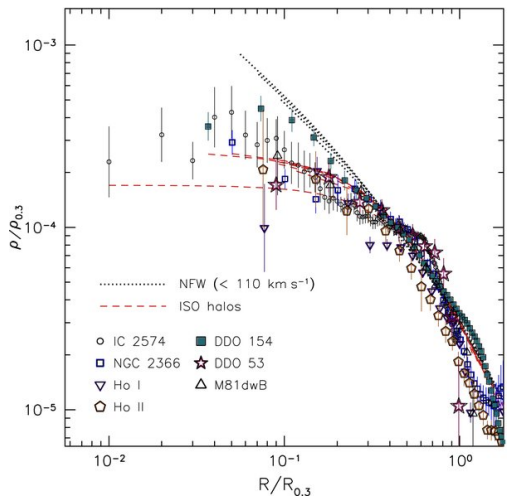

Figure 1.10. Figure from Kennicutt et al. (2011). The dark matter density profiles of the 7 THINGS dwarf galaxies. The profiles are derived using the rotation curves. The dotted lines represent the mass density profiles of NFW models The dashed lines indicate the mass density profiles of the best fit pseudo-isothermal halo models. (Kennicutt et al., 2011; Oh et al., 2015)

1.3.2 Missing satellites

The missing satellite problem emerges in the discrepancy between the over-predicted number of subhalos in the N-body simulations and the observed satellite galaxies. (Moore et al., 1999b; Klypin et al., 1999). The hierarchical structure formation in cold dark matter suggests that there should be a significant presence of dark matter substructures on smaller scales within galaxies. Precisely, it is predicted that the Milky Way (MW) should have around 500 satellite galaxies (Moore et al., 1999a). However, it is known that the MW has nine bright dSphs, Sagittarius, the LMC and the SMC.

Cosmological simulations, such as Aquarius (Springel et al., 2008), Via Lactea (Kuhlen et al., 2008), and GHALO simulations (Stadel et al., 2009), have confirmed the issue of the predicted excess of small subhalos in Milky Way-like galaxies.

Although not fully resolving the problem, the discovery of ultra-faint dwarf satellites (UFDs) (Drlica-Wagner et al., 2015) has provided some relief. By including these UFDs in the known satellites of the MW, the gap between the observed and predicted numbers can be reduced. This approach considers that only a subset of the population of satellites is visible, which helps to alleviate the discrepancy. However, this is not enough. Hence several proposals have been suggested to alleviate this issue. Essentially, they include the impact of baryonic physics in the equation. Incorporating baryonic mechanisms such as tidal stripping, re-ionization stripping, photo-ionization and gas stripping, and transfer of angular momentum (Brooks et al., 2013). Despite the numerous suggestions to address the issue of missing satellites, it continues to pose a significant challenge for current CDM models and prompts the exploration of alternative models.

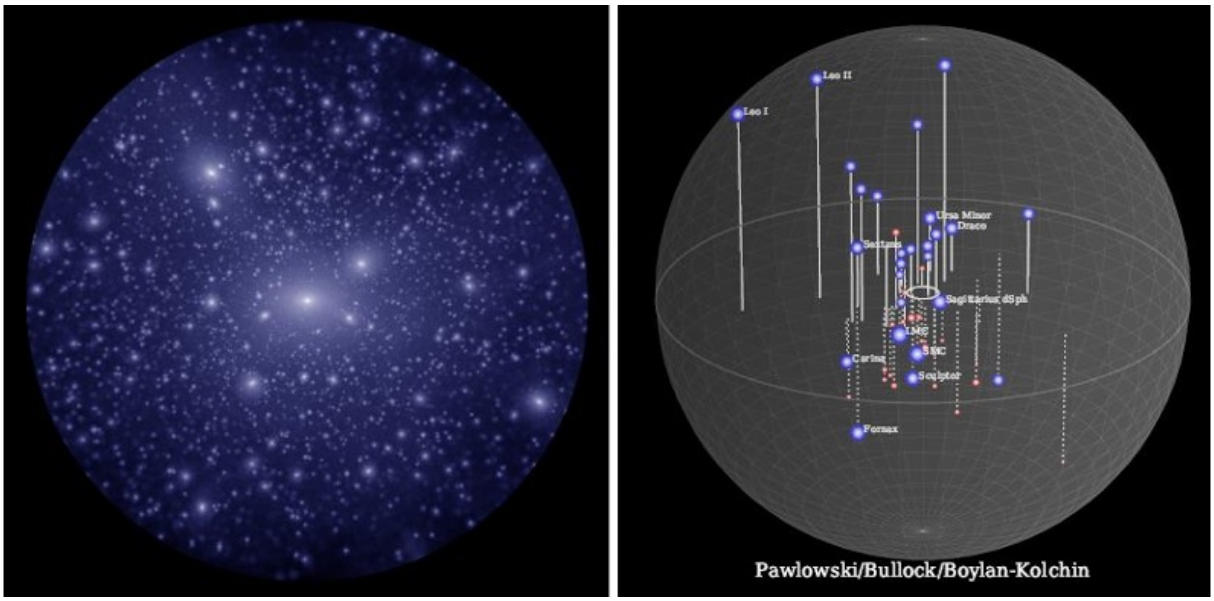

Figure 1.11. Figure from Bullock & Boylan-Kolchin (2017). *Left panel:* Predicted ΛCDM substructure within a sphere of radius 250 kpc around the center of a Milky-Way size dark matter halo (simulation by V. Robles and T. Kelley in collaboration with the authors). *Right panel:* known Milky Way satellites: The image on the right (by M. Pawlowski in collaboration with the authors) shows the current 2017 census of Milky Way satellite galaxies, with galaxies discovered since 2015 in red. The Galactic disk is represented by a circle of radius 15 kpc at the center and the outer sphere has a radius of 250 kpc.

1.3.3 Too-big-to-fail

The too-big-to-fail problem arises as a challenge in understanding the distribution of subhalos within the MW and other galaxies (Garrison-Kimmel et al., 2014). According to CDM simulations, the most massive subhalos should correspond to the visible subhalos observed in the MW (Boylan-Kolchin et al., 2011). However, the simulations predict that these massive subhalos have central masses that are too large to host the observed satellite galaxies. On the other hand, subhalos with central masses similar to those expected in the MW are not the most massive. This discrepancy is not unique to the MW and extends to other galaxies in the Local Group and Local Volume.

Several proposed solutions to the too-big-to-fail problem involve astrophysical processes driven by baryons. However, these solutions seem compelling only for the MW and require highly efficient feedback mechanisms like supernova feedback (Chan et al., 2015). There is ongoing debate, and no consensus has been reached regarding these proposed solutions. Recent claims suggest that the too-big-to-fail problem has been resolved (Ostriker et al., 2019), but this remains a topic of intense discussion.

Addressing both the missing satellite problem and the too-big-to-fail problem, scalar field dark matter models offer potential solutions. These models propose mechanisms that suppress the formation of small-scale subhalos and reduce the central densities of massive subhalos, potentially modifying the dynamics of the central regions. These alternative models provide a potential avenue for understanding the internal structure of subhalos and resolving the discrepancies observed in simulations.

1.4 SFDM as an alternative to CDM

Given the open challenges to the CDM model discussed in Section 1.3, alternative approaches have emerged that can address these issues while preserving the achievements of the CDM (see Section 1.2). These alternatives should replicate the CDM predictions about the large-scale structure of the universe, while providing a natural solution to the small-scale crisis. In addition, they should account for the lack of direct detection evidence and be well supported from a particle physics point of view. In this section we briefly outline the SFDM as an alternative to the CDM.

The main underlying assumption of SFDM is that the mass associated with the field must be extremely light, of the order of 10^{-22} eV (Hu et al., 2000; Hui et al., 2017). This corresponds to a de Broglie wavelength on the kiloparsec scale,

$$\lambda_{dB} = \frac{2\pi}{mv} = 0.48\text{kpc}\left(\frac{10^{-22}\text{eV}}{\text{m}}\right)\left(\frac{250\text{km/s}}{\text{v}}\right). \tag{1.2}$$

Thus, at scales much smaller than λ_{dB}, the field exhibits a wave-like behaviour leading to wave-like interferences such as those shown in the left panel of Fig.1.12 . We anticipate here that these wave-like effects are due to a new pressure term that arises in the equation of motions, also called *quantum pressure*, arising from the gradients of the scalar field. When this quantum pressure balances with gravity, an equilibrium solution is formed. These solutions are called solitons (Lee & Pang, 1992; Guth et al., 2015; Sikivie & Yang, 2009). They appear at the centre of the halos and give rise to a flat radial density profile at the centre, as shown in the right panel of Fig. 1.12. If the SFDM includes interactions,

the equilibrium can be obtained by balancing the self-interaction pressure with gravity. We will see this with equations in In Chapter 2.

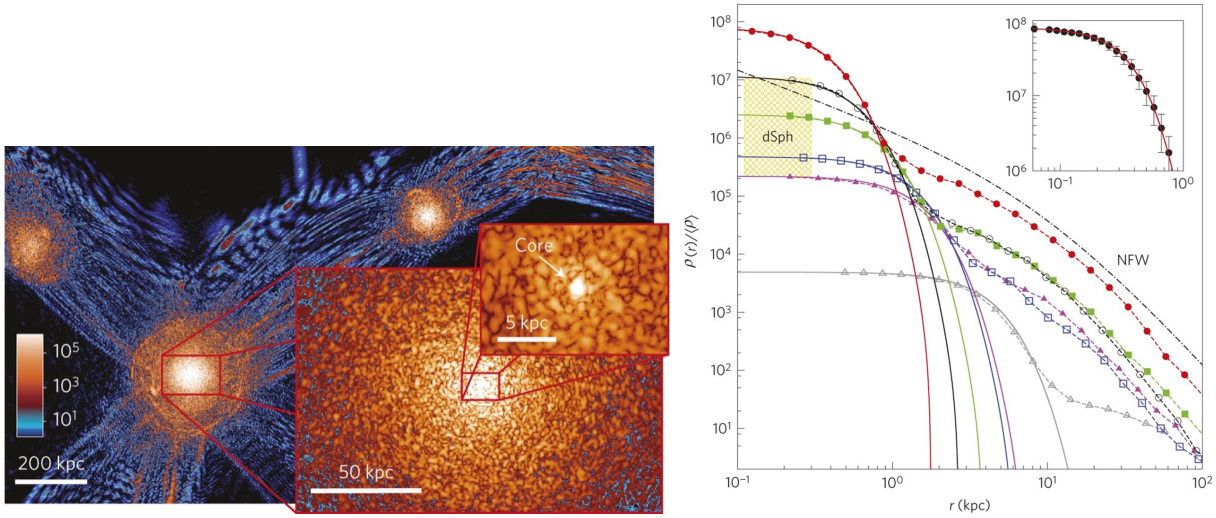

Figure 1.12. Figure from (Schive et al., 2014a). *Left panel*: A slice of the ψDM simulation density field at different scales at z = 0.1. *Right panel*: Radial density profiles of halos formed in the ψDM model.

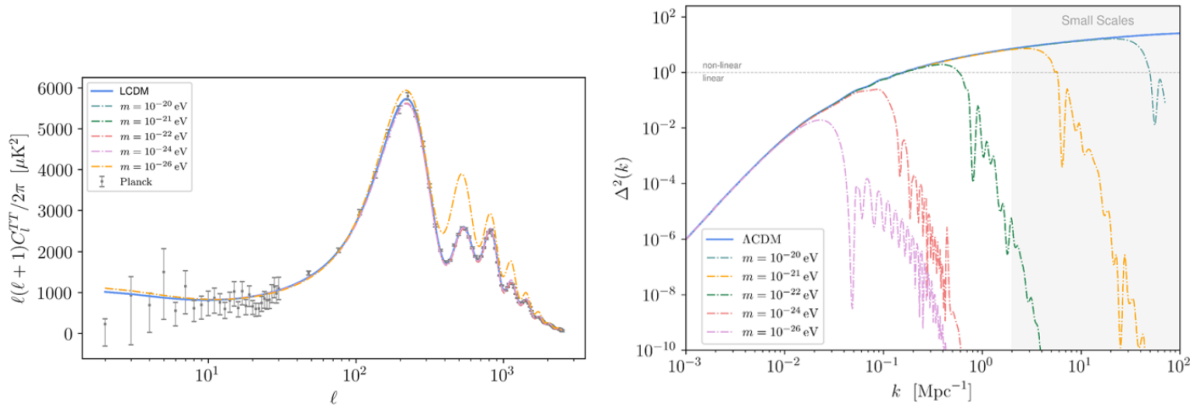

Figure 1.13. Figure from (Ferreira, 2020). *Left panel*: Angular power spectrum of the CMB temperature anisotropy for the FDM model for different masses, where the FDM is considered to be all the DM in the Universe. We compare this to the best fit of the ΛCDM model to the Planck data (Ade et al. 2018), shown by the grey data points. *Right panel*: Matter power spectrum for the same FDM model used in the left panel.

Consequently, the interplay between gravity and quantum pressure yields a redshift-dependent Jeans scale, below which structures cannot form. We can see this in the right panel of Fig.1.13, which shows the matter power spectrum for different ultra-light DM particles. We can see that on small scales there is a suppression of structure formation with a mass-dependent cut-off, and on large scales the CDM power spectrum is recovered.

On scales much larger than the de Broglie wavelength, however, the behaviour of SFDM is indistinguishable from that of CDM (Shapiro et al., 2022). Figure 1.14 shows a slice of the cosmological simulation for CDM and for SFDM. We can see that we recover the distribution of voids and filaments when we compare the two results. However, it is important to note that the CDM simulation has a clumpy behaviour. This is because

here, nothing can overcome gravity. In CDM there is no quantum pressure nor effective pressure to balance gravity and suppress structure formation. In addition, in the upper panel of Fig. 1.13 representing the CMB power spectrum, we can observe how these models reproduce the CDM success. In Chapter 3 we extend the discussion of how SFDM converges to CDM analytically . Thus, SFDM represents an innate solution to the small-scale crisis, while preserving the achievements of the CDM at larger scales (Ferreira, 2020; Hui, 2021).

From a particle physics point of view, the idea of an extremely light boson finds support in several particle physics scenarios. A notable example is the QCD axion, which solves the strong CP problem (Peccei & Quinn, 1977). As an ultra-light boson, SFDM provides a viable dark matter candidate without relying on supersymmetric extensions of the Standard Model.

Overall, SFDM is emerging as a well-supported alternative to CDM, demonstrating potential for solving the CDM small-scale challenges. At the same time, the convergence of SFDM and CDM predictions on cosmological scales ensures that this model serves as a viable candidate for reproducing observations derived from cosmological structure formation studies.

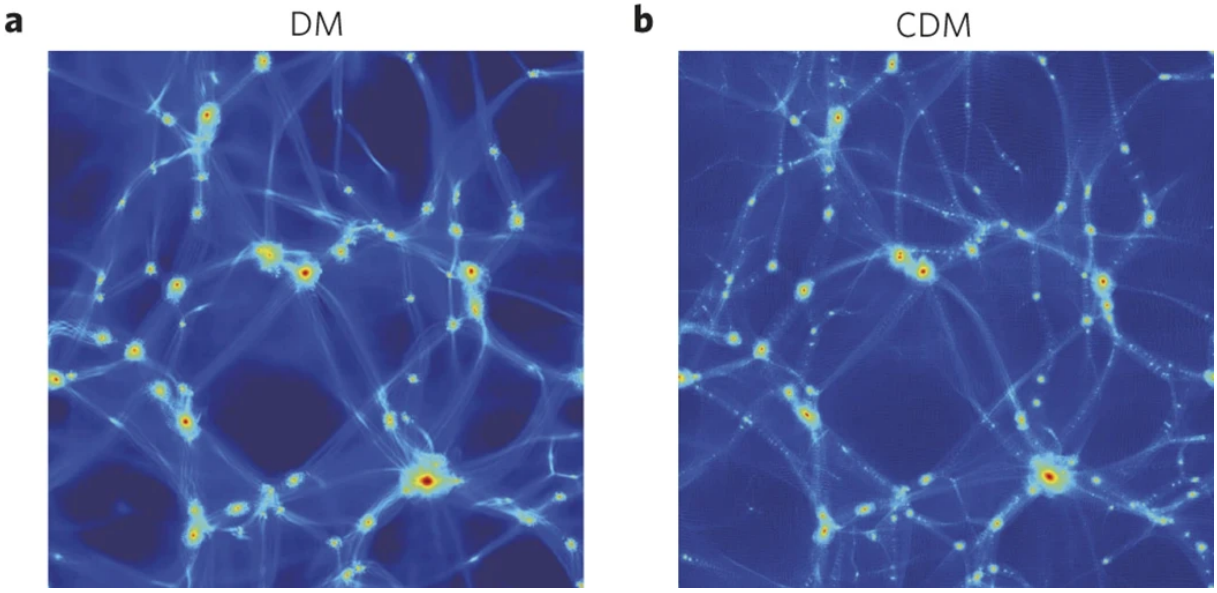

Figure 1.14. Figure from (Schive et al., 2014a). This comparison clearly demonstrates that the large-scale distribution of filaments and voids is indistinguishable between our model and ΛCDM (which has been successful in describing the observed large-scale structure)

Chapter 2

Scalar field dark matter models

In this chapter, we present how scalar fields can play the role of dark matter and the main equations of the theory. We focus on an effective model of scalar dark matter that remains valid below a specific cut-off energy scale, denoted as Λ. The theory governing the behaviour of the Universe beyond this energy scale is left open. Within this effective framework, we assume the action is local with a standard kinetic term that is quadratic over the first derivatives of the scalar field. Note that higher order Lagrangians can often lead to problematic ghost-like behaviour. However, we do not assume any specific form for them in this context. Instead, we consider that all the terms involving higher derivatives correspond to the propagation of additional degrees of freedom with a mass equal to or greater than the cut-off Λ. Consequently, their impact becomes negligible at energies below Λ. As a result, we present a scalar model featuring a light particle with mass m subject to self-interactions as defined by the Lagrangian.

This chapter is organized as follows: In Section 2.1, we introduce the Lagrangian with a potential and standard kinetic terms, and the action of a scalar field dark matter model. Section 2.2 focuses on the equation of state, while Section 2.3 explores how this model reproduces the characteristics of cold dark matter at the background level. The inclusion of gravity perturbations is discussed in Section 2.4. The dynamics of small scales in the Universe are addressed in Section 2.5. The small scale dynamics of fuzzy dark matter and the quartic potential, as well as the presence of solitonic cores in hydrostatic equilibrium, are presented in Section 2.6 and Section 2.7, respectively. The cosine model is introduced in Section 2.8. Finally, the expansion of the universe in the non-relativistic regime is introduced in Section 2.9.

2.1 Scalar field dark matter Lagrangian

Let us consider the following Lagrangian of a real scalar field ϕ,

$$\mathcal{L}_\phi = -\frac{1}{2} g^{\mu\nu} \partial_\mu \phi \partial_\nu \phi - V(\phi), \tag{2.1}$$

where $g^{\mu\nu}$ is the metric, the first term is the standard kinetic term and $V(\phi)$ is the potential. Gravitational interactions only takes place through the metric. For the moment, we are not going to detail further the potential function $V(\phi)$, but we advance that for

the scalar field to behave like dark matter, we need it to have the following form,

$$V(\phi) = \frac{m^2}{2}\phi^2 + V_I(\phi), \tag{2.2}$$

where $V_I(\phi)$ is the self-interaction potential,

$$V_I(\phi) = \Lambda^4 \sum_{n\geq 3} \frac{\lambda_p}{p}\frac{\phi^p}{\Lambda^p}. \tag{2.3}$$

Note that we are working in natural units, $c = \hbar = 1$, so the units of the field quantities will be $[\phi] = [m] =$ energy.

The Lagrangian density for the metric is

$$\mathcal{L}_{EH} = \frac{\mathcal{R}}{2\kappa^2}, \tag{2.4}$$

where $\kappa^2 = 8\pi\mathcal{G}_{\rm N}$, $\mathcal{G}_{\rm N}$ is the Newton's gravitational constant and $\mathcal{R}$ is the Ricci scalar (scalar curvature). Equation (2.4) is the Lagrangian for the Einstein-Hilbert action of General Relativity. Note that the scalar field is not coupled to the curvature, i.e. $\phi\mathcal{R}$, so it is minimally coupled to gravity and we assume that ϕ is not coupled to other fields of the Universe. The total Lagrangian of the system reads

$$\mathcal{L} = \mathcal{L}_{EH} + \mathcal{L}_\phi + \mathcal{L}_m, \tag{2.5}$$

where $\mathcal{L}_m$ is the Lagrangian of the standard model particles (baryons, photons) and possible dark energy components. Therefore, the total action is given by

$$S = \int d^4x\sqrt{-g}\,\mathcal{L}, \tag{2.6}$$

where g is the determinant of the metric tensor. The action for the scalar field only reads,

$$S_\phi = \int d^4x\sqrt{-g}\,\mathcal{L}_\phi. \tag{2.7}$$

2.2 Equation of state

The energy-momentum tensor of the scalar field is given by $T_{\mu\nu}$,

$$T_{\mu\nu} = \partial_\mu\phi\partial_\nu\phi - g_{\mu\nu}\left[\frac{1}{2}g^{\alpha\beta}\partial_\alpha\phi\partial_\beta\phi + V(\phi)\right]. \tag{2.8}$$

The last equation can be written in an analogous form to that of a perfect fluid as

$$T_{\mu\nu} = (\rho_\phi + P_\phi)\,u_\mu u_\nu + P_\phi g_{\mu\nu}, \tag{2.9}$$

where we have defined the effective energy density ρ_ϕ, the effective pressure P_ϕ and the 4-velocity for the scalar field as follows:

$$\rho_\phi = -\frac{1}{2}\partial^\mu\phi\partial_\mu\phi + V(\phi), \tag{2.10}$$

$$P_\phi = -\frac{1}{2}\partial^\mu\phi\partial_\mu\phi - V(\phi), \tag{2.11}$$

$$u^\mu = \frac{\partial^\mu\phi}{\sqrt{-\partial^\mu\phi\partial_\mu\phi}}. \tag{2.12}$$

The state parameter ω_ϕ is defined as

$$P_\phi = \omega_\phi\rho_\phi. \tag{2.13}$$

2.3 Cosmological background

To understand the evolution of the scalar field ϕ, let us apply the principle of least action $\delta S = 0$ in (2.7) to get the equations of motion. Thus, varying this action with respect to ϕ we have

$$\Box\phi + \frac{dV(\phi)}{d\phi} = 0, \tag{2.14}$$

where $\Box$ is d'Alembert operator,

$$\Box\phi = -\frac{1}{\sqrt{-g}}\partial_\mu\left[\sqrt{-g}g^{\mu\nu}\partial_\nu\phi\right]. \tag{2.15}$$

Equation (2.14) is known as the Klein-Gordon equation in General Relativity. To study the evolution of the field ϕ in a an expanding Universe, we take the appropriate Friedmann-Lemaître-Robertson-Walker (FLRW) metric,

$$ds^2 = -dt^2 + a^2(t)d\vec{x}^2, \tag{2.16}$$

where $a(t)$ is the cosmological scale factor that parametrizes the relative expansion of the universe and $\vec{x}$ the comoving spatial coordinate. Note that for a cosmological scalar field at the background level, we have, $\phi(t,x) = \phi(t)$ and $\partial_i\phi = 0$ since it does not depend on the spatial coordinates. Using this metric in equation (2.14), we obtain the equations of motion of $\phi(t)$ for a flat, isotropic homogeneous and expanding universe:

$$\ddot{\phi} + 3H(t)\dot{\phi} + \frac{dV(\phi)}{d\phi} = 0, \tag{2.17}$$

where $H(t) = \dot{a}/a$ is the Hubble expansion rate. As we can see, equation (2.17) is simply the equation of a damped harmonic oscillator ϕ. Therefore, the competition between the Hubble friction term and the potential term will determine the cosmological evolution. The energy density (2.10) and the pressure (2.11) for ϕ is given by

$$\rho_\phi = \frac{1}{2}\dot{\phi}^2 + V(\phi), \tag{2.18}$$

$$P_\phi = \frac{1}{2}\dot{\phi}^2 - V(\phi), \tag{2.19}$$

Therefore, the equation of state (2.13) for the scalar field is written as

$$\omega_\phi = \frac{\frac{1}{2}\dot{\phi}^2 - V(\phi)}{\frac{1}{2}\dot{\phi}^2 + V(\phi)}. \tag{2.20}$$

To understand fully the cosmological evolution, let us consider $V_I(\phi) = 0$, the simplest scenario to exemplify it. This model is known as Fuzzy Dark Matter and we will present it in Section 2.6. Hence, equation (2.17) translates into

$$\ddot{\phi} + 3H(t)\dot{\phi} + m^2\phi = 0. \tag{2.21}$$

At early times, when $H \gg m$, the Hubble friction prevails in (2.21) and ϕ is approximately constant. The value of the field is given by the initial conditions set by the formation mechanism of the field. In the early universe, we can see that ϕ behaves like dark energy since its equation of state (2.20) is $\omega = -1$.

Later, as the universe expands, the Hubble parameter gradually decreases until it falls below the mass of the field, $H \ll m$. In this case, the solution of (2.21) is oscillatory,

$$\phi(t) = A(t)\cos(mt). \tag{2.22}$$

As the field undergoes oscillations, and the potential $V(\phi)$ is quadratic, the equation of state (2.20) also oscillates around zero, resulting in an average equation of state $\langle\omega\rangle = 0$. In this particular regime, the scalar field behaves as pressureless cold dark matter. Note that we require that the self-interaction potential be small, from the matter-radiation equality until now, to satisfy the equation of state $\langle\omega\rangle = 0$,

$$V_I \ll \frac{m^2}{2}\phi^2. \tag{2.23}$$

By substituting the ansatz solution (2.22) into the equation (2.21), we can deduce that $A^2 \propto a^{-3}$. As a result, we can conclude that $\rho_\phi \propto a^{-3}$, which is the expected behaviour for pressureless cold dark matter.

2.4 Introducing perturbations

Previously in Section 2.3 we have derived the background evolution of the scalar field ϕ in a flat, homogeneous and isotropic universe. Furthermore, we have demonstrated how the scalar field acts as cold dark matter when $H \ll m$. In this section, we introduce gravity perturbations that depend on both space and time to the FLRW metric (2.16) i.e. the Newtonian gauge in General Relativity. Consequently, the equations of motion for the scalar field undergo modifications. These equations are the theoretical framework for Chapter 3, which presents the self-similar solutions for FDM, for Chapter 4, which develops the numerical methods for calculating the evolution of non-relativistc scalar field dark matter clouds and for Chapter 5 and Chapter 6, that both investigate the formation and evolution of solitons supported by repulsive quartic self-interactions and for cosine self-interactions inside extended halos.

In the Newtonian gauge the perturbed FLRW metric is,

$$ds^2 = -(1+2\Phi)dt^2 + a^2(t)(1-2\Psi)d\vec{x}^2, \tag{2.24}$$

where Φ and Ψ are the Newtonian potentials. Applying this metric to (2.7) we have the following action,

$$S_\phi = \int d^4x\, a^3 \left[\frac{1-\Phi-3\Psi}{2}\dot{\phi}^2 - \frac{1+\Phi-\Psi}{2a^2}(\nabla\phi)^2 - \frac{1+\Phi-3\Psi}{2}m^2\phi^2 - V_I(\phi)\right]. \tag{2.25}$$

Our final objective is to derive the equations of motion for the field within the non-relativistic regime, which is applicable to astrophysical structures. In this regime, the anisotropic stress can be considered negligible and the values of Φ and Ψ are small. Therefore, to simplify the analysis, we impose this condition in the following steps. Consequently, in the absence of anisotropic stress, we have $\Phi = \Psi$, and we retain only the terms that are significant in this context.

$$\ddot{\phi} + 3H\dot{\phi} - 4\dot{\Phi}\dot{\phi} - \frac{1}{a^2}(1+4\Phi)\nabla^2\phi + m^2(1+2\Phi)\phi + (1+2\Phi)\frac{dV_I}{d\phi} = 0. \tag{2.26}$$

Now, we consider that both ϕ and Φ exhibit slow variations. More precisely:

$$|\dot{\Phi}| \ll m|\Phi|, \tag{2.27}$$

$$|\nabla\phi| \ll m|\phi|, \tag{2.28}$$

$$|\nabla^2\phi| \ll m^2|\phi|. \tag{2.29}$$

So, we have,

$$\ddot{\phi} + 3H\dot{\phi} - \frac{1}{a^2}\nabla^2\phi + m^2(1+2\Phi)\phi + (1+2\Phi)\frac{dV_I}{d\phi} = 0. \tag{2.30}$$

Since our focus lies in studying the dynamics at small scales, it is important to note that the Hubble flow becomes decoupled within this scale. As a result, we can disregard the time evolution of the Universe for our analysis, and we take the scale factor normalized at today, $a = 1$ and $H = 0$ in the previous equations. As a result, we obtain the following expression:

$$\ddot{\phi} - \nabla^2\phi + m^2(1+2\Phi)\phi + (1+2\Phi)\frac{dV_I}{d\phi} = 0. \tag{2.31}$$

Likewise, we can use this action to get Eq.(2.31)

$$S_\phi = \int d^4x \left[\frac{1-\Phi-3\Psi}{2}\dot{\phi}^2 - \frac{1+\Phi-\Psi}{2}(\nabla\phi)^2 - \frac{1+\Phi-3\Psi}{2}m^2\phi^2 - V_I(\phi)\right]. \tag{2.32}$$

2.5 Small-scales dynamics

In this section, we present the equations governing the dynamics of the small-scales of the Universe. So this applies on astrophysical or galactic scales where the expansion of the Universe can be neglected and metric fluctuations are small, so that Newtonian gravity applies. Therefore, we assume that the field ϕ and the potential Φ are slowly varying by fulfilling conditions (2.27)-(2.29). In addition to this, we ignore the expansion of the universe. To do so, we start with equation (2.31), which describes the dynamics of the relativistic scalar field without expansion. Note that the dynamics considering the expansion of the universe i.e the scale factor a are presented in Section 2.9.

2.5.1 Complex scalar field

In the non-relativistic regime, relevant for astrophysical and large-scale structures, it is useful to introduce a complex scalar field ψ by (Hu et al., 2000; Hui et al., 2017),

$$\phi = \frac{1}{\sqrt{2m}}(\psi e^{-imt} + \psi^* e^{imt}), \tag{2.33}$$

This allows us to separate the fast oscillations at frequency $m \sim (3 \text{ months})^{-1}$ from the slower dynamics described by ψ that follow the evolution of the density field and of the gravitational potential. Note that the complex scalar field ψ also satisfies the slow varying conditions (2.28)-(2.29), that is, $\dot{\psi} \ll m\psi$ and $\nabla\psi \ll m\psi$. Replacing (2.33) into the Klein-Gordon equation for ϕ (2.31) leads to the Schrödinger equation for ψ,

$$i\frac{\partial\psi}{\partial t} = -\frac{1}{2m}\nabla^2\psi + m\Phi_{\rm N}\psi + \frac{\partial\mathcal{V}_{\mathcal{I}}}{\partial\psi^*}\,, \tag{2.34}$$

where now $\Phi_{\rm N}$ is the gravitational potential. Note that we have changed the notation from $\Phi \to \Phi_{\rm N}$. The self-interaction potential, denoted as $\mathcal{V}_{\mathcal{I}}(\psi,\psi^*)$ is derived by replacing the decomposition (2.33) in the definition of $V_I(\phi)$, (2.3). We selectively keep only the non-oscillatory terms. This implies that in the series expansion (2.3), we exclusively consider the even order terms ϕ^{2n}, where each n factor of e^{-imt} is paired with n factors of e^{imt}. Consequently, the resulting expression is:

$$\mathcal{V}_{\mathcal{I}}(\psi,\psi^*) = \Lambda^4\sum_{n=2}\frac{\lambda_{2n}}{2n}\frac{(2n)!}{(n!)^2}\left(\frac{m\psi\psi^*}{2m\Lambda^2}\right)^n. \tag{2.35}$$

Next, let us define the following self-interaction potential to make the Schrödinger equation (2.34) more user-friendly,

$$\Phi_{\rm I}(\rho) = \frac{d\mathcal{V}_{\mathcal{I}}}{d\rho}, \tag{2.36}$$

where ρ is the ultra-light scalar density,

$$\rho = m\psi\psi^*. \tag{2.37}$$

Finally, the outcome of replacing (2.36) into (2.34) is

$$i\frac{\partial\psi}{\partial t} = -\frac{1}{2m}\nabla^2\psi + m(\Phi_{\rm N} + \Phi_{\rm I})\,\psi, \tag{2.38}$$

The gravitational potential $\Phi_{\rm N}$, which is sourced by the field itself is given by the Poisson equation,

$$\nabla^2\Phi_{\rm N} = 4\pi\mathcal{G}_{\rm N}\rho. \tag{2.39}$$

The term $\Phi_{\rm I}$ describes the dark matter self-interactions and of course is model-dependent. For the moment we leave this term free to avoid losing generality in the equations. We will discuss three different scenarios according to the shape of $\Phi_{\rm I}$ in the following Section 2.7 and Section 2.6.

2.5.2 Fluid approach

Taking the Madelung transformation (Madelung, 1926), we move from the field approach to a hydrodynamic approach i.e. $\psi \to \{\rho, S, \vec{v}\}$,

$$\psi = \sqrt{\frac{\rho}{m}}\, e^{iS}, \quad \vec{v} = \frac{\nabla S}{m}, \tag{2.40}$$

where the amplitude ρ plays the role of the scalar density and $\vec{v}$ that of the scalar velocity. Replacing the form (2.40) into equation (2.38) and taking the real and imaginary part of the Schrödinger equation we have the continuity and Hamilton-Jacobi equations,

$$\frac{\partial \rho}{\partial t} + \nabla \cdot (\rho \nabla S) = 0, \tag{2.41}$$

$$\frac{\partial S}{\partial t} + \frac{(\nabla S)^2}{2m} = -m(\Phi_{\rm N} + \Phi_{\rm Q} + \Phi_{\rm I}), \tag{2.42}$$

where we have introduced the so-called *quantum pressure* $\Phi_{\rm Q}$ (Spiegel, 1980; Chavanis, 2011; Marsh, 2015), given by

$$\Phi_{\rm Q} = -\frac{\nabla^2 \sqrt{\rho}}{2m^2 \sqrt{\rho}}. \tag{2.43}$$

In terms of the curl-free velocity field $\vec{v}$, this gives the hydrodynamical continuity and Euler equations,

$$\frac{\partial \rho}{\partial t} + \nabla \cdot (\rho \vec{v}) = 0, \tag{2.44}$$

$$\frac{\partial \vec{v}}{\partial t} + (\vec{v} \cdot \nabla)\vec{v} = -\nabla \left(\Phi_{\rm N} + \Phi_{\rm Q} + \Phi_{\rm I}\right). \tag{2.45}$$

2.5.3 Conservation laws of the Schrödinger-Poisson system

2.5.3.1 Mass

The mass of the system is defined as follows:

$$M = \int d\vec{x} \rho = m \int d\vec{x}\ \psi\psi^*. \tag{2.46}$$

To calculate whether the mass is a conserved quantity of the system, we take the derivative with respect to time of this quantity,

$$\dot{M} = 2m \int d\vec{x}\ \mathrm{Re}\left[\dot{\psi}\psi^*\right]. \tag{2.47}$$

Using the Schrödinger equation (2.38) we have,

$$\dot{M} = 2m\mathrm{Re}\left[\int d\vec{x} \left(\frac{i}{2m}\vec{\nabla}^2\psi\psi^* - im(\Phi_{\rm N} + \Phi_{\rm I})\psi\psi^*\right)\right], \tag{2.48}$$

where $\psi\psi^* \in \mathbb{R}$ and consequently the second term of (2.48)vanishes. Now, by integrating by parts the first term of (2.48), we can check that the result is zero. This is because $(\vec{\nabla}\psi)(\vec{\nabla}\psi^*) \in \mathbb{R}$ and the boundary terms are also 0. Therefore,

$$\dot{M} = 0. \tag{2.49}$$

So, we have demonstrated that the mass of the system is conserved.

2.5.3.2 Momentum

We can define the density current flow of the system as follows,

$$\vec{J} = \frac{i}{2}\left(\psi\vec{\nabla}\psi^* - \psi^*\vec{\nabla}\psi\right). \tag{2.50}$$

Mapping this expression into hydrodynamical variables with the Madelung transformation (2.40) we obtain,

$$\vec{J} = \rho\vec{v}. \tag{2.51}$$

So, the total momentum of the system is expressed as follows:

$$\vec{P} = \int d\vec{x}\ \vec{J}. \tag{2.52}$$

Thus, for the j-component of the vector $\vec{P}$ we have,

$$P_j = \int d\vec{x}\ \frac{i}{2}\left(\psi\frac{\partial\psi^*}{\partial x_j} - \psi^*\frac{\partial\psi}{\partial x_j}\right) = -\mathrm{Im}\int d\vec{x}\ \psi\frac{\partial\psi^*}{\partial x_j}. \tag{2.53}$$

Then, taking the derivative of this quantity with respect to time, we get,

$$\dot{P}_j = -\mathrm{Im}\int d\vec{x}\ \left(\dot{\psi}\frac{\partial\psi^*}{\partial x_j} + \psi\frac{\partial\dot{\psi}^*}{\partial x_j}\right) = -\mathrm{Im}\int d\vec{x}\ \left(\dot{\psi}\frac{\partial\psi^*}{\partial x_j} - \frac{\partial\dot{\psi}}{\partial x_j}\psi^*\right). \tag{2.54}$$

Integrating by parts assuming that the boundary terms $\left[\psi\dot{\psi}^*\right]_{-\infty}^{\infty}$ are zero, we obtain,

$$\dot{P}_j = -2\mathrm{Im}\int d\vec{x}\ \dot{\psi}\frac{\partial\psi^*}{\partial x_j}. \tag{2.55}$$

Using the Schrödinger equation (2.38) and replacing in (2.55) we arrive at,

$$\dot{P}_j = -2\mathrm{Re}\int d\vec{x}\left[\frac{1}{2m}\frac{\partial^2\psi}{\partial x_k^2}\frac{\partial\psi^*}{\partial x_j} - m(\Phi_\mathrm{N} + \Phi_\mathrm{I})\psi\frac{\partial\psi^*}{\partial x_j}\right]. \tag{2.56}$$

Next, integrating again by parts and considering negligible the boundary terms, we get,

$$\dot{P}_j = \int d\vec{x}\ \ (\Phi_\mathrm{N} + \Phi_\mathrm{I})\frac{\partial\rho}{\partial x_j}. \tag{2.57}$$

Finally, for the first term in (2.57) we use the Poisson equation (2.39) and integrate by parts giving 0 as a result. For the second term in (2.57) we use the fact that

$$\Phi_\mathrm{I} = \frac{d\mathcal{V}_I}{d\rho}, \tag{2.58}$$

with $[\mathcal{V}_I]_{-\infty}^{\infty} = 0$, leading to a zero result too. Therefore,

$$\dot{P}_j = 0. \tag{2.59}$$

Consequently, P_j is constant so $\vec{P}$ is a conserved quantity.

2.5.3.3 Energy

The total energy of the Schrödinger (2.38) Poisson (2.39) system is:

$$E = \int d\vec{x} \left[\frac{1}{2m} \vec{\nabla}\psi \vec{\nabla}\psi^* + \frac{m}{2}\psi\psi^*\Phi_{\rm N} + \mathcal{V}_I \right], \tag{2.60}$$

where we can split the different contributions of the kinetic energy,

$$E_{\rm K} = \int d\vec{x} \ \frac{1}{2m} \vec{\nabla}\psi \vec{\nabla}\psi^*, \tag{2.61}$$

the gravitational energy,

$$E_{\rm N} = \int d\vec{x} \ \frac{m}{2}\psi\psi^*\Phi_{\rm N}, \tag{2.62}$$

and the self-interaction energy,

$$E_{\rm I} = \int d\vec{x} \ \mathcal{V}_I. \tag{2.63}$$

Knowing the relation between the ultralight density and the complex field ψ, (2.37) we can rewrite equation (2.60) as follows,

$$E = \int d\vec{x} \left[\frac{1}{2m} \vec{\nabla}\psi \vec{\nabla}\psi^* + \frac{1}{2}\rho\Phi_{\rm N} + \mathcal{V}_I \right]. \tag{2.64}$$

As we previously did, we take the time derivative of this quantity to show that it is a conserved quantity of the system. Doing so, we get,

$$\dot{E} = \int d\vec{x} \left[-\frac{1}{2m} \left(\dot{\psi}\vec{\nabla}^2\psi^* + \dot{\psi}^*\vec{\nabla}^2\psi \right) + \frac{1}{2}\frac{\partial\rho}{\partial t}\Phi_{\rm N} + \frac{1}{2}\frac{\partial\Phi_{\rm N}}{\partial t} + \Phi_{\rm I}\frac{\partial\rho}{\partial t} \right]. \tag{2.65}$$

Using the fact that,

$$\int d\vec{x}\ \rho\frac{\partial\Phi_{\rm N}}{\partial t} = \int d\vec{x}\ \frac{\partial\rho}{\partial t}\Phi_{\rm N}, \tag{2.66}$$

we can replace (2.66) into (2.65) and we have,

$$\dot{E} = \int d\vec{x} \left[-\frac{1}{2m} \left(\dot{\psi}\vec{\nabla}^2\psi^* + \dot{\psi}^*\vec{\nabla}^2\psi \right) + \frac{\partial\rho}{\partial t}(\Phi_{\rm N} + \Phi_{\rm I}) \right]. \tag{2.67}$$

Taking again (2.37) and plugging (2.38) into the last expression, we get,

$$\dot{E} = \int d\vec{x} \left[\dot{\psi} \left(-\frac{\vec{\nabla}^2\psi^*}{2m} + m\psi^*(\Phi_{\rm N} + \Phi_{\rm I}) \right) + \dot{\psi}^* \left(-\frac{\vec{\nabla}^2\psi}{2m} + m\psi(\Phi_{\rm N} + \Phi_{\rm I}) \right) \right]. \tag{2.68}$$

Finally, using (2.38), we obtain,

$$\dot{E} = \int d\vec{x} \left[\dot{\psi} \left(-i\dot{\psi}^* \right) + \dot{\psi}^* \left(i\dot{\psi} \right) \right]. \tag{2.69}$$

Therefore,

$$\dot{E} = 0. \tag{2.70}$$

Consequently, the energy of the system is constant.

2.5.3.4 Virial theorem

As we have introduced in Section 1.4, solitons are the equilibrium configurations of the SFDM models that are present in the core of the DM halos. These states also correspond to a minimum or a saddle point of energy i.e. $\delta E = 0$. To calculate the virial quantity, let us take a perturbation of the system at constant mass. We can write this dilatation of the profile as follows,

$$\vec{x} \to \alpha\vec{x}, \quad \rho \to \alpha^{-3}\rho, \quad \psi \to \alpha^{-3/2}\psi. \tag{2.71}$$

Thus, replacing (2.71) into the energy functional (2.60), we obtain, for a quartic self-interaction (See Section 2.7),

$$E(\alpha) = \alpha^{-2}E_{\rm K} + \alpha^{-1}E_{\rm N} + \alpha^{-3}E_{\rm I}. \tag{2.72}$$

For the quartic self-interaction:, at linear order on $\delta\alpha$ we have $\delta E = 0$, $\frac{dE}{d\alpha}\Big|_{\alpha=1} = 0$, so the virial quantity reads,

$$2E_{\rm K} + E_{\rm N} + 3E_{\rm I} = 0. \tag{2.73}$$

For FDM (Section 2.6) we have the usual expression

$$2E_{\rm K} + E_{\rm N} = 0. \tag{2.74}$$

2.6 Fuzzy Dark Matter

The purpose of this section is to provide an overview of the action of the FDM model and the equations that describe the dynamics in the non-relativistic regime, focusing on astrophysical or galactic scales. At these scales, the expansion of the universe can be neglected, and metric fluctuations are small, so that Newtonian gravity applies.

Fuzzy dark matter is the scalar field dark matter model, which considers the most straightforward possibility for the potential $V(\phi)$ in (2.2). Thus, the scalar field is minimally coupled to gravity, and it does not have any self-interaction, (Hui et al., 2017)

$$V_I(\phi) = 0. \tag{2.75}$$

This potential leads to the following action,

$$S_\phi = \int d^4x\sqrt{-g}\left[-\frac{1}{2}g^{\mu\nu}\partial_\mu\phi\partial_\nu\phi - \frac{m^2}{2}\phi^2\right]. \tag{2.76}$$

By applying the principle of least action, we can derive the Klein-Gordon equation for the relativistic field ϕ in the absence of an interaction potential ($V_I = 0$), as shown in equation (2.31). Furthermore, utilizing equation (2.33), we can separate the rapid oscillations at frequency m from the slower dynamics governed by ψ, which describe the evolution of the density field and gravitational potential on these scales. Consequently, the Klein-Gordon equation for ϕ can be transformed into the Schrödinger equation for ψ.

$$i\frac{\partial\psi}{\partial t} = -\frac{1}{2m}\nabla^2\psi + m\Phi_{\rm N}\psi, \tag{2.77}$$

where $\Phi_{\rm N}$ is the gravitational potential given by equation (2.39). Note that the only free parameter in the model is the mass of the scalar field. As we have seen in Section 1.4 we usually consider an exceptionally light boson, typically with a mass on the order of 10^{-22} eV. As wee have seen in Section 1.4 this tiny mass corresponds to a de Broglie wavelength at the kiloparsec scale.

2.6.1 Scaling laws

One interesting feature of this Schrödinger–Poisson (2.77)-(2.39) system is that equations of motion are invariant under this scaling law (Guzman & Urena-Lopez, 2003),

$$\{t \to \alpha^{-2}t,\ \vec{x} \to \alpha^{-1}\vec{x},\ \Phi_{\rm N} \to \alpha^2\Phi_{\rm N},\ \rho \to \alpha^4\rho,\ \psi \to \alpha^2\psi,\ M \to \alpha M,\ E \to \alpha^3 E\} \quad (2.78)$$

This means, that once we have obtained an equilibrium or a dynamical solution a complete family of solutions can be derived through this scaling transformation. In particular, from an equilibrium solution with mass M_1, we obtain the equilibrium solution with mass M_2 by the following rescaling,

$$\alpha = \frac{M_2}{M_1}. \quad (2.79)$$

2.6.2 Fuzzy dark matter solitons

The static equilibrium profiles, called solitons, have a zero velocity $\vec{v}$. This leads through the Euler equation (2.45) with $\Phi_{\rm I} = 0$ to the following hydrostatic equilibrium condition,

$$\Phi_{\rm N} + \Phi_{\rm Q} = \frac{E}{m}. \quad (2.80)$$

The soliton wavefunction reads $\psi(r,t) = e^{-iEt}\hat{\psi}(r)$. Thus, the soliton arises from the balance between the repulsive quantum pressure and the attractive force of gravity in the non-relativisitic limit. In the right panel of Fig.1.12, we present the radial density profile for different FDM solitons.

2.7 The quartic model

The goal of this section is to introduce the action of the quartic model and the equations that describe the dynamics on small-scales, as we did in Section 2.6 for the FDM model. In this model, the self-interaction (2.3) is quartic, so $V_I(\phi)$ is the following,

$$V_I(\phi) = \frac{\lambda_4}{4}\phi^4, \quad (2.81)$$

where λ_4 dictates the strength of the self-interactions. The self-interaction parameter can be positive (repulsive self-interaction) or negative (attractive force). Note that it is required that $V_I(\phi)$ to be small compared with the quadratic term of the potential $V(\phi)$ (2.2) as we have discussed in (2.23) for the scalar field to behave as pressureless dark matter at late times. Plugging (2.81) into (2.1) brings the following action,

$$S_\phi = \int d^4x\sqrt{-g}\left[-\frac{1}{2}g^{\mu\nu}\partial_\mu\phi\partial_\nu\phi - \frac{m^2}{2}\phi^2 - \frac{\lambda_4}{4}\phi^4\right]. \quad (2.82)$$

We take the non-relativistic limit by decomposing the real field ϕ in terms of a complex field ψ according to (2.33). From this we can arrive to the equations of motion for the complex field, known as the Gross–Pitaevskii–Poisson equations (GPP) or the non-linear Schrödinger–Poisson (NSP) equations.

$$i\frac{\partial\psi}{\partial t} = -\frac{1}{2m}\nabla^2\psi + m(\Phi_{\rm N} + \Phi_{\rm I})\psi, \tag{2.83}$$

where $\Phi_{\rm N}$ is the gravitational potential provided by equation (2.39), and the self-interaction potential $\Phi_{\rm I}(\rho)$ reads,

$$\Phi_{\rm I}(\rho) = \frac{3\lambda_4}{4m^4}\rho. \tag{2.84}$$

where we can group all model parameters with the definition of ρ_a:

$$\rho_a = \frac{4m^4}{3\lambda_4}. \tag{2.85}$$

Thus, the quartic potential (2.84) can be written as follows.

$$\Phi_{\rm I}(\rho) = \frac{\rho}{\rho_a}. \tag{2.86}$$

It should be emphasised that (2.84) comes from the "non-relativistic" potential (2.35) for $n = 2$,

$$\mathcal{V}_{\mathcal{I}}(\psi,\psi^*) = \Lambda^4\frac{\lambda_4}{4}\frac{4!}{4}\left(\frac{\psi\psi^*}{2m\Lambda^2}\right)^2 = \frac{3\lambda_4}{8m^2}(\psi\psi^*)^2 = \frac{3\lambda_4}{8m^4}\rho^2. \tag{2.87}$$

This model has two free parameters: the mass of the scalar field m and the strength of the repulsive self-interactions λ_4. In the following Fig. 2.1, we can see the allowed regions for the space of parameters (m, λ_4).

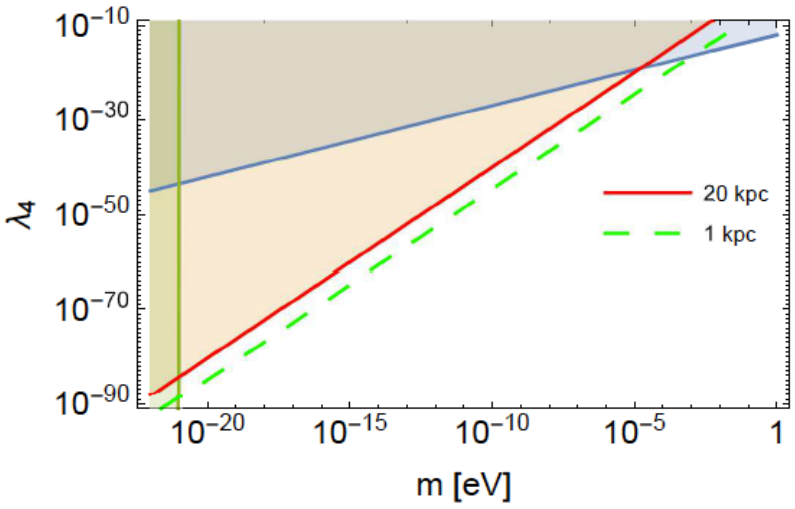

Figure 2.1. Figure from (Brax et al., 2019b). Range of interest in the plane (m, λ_4).

2.7.1 Thomas-Fermi limit

As seen from Eq.(2.45), such scalar field models admit hydrostatic equilibria given by $\vec{v} = 0$ and $\Phi_N + \Phi_I + \Phi_Q = \text{constant}$. In the Thomas–Fermi regime this soliton is governed by the balance between gravity and the repulsive force associated with the self-interactions (for $\lambda_4 > 0$). This means that $\Phi_Q \ll \Phi_I$ over most of the extent of the soliton and the Laplacian term $-\frac{\nabla^2\psi}{2m}$ can be neglected in Eq.(2.83). Then, the wavefunction reads $\psi(r,t) = e^{-iEt}\hat{\psi}(r)$ with

$$\Phi_N + \Phi_I = \frac{E}{m}. \tag{2.88}$$

The soliton density profile is given by Chavanis (2011); Harko (2011); Brax et al. (2019a)

$$\rho_{\rm sol}(r) = \rho_{0\rm sol}\frac{\sin(\pi r/R_{\rm sol})}{\pi r/R_{\rm sol}}, \tag{2.89}$$

with the radius

$$R_{\rm sol} = \pi r_a, \quad \text{with} \quad r_a^2 = \frac{3\lambda_4}{16\pi\mathcal{G}_N m^4} = \frac{1}{4\pi\mathcal{G}_N\rho_a}. \tag{2.90}$$

In fact, outside of the radius r_a where Eq.(2.89) would give a zero density we can no longer neglect Φ_Q and the exact solution develops an exponential tail at large radii. Nevertheless, we can see that the approximation (2.89) is valid up to $r \lesssim R_{\rm sol}$ for

$$\Phi_Q \ll \Phi_I : \quad \frac{\rho_{0\rm sol}}{\rho_a} \gg \frac{1}{r_a^2 m^2}. \tag{2.91}$$

2.7.2 Scaling laws

An important characteristic of this non-linear Schrödinger–Poisson (2.77)-(2.39) system is its property of invariance under the following scaling law (Guzman & Urena-Lopez, 2003).

$$\{t \to \alpha^{-2}t,\ \vec{x} \to \alpha^{-1}\vec{x},\ \Phi_{\rm N} \to \alpha^2\Phi_{\rm N},\ \rho \to \alpha^4\rho,\ \psi \to \alpha^2\psi,\ \Phi_{\rm I} \to \alpha^2\Phi_{\rm I},\ \lambda_4 \to \alpha^2\lambda_4,$$
$$E_{\rm I} \to \alpha^3 E_{\rm I},\ E \to \alpha^3 E\}. \tag{2.92}$$

This implies that once we have obtained an equilibrium or a dynamical solution, a complete family of solutions can be derived through the application of this scaling transformation. It should be highlighted that the scaling law links different theories, with a different λ_4 coupling.

2.8 The cosine model

In this section, we present the last scenario that we consider in this thesis. This model corresponds to a bounded potential such as a cosine with a standard kinetic term. Keeping the two-scale scenario (2.23), we express the scalar field potential (2.2) as the sum of a dominant quadratic term and a secondary non-linear self-interacting potential (2.3), specifically chosen to be a cosine function:

$$V_I(\phi) = M_I^4\left[\cos(\phi/\Lambda) - 1 + \frac{\phi^2}{2\Lambda^2}\right]. \tag{2.93}$$

It is important to highlight that for $\phi \ll \Lambda$ we recover a quartic potential $\lambda_4 = M_I^4/(6\Lambda^4)$. M_I refers to a new scale. In axion models, for instance in QC, it is the scale of breaking of the shift symmetry $\phi \to \phi + c$. To obtain the equations of motion for small scales, we begin by inserting the potential (2.93) into the relativistic equation for ϕ (2.31). Subsequently, we decompose the real field ϕ into a complex field ψ, as explained in equation (2.33). This decomposition gives rise to the equations of motion for the complex field, precisely the Schrödinger equation (2.38), featuring the following self-interaction potential,

$$\Phi_{\rm I}(\rho) = \frac{8\rho_b}{\rho_a}\left[1 - \frac{2J_1(\sqrt{\rho/\rho_b})}{\sqrt{\rho/\rho_b}}\right], \tag{2.94}$$

with

$$\rho_a = \frac{8m^4\Lambda^4}{M_I^4}, \quad \rho_b = \frac{m^2\Lambda^2}{2}, \quad \rho_b \ll \rho_a. \tag{2.95}$$

It is important to note that at low densities we again recover the case of the quartic potential (2.86), while at high densities the self-interaction potential converges to a finite value:

$$\rho \ll \rho_b: \quad \Phi_{\rm I}(\rho) = \frac{\rho}{\rho_a} + ... \tag{2.96}$$

$$\rho \gg \rho_b: \quad \Phi_{\rm I}(\rho) = \frac{8\rho_b}{\rho_a} \ll 1 \tag{2.97}$$

2.9 Non-relativistic regime in cosmology

In this section we introduce the equations of the non-relativistic regime taking into account the expansion of the universe. To do so, we take the following ansatz solution which takes into account the scale factor a:

$$\phi = \frac{1}{\sqrt{2ma^3}}(\psi e^{-imt} + \psi^* e^{imt}), \tag{2.98}$$

Note that ψ satisfies the same conditions for ϕ. Replacing (2.98) in (2.25) we get,

$$\begin{aligned} S_\phi = \int d^4x\, a^3 \{ & e^{-2imt}\left[\frac{1-\Phi-3\Psi}{4m}(\dot\psi^2 - 2im\dot\psi\psi) - \frac{1+\Phi-\Psi}{4ma^2}(\nabla\psi)^2 - \frac{1-3\Psi}{2}m\psi^2\right] \\ & + e^{2imt}[\text{c.c.}] + \frac{1-\Phi-3\Psi}{2m}(\dot\psi\dot\psi^* + im\dot\psi\psi^* - im\psi\dot\psi^*) \\ & - \frac{1+\Phi-\Psi}{2ma^2}(\nabla\psi)\cdot(\nabla\psi^*) - m\Phi\psi\psi^* - V_I(\phi)\}. \end{aligned} \tag{2.99}$$

Next, we neglect the fast oscillatory terms, therefore we obtain,

$$\begin{aligned} S_\phi = \int d^4x\, a^3 \Big(& \frac{1-\Phi-3\Psi}{2m}(im\dot\psi\psi^* - im\psi\dot\psi^*) - \frac{1+\Phi-\Psi}{2ma^2}(\nabla\psi)\cdot(\nabla\psi^*) \\ & - m\Phi\psi\psi^* - \mathcal{V}_{\mathcal{I}}(\psi,\psi^*)\Big). \end{aligned} \tag{2.100}$$

2.9.1 Field picture

Employing the principle of least action in (2.101), the Euler–Lagrange equations give rise to the following Schrödinger equation for an expanding universe,

$$i\left(\dot{\psi}+\frac{3}{2}H\psi\right)=-\frac{\nabla^2\psi}{2ma^2}+m\Phi_{\rm N}\psi+\frac{\partial\mathcal{V}_{\mathcal{I}}}{\partial\psi^*}. \tag{2.101}$$

Recasting (2.101) with the self-interaction potential $\Phi_{\rm I}$, we have,

$$i\dot{\psi}=-\frac{3}{2}iH\psi-\frac{1}{2ma^2}\nabla^2\psi+m(\Phi_{\rm N}+\Phi_{\rm I}), \tag{2.102}$$

where the Poisson equation is,

$$\nabla^2\Phi_{\rm N}=4\pi Gma^2|\psi|^2. \tag{2.103}$$

2.9.2 Fluid picture

Taking the Madelung transformation (Madelung, 1926) the complex scalar field ψ can be mapped to a hydrodynamical system,

$$\psi=\sqrt{\frac{\rho}{m}}e^{iS}\ \text{ with }\vec{v}=\frac{\nabla S}{ma}. \tag{2.104}$$

Where ρ represents the density and $\vec{v}$ represents the fluid velocity. $\sqrt{\rho/m}$ defines the amplitude and the phase, S. As it is widely recognized, the equation of motion (2.102) can be expressed as the continuity and Euler equations of hydrodynamics. In this case, the continuity equation reads,

$$\dot{\rho}+3H\rho+\frac{1}{ma^2}\nabla(\rho\nabla S)=0. \tag{2.105}$$

It is important to observe that the self-interactions do not alter this continuity equation. The Euler-Lagrange equation for ρ yields the second equation of motion.

$$\dot{S}+\frac{(\nabla S)^2}{2ma^2}=-m\Phi_{\rm N}-m\frac{d\mathcal{V}_{\mathcal{I}}}{d\rho}+\frac{1}{2ma^2}\frac{\nabla^2\sqrt{\rho}}{\sqrt{\rho}}. \tag{2.106}$$

The hydrodynamical Euler equation in an expanding univese can be derived by taking the gradient of this equation (2.106),

$$\vec{v}+H\vec{v}+\frac{1}{a}(\vec{v}\cdot\nabla)\vec{v}=-\frac{1}{a}\nabla(\Phi_{\rm N}+\Phi_{\rm I}+\Phi_{\rm Q}), \tag{2.107}$$

where the quantum pressure now reads,

$$\Phi_{\rm Q}=-\frac{\nabla^2\sqrt{\rho}}{2m^2a^2\sqrt{\rho}}. \tag{2.108}$$

Hence, we rediscover the dynamics observed in the standard cold dark matter scenario, characterized by density ρ and fluid velocity $\vec{v}$. In addition, we introduce the interaction potential $\Phi_{\rm I}$ and the quantum potential $\Phi_{\rm Q}$ (Marsh, 2015). These additional terms should remain negligible on large scales to align with observational data. However, they have the potential to induce substantial effects at galactic scales, where the cold dark matter scenario faces certain discrepancies with observational evidence.

Chapter 3

Self-similar solutions for Fuzzy dark matter

In this chapter, we focus on exploring the self-similar solutions within the framework of the Fuzzy Dark Matter (FDM) model (Galazo-García et al., 2022). Self-similarity refers to the property of remaining unchanged in form and appearance under appropriate scaling transformations. The main motivations to investigate these particular solutions are:

1. Moving beyond hydrostatic equilibrium: By considering self-similar solutions, we aim to extend our understanding beyond the hydrostatic equilibrium exhibited by solitons. This allows us to explore possible time-dependent analytical solutions, providing us with a valuable tool to gain better control and comprehension of the model dynamics. With these self-similar solutions we can examine dynamical configurations embedded in an expanding cosmological background.

2. Comparisons with CDM: Another motivation behind investigating self-similar solutions for FDM is to establish a connection and facilitate comparisons with self-similar solutions within the CDM framework. In the CDM scenario, self-similar solutions exhibit a well-known hierarchical collapse pattern (Fillmore & Goldreich, 1984; Bertschinger, 1985; Teyssier et al., 1997). Initially, small linear density perturbations arise on top of a homogeneous background, with their amplitudes decaying as a power law at large radii. As time progresses, larger mass shells turn around and collapse. For sufficiently steep initial profiles, the inner core stabilizes in physical coordinates, leading to the formation of a virialized halo. The density profile within the non-linear region follows a power-law distribution, growing in mass and radius as more distant shells separate from the Hubble flow and collapse. Therefore, by exploring these solutions, we can better understand the similarities and differences between FDM and CDM models.

3. Bridging the semiclassical limit: The study of self-similar solutions also helps us to grasp the relationship between the FDM and CDM models within the semiclassical limit. This limit allows us to investigate the behavior of FDM in the regime where quantum effects are significant, but classical gravity is still the dominant force.

This chapter is arranged as follows. In Section 3.1, we briefly recall the dynamics of fuzzy dark matter, its equations of motion and we describe the semiclassical limit.

In Section 3.2, we present the static solitons and we derive the critical exponents that characterize self-similar solutions. In Section 3.3, we study spherical cosmological self-similar solutions, which converge to the background universe at large radii. We obtain their large-density asymptotic shape in Section 3.4. Finally, in Section 3.5 we compare with the CDM self-similar solutions, we discuss the semiclassical limit and conclude.

3.1 Equations of motion

3.1.1 Field approach

As we discussed in Section 2.6 the action of Fuzzy Dark Matter (2.76) is that of a classical scalar field ϕ with minimal coupling to gravity and no self-interactions. In the following two sections, our focus lies on astrophysical or galactic scales, where the expansion of the Universe can be disregarded, and metric fluctuations are small, allowing us the application of Newtonian gravity. The inclusion of Hubble expansion will be discussed in Section 3.3. Interestingly, we will discover that the self-similar exponents remain the same for both the Minkowski background and the expanding Einstein-de Sitter background. In this context, where the non-relativistic regime applies, it is helpful to introduce the complex scalar field denoted as ψ given by (2.33) as we have seen in Section 2.5.1. Using this, we can effectively separate the fast oscillations of frequency m from the slower dynamics governed by ψ, which describes the evolution of the density field and gravitational potential. These considerations simplify the dynamics of the system to the Schrödinger equation for ψ.

$$i\frac{\partial\psi}{\partial t} = -\frac{1}{2m}\nabla^2\psi + m\Phi_{\rm N}\,\psi, \tag{3.1}$$

where $\Phi_{\rm N}$ is the gravitational potential, given by the Poisson equation

$$\nabla^2\Phi_{\rm N} = 4\pi\mathcal{G}_{\rm N}\rho, \quad \rho = m\psi\psi^*, \tag{3.2}$$

where ρ is the FDM density. As highlighted in Section 2.6.1, an important characteristic of the Schrödinger-Poisson (SP) system, is its invariance under the scaling law (Guzman & Urena-Lopez, 2003).

$$\{t, \vec{r}, \Phi_{\rm N}, \psi, \rho\} \to \left\{\lambda^{-2}t, \lambda^{-1}\vec{r}, \lambda^2\Phi_{\rm N}, \lambda^2\psi, \lambda^4\rho\right\}. \tag{3.3}$$

This implies that once we have obtained an equilibrium or dynamic solution, a whole range of solutions can be derived by applying this scaling transformation.

3.1.2 Semiclassical limit

Using dimensionless coordinates suited to the system under study is often helpful. Considering galactic cores or astrophysical objects such as FDM halos, we take a system of typical length $L_\star$, time scale $T_\star$, and velocity $V_\star = L_\star/T_\star$. The virial theorem applied to these systems, primarily influenced by gravity and near equilibrium, implies that the gravitational potential is on the order of $V_\star^2$. By employing the appropriate rescalings,

$$\begin{aligned} t = T_\star\,\tilde{t}, \quad \vec{r} = L_\star\,\tilde{\vec{r}}, \quad \Phi_{\rm N} = \frac{L_\star^2}{T_\star^2}\,\tilde{\Phi}_{\rm N}, \\ \psi = \frac{\tilde{\psi}}{\sqrt{\mathcal{G}_{\rm N}m}T_\star} = \psi_\star\tilde{\psi}, \quad \rho = \frac{\tilde{\rho}}{\mathcal{G}_{\rm N}T_\star^2} = \rho_\star\tilde{\rho}, \end{aligned} \tag{3.4}$$

we obtain the SP (3.1)-(3.2) system in dimensionless variables denoted with a tilde

$$i\epsilon\frac{\partial\tilde{\psi}}{\partial\tilde{t}} = -\frac{\epsilon^2}{2}\tilde{\nabla}^2\tilde{\psi} + \tilde{\Phi}_{\rm N}\,\tilde{\psi}, \tag{3.5}$$

$$\tilde{\nabla}^2\tilde{\Phi}_{\rm N} = 4\pi\tilde{\rho}, \quad \tilde{\rho} = \tilde{\psi}\tilde{\psi}^*, \tag{3.6}$$

where ϵ is given by

$$\epsilon = \frac{T_\star}{mL_\star^2}. \tag{3.7}$$

If we compare this quantity with the de Broglie wavelength $\lambda_{\rm dB} = 2\pi/(mV_\star)$, we have

$$\epsilon \sim \frac{\lambda_{\rm dB}}{L_\star}. \tag{3.8}$$

Therefore, the parameter ϵ, which appears in the dimensionless Schrödinger equation (3.5) plays the role of $\hbar$ in quantum mechanics. It represents the ratio between the de Broglie wavelength $\lambda_{\rm dB}$ and the size of the system. As we have seen in Section 2.6.2, FDM proposes the formation of DM cores, solitons, with a radius approximately equal to the de Broglie wavelength $\lambda_{\rm dB}$. In this regime, the wave-like effects become significant. On larger scales, the system behaves like a collection of particles, and numerical simulations indicate that the core is surrounded by an NFW-like halo, similar to the standard CDM scenario (Schive et al., 2014a; Schwabe et al., 2016; Mocz et al., 2017; Veltmaat et al., 2018). To ensure that the de Broglie wavelength $\lambda_{\rm dB}$ aligns with galactic scales, it is necessary to set the mass of the scalar field to approximately $10^{-22}\,$eV (Schive et al., 2014a). Consequently, $\epsilon \sim 1$ indicates the significance of wave-like effects on these scales. In the subsequent discussion, we adopt the dimensionless variables (3.4) and simplify the notation by removing the tildes.

In the limit $\epsilon \to 0$, known as the "semiclassical" limit, FDM behaves similarly to CDM on all relevant scales. In this regime, the Schrödinger-Poisson (SP) system (3.5)-(3.6) has been proposed as an alternative framework for cosmological simulations of CDM. This approach offers an alternative to the standard CDM N-body simulations, which aim to replicate the Vlasov equation (Widrow & Kaiser, 1993; Uhlemann et al., 2014; Mocz et al., 2018; Garny et al., 2020). In the semiclassical limit, $\epsilon \to 0$, we expect that average quantities, such as the density averaged over the fast oscillations at the frequency m, converge to values obtained from the Vlasov equation. To be more precise, we can define the Wigner distribution (Wigner, 1932) as follows,

$$f_{\rm W}(\vec{r},\vec{v}) = \int \frac{d\vec{r}'}{(2\pi)^3}\, e^{i\vec{v}\cdot\vec{r}'}\,\psi\left(\vec{r}-\frac{\epsilon}{2}\vec{r}'\right)\psi^*\left(\vec{r}+\frac{\epsilon}{2}\vec{r}'\right), \tag{3.9}$$

and its coarse-grained version, the Husimi distribution (Husimi, 1940), by

$$f_{\rm H}(\vec{r},\vec{v}) = \int \frac{d\vec{r}'d\vec{v}'}{(2\pi\epsilon)^3\sigma_r^3\sigma_v^3}\, e^{-(\vec{r}-\vec{r}')^2/(2\epsilon\sigma_r^2)-(\vec{v}-\vec{v}')^2/(2\epsilon\sigma_v^2)} \times f_{\rm W}(\vec{r}',\vec{v}'), \tag{3.10}$$

The Husimi distribution and the Wigner distribution satisfy an equation of motion that deviates from the Vlasov equation in terms of order ϵ and higher (Skodje et al., 1989; Widrow & Kaiser, 1993; Uhlemann et al., 2014). In the limit where $\sigma_r \to 0$ and $\sigma_v \to 0$, the Husimi distribution converges in a weak sense to the Wigner distribution which can

take negative values and display fast oscillations, in contrast with classical phase-space distributions. However, when $\sigma_r\sigma_v \geq 1/2$, the Husimi distribution is positive (Cartwright, 1976), providing a better correspondence with classical physics.

The lower bound $\sigma_r\sigma_v \geq 1/2$ is directly connected to the Heisenberg uncertainty principle inherent in the properties of all wave-like systems. This principle states that we cannot achieve arbitrary precision simultaneously in both the spatial and momentum coordinates. Consequently, there is a fundamental limit to the accuracy attainable in these two quantities. We will adopt $\sigma_r\sigma_v = 1/2$ as it represents the optimal choice in our numerical computations. This option strikes a balance between spatial accuracy and velocity resolution. As shown in Figures 3.6 and 3.7, decreasing σ_r improves spatial accuracy but degrades velocity resolution. For $\sigma_r\sigma_v = 1/2$, the Husimi distribution (3.10) can also be expressed as follows:

$$f_{\rm H}(\vec{r},\vec{v}) = \left| \int \frac{d\vec{r}\,'}{(2\pi\epsilon)^{9/4}\sigma_r^{3/2}}\, e^{-(\vec{r}-\vec{r}\,')^2/(4\epsilon\sigma_r^2) - i\vec{v}\cdot\vec{r}\,'/\epsilon}\psi(\vec{r}\,') \right|^2 . \tag{3.11}$$

This expression emphasises that the Husimi distribution is always positive, similar to classical phase space distributions. For this reason, the semiclassical limit is better analysed in terms of the Husimi distribution than in terms of the Wigner distribution, which is not definitely positive and typically often exhibits rapid oscillations. Nevertheless, the semiclassical limit remains a complex problem (Jin et al., 2011), and only coarse-grained quantities, averaged over the fast oscillations, are expected to converge to their classical counterparts. The wave function ψ retains strong oscillations at increasingly smaller wavelengths $\lambda_{\rm dB} \sim \epsilon L$ as ϵ approaches zero, with the macroscopic scale L held constant.

3.1.3 Hydrodynamical picture

As we have presented in Section 2.5.2, we can recast the SP system (3.5)-(3.6) with hydrodynamic variables, $\psi \to \{\rho, S, \vec{v}\}$, using the Madelung transformation (2.40) (Madelung, 1926). In dimensionless coordinates, it reads,

$$\psi = \sqrt{\rho}\, e^{iS/\epsilon}, \quad \vec{v} = \nabla S. \tag{3.12}$$

The real and imaginary parts of the dimensionless Schrödinger equation lead to the continuity and Hamilton-Jacobi equations,

$$\frac{\partial \rho}{\partial t} + \nabla\cdot(\rho\nabla S) = 0, \tag{3.13}$$

$$\frac{\partial S}{\partial t} + \frac{1}{2}(\nabla S)^2 = -(\Phi_{\rm N} + \Phi_{\rm Q}), \tag{3.14}$$

where we $\Phi_{\rm Q}$ is the dimensionless quantum pressure, (Spiegel, 1980; Chavanis, 2011; Marsh, 2015) $\Phi_{\rm Q}$,

$$\Phi_{\rm Q} = -\frac{\epsilon^2}{2}\frac{\nabla^2\sqrt{\rho}}{\sqrt{\rho}}. \tag{3.15}$$

In terms of the curl-free velocity field $\vec{v}$, this gives the dimensionless hydrodynamical continuity and Euler equations,

$$\frac{\partial \rho}{\partial t} + \nabla\cdot(\rho\vec{v}) = 0, \tag{3.16}$$

$$\frac{\partial \vec{v}}{\partial t} + (\vec{v}\cdot\nabla)\vec{v} = -\nabla\left(\Phi_{\rm N} + \Phi_{\rm Q}\right). \tag{3.17}$$

The Poisson equation still reads

$$\nabla^2 \Phi_{\rm N} = 4\pi\rho. \tag{3.18}$$

The parameter ϵ controls the importance of wavelike effects and it only appears as a prefactor in the expression for the quantum pressure (3.15). In the semi-classical limit,$\epsilon \to 0$, the FDM continuity and Euler equations revert to their standard form, describing CDM on large scales where shell crossing can be neglected. This shows that in the semi-classical limit, or on large scales where the Laplacian ∇^2 suppresses the quantum pressure, FDM behaves similarly to CDM.

However, it is important to note that the limit $\epsilon \to 0$ is not uniform and can break down on small scales. As $\epsilon \to 0$, the fields can exhibit increasingly steep gradients, meaning variations on increasingly small scales of the order of ϵ. This counterbalances the ϵ^2 prefactor in equation (3.15), and the quantum pressure cannot be neglected uniformly across all spatial regions. Thus, the quantum pressure remains significant in certain regions of space, even in the limit $\epsilon \to 0$.

As noted in Wallstrom (1994), the hydrodynamical equations (3.16)-(3.17) are not strictly equivalent to the Schrödinger equation (3.5) due to the ill-defined mapping $\psi \leftrightarrow \{\rho, S, \vec{v}\}$ as the density vanishes (leading to non-uniqueness of the phase). This can lead to the generation of vorticity along the lines where $\rho = 0$, although the velocity field $\vec{v}$ defined in equation (2.40) is always free of curl, representing the gradient of a scalar

Nevertheless, in regimes where the density does not vanish (or when such discrepancies can be neglected) the hydrodynamical picture remains useful, as it is simpler to interpret and provides a more direct comparison with the density and velocity fields used to describe the cosmological distribution of DM. In this thesis, we shall focus on spherically symmetric solutions, where the equivalence is exact. Indeed, this makes the problem one-dimensional in space and any radial velocity v_r can be written as the gradient of a phase S, so that one can go back from the hydrodynamical picture to the Schrödinger picture with $S = \int dr\, v_r$. Besides, we shall find that for our self-similar solutions the density never vanishes if $\epsilon > 0$.

3.1.4 Convergence to the classical distribution and multistreaming

As FDM has been used as an alternative tool from N-body simulations to study CDM, and because we shall find that the properties of FDM self-similar solutions are quite different from those of CDM self-similar solutions, we discuss here in more details the semiclassical limit. In particular, we present the link between the wave function ψ, the Husimi phase space distribution and its semiclassical limit, and the hydrodynamical picture. From Eqs.(3.11) and (3.12), we write

$$f_{\rm H}(\vec{r},\vec{v}) = \left| \int \frac{d\vec{r}\,'}{(2\pi\epsilon)^{9/4}\sigma_r^{3/2}} \sqrt{\rho(\vec{r}\,')}\, e^{-\frac{(\vec{r}\,'-\vec{r})^2}{4\sigma_r^2\epsilon} - \frac{i}{\epsilon}\vec{v}\cdot\vec{r}\,' + \frac{i}{\epsilon}S(\vec{r}\,')} \right|^2 . \tag{3.19}$$

Making the change of variables $\vec{r}\,' = \vec{r} + \sqrt{\epsilon}\vec{r}\,''$ and expanding $\rho(\vec{r}\,')$ and $S(\vec{r}\,')$, we obtain at leading order over ϵ

$$f_{\rm H} \simeq \rho(\vec{r}) \left| \int \frac{d\vec{r}\,''}{(2\pi)^{9/4}\epsilon^{3/4}\sigma_r^{3/2}} e^{\frac{i}{\sqrt{\epsilon}}(S_{,j}-v_j)r_j'' - \frac{r''^2}{4\sigma_r^2} + \frac{i}{2}S_{,jk}r_j''r_k''} \right|^2 , \tag{3.20}$$

where we sum over the spatial indices j, k and we denoted the spatial derivatives $S_{,j} = \partial_j S$ and $S_{,jk} = \partial_j \partial_k S$. Being real symmetric, the matrix $S_{,jk}$ is diagonalizable with real eigenvalues s_j. Then, the complex matrix M defined by

$$M_{jk} = \delta_{jk} - i2\sigma_r^2 S_{,jk}, \tag{3.21}$$

is also diagonalizable with eigenvalues $m_j = 1 - i2\sigma_r^2 s_j$, with strictly positive real parts. Therefore, we can perform the Gaussian integral,

$$f_{\rm H}(\vec{r},\vec{v}) \simeq \rho(\vec{r}) \left(\frac{2\sigma_r^2}{\pi\epsilon}\right)^{3/2} (\det(M)\det(M^*))^{-1/2} \times e^{-\frac{\sigma_r^2}{\epsilon}(M^{-1}+M^{*-1})_{jk}(S_{,j}-v_j)(S_{,k}-v_k)}. \tag{3.22}$$

Using (3.21) we also have

$$M^{-1} + M^{*-1} = M^{-1}(M + M^*)M^{*-1} = 2M^{-1}M^{*-1}. \tag{3.23}$$

This is then a diagonalizable matrix with strictly positive real eigenvalues. Therefore, in the limit $\epsilon \to 0$ the Gaussian velocity factor gives a Dirac term with a normalization that cancels the determinant prefactor,

$$\epsilon \to 0 : \quad f_{\rm H}(\vec{r},\vec{v}) = \rho(\vec{r})\,\delta_D(\vec{v} - \nabla S). \tag{3.24}$$

This is the classical distribution in phase space for a single-stream flow with density ρ and velocity $\vec{v} = \nabla S$. Of course, this result only holds if the wave function only varies on the macroscopic scale of interest L and does not show structures at scale $\sqrt{\epsilon}L$, so that we can use a Taylor expansion for the density and the phase. This is violated if the dynamics generate structures on increasingly small scales as $\epsilon \to 0$. This is why the semiclassical limit can be a delicate matter.

In the multistreaming regime, the wave function reads as (Jin et al., 2011)

$$\psi = \sum_{\text{stream } j} \sqrt{\rho_j(\vec{r})}\, e^{iS_j(\vec{r})/\epsilon}, \tag{3.25}$$

where we sum over the streams, and we obtain

$$\epsilon \to 0 : \quad f_{\rm H}(\vec{r},\vec{v}) = \sum_j \rho_j(\vec{r})\,\delta_D(\vec{v} - \nabla S_j). \tag{3.26}$$

Indeed, the cross-terms that arise from the modulus squared show two Gaussian velocity factors with well separated peaks and are therefore negligible in the limit $\epsilon \to 0$. At least locally we can always write ψ in the form (3.12). It is interesting to see why the derivation (3.24) fails in this case. Let us choose for simplicity two streams in a one-dimensional system, with constant densities ρ_1 and ρ_2, constant velocities $v_1 = 0$ and v_2, and hence $S_1 = 0$ and $S_2 = v_2 x$,

$$\psi = \sqrt{\rho_1} + \sqrt{\rho_2} e^{iv_2 x/\epsilon} = \sqrt{\rho}\, e^{iS/\epsilon}. \tag{3.27}$$

This gives for the total density ρ and phase S the expressions

$$\begin{aligned} \rho &= \rho_1 + \rho_2 + \sqrt{\rho_1\rho_2}2\cos(v_2 x/\epsilon), \\ S &= \epsilon \arccos\left[\frac{1}{\sqrt{\rho}}\left(\sqrt{\rho_1} + \sqrt{\rho_2}\cos(v_2 x/\epsilon)\right)\right]. \end{aligned} \tag{3.28}$$

We can see that the total density ρ and phase S now show fast oscillations at scale ϵ. Therefore, the Gaussian approximation used above no longer applies if ψ is written as $\sqrt{\rho}e^{iS/\epsilon}$. It however applies on each of the two terms of the expression $\sqrt{\rho_1} + \sqrt{\rho_2}e^{iv_2 x/\epsilon}$, as their densities ρ_j and phases S_j do not show fast oscillations.

This illustrates that, while by going from the 6D phase space of the classical distribution $f(\vec{r}, \vec{v})$ to the 3D configuration space of the wave function $\psi(\vec{r})$, we can hope to obtain a competitive tool to simulate CDM as compared with usual N-body simulations, the difficulties associated with shell crossings reappear as small-scale oscillations. Thus, one needs a high accuracy to resolve the different streams and this also sets a practical lower bound on the semiclassical parameter ϵ to avoid too large computer times.

In the self-similar solutions studied here, we do not have multistreaming but the width of the solutions shrinks with ϵ, as shown by the scaling (3.60) below. This again implies that the semiclassical limit is not given by a Gaussian approximation as above and it is not trivial. This is why we shall not recover the CDM self-similar solutions in the limit $\epsilon \to 0$. Instead, these solutions vanish as their width becomes infinitesimal, while never reaching a classical regime.

3.2 Equilibrium and self-similar solutions

3.2.1 Static equilibria: solitons

As we have discussed in Section 2.6.2, solitons are static equilibrium profiles, i.e zero velocity $\vec{v}$. This leads to the hydrostatic equilibrium condition, as derived from the Euler equation (3.17), Chavanis (2011)

$$\Phi_{\rm N} + \Phi_{\rm Q} = \alpha, \tag{3.29}$$

where α is a constant. The FDM soliton arises from the balance between the repulsive quantum pressure and the attractive force of gravity. Then, the Hamilton-Jacobi equation (3.14) leads to

$$S = -\alpha t, \quad \text{hence} \quad \psi = e^{-i\alpha t/\epsilon}\psi_{\rm sol}(r), \quad \rho_{\rm sol} = \psi_{\rm sol}^2, \tag{3.30}$$

where we consider for spherically symmetric solutions. Replacing this into the Schrödinger equation (3.5) we have,

$$\epsilon^2\nabla^2\psi_{\rm sol} = 2(\Phi_{\rm N} - \alpha)\psi_{\rm sol}, \tag{3.31}$$

which, coupled with the Poisson equation, $\nabla^2\Phi_{\rm N} = 4\pi\psi_{\rm sol}^2$, determines the soliton profile. The boundary conditions are $\psi'_{\rm sol} = 0$ at $r = 0$ and $\psi_{\rm sol} \to 0$ for $r \to \infty$. Different values of α correspond to different values of the soliton mass and central density. These different profiles are related through the scaling law (2.78).

3.2.2 Self-similar exponents

As we have already explained, seeking self-similar solutions offers a valuable approach to explore dynamics beyond static equilibrium profiles. Self-similar solutions provide time-dependent solutions that can be effectively analyzed using semi-analytical tools. In this section we explain how we calculate the scaling variable of the self-similar solutions for the SP system.

3.2.2.1 Field picture

In the setting of the complex field ψ and the gravitational potential $\Phi_{\rm N}$, we search for self-similar solutions using the self-similar ansatz, which are represented in the following form:

$$\psi = t^{-\alpha} f\left(\frac{r}{t^{\beta}}\right), \qquad \Phi_{\rm N} = t^{-\mu} h\left(\frac{r}{t^{\beta}}\right), \tag{3.32}$$

where f and h are unknown functions to be determined, as well as the scaling exponents α, β and μ. Replacing this into the SP system (3.5)-(3.6), we get,

$$-i\epsilon t^{-\alpha-1}(\alpha f + \beta\eta f') = -\frac{\epsilon^2}{2} t^{-\alpha-2\beta}\left(f'' + \frac{2}{\eta} f'\right) + t^{-\mu-\alpha} h f, \tag{3.33}$$

$$t^{-\mu-2\beta}\left(h'' + \frac{2}{\eta} h'\right) = 4\pi t^{-\alpha-\alpha^*} f f^*, \tag{3.34}$$

where the prime notation represents the derivative with respect to the new variable $\eta = r/t^{\beta}$. The compatibility conditions of these equations, when expressed solely in terms of η, provide us with the values of the scaling exponents,

$$\beta = 1/2, \quad \mu = 1, \quad \alpha = 1 + i\, b, \tag{3.35}$$

where b is a real undetermined parameter. Thus, the fields take the form

$$\psi = t^{-1-ib} f\left(\frac{r}{\sqrt{t}}\right), \qquad \Phi_{\rm N} = t^{-1} h\left(\frac{r}{\sqrt{t}}\right). \tag{3.36}$$

We recognize the diffusive scaling $\sqrt{t}$ arising from the Laplacian in the Schrödinger equation. The functions f and h must then be determined by solving the ordinary differential equations (3.34)-(3.34).

3.2.2.2 Fluid picture

By examining the dynamics from a hydrodynamic perspective, we can verify the consistency of the self-similar exponents. To do so, we search for solutions characterised by the self-similar ansatz:

$$\rho = t^{-\alpha} f\left(\frac{r}{t^{\beta}}\right), \quad v = t^{-\delta} g\left(\frac{r}{t^{\beta}}\right), \quad \Phi_{\rm N} = t^{-\mu} h\left(\frac{r}{t^{\beta}}\right), \tag{3.37}$$

and substituting into the continuity, Euler and Poisson equations (3.16)-(3.18), we have,

$$-t^{-\alpha-1}\left(\alpha f + \beta\eta f'\right) + t^{-\alpha-\beta-\delta}\left(\frac{2}{\eta} f g + f' g + f g'\right) = 0, \tag{3.38}$$

$$-t^{-\delta-1}\left(\delta g + \beta\eta g'\right) + t^{-2\delta-\beta} g g' = -t^{-\mu-\delta} h' + \frac{\epsilon^2}{4} t^{-3\beta} \frac{d}{d\eta}\left(\frac{f''}{f} + \frac{2}{\eta}\frac{f'}{f} - \frac{1}{2}\left(\frac{f'}{f}\right)^2\right), \tag{3.39}$$

$$t^{-\mu-2\beta}\left(h'' + \frac{2}{\eta} h'\right) = 4\pi t^{-\alpha} f. \tag{3.40}$$

The compatibility conditions now give

$$\beta = 1/2, \quad \mu = 1, \quad \alpha = 2, \quad \delta = 1/2, \tag{3.41}$$

and the fields take the form

$$\rho = t^{-2} f\left(\frac{r}{\sqrt{t}}\right), \quad v = t^{-1/2} g\left(\frac{r}{\sqrt{t}}\right), \quad \Phi_{\rm N} = t^{-1} h\left(\frac{r}{\sqrt{t}}\right). \tag{3.42}$$

Knowing that $\vec{v} = \vec{\nabla} S$ and using the Hamilton-Jacobi equation (3.14), we obtain the phase S from the velocity $\vec{v}$ as

$$S = s\left(\frac{r}{\sqrt{t}}\right) + c_0 \ln t + c_1, \quad \text{with} \quad s' = g, \tag{3.43}$$

and c_0 and c_1 are undetermined real constants. This gives for the complex field ψ, using the Madelung transformation (2.40),

$$\psi = t^{-1} \sqrt{f\left(\frac{r}{\sqrt{t}}\right)} e^{i[s(r/\sqrt{t}) + c_0 \ln t + c_1]/\epsilon}, \tag{3.44}$$

which takes the same scaling form as the previous result (3.36) (with different meanings for the function f and the parameters b, c_0 and c_1).

3.3 Cosmological self-similar solutions

3.3.1 Cosmological background

Given our interest in FDM in the cosmological context, our attention now shifts towards self-similar solutions within this cosmological framework. Similar to CDM, these solutions can only be found during cosmological epochs where the scale factor follows a power law with respect to time. This ensures that the cosmological background does not introduce any specific time or length scales, preserving the self-similarity. Hence, we focus on the Einstein-de Sitter universe, which accurately describes the matter-dominated era during which applies to the matter era when most large-scale structures are formed, until $z \sim 1$. On scales significantly smaller than the horizon, Newtonian gravity can effectively describe the dynamics. The scale factor grows as $a \propto t^{2/3}$, and the Hubble expansion can be expressed as follows:

$$H = \frac{2}{3t}, \quad a = t^{2/3}, \tag{3.45}$$

in dimensionless units. Then, the background density $\bar{\rho}$, the Hubble-flow radial velocity $\bar{v}$ and the background Newtonian potential $\bar{\Phi}_{\rm N}$ read

$$\bar{\rho} = \frac{1}{6\pi t^2}, \quad \bar{v} = \frac{2r}{3t}, \quad \bar{\Phi}_{\rm N} = \frac{r^2}{9t^2}. \tag{3.46}$$

We can verify that these expressions satisfy the continuity, Euler, and Poisson equations (3.16)-(3.18). Furthermore, these background expressions also exhibit self-similar forms (3.42). Consequently, we can seek self-similar solutions related to perturbations around this expanding background as well.

3.3.2 Comoving coordinates

To facilitate comparison with the standard CDM scenario, we choose to work within the hydrodynamical framework. Consequently, we introduce comoving spatial coordinates $\vec{x} = \vec{r}/a$ and express the density, velocity fields, and gravitational potential as follows:

$$\rho = \bar{\rho}(1+\delta), \quad \vec{v} = \bar{\vec{v}} + \vec{u}, \quad \Phi_{\rm N} = \bar{\Phi}_{\rm N} + \varphi_{\rm N}, \tag{3.47}$$

Here, δ represents the density contrast, and $\vec{u}$ corresponds to the peculiar velocity. Substituting these expressions into the continuity, Euler, and Poisson equations (3.16)-(3.18), we obtain:

$$\frac{\partial \delta}{\partial t} + \frac{1}{a}\nabla_x \cdot [(1+\delta)\vec{u}] = 0, \tag{3.48}$$

$$\frac{\partial \vec{u}}{\partial t} + \frac{1}{a}(\vec{u}\cdot\nabla_x)\vec{u} + H\vec{u} = -\frac{1}{a}\nabla_x(\varphi_{\rm N} + \Phi_{\rm Q}), \tag{3.49}$$

$$\nabla_x^2 \varphi_{\rm N} = \frac{2}{3}\frac{\delta}{a}. \tag{3.50}$$

These equations resemble the standard comoving fluid equations, except for the additional term accounting for quantum pressure on the right-hand side of the Euler equation. This additional term is represented by:

$$\Phi_{\rm Q} = -\frac{\epsilon^2}{2a^2}\frac{\nabla_x^2\sqrt{\rho}}{\sqrt{\rho}}. \tag{3.51}$$

Note that these hydrodynamical equations can be derived in a more rigorous way from the action of the scalar field ϕ as we have discussed in Section 2.9. This action is formulated in an expanding metric with linear-gravity perturbations around the FLRW metric (Brax et al., 2019a). In the nonrelativistic limit, the comoving Schrödinger equation takes the following form:

$$i\epsilon\frac{\partial \psi}{\partial t} = -\frac{\epsilon^2}{2a^2}\nabla_x^2\psi + \varphi_{\rm N}\psi, \tag{3.52}$$

where we have factored out the term $1/(\sqrt{6\pi}t)$ from the amplitude of ψ, associated with the decrease of the background density (Widrow & Kaiser, 1993).

The comoving Schrödinger-Poisson system is a suitable description for the dynamics of large-scale structures within the Hubble radius, where relativistic corrections can be safely neglected. This approximation is commonly employed when studying the formation of large-scale structures during the matter era, both in analytical works and N-body simulations (Peebles, 1980; Peacock, 1998; Mo et al., 2010). It is justified by the fact that the scale at which the density field becomes non-linear (around $\lesssim 10$ Mpc) is much smaller than the Hubble horizon.

In the usual approach, these Newtonian equations of motion are extended to infinite space. This can be achieved through continuous Fourier transforms involving an integral over all space or by employing N-body simulations within a finite box with periodic boundary conditions. Such a procedure is valid as long as the focus is on scales significantly smaller than the Hubble radius.

By expressing the comoving Madelung transformation as follows:

$$\psi = \sqrt{1+\delta}\, e^{iS/\epsilon}, \quad \vec{p} = a\vec{u} = \vec{\nabla}_x S, \tag{3.53}$$

where $\vec{p}$ represents the comoving momentum and $\vec{u}$ the peculiar velocity, we recover the continuity and Euler equations (3.48)-(3.49). Additionally, the comoving Hamilton-Jacobi equation for the phase S reads

$$\frac{\partial S}{\partial t} + \frac{(\vec{\nabla}_x S)^2}{2a^2} = -\varphi_{\rm N} - \Phi_{\rm Q}. \tag{3.54}$$

Furthermore, the comoving Wigner distribution now becomes,

$$f_{\rm W}(\vec{x},\vec{p}) = \int \frac{d\vec{x}\,'}{(2\pi)^3}\, e^{i\vec{p}\cdot\vec{x}\,'}\, \psi\left(\vec{x} - \frac{\epsilon}{2}\vec{x}\,'\right) \psi^*\left(\vec{x} + \frac{\epsilon}{2}\vec{x}\,'\right). \tag{3.55}$$

Approximately, up to corrections of order ϵ, this distribution satisfies the comoving Vlasov equation:

$$\frac{\partial f_{\rm W}}{\partial t} + \frac{\vec{p}}{a^2}\cdot\frac{\partial f_{\rm W}}{\partial \vec{x}} - \vec{\nabla}_x\varphi_{\rm N}\cdot\frac{\partial f_{\rm W}}{\partial \vec{p}} + \mathcal{O}(\epsilon) = 0. \tag{3.56}$$

The background comoving field $\bar{\psi}$ and distribution $\bar{f}_{\rm W}$ are

$$\bar{\psi} = 1, \quad \bar{S} = 0, \quad \bar{f}_{\rm W} = \delta_D(\vec{p}), \tag{3.57}$$

which coincides with the phase-space distribution of the CDM background.

3.3.3 Self-similar coordinates

Consistent with the fields in (3.42), we can verify that spherical self-similar solutions will exhibit the following form:

$$\begin{aligned}
&\delta(x,t) = \hat{\delta}(\eta),\\
&u(x,t) = \epsilon^{1/2}\, t^{-1/2}\, \hat{u}(\eta),\\
&\varphi_{\rm N}(x,t) = \epsilon\, t^{-1}\, \hat{\varphi}_{\rm N}(\eta),\\
&\Phi_{\rm Q}(x,t) = \epsilon\, t^{-1}\, \hat{\Phi}_{\rm Q}(\eta),\\
&\delta M(x,t) = \epsilon^{3/2}\, t^{-1/2}\, \delta\hat{M}(\eta),
\end{aligned} \tag{3.58}$$

where the perturbed mass δM is defined as follows:

$$\delta M(r) = 4\pi \int_0^r dr\, r^2 \delta\rho(r) = \frac{2}{3}\int_0^x dx\, x^2 \delta(x), \tag{3.59}$$

and we have introduced the scaling variable

$$\eta = \frac{t^{1/6}x}{\epsilon^{1/2}} = \frac{r}{\sqrt{\epsilon t}}. \tag{3.60}$$

This scaling is in agreement with the self-similar exponents derived in Section 3.2.2 and we have additionally incorporated the scaling with respect to ϵ. Consequently, the self-similar exponents remain unchanged for both the Minkowski and Einstein-de Sitter backgrounds.

Accordingly, the characteristic length scale exhibits growth as $\sqrt{t}$ in physical units, while it decreases as $t^{-1/6}$ in comoving units. The associated mass follows a decreasing trend as $M \propto 1/\sqrt{t}$. Therefore, these self-similar solutions differ significantly from those obtained for CDM. While their size expands in physical units, it does so at a slower rate

compared to the scale factor, resulting in a contraction in comoving units. Consequently, their mass also decreases over time, in contrast to the self-similar CDM solutions that exhibit growth in both comoving size and mass (Fillmore & Goldreich, 1984; Bertschinger, 1985). This behaviour can be attributed to the diffusive scaling $r \sim \sqrt{t}$, which remains independent of the shape of the self-similar solution and the Einstein-de Sitter expansion.

The Euler equation (3.49) can be expressed in terms of the scaling variable η as follows,

$$\frac{1}{6}(\hat{u} + \eta\hat{u}') + \hat{u}\hat{u}' + \hat{\varphi}'_{\rm N} + \hat{\Phi}'_{\rm Q} = 0, \tag{3.61}$$

which can be integrated as

$$\frac{1}{6}\eta\hat{u} + \frac{1}{2}\hat{u}^2 + \hat{\varphi}_{\rm N} + \hat{\Phi}_{\rm Q} = 0. \tag{3.62}$$

By imposing the boundary condition that all fields vanish at infinity, where they converge to the cosmological background, we obtain from the integration of the Euler equation a Bernoulli-like equation (3.62). This integration is possible because the Euler equation itself is derived from the Hamilton-Jacobi equation (3.14). The Bernoulli equation (3.62) is really helpful since it takes into account the contribution of kinetic energy, in contrast to the hydrostatic equilibrium (3.29) that determines the soliton profiles based on the balance between gravity and quantum pressure.

In terms of the ψ field, we obtain the self-similar scalings

$$S = \epsilon\hat{S}(\eta), \quad \psi = \hat{\psi}(\eta) = \sqrt{1+\hat{\delta}}\, e^{i\hat{S}}. \tag{3.63}$$

By comparing the self-similar form of the Hamilton-Jacobi equation (3.54) with the Bernoulli equation (3.62), we find that

$$\hat{S}' = \hat{u}. \tag{3.64}$$

Defining as in (3.60) and (3.58) the rescaled position $\vec{\eta}$ and momentum $\vec{\nu}$,

$$\vec{x} = \epsilon^{1/2} t^{-1/6}\vec{\eta}, \quad \vec{p} = \epsilon^{1/2} t^{1/6}\vec{\nu}, \tag{3.65}$$

the Wigner distribution takes the self-similar form

$$f_{\rm W} = \epsilon^{-3/2} t^{-1/2} \int \frac{d\vec{\eta}'}{\pi^3}\, e^{2i\vec{\eta}'\cdot\vec{\nu}} \hat{\psi}(\vec{\eta} - \vec{\eta}')\hat{\psi}^*(\vec{\eta} + \vec{\eta}'). \tag{3.66}$$

To obtain a self-similar form for the Husimi distribution, we need to smooth the Wigner distribution while following the self-similar scaling $t^{-1/6}$ of spatial coordinates, as in (3.60). We choose:

$$\sigma_x = 2^{-1/2} t^{-1/6}\sigma, \quad \sigma_p = 1/(2\sigma_x), \tag{3.67}$$

where,as discussed for Eq.(3.11), we take $\sigma_x\sigma_p = 1/2$ to achieve the best possible resolution for the positive Husimi distribution. The self-similar Husimi distribution is then given by:

$$f_{\rm H}(\vec{x}, \vec{p}) = \epsilon^{-3/2} t^{-1/2} \hat{f}_{\rm H}(\vec{\eta}, \vec{\nu}), \tag{3.68}$$

with

$$\hat{f}_{\rm H} = \left| \int \frac{d\vec{\eta}'}{2^{3/2}\pi^{9/4}\sigma^{3/2}}\, e^{-(\vec{\eta}-\vec{\eta}')^2/(2\sigma^2) - i\vec{\nu}\cdot\vec{\eta}'} \hat{\psi}(\vec{\eta}') \right|^2. \tag{3.69}$$

The parameter σ sets the spatial resolution of the self-similar Husimi distribution. At the background level, this gives

$$\bar{\hat{f}}_{\rm H}(\vec{\eta},\vec{\nu}) = \sigma^3\pi^{-3/2}\, e^{-\sigma^2\nu^2}. \tag{3.70}$$

The time dependence of the smoothing σ_x introduces additional corrections to the equation of motion followed by the Husimi distribution compared to the classical Vlasov equation. However, this is not significant when considering the Wigner distribution as the fundamental distribution, which satisfies equation (3.56). This equation deviates from the Vlasov equation only by terms of order ϵ and higher. Therefore, we can choose any smoothing for the Husimi distribution, determining the desired resolution. The choice of smoothing can also depend on time to accommodate the growth or shrinking of the underlying dynamics.

Moreover, these corrections are again higher order in ϵ. As a result, as $\epsilon \to 0$, we can expect to recover classical dynamics on scales much larger than σ_x, unless small scales continue to have a non-negligible impact on larger scales.

3.3.4 Linear regime

Studying small linear perturbations around the expanding background is a valuable approach that enables us to obtain explicit analytical expressions. Additionally, it offers an insightful comparison with the CDM. By linearizing the equations of motion (3.48)-(3.50) with respect to the density and velocity fields and combining the continuity and Euler equations, we arrive at a closed equation for the linear density contrast δ_L,

$$\ddot{\delta}_L + \frac{4}{3t}\dot{\delta}_L - \frac{2}{3t^2}\delta_L + \frac{\epsilon^2}{4t^{8/3}}\nabla_x^4\delta_L = 0, \tag{3.71}$$

where derivative with respect to cosmic time t is denoted by a dot. The resulting equation is a standard second-order equation in time, similar to what is obtained for CDM, with the exception of an additional term associated with quantum pressure. This term carries an ϵ prefactor, as anticipated. While this term is negligible on large scales, it damps modes on small scales due to the presence of the Laplacian squared operator.

3.3.4.1 Fourier space

To facilitate comparison with the conventional CDM model, it is instructive to examine (3.71) in Fourier space. In this representation, it takes the form

$$\ddot{\delta}_L + \frac{4}{3t}\dot{\delta}_L - \frac{2}{3t^2}\delta_L + \frac{\epsilon^2 k^4}{4t^{8/3}}\delta_L = 0. \tag{3.72}$$

Similar to CDM, different wavenumbers are decoupled, and this second-order differential equation of the linear density contrast admits two independent solutions, denoted as $D_\pm(k,t)$, corresponding to the growing and decaying modes

$$\begin{aligned} D_+(k,t) &= t^{-1/6} J_{-5/2}\left(\frac{3}{2}\epsilon k^2 t^{-1/3}\right), \\ D_-(k,t) &= t^{-1/6} J_{5/2}\left(\frac{3}{2}\epsilon k^2 t^{-1/3}\right). \end{aligned} \tag{3.73}$$

In the semiclassical limit, $\epsilon \to 0$, or on large scales, $k \to 0$, we recover the time dependence of the CDM linear growing modes, $D_+(k,t) \propto t^{2/3} \propto a$ and $D_-(k,t) \propto t^{-1}$.

However, in contrast with the CDM modes, for nonzero ϵ the modes $D_\pm(k,t)$ depend on the wavenumber k and differ from power laws. At high k or at small time, we have $D_+(k,t) \sim \cos\left(3\epsilon k^2 t^{-1/3}/2\right)$ and $D_-(k,t) \sim \sin\left(3\epsilon k^2 t^{-1/3}/2\right)$. Thus, we obtain acoustic waves when the quantum pressure is dominant (but with a higher power of k because of the k^4 factor in (3.72)). At late times we always recover the CDM behavior. This is due to the damping of the quantum-pressure term in Eq.(3.72) by the factor $t^{-8/3}$. This is also related to the scalings $r \propto \sqrt{t}$ and $x \propto t^{-1/6}$ found in (3.58): the scale where wavelike effects, or the quantum pressure, are important decreases in time, in comoving coordinates. Thus, deviations from CDM become confined to increasingly small scales. Further detailed comparison, can be found in Section 3.3.5.

Then, the linear density contrast takes the form

$$\delta_L(\vec{k},t) = D_+(k,t)\delta_{L+}(\vec{k}) + D_-(k,t)\delta_{L-}(\vec{k}), \tag{3.74}$$

where the functions $\delta_{L\pm}(\vec{k})$ are determined by the initial conditions for δ and $\dot{\delta}$ at some initial time. From Eq.(3.58) we find that spherically symmetric and self-similar solutions are of the form

$$\delta(\vec{k},t) = t^{-1/2}\,\delta(t^{-1/6}k). \tag{3.75}$$

Comparing with Eqs.(3.73) and (3.74), we obtain $\delta_{L\pm}(\vec{k}) \propto k^{-2}$. We require $\delta_L(k) \to 0$ for $k \to 0$, as we wish to recover the background density on large scales. This rules out the mode $D_+(k,t)$ and we obtain

$$\delta_L(\vec{k},t) \propto t^{-1/6}k^{-2}J_{5/2}\left(\frac{3}{2}\epsilon k^2 t^{-1/3}\right). \tag{3.76}$$

Note that in the FDM regime, where the quantum pressure is important, the two modes $D_\pm$ oscillate with a constant amplitude and no longer correspond to growing and decaying modes. Therefore, it is not unphysical to keep only the mode D_-, as a small perturbation by a mode D_+ will remain small as long as we remain in the FDM regime.Going back to real space by taking the inverse Fourier transform, we obtain

$$\delta_L(x,t) = 1 + \frac{\eta^4}{45} - \frac{8\eta^2}{9\pi}\,{}_2F_3\left(-\frac{1}{2},2;\frac{3}{2},\frac{5}{4},\frac{7}{4};-\frac{\eta^4}{144}\right), \tag{3.77}$$

where ${}_2F_3$ is a hypergeometric function, η is the scaling variable defined in (3.60), and we normalized the linear mode to unity at the center. As already explained below (3.58), this self-similar solution (3.77) expands in physical coordinates $\vec{r}$ but shrinks in comoving coordinates $\vec{x}$. Another difference with the CDM self-similar solutions is that the amplitude of the linear density contrast near the center does not grow with time and remains constant, $\delta(x,t) = \hat{\delta}(\eta)$. Thus, it is not unstable and does not reach the non-linear regime at late times: a small-amplitude perturbation δ_L will always keep a small amplitude and to reach the non-linear regime we must start with a large non-linear perturbation.

3.3.4.2 Real space

Because we look for spherically-symmetric self-similar solutions of the form (3.58), we can actually solve the equation of motion (3.71) in real space. Looking for a solution $\delta(\eta)$,

in terms of the self-similar scaling variable (3.60), the partial differential equation (3.71) becomes the ordinary differential equation

$$\delta_L^{(4)} + \frac{4}{\eta}\delta_L^{(3)} + \frac{\eta^2}{9}\delta_L'' + \frac{\eta}{3}\delta_L' - \frac{8}{3}\delta_L = 0, \tag{3.78}$$

where the prime denotes the derivative with respect to η.

The fourth and third derivatives come from the quantum pressure term, which changes the order of the equation from two to four, as compared with the usual CDM case. Therefore, we now have four independent linear modes instead of two, which read

$$\begin{aligned}
\delta_{L1} &= 45 + \eta^4, \quad \delta_{L2} = \frac{1}{\eta}\,{}_2F_3\left(-\frac{5}{4}, \frac{5}{4}; \frac{1}{4}, \frac{1}{2}, \frac{3}{4}; -\frac{\eta^4}{144}\right), \\
\delta_{L3} &= \eta\,{}_2F_3\left(-\frac{3}{4}, \frac{7}{4}; \frac{3}{4}, \frac{5}{4}, \frac{3}{2}; -\frac{\eta^4}{144}\right), \\
\delta_{L4} &= \eta^2\,{}_2F_3\left(-\frac{1}{2}, 2; \frac{5}{4}, \frac{3}{2}, \frac{7}{4}; -\frac{\eta^4}{144}\right).
\end{aligned} \tag{3.79}$$

Their asymptotic behaviors at the center read

$$\eta \to 0: \quad \delta_{L2} = \frac{1}{\eta} + \ldots, \quad \delta_{L3} = \eta + \ldots, \quad \delta_{L4} = \eta^2 + \ldots \tag{3.80}$$

where the dots stand for higher-order terms. This rules out δ_{L2} and δ_{L3} if we look for a smooth solution with an even Taylor expansion in the radius x at the center. The asymptotic behavior of δ_{L4} at large distance reads

$$\eta \to \infty: \quad \delta_{L4} = \frac{\pi\eta^4}{40} + \frac{9\pi}{8} - \frac{243}{5\eta^6} + \cdots + \cos\left(\eta^2/6\right) \times \left[\frac{27\sqrt{3\pi}}{2\eta^3} + \ldots\right] + \sin\left(\eta^2/6\right)\left[\frac{27\sqrt{3\pi}}{2\eta^3} + \ldots\right], \tag{3.81}$$

where the dots stand for higher order terms in $1/\eta$. Therefore, the only combination of the four modes that satisfies the boundary conditions at the center and at infinity is

$$\delta_L = -\frac{8}{9\pi}\left(\delta_{L4} - \frac{\pi}{40}\delta_{L1}\right), \tag{3.82}$$

where we chose the normalization $\delta_L(0) = 1$, and we recover Eq.(3.77), as expected. From the density contrast δ_L we can derive the velocity u_L and the perturbed mass δM_L, which can also be expressed in terms of hypergeometric functions.

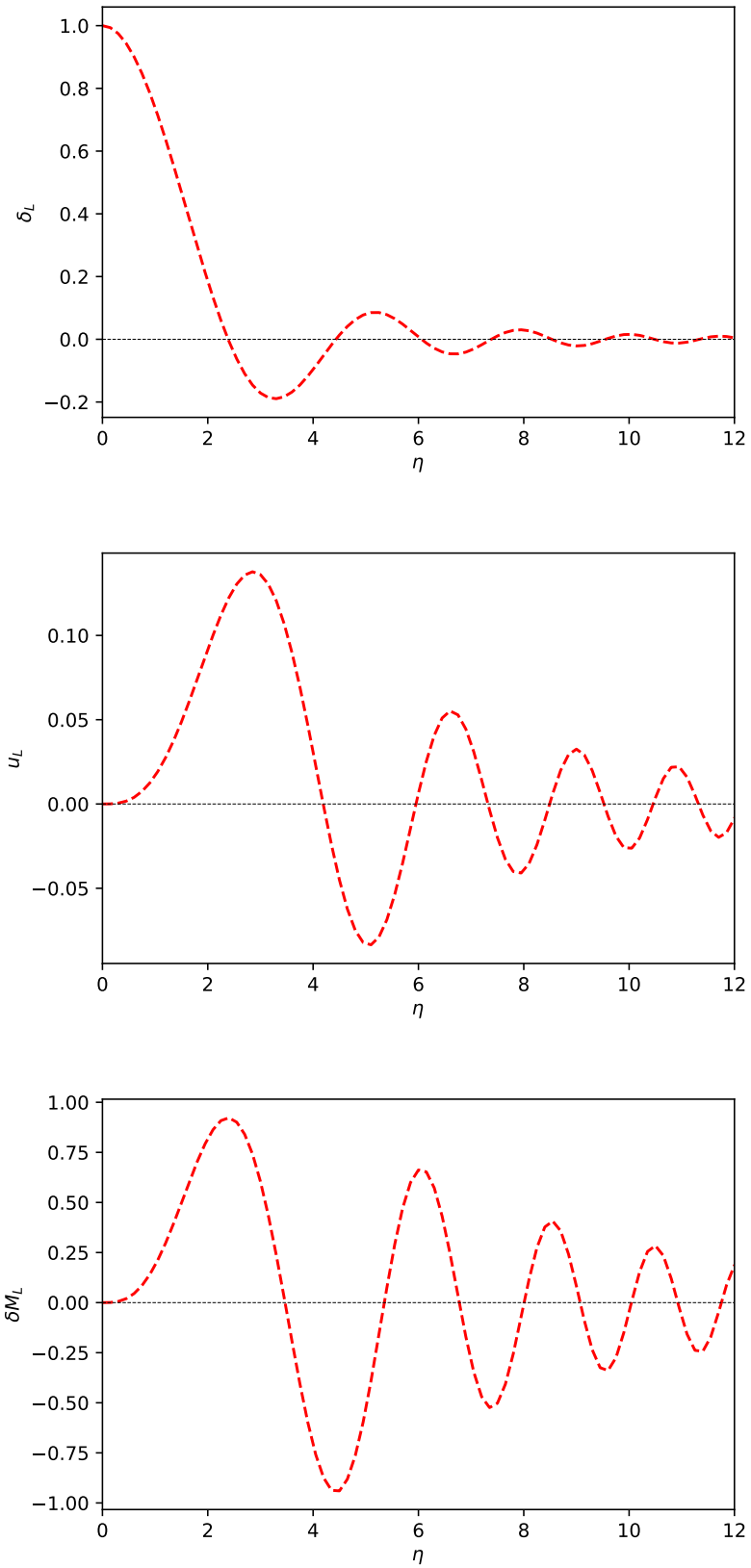

Figure 3.1. From top to bottom: linear density contrast $\hat{\delta}_L$ from Eq.(3.77), linear velocity perturbation $\hat{u}_L$ and linear mass perturbation $\delta\hat{M}_L$, for $\hat{\delta}_L(0) = 1$.

3.3.4.3 Numerical results

Figure 3.1 illustrates the linear density contrast, velocity and mass perturbations, normalized to $\hat{\delta}_L(0) = 1$. In contrast with CDM self-similar solutions, which show a power-law falloff at large distance without oscillations, the fields oscillate around zero at the same frequency.

Notably, these self-similar solutions correspond to compensated profiles, as the mass perturbation approaches zero at infinity and undergoes an infinite number of sign changes. Positive density peaks roughly correspond to minima of the radial velocity perturbation and zero crossings of the mass perturbation. These oscillatory features arise from the presence of quantum pressure (absent in CDM), which generates acoustic waves with a different dispersion relation from conventional sound waves.

The central density peak is significantly higher than the subsequent peaks, which decrease as $1/\eta^3$ at large distances. This behaviour arises from the three-dimensional nature of space (i.e. the volume factor η^3), resulting in more regular velocity and mass oscillations.

As time progresses, the profiles shrink in comoving coordinates according to $x \propto t^{-1/6}$ as stated in Eq.(3.60). The central peak becomes confined to an increasingly narrow region in comoving coordinates, with a decreasing mass. However, in physical coordinates, the peak actually expands with $r \propto \sqrt{t}$.

In contrast to CDM self-similar solutions, the amplitude of the linear density contrast profile remains constant over time. However, the velocity and mass perturbations decay as $1/\sqrt{t}$, as indicated by the scaling laws in equation (3.58).

3.3.4.4 Balance of kinetic, gravitational and quantum-pressure terms

While the static solitons (3.31) are characterized by the balance between gravity and the quantum pressure in (3.29), the self-similar solutions are dynamical and encompass kinetic effects due to the nonzero velocity, as indicated by (3.62). Notably, at large distance we obtain for $\eta \to \infty$,

$$\begin{aligned}
\hat{u}_L &\sim \eta^{-5} + \eta^{-2}[\cos(\eta^2/6) + \sin(\eta^2/6)],\\
\hat{\varphi}_{\mathrm{N}L} &\sim \eta^{-4} + \eta^{-5}[\cos(\eta^2/6) + \sin(\eta^2/6)],\\
\hat{\Phi}_{\mathrm{Q}L} &\sim \eta^{-8} + \eta^{-1}[\cos(\eta^2/6) + \sin(\eta^2/6)],
\end{aligned} \tag{3.83}$$

where we have only provided the leading smooth and oscillatory terms, omitting the numerical factors. Hence, we observe that the Bernoulli equation (3.62) in the limit of large distances is governed by the interplay between kinetic energy and quantum pressure, while gravity becomes negligible. This phenomenon arises due to the oscillations of the perturbed mass $\delta\hat{M}$ around zero, resembling a compensated density profile. Consequently, the central density peak and its gravitational attraction are effectively screened, rendering gravity insignificant at large radii. This outcome is not totally surprising. Gravity is a long-range force, as shown by the inverse Laplacian in the Poisson equation (3.18), whereas the quantum pressure is a short-range force, as indicated by the Laplacian in Equation (3.15). As a result, the quantum pressure alone cannot counterbalance gravity at large distances. Therefore, either the kinetic energy balances gravity (as seen in the Hubble flow within the Einstein-de Sitter background) or gravity is screened by the compensated density profile. In the latter scenario, the residual gravitational effects can

be counteracted by the quantum pressure. However, in our solution (3.83), the screening effect is remarkably efficient, resulting in the emergence of free waves at large distances. These waves exhibit a delicate equilibrium between the quantum pressure and kinetic terms, superimposed on the cosmological background.

However, at the central region where velocity vanishes due to symmetry, a balance is achieved between gravity and the quantum pressure. Consequently, the nature of the dynamics undergoes a transition with radius: gravity versus quantum pressure at the center, and kinetic terms versus quantum pressure at large distances.

3.3.5 Comparison with CDM

First, let us review the CDM self-similar solutions. In CDM, as the universe expands, the matter inside an overdense region of radius R experiences a greater degree of deceleration compared to the matter outside of this region. Consequently, this leads to a further amplification of the density contrast. The density contrast within region R can be expressed as $\rho = (1 + \delta_{\rm CDM})\bar{\rho}$ in the linear regime $\delta_{\rm CDM} << 1$ (Peebles, 1980) [1] :

$$\delta_{\rm CDM} = \delta_i \left(\frac{3}{5} t^{2/3} + \frac{2}{5} t^{-1} \right) . \tag{3.84}$$

Therefore, in CDM we can identify two linear modes $D_+(t) \propto t^{2/3}$ and $D_-(t) \propto t^{-1}$ that are scale-independent. Consequently at the linear level, we can already see that the FDM self-similar (3.73) solutions are very different from the CDM ones. However, it is important to note that (3.73) in the semiclassical limit, $\epsilon \to 0$, or on large scales, $k \to 0$, recover the time dependence of the CDM linear growing modes, $D_+(k,t) \propto t^{2/3} \propto a$ and $D_-(k,t) \propto t^{-1}$.

Since for CDM the space and time dependences factorize in Eq.(3.74), requirements on the shape of the density profile at an initial time do not rule out the growing nor the decaying mode. Then, one usually only keeps the growing mode, assuming that the decaying mode has had time to become negligible. In contrast, in Eq.(3.76) we only kept the mode D_- because of the requirement to converge to the cosmological background on large scales. However, as we noticed below Eq.(3.76), for FDM the linear modes $D_\pm$ are no longer growing and decaying modes but acoustic oscillations of similar amplitude. Therefore, the self-similar solution associated with the mode D_- is physical, as a small perturbation associated with the mode D_+ will remain small as long as we remain in the FDM regime where the quantum pressure is important. As seen in Eq.(3.83), this is valid at large radii in the linear regime. In fact, as seen in the lower panels in Figs. 3.2 and 3.3 below, this is valid at all radii at the non-linear level for the self-similar solutions studied in this chapter.

As the Newtonian equations of motion (3.48)-(3.50) only apply to sub-Hubble scales, one may consider introducing a large-scale cutoff at the Hubble radius, so that the FDM mode $D_+(k,t)$ does not lead to divergent quantities. Then, one may wonder whether one could recover the CDM self-similar solutions by first taking the semiclassical limit $\epsilon \to 0$ and next $c/H_0 \to \infty$. This is better discussed in real space, as we detail below.

Now, let us recall the main properties of the CDM self-similar solutions for the Einstein-de Sitter cosmology (Fillmore & Goldreich, 1984), associated with overdensi-

[1] The prefactors in the linear and growing modes are dependent of the mass shell

ties and the formation of spherical virialized halos. For an initial overdense power-law profile

$$0 < \gamma < 3 : \quad \delta_L(r) \propto r^{-\gamma}, \tag{3.85}$$

of the linear density contrast, one obtains non-linear self-similar solutions, with a turnaround radius that grows with time as

$$r_{\rm ta}(t) \propto t^{2/3+2/(3\gamma)}, \tag{3.86}$$

and a non-linear density profile in the inner virialized regions, for $r \ll r_{\rm ta}$, that shows a different power law,

$$\gamma \leq 2 : \quad \rho \propto r^{-2}, \quad \gamma \geq 2 : \quad \rho \propto r^{-3\gamma/(1+\gamma)}. \tag{3.87}$$

For shallow initial profiles, $\gamma < 2$, the mass within a small radius R is dominated by the particles that have just collapsed, whereas for steep initial profiles, $\gamma > 2$, the mass within R is dominated by the particles that have collapsed long ago, when the turnaround radius was of the order of R (Fillmore & Goldreich, 1984). These solutions, which exhibit gravitational instability and collapse of increasingly massive and distant shells, originate from the growing mode $D_+(t)$ in the linear regime, with the power-law radial profile (3.85).

In the case of FDM, the mode denoted as D_+ in Equation (3.74) exhibits a profile proportional to k^{-7} in the semiclassical limit. However, this profile is neglected due to its divergence at low values of k. By performing power counting, we find that this corresponds to a profile in real space that behaves as x^4. This result aligns with the analysis conducted in real space in Section 3.3.4.2, specifically in the linear mode δ_{L1} described by Equation (3.79), which demonstrates growth proportional to η^4 at large values of η (where the semiclassical limit, $\epsilon \to 0$, corresponds to $\eta \to \infty$ as determined by Equation (3.60)). By comparing this with equation (3.85), we can formally assign $\gamma = -4$, and equation (3.86) provides the characteristic scale at time t with the power law relationship $r_{\rm ta} \propto \sqrt{t}$. Therefore, we recover the square-root growth in physical coordinates as derived in Equation (3.60).

Thus, for CDM the self-similar exponents, such as the growth of the characteristic scale in Eq.(3.86), encompass a continuous range that is determined by the slope γ of the initial density contrast profile. This range allows for a variety of self-similar solutions.

However, in the context of FDM, the inclusion of the quantum pressure term in the hydrodynamical equations of motion adds a new restriction. This term, being in the form of a power law, still permits the existence of self-similar solutions, but with a unique exponent. This exponent corresponds to the square-root growth of the physical scale as indicated in Equation (3.60).

Consequently, among the self-similar solutions of CDM (given by Equations (3.85)-(3.87)), FDM selects the one obtained for $\gamma = -4$ since it is the only exponent compatible with the quantum pressure term. However, it is important to note that this selection only holds at a formal level because the value of the exponent γ falls outside the allowed range specified in Equation (3.85).

In this regard, the semiclassical limit causes the FDM self-similar solution to converge towards a specific CDM self-similar solution, one that shares the same exponent γ. However, this convergence is neither feasible nor relevant in practice because this specific solution, applicable to both CDM and FDM, fails to approach the background on

large scales and exhibits undesirable behaviour. Hence, the permitted self-similar solution for FDM, which we will delve into in subsequent sections, differs from the standard self-similar solution for CDM. Specifically, it corresponds to a different CDM self-similar solution associated with a decaying mode. In the case of CDM, such a solution is not particularly relevant in practical terms since it is expected to be dominated by growing modes. In contrast, as mentioned earlier, the linear modes $D_{\pm}$ in FDM do not exhibit the characteristics of growing and decaying modes but instead manifest as acoustic oscillations with similar amplitudes. Consequently, the self-similar solution associated with the D_{-} mode is physically meaningful, as any small perturbation linked to the D_{+} mode remains negligible. Notably, as we will explore in Section 3.3.6, non-linearity remains significant across all scales. This means that the self-similar solution does not converge to the linear-theory prediction (3.82) at large radii, as it includes additional contributions related to the modes δ_{L2} and δ_{L3}.

Despite lacking a standard counterpart in CDM, the study of this FDM self-similar solution remains intriguing in its own right. It allows for an analytical or semi-analytical treatment beyond static solitons and explicitly illustrates the gravitational cooling. Consequently, it helps to the dynamics that arise from the interplay between quantum pressure, gravity, and kinetic effects.

3.3.6 Non-linear regime

3.3.6.1 Closed equation over δM

We now turn to the non-linear regime and look for exact self-similar solutions of the equations of motion (3.48)-(3.50) of the form (3.58). In terms of the self-similar coordinate η, the Poisson equation reads

$$\frac{1}{\eta^2}\frac{d}{d\eta}\left(\eta^2\frac{d\hat{\varphi}_{\mathrm{N}}}{d\eta}\right) = \frac{2}{3}\hat{\delta}, \tag{3.88}$$

while the quantum pressure reads

$$\hat{\Phi}_{\mathrm{Q}} = -\frac{1}{2\eta^2\sqrt{1+\hat{\delta}}}\frac{d}{d\eta}\left(\eta^2\frac{d}{d\eta}\sqrt{1+\hat{\delta}}\right). \tag{3.89}$$

The density contrast is given by the first derivative of the mass perturbation,

$$\hat{\delta} = \frac{3}{2\eta^2}\delta\hat{M}'. \tag{3.90}$$

By performing a single integration of the continuity equation with respect to the radial coordinate, the expression for the radial velocity can be obtained in terms of the perturbed mass as,

$$\hat{u} = \frac{3\delta\hat{M} - \eta\delta\hat{M}'}{4\eta^2 + 6\delta\hat{M}'}. \tag{3.91}$$

Replacing these expressions into the Euler equation (3.61), we obtain a closed non-linear equation for the perturbed mass $\delta\hat{M}$,

$$\begin{aligned}
&9(2\eta^3+3\eta\delta\hat{M}')^2\delta\hat{M}^{(4)}-(144\eta^5+216\eta^3\delta\hat{M}'+108\eta^4\delta\hat{M}''+162\eta^2\delta\hat{M}'\delta\hat{M}'')\delta\hat{M}^{(3)}\\
&+(4\eta^8+288\eta^4+36\eta^5\delta\hat{M}-216\eta^2\delta\hat{M}'+324\eta^3\delta\hat{M}''+81\eta^2\delta\hat{M}^2+81\eta^2\delta\hat{M}''^2)\delta\hat{M}''\\
&-3(4\eta^7+96\eta^3+180\eta^4\delta\hat{M}+243\eta^2\delta\hat{M}\delta\hat{M}'-3\eta^3\delta\hat{M}'^2+108\delta\hat{M}\delta\hat{M}'^2)\delta\hat{M}'\\
&-12\eta^3(7\eta^3-9\delta\hat{M})\delta\hat{M}=0.
\end{aligned} \tag{3.92}$$

3.3.6.2 Comparison with the linear equation

If we linearize Eq.(3.92) we obtain the fourth-order linear equation

$$\text{(L1)}: \quad 9\eta^3\delta\hat{M}^{(4)}-36\eta^2\delta\hat{M}^{(3)}+(72\eta+\eta^5)\delta\hat{M}''-3(24+\eta^4)\delta\hat{M}'-21\eta^3\delta\hat{M}=0, \tag{3.93}$$

whereas from the linear equation (3.78), using (3.90) we obtain the fifth-order linear equation

$$\text{(L2)}: \quad 9\eta^4\delta\hat{M}_L^{(5)}-36\eta^3\delta\hat{M}_L^{(4)}+(108\eta^2+\eta^6)\delta\hat{M}_L^{(3)}-(216\eta+\eta^5)\delta\hat{M}_L''+24(9-\eta^4)\delta\hat{M}_L'=0. \tag{3.94}$$

As it should, we can check that these two equations are related,

$$\text{(L2)}=\eta^4\frac{d}{d\eta}\left[\eta^{-3}\text{(L1)}\right]. \tag{3.95}$$

Hence, the solutions of equation (L1) are also valid solutions of equation (L2). The latter equation, being of order five instead of four, encompasses an additional solution: (L1) proportional to η^3, which corresponds to a constant δM_L and thus yields $\delta_L=0$. As a result, the linearized equation (3.93) aligns perfectly with the linear theory examined in Section 3.3.4.

3.3.6.3 Numerical procedure

We solve the non-linear equation (3.92) with a shooting method (Press et al., 1992), subdividing the spatial domain $\eta\geq 0$ in three regions: a central region $\eta\lesssim 0.1$, an intermediate region $0.1\lesssim\eta\lesssim 10$, and a large-distance region $\eta\gtrsim 10$. This allows for a convenient implementation of the boundary conditions.

We look for solutions that converge to the cosmological background at large distance, so that the density contrast and the perturbed mass go to zero. Therefore, at large distances we can use the linearized equation (3.93). This gives the four independent linear modes,

$$\begin{aligned}
\delta\hat{M}_{L1}&=\eta^3\left(105+\eta^4\right),\\
\delta\hat{M}_{L2}&={}_2F_3\left(-\frac{7}{4},\frac{3}{4};-\frac{1}{4},\frac{1}{4},\frac{1}{2};-\frac{\eta^4}{144}\right)+\frac{\sqrt{\pi}}{180\sqrt{3}}\delta\hat{M}_{L1},\\
\delta\hat{M}_{L3}&=\eta^2\,{}_2F_3\left(-\frac{5}{4},\frac{5}{4};\frac{1}{4},\frac{3}{4},\frac{3}{2};-\frac{\eta^4}{144}\right)-\frac{\sqrt{\pi}}{126\sqrt{3}}\delta\hat{M}_{L1},\\
\delta\hat{M}_{L4}&=\eta^5\,{}_2F_3\left(-\frac{1}{2},2;\frac{3}{2},\frac{7}{4},\frac{9}{4};-\frac{\eta^4}{144}\right)-\frac{\pi}{56}\delta\hat{M}_{L1}.
\end{aligned} \tag{3.96}$$

Therefore, at large distance the perturbed mass is a combination of these four modes,

$$\eta \to \infty : \quad \delta\hat{M} = \sum_{i=1}^{4} c_i \, \delta\hat{M}_{Li}, \tag{3.97}$$

whith coefficients c_i to be determined. For $\eta \to \infty$ the linear modes show the large-distance behaviors

$$\begin{aligned}
\delta\hat{M}_{L2} &= \cos(\eta^2/6)\left[\frac{2079}{\eta^4} + \dots\right] - \sin(\eta^2/6)\left[\frac{63}{\eta^2} + \dots\right], \\
\delta\hat{M}_{L3} &= -\cos(\eta^2/6)\left[\frac{90}{\eta^2} + \dots\right] - \sin(\eta^2/6)\left[\frac{2970}{\eta^4} + \dots\right], \\
\delta\hat{M}_{L4} &= -\cos(\eta^2/6)\left[\frac{405\sqrt{3\pi}}{2\eta^2} + \dots\right] + \sin(\eta^2/6)\left[\frac{405\sqrt{3\pi}}{2\eta^2} + \dots\right].
\end{aligned} \tag{3.98}$$

Therefore, we can see that the three modes $\delta\hat{M}_{L2}$, $\delta\hat{M}_{L3}$ and $\delta\hat{M}_{L4}$ obey the boundary condition $\delta\hat{M} \to 0$, while the divergent contribution from the mode $\delta\hat{M}_{L1}$ is ruled out. This gives the large-distance boundary condition

$$c_1 = 0. \tag{3.99}$$

To implement the boundary condition at the center, we write the Taylor expansion

$$\eta \to 0 : \quad \delta\hat{M} = a_3\eta^3 + a_5\eta^5 + a_7\eta^7 + \dots, \tag{3.100}$$

corresponding to a density contrast with is finite and smooth at the center, with an expansion in even powers of x. In particular, the density contrast at the origin is

$$\hat{\delta}(0) = 9a_3/2. \tag{3.101}$$

Thus, the central density contrast $\hat{\delta}(0)$ specifies the value of a_3. Next, substituting the expansion (3.100) into the differential equation (3.92) gives a hierarchy of equations that determines all higher-order coefficients $\{a_7, a_9, ...\}$ in terms of $\{a_3, a_5\}$. Thus, we are left with only one free parameter a_5, which is set by the boundary condition (3.99) at infinity.

In practice, we first choose the value of $\hat{\delta}(0)$, hence of a_3, of the profile we aim to compute. Then, for a trial value of a_5, we compute the profile $\delta\hat{M}(\eta)$ up to $\eta_- \sim 0.1$ with the Taylor expansion (3.100), all higher-order coefficients being known from the substitution into the differential equation (3.92). Next, we advance up to $\eta_+ \sim 10$ by solving the non-linear differential equation (3.92) with a Runge-Kutta algorithm. Then, at η_+, far enough in the linear regime, we match to the linear expansion (3.97). For a random initial guess a_5 at the center, this will give a nonzero coefficient c_1. Therefore, we use an iterative scheme over a_5 until the matching coefficient c_1 at the outer boundary η_+ vanishes. This sets the value of a_5.

In general, all three coefficients c_2, c_3 and c_4 in the linear expansion (3.97) are nonzero. In contrast, the linear-theory solution (3.82) actually corresponds to the linear mode $\delta\hat{M}_{L4}$ only, with $c_2 = c_3 = 0$. This corresponds to the fact that the linear modes $\delta\hat{M}_{L2}$ and $\delta\hat{M}_{L3}$ do not satisfy the appropriate boundary conditions at the center, $\eta \to 0$, which only leaves $\delta\hat{M}_{L4}$ as the unique solution (up to a normalization) for a linear solution valid

over the full range $0 \leq \eta < \infty$. This agrees with the fact that we obtained only one linear solution in Sec. 3.3.4.

Once we consider the exact non-linear differential equation (3.92), matters are different and the modes $\delta\hat{M}_{L2}$ and $\delta\hat{M}_{L3}$ show nonzero contributions at large distances. This is because at the center the perturbations do not asymptotically vanish (contrary to what happens at $\eta \to \infty$) but remain finite, so that non-linear contributions cannot be fully neglected. This changes the mapping between the boundary conditions at the center and at infinity and the large-distance modes $\delta\hat{M}_{L2}$ and $\delta\hat{M}_{L3}$ are no longer excluded because the behavior at the center of the linear modes is no longer relevant, as this central region is beyond strict linear theory. However, for $\hat{\delta}(0) \to 0$ the contributions from the modes $\delta\hat{M}_{L2}$ and $\delta\hat{M}_{L3}$ become small as compared with that from $\delta\hat{M}_{L4}$, as the solution converges to the linear theory.

Therefore, in contrast with the CDM self-similar solutions, for a finite central density there is never convergence to the linear theory at large distance, in the sense that $\delta\hat{M}(\eta)$ does not converge to $\delta\hat{M}_L(\eta) \propto \delta\hat{M}_{L4}(\eta)$. Indeed, the additional modes $\delta\hat{M}_{L2}$ and $\delta\hat{M}_{L3}$ also decrease as $1/\eta^2$, with oscillatory prefactors. This is due to a strong coupling between the behaviors at the center and at infinity. This arises from the self-similarity of the solution and from the quantum pressure (absent for CDM) which propagates information from the center to infinity and vice versa (by looking for a self-similar solution we have implicitly provided an infinite amount of time to acoustic waves to propagate over all space). Physically, the blow-up character of the solutions means that the scalar matter starts in the non-linear regime at small radii, and ends in the linear regime (i.e. converges to the Hubble flow) at late times and large radii, as explicitly seen in Sec. 3.3.10. This is the opposite of the usual CDM collapsing solutions, where matter shells start in the linear regime and finally collapse and virialize in the non-linear inner regions. This couples the final linear era to the initial non-linear era.

3.3.7 Overdensities

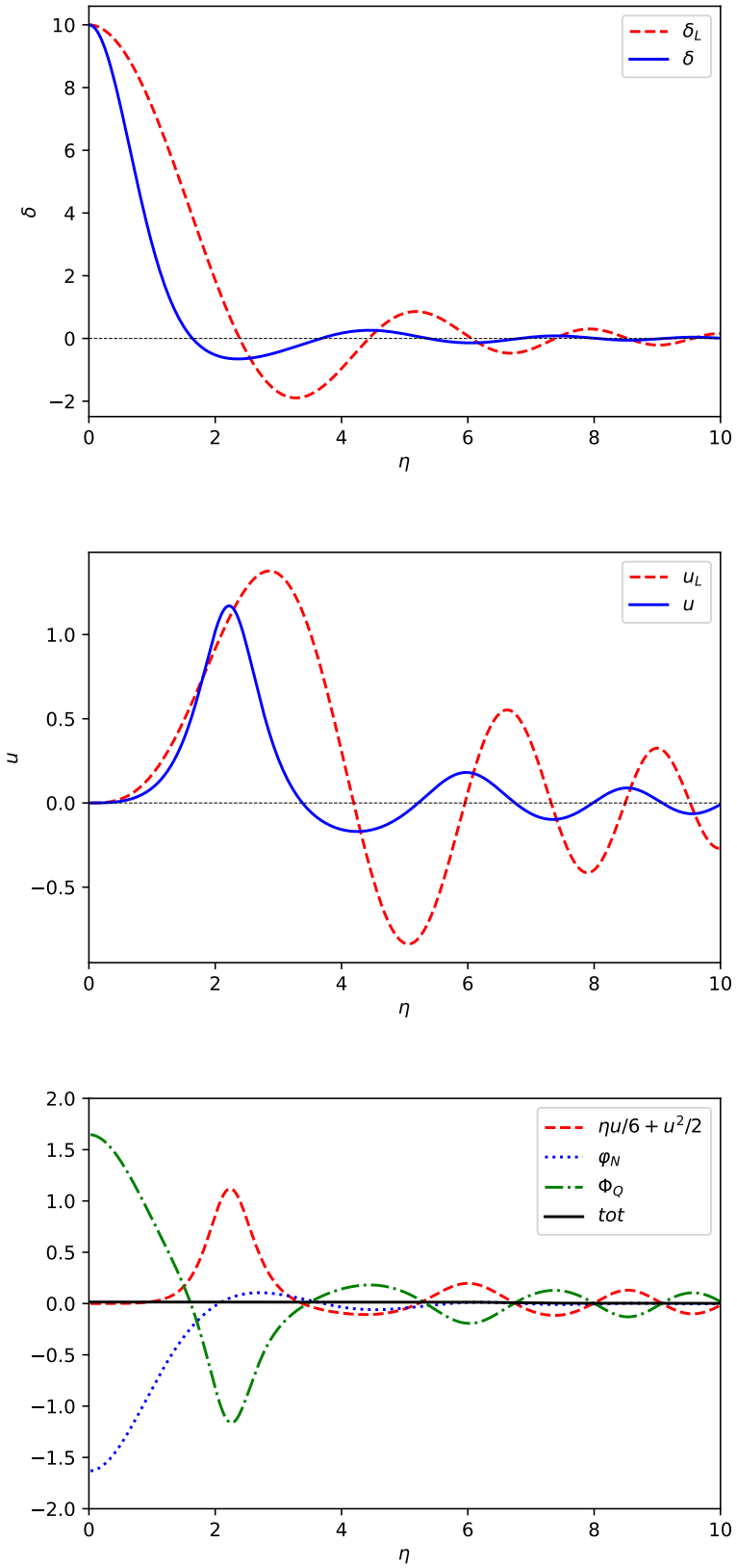

Figure 3.2. *Upper panel:* nonlinear density contrast $\hat{\delta}$ (blue solid line) and linear density contrast $\hat{\delta}_L$ (red dashed line), for $\hat{\delta}(0) = 10$. *Middle panel:* non-linear and linear velocity fields. *Lower panel:* comparison of the terms in the Bernoulli equation (3.62). We show the kinetic part (red dashed line), the Newtonian gravitational potential (blue dotted line), the quantum pressure (green dot-dashed line), and their sum which must be zero (black solid line).

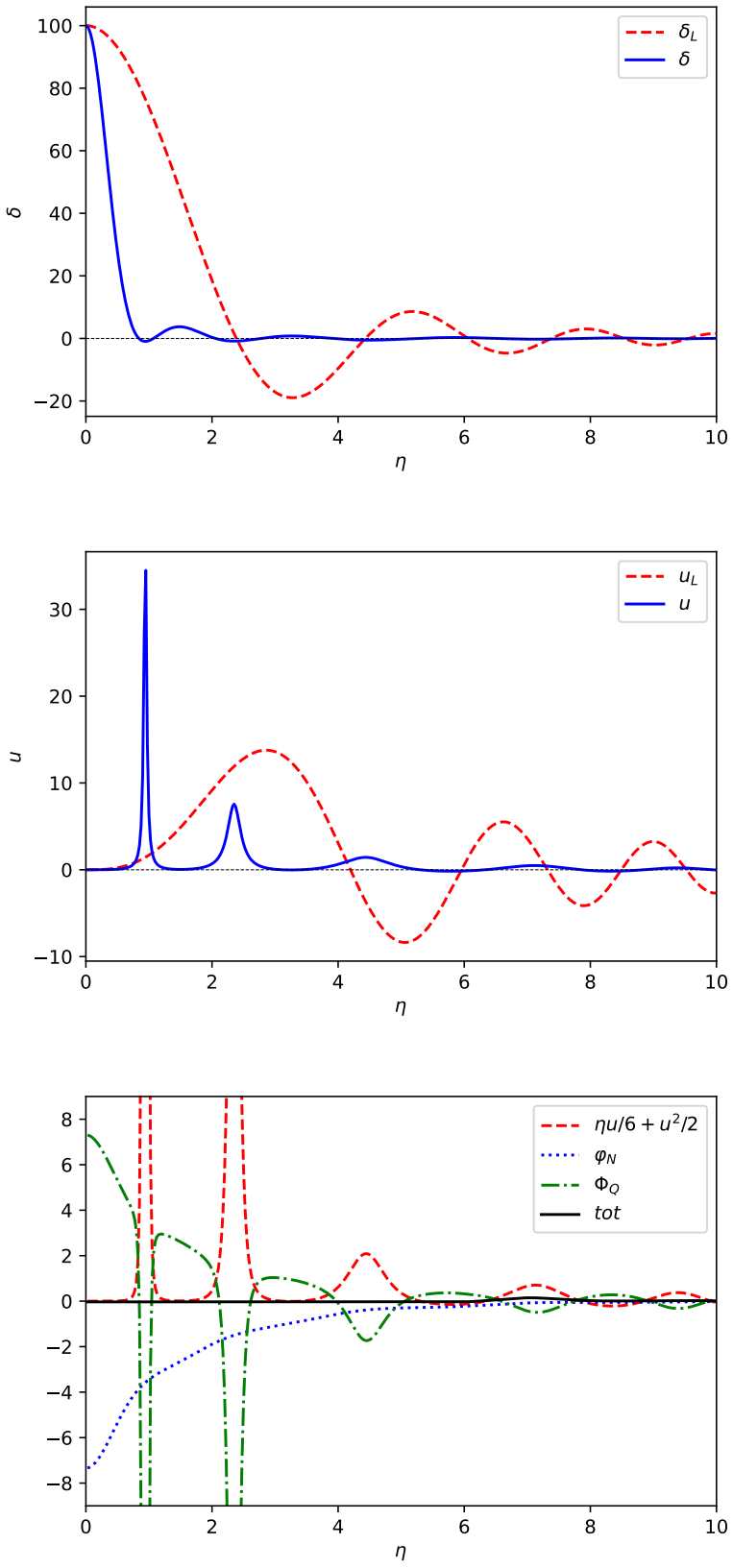

Figure 3.3. Non-linear and linear solutions as in Fig. 3.2, but for $\hat{\delta}(0) = 100$.

In Figures 3.2 and 3.3, we compare the non-linear and linear densities, as well as the velocity perturbations, for two cases: $\hat{\delta}(0) = 10$ and $\hat{\delta}(0) = 100$.

Observing the figures, we can notice that as the central density peak increases in height, the non-linear corrections cause the peak to become narrower, and all the higher-order peaks shift closer to the center. The oscillations in the velocity field also intensify and become much sharper. These oscillations are no longer symmetric, and the velocity exhibits pronounced, narrow positive spikes at the density minima, where $\hat{\delta} \simeq -1$ and $\rho \simeq 0$.

This behaviour can be understood by considering the scalar matter flux. As explained in Section 3.3.4.3, the profile contracts in comoving coordinates and loses mass over time. Thus, for scalar mass to escape from the central peak through the radius $R_1(t)$, which corresponds to the first minimum of the density, the velocity must be high to ensure a substantial flux despite the low local density. This trend extends to the subsequent peaks, where the density minima are also significantly below the background density.

This phenomenon of scalar matter being expelled through successive clumps, which escape from the central density peak and move towards infinity, is commonly observed in numerical simulations and referred to as "gravitational cooling" (Seidel & Suen, 1994; Guzman & Urena-Lopez, 2006). This process allows the system to approach equilibrium configurations, even in the absence of dissipative processes, by ejecting additional matter and energy out to infinity. It is important to note that while simulations, particularly those involving the collisions of DM halos, exhibit a somewhat chaotic transient process, our self-similar solutions demonstrate a well-ordered version of this process that occurs continuously, but with a rescaling of length and mass scales. It is nonetheless intriguing to observe this matter ejection phenomenon in the simple and semi-analytical self-similar solutions investigated in here. In the subsequent Section Section 3.3.10, we will delve deeper into this matter ejection as we compute the trajectories of constant-mass shells.

As described in Section Section 3.3.4.3, the dynamics of the system involve a complex interplay between gravity, quantum pressure, and kinetic effects. This interplay remains significant even in the non-linear regime, as evident from the lower panels that depict the terms in the Bernoulli equation (3.62).

In the vicinity of the central region, gravity and quantum pressure play the primary roles, given that the velocity vanishes at the center due to symmetry. Gravity ensures that the central overdensity does not decay too rapidly and closely follows the cosmological background density. On the other hand, the quantum pressure resists the gravitational pull and expels some matter from the central peak. As the central density becomes extremely high (refer to Fig. 3.3), the dominance of gravity and quantum pressure extends across multiple density peaks. This dominance is marked by sharp transitions at the density minima, which correspond to spikes in the velocity field and, consequently, the kinetic terms. These kinetic terms are counterbalanced by spikes in the quantum pressure. The gravitational potential $\varphi_{\rm N}$, being an integral of the matter density, appears very smooth and cannot capture the abrupt changes in velocity. Conversely, the quantum pressure (3.51), being the second derivative of the density, is a local quantity that responds to localized changes in the system.

At larger distances, where the system returns to the linear regime, the gravitational potential becomes negligible as the mass perturbation is screened, similar to a compensated profile. In this region, the quantum pressure and kinetic terms assume dominant roles, and scalar fluctuations propagate over long distances in a wave-like manner. Thus,

we observe that the gravitational cooling phenomenon is closely linked to the wave-like characteristics of FDM dynamics, primarily due to the significant influence of quantum pressure. The numerical calculation consistently demonstrates that the density contrast always remains above -1, ensuring that the density never reaches zero and remains strictly positive. We can establish this analytically by seeking a regular solution in which the density vanishes at a specific point η_0,

$$\delta\hat{M}(\eta) = a_0 + a_1(\eta - \eta_0) + a_2(\eta - \eta_0)^2 + \dots, \tag{3.102}$$

with the zero-density constraint

$$\hat{\delta}(\eta_0) = -1: \quad a_1 = -\frac{2}{3}\eta_0^2. \tag{3.103}$$

By substituting into the equation of motion (3.92), we can determine the coefficients $a_2, a_3, ...$ and obtain the solution:

$$\delta\hat{M}(\eta) = a_0 - \frac{2}{9}(\eta^3 - \eta_0^3), \tag{3.104}$$

where a_0 remains undetermined. We can verify that this solution indeed satisfies Eq. (3.92) and yields $\hat{\delta}(\eta) = -1$, representing the constant zero-density solution $\rho = 0$. Therefore, the only regular self-similar solution in which the density vanishes at a specific point is the homogeneous vacuum. As a consequence, the non-linear density profiles depicted in Figs. 3.2 and 3.3 can never reach the zero-density threshold. The fact that the density always remains strictly positive implies that the Madelung transformation (3.12) is well-defined, and the ψ-field and $\{\rho, \vec{v}\}$-hydrodynamical descriptions are equivalent. Thus, the self-similar solutions obtained from (3.92) in terms of $\{\rho, \vec{v}\}$ simultaneously provide the self-similar solutions in terms of ψ, ensuring that we do not miss any solutions when working within the hydrodynamical framework.

Furthermore, due to the spherical symmetry of our solutions, the spatial dimensionality reduces to one, allowing us to express the radial velocity as the gradient of a phase $S = \int dr\, v_r$. Consequently, the Schrödinger and hydrodynamical pictures are equivalent.

3.3.8 Underdensities

Figures 3.4 and 3.5 illustrate the cases of underdense central regions with $\hat{\delta}(0) = -0.8$ and -0.99. Compared to the linear profiles, we observe that the non-linear corrections now shift the density peaks towards larger distances and widen the central void, contrary to the behaviour observed in the overdense case.

Again, symmetry makes the velocity vanish at the center. Consequently, in the Bernoulli equation (3.62), the dominant terms are the gravitational and quantum pressure terms near the center, while in the linear regime at larger distances, the kinetic and quantum pressure terms assume dominance. In this linear regime, the mass perturbation is screened, resembling a compensated profile.

Once again, it is important to note that the density contrast always remains above -1, ensuring that the density ρ is strictly positive. This confirms the validity of the equivalence between the ψ-field and $\{\rho, \vec{v}\}$-hydrodynamical descriptions.

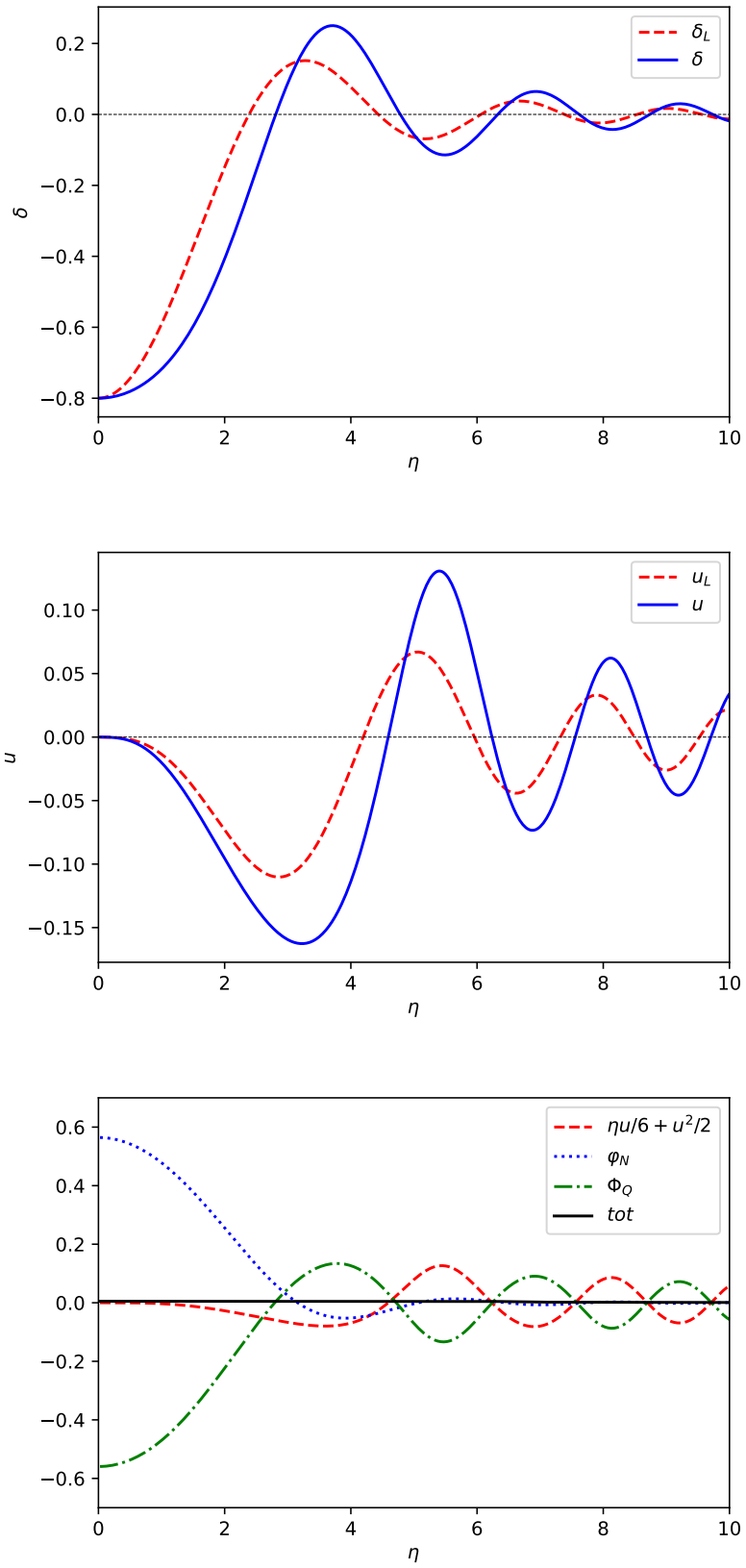

Figure 3.4. Nonlinear and linear solutions as in Fig. 3.2, but for $\hat{\delta}(0) = -0.8$.

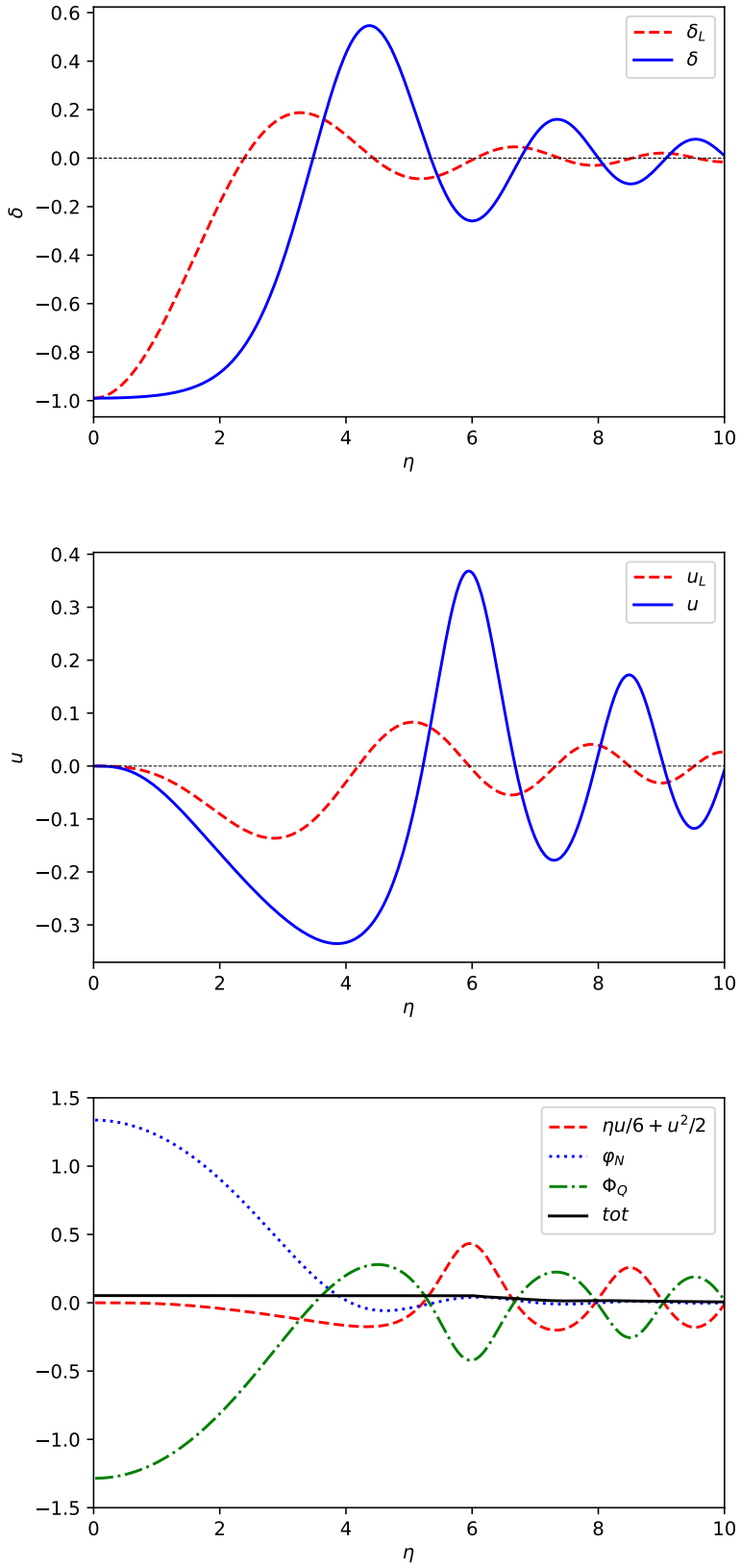

Figure 3.5. Nonlinear and linear solutions as in Fig. 3.2, but for $\hat{\delta}(0) = -0.99$.

3.3.9 Husimi distribution

3.3.9.1 Overdensities

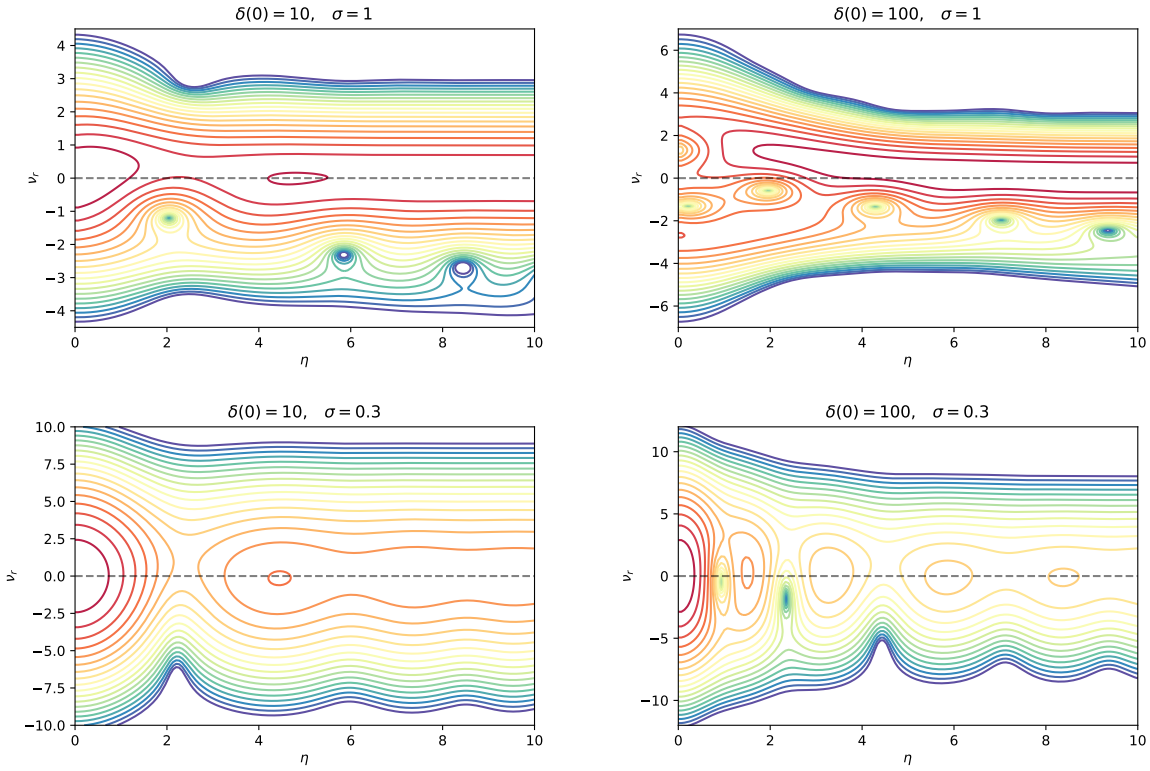

Figure 3.6. Isodensity contours for the radial Husimi distribution function $\hat{f}_{\rm H}(\eta, \nu_r)$ for $\sigma = 1$ (upper row, $\delta(0) = 10$ and 100) and for $\sigma = 0.3$ (lower row, $\delta(0) = 10$ and 100).

In Figures 3.6, we present the radial Husimi distributions $\hat{f}_{\rm H}(\eta, \nu_r)$, where ν_r represents the radial velocity. As shown in Figures 3.2 and 3.3, as the central density increases, successive density peaks become more clearly defined and separated by almost void regions. This pattern is also evident in the Husimi distribution, where the number of well-defined peaks increases with $\delta(0)$. At large distance, where the profile converges to the cosmological background, the finite smoothing parameter σ used in defining the Husimi distribution smears out the density and velocity perturbations, causing the Husimi distribution to approach the background result given by Eq. (3.70).

Decreasing the spatial coarsening parameter σ_x, which is proportional to σ, leads to an increase in the velocity coarsening parameter σ_p, following the Heisenberg uncertainty principle (Eq. (3.67)). Therefore, in the case of $\delta(0) = 10$ with $\sigma = 1$, we observe velocity asymmetry within the central peak where the radial velocity is positive, as shown in Figure 3.2, but the spatial profile appears somewhat smoothed. Reducing σ to 0.3 improves the separation between the first two peaks and preserves the signs of density fluctuations at larger radii, but this comes at the cost of significant smoothing along the velocity axis, making it difficult to discern the asymmetry of the velocity distribution within the central peak. It is important to note that the vertical velocity axis scale is larger in the lower panels corresponding to $\sigma = 0.3$. In the limit of $\sigma \to 0$, we have $\hat{f}_{\rm H} \sim \sigma^3 \pi^{-3/2} \hat{\rho}(\eta)$ at fixed $\vec{\nu}$.

For $\delta(0) = 100$, the spatial width of the central peak and subsequent peaks decreases, as observed in Figure 3.3. Consequently, the coarsening parameter of $\sigma = 1$ is no longer sufficient to separate these initial peaks, resulting in artificial interferences between them giving a Husimi distribution that is challenging to interpret and deviates significantly from semiclassical expectations. Decreasing σ to 0.3 provides a more accurate representation of the system, allowing us to clearly observe the sequence of scalar-field clumps. However, this smoothing erases much of the information about the velocity field.

These findings highlight that employing the Schrödinger equation (3.52) and the Husimi distribution as an alternative to N-body simulations for computing the classical phase-space distribution governed by the Vlasov equation is not always straightforward. Different choices of the smoothing parameter σ can lead to substantially different outcomes, making it challenging to establish a direct connection to the underlying dynamics. This issue may become particularly relevant in systems with a wide range of scales, such as those exhibiting hierarchical gravitational clustering observed in cosmological structures. For the self-similar solutions investigated in this thesis, where the density is strictly positive everywhere and the hydrodynamical mapping (3.12) is well-defined, the density and velocity fields offer a clearer depiction of the dynamics compared to the phase-space Husimi distribution.

3.3.9.2 Underdensities

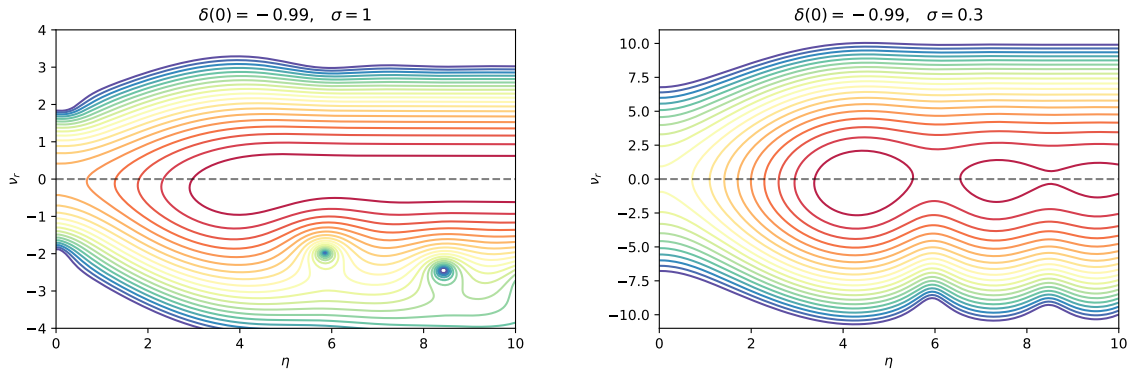

Figure 3.7. Isodensity contours for the radial Husimi distribution function $\hat{f}_{\mathrm{H}}(\eta, \nu_r)$, for $\sigma = 1$ (upper panel) and $\sigma = 0.3$ (lower panel) with $\delta(0) = -0.99$.

In Figure 3.7, we present the case of a central underdensity with $\delta(0) = -0.99$. Once again, we observe that a smaller value of the smoothing parameter σ enhances the separation between the successive density peaks. However, this reduction in σ comes at the cost of erasing the velocity asymmetries within the system.

3.3.10 Trajectories associated to the self-similar solutions

The self-similar solutions can be understood from both Eulerian and Lagrangian perspectives. While the density and velocity fields, as well as the Husimi distribution, offer an Eulerian viewpoint, considering a complementary Lagrangian perspective provides additional insights.

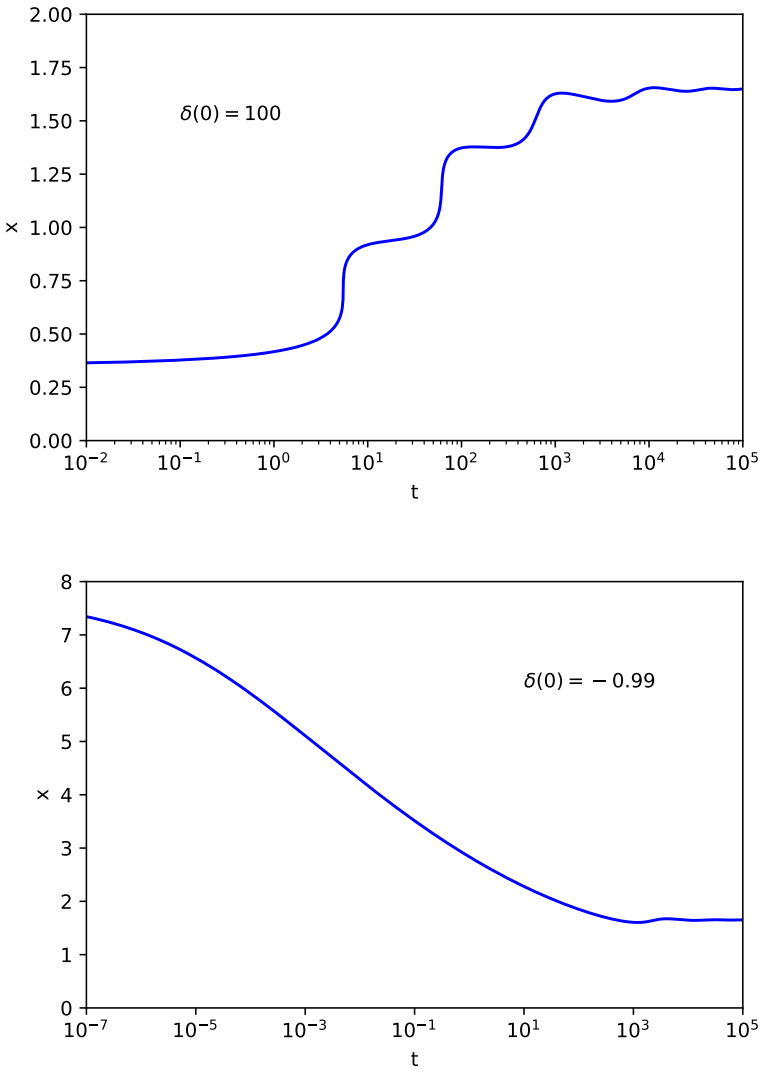

Figure 3.8. Trajectory $x(t)$ of the comoving radius associated with a fixed mass, as a function of cosmic time t. We show the case of the self-similar solutions defined by the central density contrasts $\delta(0) = 100$ (upper panel) and $\delta(0) = -0.99$ (lower panel).

In the Lagrangian viewpoint, the motion of the radius $r(t)$ that encloses a fixed mass $M(< r) = M$ serves as an analogue to particle trajectories in the hydrodynamical picture. From Eq. (3.58), the mass $M(< r) = \bar{M} + \delta M$ can be expressed as

$$M = \bar{M} + \delta M = \epsilon^{3/2} t^{-1/2} \left[\frac{2}{9}\eta^3 + \delta\hat{M}(\eta) \right]. \tag{3.105}$$

This equation implicitly provides the trajectory $\eta(t)$ as a function of time for a given mass. Furthermore, Eq. (3.105) yields the scaling law

$$\eta(t|M, \epsilon) = \eta(\epsilon^{-3} M^2 t), \tag{3.106}$$

where η only depends on the combination $\epsilon^{-3} M^2 t$. Thus, trajectories associated with different masses or different values of ϵ can be obtained from a single trajectory through time rescaling, given by

$$t \propto \epsilon^3 M^{-2}. \tag{3.107}$$

However, the shape of the trajectory depends on the self-similar profile, defined for instance by the central density contrast $\delta(0)$.

The scaling law (3.107) reveals an interesting feature: in the FDM self-similar solutions, large masses correspond to small times. This is in contrast to CDM self-similar solutions, which describe a hierarchical collapse where large masses collapse later (Fillmore & Goldreich (1984); Bertschinger (1985)). On the other hand, the FDM self-similar solutions exhibit a slow blow-up that roughly follows the Hubble expansion. As the total overdensity $1 + \delta$ is always positive, both $M(\eta)$ and $\eta(M)$ are monotonically increasing functions at fixed time. Consequently, the scaling law (3.106) implies that $\eta(t)$ is also a monotonically increasing function of t for fixed M. This behaviour leads to $\eta \to 0$ as $t \to 0$ and $\eta \to \infty$ as $t \to \infty$. Therefore, in terms of the rescaled radius η, at early times, the mass shell starts close to the origin, inside the central peak or void, residing in the non-linear regime if the self-similar solution is non-linear at the center. At late times, the mass shell moves further into the linear regime, at large distances.

Thus, the trajectories in FDM self-similar solutions exhibit an expansion from the non-linear to the linear regime, independently of whether the central region is overdense or underdense, whereas the trajectories found in the CDM self-similar solutions describe a spherical collapse that runs from the linear to the non-linear regime.

In Figure 3.8, we depict the trajectories obtained within the self-similar solutions defined by $\delta(0) = 100$ and -0.99. The trajectories $x(t)$ are plotted in terms of the comoving coordinate using Eq. (3.60), which gives $x(t) = \epsilon^{1/2} t^{-1/6} \eta(t)$. For the numerical computations, we set $\epsilon = 1$ and $M = 1$. It is important to note that other values of ϵ or M only lead to a rescaling of time and radius.

We observe that all trajectories roughly follow the Hubble expansion, as the comoving radius $x(t)$ approaches nonzero finite values at both small and large times. This behaviour is consistent with the scaling $\delta = \hat{\delta}(\eta)$ in Eq. (3.58), indicating that the typical density ρ follows the decrease of the background density $\bar{\rho} \propto t^{-2}$. Consequently, mass shells cannot expand much slower or faster than the Hubble flow. At late times, when η is large, the background term $2\eta^3/9$ dominates in Eq. (3.105), leading to the recovery of the Hubble flow with $x(t) \simeq \bar{x}$, where $\bar{x} = (9/2)^{1/3} M^{1/3}$ represents the background comoving radius associated with the mass M. Subdominant oscillations associated with the linear regime can also be observed on top of this asymptotic value.

For the overdense case, we observe that the comoving radius $x(t)$ increases from its initial to its final value. This is because the mass shell is initially inside the central density peak, close to the origin. This overdense configuration implies an initial radius x_i that is smaller than its counterpart $\bar{x}$ in the background universe, for the same mass M (as $\rho \propto M/x^3$). At late time, as the system approaches the Hubble flow with increasingly small perturbations, the trajectory converges to $\bar{x} > x_i$. Conversely, for the underdense case, the comoving radius $x(t)$ decreases from its initial to its final value. In the case of the high central overdensity $\delta(0) = 100$, characterized by three distinct density peaks separated by velocity spikes (see Fig. 3.3), the trajectory exhibits an intermittent character with well-defined steps in the non-linear regime. The comoving radius grows very slowly while the mass shell is inside the density peaks or clumps, and it shows rapid acceleration as it transitions from one clump to the next due to the presence of velocity spikes found in Fig. 3.3, associated with the voids separating the clumps.

For the underdense case $\delta(0) = -0.99$ the secondary peaks and their velocity spikes

spikes are weaker (as seen in Fig. 3.5), making it difficult to identify well-defined steps in the trajectory.

Although the self-similar profile shrinks in comoving coordinates, as $x \propto t^{-1/6}$ at fixed η from Eq.(3.60), the mass-shell trajectories remain roughly constant, with a global finite increase for overdense cases and a global finite decrease for underdense cases.

Thus, similar to wave packets where the group and phase velocities need to be distinguished, two velocities or trajectories can be discerned in the self-similar solutions. The "geometric" trajectory, described by $x \propto t^{-1/6}$, captures the shrinking of the self-similar profile, while the "matter" trajectory, characterized by $x \sim$ constant, represents the flow of matter. These correspond to $r \propto t^{1/2}$ and $r \sim t^{2/3}$ in physical coordinates, respectively. Specifically, matter flows "through" the self-similar profile towards the linear regime at large distances. It escapes from the non-linear central region, passing through a series of clumps and experiencing velocity bursts until it ultimately converges to the Hubble flow. This behaviour of matter moving through the clumps is reminiscent of the gravitational cooling phenomenon observed in numerical simulations.

Therefore, the matter content of a given clump is not fixed over time, as matter gradually flows through it, attaining significant velocities at the boundaries where the density becomes very small. This behaviour shares similarities with systems governed by wave equations, which exhibit wavelike and interference phenomena. In the case of self-similar solutions, this phenomenon arises from the quantum pressure originating from the Schrödinger equation that displays well-known wavelike and interference features.

3.4 High-density asymptotic limit

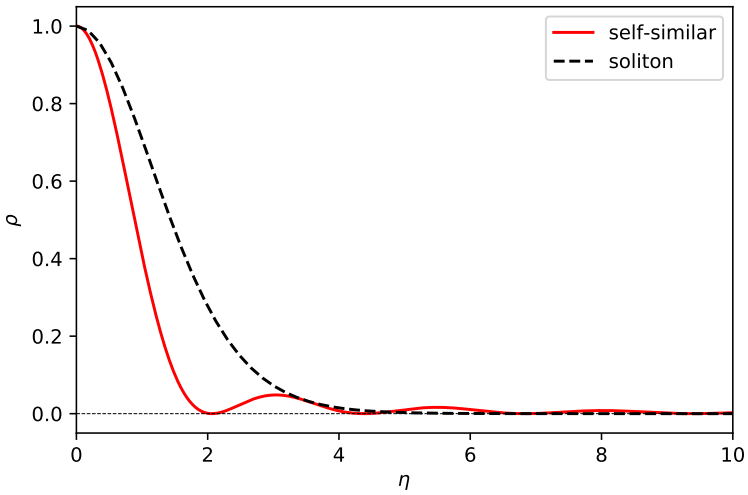

Figure 3.9. Asymptotic self-similar (red solid line) and soliton (black dashed line) density profiles, normalized to $\rho(0) = 1$.

In Section 3.1, we recalled the scale invariance of the SP system (3.1)-(3.2) under the scaling law (3.3). However, in the case of cosmological self-similar solutions, this symmetry is broken by the presence of an Einstein-de Sitter background, which imposes a boundary condition at large distances. Unlike the solitonic solutions (3.31) in a vacuum,

we cannot obtain a family of self-similar solutions through the rescaling (3.3), as it would also change the density at infinity, corresponding to a different boundary condition.

Nevertheless, in the limit of large density contrasts, the background density becomes negligible as compared with the central density and we can expect the inner profile to converge to a limiting shape that obeys the scaling law (3.3), which reads here

$$\{\eta, \psi, \rho, M\} \to \left\{\lambda^{-1}\eta, \lambda^2\psi, \lambda^4\rho, \lambda M\right\}. \tag{3.108}$$

We can obtain the equation satisfied by this limiting profile by replacing these scalings into Eq.(3.92) and keeping only the leading terms in the limit $\lambda \to \infty$. This gives

$$M'^2 M^{(4)} - 2M'M''M^{(3)} + M''^3 = \frac{4}{\eta^2} M M'^3 . \tag{3.109}$$

In this limit we identified $M \simeq \delta\hat{M}$ and $\rho \simeq \hat{\delta}$, so that the density is given by $\rho = 3M'/(2\eta^2)$. Notably, this non-linear equation remains invariant under the symmetry (3.108). Consequently, by rescaling a single solution normalized, for example, by setting $\rho(0) = 1$ using the transformation (3.108), we can obtain a complete family of solutions. Solving Eq.(3.109) is more challenging compared to finding solutions of Eq.(3.92), as the density minima between successive peaks now reach the vacuum value $\rho = 0$. These points, where $M' = M'' = 0$, represent singular points of the differential equation (3.109). In practice, we compute the finite-λ profile defined by Eq.(3.92) and check that for large $\delta(0)$ the curves collapse to a unique profile normalized to $\rho(0) = 1$ after applying the scaling (3.108). Additionally, we verify that this profile approximately satisfies Eq.(3.109).

In Fig. 3.9, we compare the asymptotic self-similar profile with the soliton profile derived from Eq.(3.31). The soliton profile, expressed in terms of dimensionless variables, is given by

$$\nabla_\eta^2 \psi_{\rm sol} = 2(\varphi_{\rm N} - \alpha)\psi_{\rm sol}, \quad \nabla_\eta^2 \varphi_{\rm N} = \frac{2}{3}\psi_{\rm sol}^2. \tag{3.110}$$

The comparison between the two profiles reveals that they do not coincide. Despite the increase in central density, the shape of the central peak in the self-similar profile does not converge to the equilibrium of the soliton profile. This discrepancy arises from the significant influence of kinetic effects, which dominate near the boundary of the central peak, as observed in the lower panel of Fig. 3.3. Furthermore, in addition to the kinetic terms, the soliton balance equation (3.29) differs from the self-similar Bernoulli equation (3.62) due to the presence of the α parameter on the right-hand side. As a result, the two profiles exhibit distinct characteristics, with the central peak of the self-similar solution being narrower than that of the soliton profile. Consequently, even when the local timescale inside the central peak becomes significantly smaller than the Hubble time at high densities, the profile does not relax towards the static soliton profile. This indicates that the convergence towards the soliton core is not guaranteed in all configurations.

In the limit of large radius, we can neglect the right-hand side of Eq.(3.109), resulting in a homogeneous equation. The solution to this equation can be expressed as follows,

$$\begin{aligned} \eta \to \infty : \quad & \rho \simeq \frac{3b}{2\eta^2} \cos^2\left[\frac{a(\eta - \eta_0)}{\sqrt{2}}\right], \\ & M \simeq M_0 + b\left[\frac{\eta - \eta_0}{2} + \frac{\sin[\sqrt{2}a(\eta - \eta_0)]}{2\sqrt{2}a}\right], \end{aligned} \tag{3.111}$$

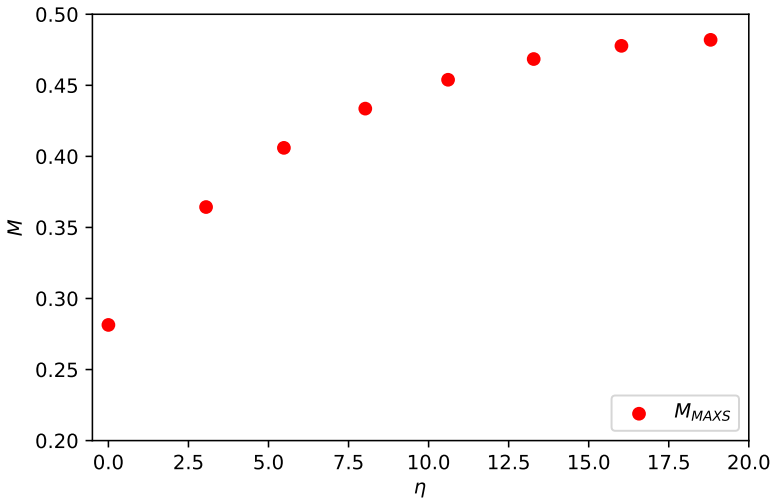

Figure 3.10. Mass of the density peaks for the asymptotic self-similar density profile normalized to $\rho(0) = 1$

where M_0, η_0, a, and b are undetermined parameters that can be obtained by solving the complete equation (3.109). It should be noted that the density is always positive but now vanishes on an almost periodic set of radii. Thus, the oscillations of the asymptotic profile have equal length in the radius η, whereas the oscillations in the linear profile had equal lengths in η^2, as shown in Eq.(3.81). The non-linear effects not only shift the density peaks towards the center but also alter their scaling with distance. The envelope of the density oscillations decreases $1/\eta^2$, while the soliton density exhibits an exponential falloff. This also implies that the mass grows linearly with the radius, so that each peak (or more precisely each shell in the 3D space) contains the same mass. Consequently, the outer shells are not as negligible as they may appear in the density plots. This is also depicted in Fig. 3.11, where we plot the mass associated with the first few density peaks (i.e., the mass within each spherical shell delimited by density minima).

3.5 CDM comparison, semiclassical limit and conclusion

As mentioned in Eqs.(3.85)-(3.87), self-similar solutions for collisionless matter in a perturbed Einstein-de Sitter universe were derived by by Fillmore & Goldreich (1984). Later, using a different method these results were recovered and extended to a collisional gas by Bertschinger (1985). These self-similar solutions describe the gravitational collapse of spherical overdense regions or the expansion of voids. At early times, starting with a small linear perturbation $\delta_L(r, t_i)$, which follows the power-law profile (3.85), the density contrast grows as $t^{2/3}$ in accordance with the linear growing mode until it enters the non-linear regime. Subsequently, non-linear effects come into play and modify the shape of the density profile in the inner regions. At small radii, the profile follows a power-law form (3.87), but with a different exponent determined by the slope of the linear perturbation. This gives rise to a family of solutions characterized by the slope γ of the density pertur-

bation at large distance. In the case of a collisional scenario, the profile also depends on the adiabatic index $\gamma_{\rm ad}$.

In the case of overdense regions, these self-similar solutions display a gravitational instability and increasingly distant shells collapse. They typically stabilize at a fixed fraction of their turnaround radius, as gravity is balanced either by the radial velocity dispersion or by the thermal pressure (in the collisional case). This leads to a virial equilibrium in the inner non-linear core, with a mass and a radius that grow with time, both in physical and comoving coordinates.

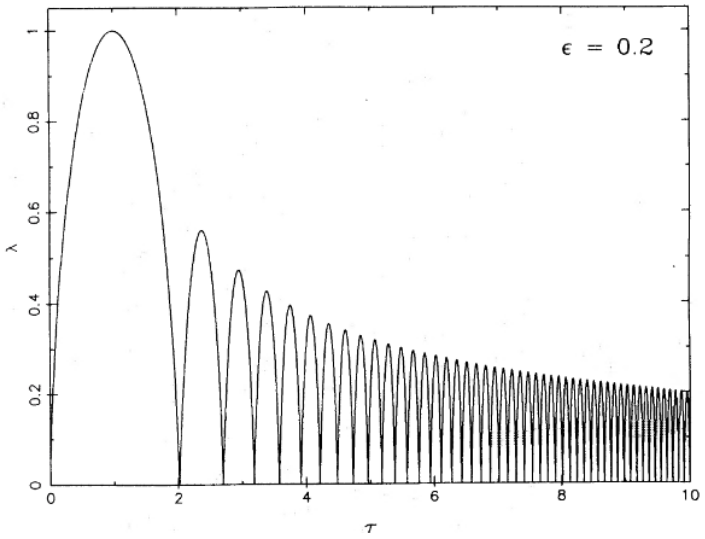

Figure 3.11. Figure from Fillmore & Goldreich (1984). CDM self-similar particle trajectory for ϵ=0.2 (γ in (3.85))

The self-similar solutions we have derived for FDM in this study exhibit significant differences compared to the CDM case. These solutions do not follow power-law shapes, and their amplitude does not grow over time. Consequently, the density contrast at the center, $\delta(0)$, remains constant. This suggests that the gravitational instability is counterbalanced by the quantum pressure, preventing the profile from transitioning from the linear to the non-linear regime as time progresses. Instead, the profile remains linear on all scales and at all times, or it remains non-linear in the central region.

In contrast to the CDM case, the limits of large distances and linear theory no longer coincide for FDM. While the density perturbation becomes small at large radii, allowing for a valid linear treatment, the profile does not converge to the linear-theory profile. This discrepancy arises because at large distances, there are non-zero contributions from all three linear modes, which exhibit well-behaved behaviour at infinity. In contrast, the linear theory selects only one mode that satisfies the boundary condition at the center.

The constant amplitude of these solutions over time indicates the absence of gravitational collapse. In both underdense and overdense central regions, the mass inside the central peak or "void" decreases over time, following a scaling relation of $M \propto t^{-1/2}$. Meanwhile, the associated radius expands as $t^{1/2}$ in physical coordinates but contracts as $t^{-1/6}$ in comoving coordinates. Consequently, rather than accreting mass, the central region continuously ejects matter. During the non-linear regime, this process takes the form of well-separated clumps that propagate outward in physical coordinates, reminiscent of the expulsion of matter observed in gravitational cooling. However, in these self-similar

solutions, matter does not remain confined within each clump but instead moves outward at an accelerated pace, leaking from one clump to the next through a narrow region characterized by low density but high velocity. In the linear regime, at large radii, acoustic waves emerge around the cosmological background due to the screening effect of the central overdensity, resembling a compensated profile. As a result, the gravitational force becomes negligible compared to the kinetic and quantum-pressure terms. The characteristic exponents $M \propto t^{-1/2}$ and $r \propto t^{1/2}$ exhibited by the FDM self-similar solutions are universal, in contrast to the continuous range of exponents observed in the CDM case, which depend on the slope γ of the linear seed. As explained in Sec. 3.3.5, this discrepancy arises due to the presence of the the new force associated with the quantum pressure, in addition to gravity. This new term in the equations of motion is only compatible with the exponent $\gamma = -4$. However, this value lies outside the allowed range defined by Equation (3.85) for standard CDM self-similar solutions. In fact, the self-similar FDM solutions explored in this study are associated with a non-standard CDM solution, which corresponds to a decaying mode in the linear regime and is therefore unphysical.

Nevertheless, in the FDM regime, the distinction between growing and decaying modes vanishes as the quantum pressure transforms both modes into acoustic oscillations of constant amplitude. As a result, the FDM case exhibits significant qualitative differences compared to the CDM case. These differences persist in the self-similar solutions studied throughout this chapter, at all times and scales, and are not eliminated even in the limit as ϵ approaches zero. This is because ϵ is fully absorbed through the transformation to the self-similar coordinate η in Equation (3.60). As discussed earlier, the profile at large distance, although still within the linear regime of small perturbations, deviates from the linear-theory profile due to the presence of two additional linear modes with coefficients that depend on the central density. This introduces a strong coupling between the small inner radii and the large outer radii, in contrast to the CDM case. In the non-collisional case of CDM Fillmore & Goldreich (1984); Bertschinger (1985), outer shells behave independently and undergo spherical collapse, which is only determined by the inner mass according to Gauss theorem, and not on the density profile. As a result, they collapse freely, similar to free fall with an initial outward velocity close to the Hubble flow, until shell crossing occurs at non-linear radii. This signifies that the mass within each shell is no longer constant, and the dynamics become more complex. Similarly, in the case of collisional collapse of a polytropic gas, the pressure beyond the shock (located around the virial radius) is zero due to cold initial conditions, allowing for free-fall spherical collapse. However, the pressure becomes non-zero at the shock, accompanied by a jump in temperature and entropy, and balances gravity at smaller radii Bertschinger (1985); Teyssier et al. (1997).

In contrast, for the self-similar solutions of FDM, the outer shells do not follow a spherical free fall. This is because the effective pressure associated with the quantum pressure is non-zero and dominates over gravity in conjunction with the kinetic terms. Consequently, this leads to acoustic-like oscillations or waves that propagate information from small to large scales, establishing a coupling between the small and large scales.

The Schrödinger equation (3.52) has been proposed as an alternative approach, in the semiclassical limit, $\epsilon \to 0$, to simulate the evolution of CDM without relying on N-body simulations (Widrow & Kaiser, 1993; Uhlemann et al., 2014; Mocz et al., 2018; Garny et al., 2020). One might expect that in this semiclassical limit, the dynamics of FDM would converge towards CDM dynamics. However, the situation is more nuanced.

The semiclassical limit is a weak limit and its interpretation is not straightforward. The scaling relations (3.58) and (3.60) reveal that in the semiclassical limit, the FDM self-similar solutions "vanish" as their size and mass decrease as $\epsilon^{1/2}$ and $\epsilon^{3/2}$ respectively, as ϵ tends to zero. Consequently, in the semiclassical limit, these solutions become confined to an increasingly small radius. This counteracts the ϵ^2 factor in front of the Laplacian in the Schrödinger equation (3.52), allowing for a self-similar solution where the quantum pressure remains capable of balancing gravity near the center, for any finite value of ϵ. However, from a macroscopic perspective, this configuration becomes irrelevant as it becomes infinitesimally small.

The standard CDM self-similar solutions are only exactly recovered at $\epsilon = 0$, or as approximate solutions at small ϵ with a slight breaking of the self-similarity. In other words, the standard CDM self-similar solutions are not the limit at $\epsilon \to 0$. This highlights the need for careful consideration when approaching the semiclassical limit. If the gradients become sufficiently steep as $\epsilon \to 0$, they can sustain dynamics that differ significantly from the CDM Vlasov case, resulting in a nontrivial limit.

Chapter 4

Numerical methods

This chapter fully presents the numerical methods that we used to simulate scalar field dark matter clouds. As we have seen in Chapter 2, specifically in Section2.5, in the non-relativistic regime and neglecting the expansion of the Universe, the equations of motion for the complex scalar field ψ are given by the coupled equations of the Schrödinger–Poisson (SP) system or of the Gross–Pitaevskii–Poisson system for a self-interacting scalar field:

$$i\frac{\partial\psi}{\partial t} = -\frac{\nabla^2\psi}{2m} + m(\Phi_{\rm N} + \Phi_{\rm I})\psi, \tag{4.1}$$

$$\nabla^2\Phi_{\rm N} = 4\pi\mathcal{G}_{\rm N}m|\psi|^2, \tag{4.2}$$

where m is the mass of the scalar field, $\Phi_{\rm N}$ the gravitational potential and $\mathcal{G}_{\rm N}$ is Newton's gravitational constant. As we have discussed in Chapter 2, the term $\Phi_{\rm I}$ describes the self-interactions, if any, being null for the FDM case and taking the form of other functions for other scenarios. For further details of these scenarios we consider see Section 2.6 for FDM, Section 2.7 for self-interactions described with the quartic potential and Section 2.8 for a bounded potential. In this chapter, we will leave the $\Phi_{\rm I}$ function open to focus on discussing the the numerical methods developed.

4.1 Dimensionless variables

It is convenient to work with dimensionless quantities denoted with a tilde,

$$\psi = \psi_\star\tilde{\psi}, \quad t = t_\star\tilde{t}, \quad \vec{x} = L_\star\tilde{\vec{x}}, \quad \Phi = \frac{L_\star^2}{t_*^2}\tilde{\Phi}, \tag{4.3}$$

where $t_\star$ and $L_\star$ are the characteristic time and length scales of the system. This gives the dimensionless Schrödinger equation

$$i\epsilon\frac{\partial\tilde{\psi}}{\partial\tilde{t}} = -\frac{\epsilon^2}{2}\tilde{\nabla}^2\tilde{\psi} + (\tilde{\Phi}_N + \tilde{\Phi}_I)\tilde{\psi}, \tag{4.4}$$

with

$$\epsilon = \frac{t_\star}{mL_\star^2}. \tag{4.5}$$

Where we have introduced the parameter ϵ, which plays the role of $\hbar$ and measures the relevance of wave effects, such as interferences or the quantum pressure. The Poisson equation now takes the following dimensionless form

$$\tilde{\nabla}^2\tilde{\Phi}_{\rm N} = 4\pi\tilde{\rho}, \quad \text{with} \quad t_\star = \frac{1}{\sqrt{\mathcal{G}_{\rm N}\rho_\star}}, \quad \rho = \rho_\star\tilde{\rho}, \tag{4.6}$$

where $t_\star$ is the gravitational dynamical time associated with the characteristic density $\rho_\star$ of the system. We also define the characteristic mass $M_\star$,

$$\tilde{M} = \int d\tilde{\vec{x}}\,\tilde{\rho}, \quad \text{with} \quad M = M_\star\tilde{M}, \quad M_\star = \rho_\star L_\star^3 \tag{4.7}$$

and the characteristic wavefunction amplitude $\psi_\star$,

$$\tilde{\rho} = \tilde{\psi}\tilde{\psi}^*, \quad \text{with} \quad \psi_\star = \sqrt{\rho_\star/m}. \tag{4.8}$$

In practice, we consider a system of characteristic size $L_\star$ and timescale $t_\star$ and use this to define the dimensionless coordinates of our system. These could be kpc and Gyrs for a galactic system or AU and yr for a cloud of solar-system size. The unit of length is somewhat arbitrary and can be taken as pc or Gpc as desired, as long as it is well below the Hubble scale, far in the Newtonian gravitational regime. In the following, we remove the tildes for simplicity, as we always work with the dimensionless variables. We will choose $L_\star$ as the radius of our initial spherical halo, so that in dimensionless coordinates we have $R_{\rm halo} = 1$.

4.2 Dynamical evolution: Pseudo-spectral method

In this section we present the final method we have developed to solve the time evolution of scalar clouds (Pathria & Morris, 1990; Zhang & Hayee, 2008; Edwards et al., 2018). As we have seen, the nonlinear Schrödinger–Poisson system is given by the set of equations (4.4) and (4.6). Note that these equations (4.4 and 4.6) are applicable when dealing with open boundary conditions. However, the code we have developed is specifically designed to handle the Schrödinger–Poisson system under periodic boundary conditions. In this particular situation, equation (4.6) takes the following form,

$$\nabla^2\Phi_{\rm N} = 4\pi(|\psi|^2 - \langle|\psi|^2\rangle), \tag{4.9}$$

as it is derived from Gauss' law and the property that the surface integral of the field's gradient along the simulation grid's perimeter becomes zero under the periodic boundary conditions. Integrating the equation (4.4) gives the form of the time evolution for a time step Δt of the wave function,

$$\psi(\vec{x}, t+\Delta t) = \exp\left[i\int_t^{t+\Delta t} dt'\left(\frac{\epsilon}{2}\nabla^2 - \frac{1}{\epsilon}\Phi\right)\right]\psi(\vec{x}, t), \qquad \text{with} \quad \Phi = \Phi_{\rm N} + \Phi_{\rm I}. \tag{4.10}$$

If the timestep Δt is small enough, we can use the trapezoidal rule for Φ,

$$\int_t^{t+\Delta t} dt'\Phi\left(\vec{x}, t\right) \approx \frac{\Delta t}{2}\left(\Phi\left(\vec{x}, t+\Delta t\right) + \Phi\left(\vec{x}, t\right)\right), \tag{4.11}$$

replacing this in (4.10) we have

$$\psi(\vec{x}, t+\Delta t) \approx \exp\left[i\frac{\Delta t}{2}\left(\epsilon\nabla^2 - \frac{1}{\epsilon}\Phi(\vec{x}, t+\Delta t) - \frac{1}{\epsilon}\Phi(\vec{x}, t)\right)\right]\psi(\vec{x}, t). \tag{4.12}$$

The operator $\Phi\psi$ is diagonal in configuration space while the operator $\nabla^2\psi$ is diagonal in Fourier space. Therefore, we can evaluate each term in its own domain by splitting the exponential:

$$\psi(\vec{x}, t+\Delta t) \approx \exp\left[-i\frac{\Delta t}{2\epsilon}\Phi(\vec{x}, t+\Delta t)\right]\exp\left[i\frac{\Delta t\epsilon}{2}\nabla^2\right]\exp\left[-i\frac{\Delta t}{2\epsilon}\Phi(\vec{x}, t)\right]\psi(\vec{x}, t). \tag{4.13}$$

However, this expression is valid up to order two, as we will discuss in Section 4.2.1, thanks to the symmetric splitting. We can go to higher orders by splitting over more intervals with precise coefficients and we have performed the calculation up to order six. However, to solve the scalar cloud dynamics going up to order two is sufficient. Now, with the standard splitting expresion (4.13) we can compute the time evolution of ψ with the symmetrised split-step Fourier method. The algorithm can be schematically described as follows

$$\psi(\vec{x}, t+\Delta t) = \exp\left[-\frac{i\Delta t}{2\epsilon}\Phi(\vec{x}, t+\Delta t)\right]\mathcal{F}^{-1}\exp\left[-\frac{i\epsilon\Delta t}{2}k^2\right]\mathcal{F}\exp\left[-\frac{i\Delta t}{2\epsilon}\Phi(\vec{x}, t)\right]\psi(\vec{x}, t).$$

where $\mathcal{F}$ and $\mathcal{F}^{-1}$ are the discrete Fourier transform and its inverse, and k is the wavenumber in Fourier space. Note that the choice to place the ∇^2 operator in the middle is because it is more expensive since it involves Fourier transforms.

The sequence of the operations is from right to left, and in a nutshell the algorithm can be explained as follows: first, half time step is taken where only the non-linear potential operator is applied, followed by a complete time step in the linear term. Afterwards, the potential field is updated, and a final partial time step is performed in the non-linear term.

$$\Phi_{\rm N}(\vec{x}, t+\Delta t) = \mathcal{F}^{-1}\left(-\frac{4\pi}{k^2}\right)\mathcal{F}|\psi|^2 \tag{4.14}$$

and the computation of the self-interaction potential $\Phi_{\rm I}$ is done in the configuration space according to the model of interest.

As a pseudo-spectral code, it performs linear differential operators through direct multiplication in the Fourier domain, while non-linear terms are evaluated in position space. Consequently, the code avoids the noise associated with spatial derivatives computed using finite-differencing methods. Although there is a computational cost associated with Fourier and inverse Fourier transforms, the code optimizes these transforms by employing FFTW3 (Frigo & Johnson, 2005) to compute the discrete Fourier transform (DFT). These libraries adapt the DFT algorithm to details of the underlying hardware to maximize performance. In addition, the FFTW3 libraries offer parallelization capabilities, taking the advantage of using multiple cores in a user's PC or a shared-memory environment. We have taken advantage of the OPENMP tools to parallelize the multi-threaded routines (OpenMP Architecture Review Board, 2005–*present*; Miguel Hermanns, 1997). However, due to the high computation time when executing the operations, it would be necessary to go further and implement an MPI version, which we leave for future work.

4.2.1 Commutator

Using the spectral method, as we have seen, we write

$$\psi(\vec{x}, t+\Delta t) = \exp\left[-i\frac{\Delta t}{2\epsilon}\Phi\right]\exp\left[i\frac{\Delta t\epsilon}{2}\nabla^2\right]\exp\left[-i\frac{\Delta t}{2\epsilon}\Phi\right]\psi(\vec{x}, t), \tag{4.15}$$

i.e. we can conveniently rewrite it as follows,

$$\psi(\vec{x}, t+\Delta t) = e^{\frac{A}{2}}e^{B}e^{\frac{A}{2}}\psi(\vec{x}, t), \tag{4.16}$$

We integrate exactly each operation, $e^{\frac{A}{2}}$ and e^{B}, so if the 2 operators commute the code is exact (with the same spatial resolution). So we can think that the criterion on Δt is not necessarily $A << 1$ and $B << 1$, but $[A, B] << 1$. We have Baker-Campbell-Hausdorff's formula:

$$e^{X}e^{Y} = e^{Z} \tag{4.17}$$

with

$$Z = X + Y + \frac{1}{2}[X, Y] + \frac{1}{12}[X, [X, Y]] - \frac{1}{12}[Y, [X, Y]] + ... \tag{4.18}$$

here

$$e^{B}e^{\frac{A}{2}} = e^{B+\frac{A}{2}+\frac{1}{2}\left[B,\frac{A}{2}\right]+\frac{1}{12}\left[B,\left[B,\frac{A}{2}\right]\right]-\frac{1}{12}\left[\frac{A}{2},\left[B,\frac{A}{2}\right]\right]+...} = e^{Z_1} \tag{4.19}$$

$$Z_1 = B + \frac{A}{2} + \frac{1}{2}\left[B, \frac{A}{2}\right] + \frac{1}{12}\left[B, \left[B, \frac{A}{2}\right]\right] - \frac{1}{12}\left[\frac{A}{2}, \left[B, \frac{A}{2}\right]\right] \tag{4.20}$$

$$e^{\frac{A}{2}}e^{B}e^{\frac{A}{2}} = e^{\frac{A}{2}}e^{Z_1} = e^{Z} \tag{4.21}$$

$$Z = \frac{A}{2} + Z_1 + \frac{1}{2}\left[\frac{A}{2}, Z_1\right] + \frac{1}{12}\left[\frac{A}{2}, \left[\frac{A}{2}, Z_1\right]\right] - \frac{1}{12}\left[Z_1, \left[\frac{A}{2}, Z_1\right]\right] + ... \tag{4.22}$$

We calculate up to the order $(\Delta t)^3$.

$$Z = \frac{A}{2} + B + \frac{A}{2} + \frac{1}{2}\left[B, \frac{A}{2}\right] + \frac{1}{12}\left[B, \left[B, \frac{A}{2}\right]\right] - \frac{1}{12}\left[\frac{A}{2}, \left[B, \frac{A}{2}\right]\right] \tag{4.23}$$

$$+\frac{1}{2}\left[\frac{A}{2}, B + \frac{A}{2} + \frac{1}{2}\left[B, \frac{A}{2}\right]\right] + \frac{1}{12}\left[\frac{A}{2}, \left[\frac{A}{2}, B + \frac{A}{2}\right]\right] \tag{4.24}$$

$$-\frac{1}{12}\left[B + \frac{A}{2}, \left[\frac{A}{2}, B + \frac{A}{2}\right]\right] \tag{4.25}$$

Using the properties of the commutators, finally we get:

$$Z = A + B + \frac{1}{12}[B, [B, A]] + \frac{1}{24}[A, [B, A]] \tag{4.26}$$

therefore,

$$e^{\frac{A}{2}}e^{B}e^{\frac{A}{2}} = e^{A+B+\frac{1}{12}[B,[B,A]]+\frac{1}{24}[A,[B,A]]+...} \tag{4.27}$$

We can see that we have a scheme of order 2 since the term of order $(\Delta t)^2$ is zero and the error is of order $(\Delta t)^3$.

4.2.2 Approximation error of the Pseudo-spectral method

Let us define the error contributions of the pseudo-spectral approximation in the following way: the total error is $E = E_1 + E_2$ with

$$E_1 = \frac{1}{12}[B,[B,A]] = \frac{1}{12}B^2A - \frac{1}{6}BAB + \frac{1}{12}AB^2 \tag{4.28}$$

$$E_2 = \frac{1}{24}[A,[B,A]] = \frac{1}{12}ABA - \frac{1}{24}A^2B - \frac{1}{24}BA^2 \tag{4.29}$$

where the operators A and B are $A = -i\frac{\Delta t}{\epsilon}\Phi$ and $B = i\frac{\epsilon\Delta t}{2}\nabla^2$.

Now we consider the following Fourier modes: $\psi = e^{i\vec{k}\vec{x}}$, $\phi = \tilde{\phi}_{\vec{q}}e^{i\vec{q}\vec{x}}$. By replacing these modes in (4.28) and (4.29) we have:

$$E_1 = i\frac{(\Delta t)^3\epsilon}{48}\tilde{\phi}_q e^{i(k+q)x}\left[4k^2q^2 + 4kq^3 + q^4\right] \tag{4.30}$$

We can check that $E_1 = 0$ if $q = 0$, which means that ϕ is constant and commutes with ∇^2. Note that the density ρ and the potential Φ are smoother than ψ since it oscillates so fast. Therefore $q \leq k$ and:

$$|E_1| \leq \frac{3}{16}(\Delta t)^3\epsilon k_{max}^2 Max_q[\tilde{\phi}_q q^2] \tag{4.31}$$

and

$$|E_2| \leq \frac{(\Delta t)^3}{24\epsilon}Max_q[(\tilde{\phi}_q q)^2] \tag{4.32}$$

4.3 Code validation

To check the validity of the code, we use the conservation laws of the SP system. As we have seen in Section 2.5.3, the mass of the system must be constant throughout the time evolution, as well as the total energy and the linear momentum. On the other hand, when we are solving the time evolution of an equilibrium configuration, i.e., the soliton, we check that the virial quantity is always zero.

4.4 Initial densities profiles

In this section we present the different subroutines of the code that calculate different initial density profiles. In addition to those developed in the following sections, a Gaussian anstaz can also be used.

4.4.1 Soliton profile

As we have seen in Section 1.4, the soliton is the equilibrium configuration of the system, so we can represent this state with ψ_e given by

$$\alpha\psi_e = H\psi_e. \tag{4.33}$$

Assuming spherical symmetry, the wave function for the equilibrium configurations is of the form:

$$\psi(\vec{x},t) = \psi_e(r)\exp^{-i\alpha t}. \tag{4.34}$$

where $r = |\vec{x}|$. So, the soliton profile is the solution of the time independent Schrödinger–Poisson system of the radial density profile:

$$\epsilon^2\nabla^2\psi_e = 2\left(\Phi_{\rm N} + \Phi_{\rm I} - \alpha\right)\psi_e \quad \text{and} \quad \nabla^2\Phi_{\rm N} = 4\pi|\psi_e|^2. \tag{4.35}$$

Absorbing $\Phi_{\rm N}(0)$ in α, we have:

$$\Phi_{\rm N}(r) = \Phi_{\rm N}(0) + \hat{\Phi}_{\rm N}(r) \quad \text{with} \quad \hat{\Phi}_{\rm N}(0) = 0 \quad \text{and} \quad \alpha = \hat{\Phi}_{\rm N}(0) + \hat{\alpha}. \tag{4.36}$$

Therefore, the consequent set of equations are:

$$\epsilon^2\nabla^2\psi_e = 2\left(\hat{\Phi}_{\rm N} + \Phi_{\rm I} - \hat{\alpha}\right), \quad \nabla^2\hat{\Phi}_{\rm N} = 4\pi|\psi_e|^2, \quad \hat{\Phi}_{\rm N}(0) = 0 \tag{4.37}$$

To proceed with the calculation, it is important to note that both ψ_e and $\hat{\Phi}_{\rm N}$ are even functions by construction. The profile is computed using a *shooting method*, starting from the origin. The shooting method, is an approach to solve a boundary value problem by transforming it into an initial value problem. Essentially, we search for solutions to the initial value problem using different initial conditions until one solution satisfies the boundary conditions of the original problem.

Around the centre, when $r \to 0$ we can expand ψ_e is as follows taking into account that $\psi_e'(0) = 0$

$$\psi_e \approx \psi_0 + \frac{\psi_2}{2}r^2 + ... \to \rho = |\psi_e|^2 = \psi_0^2 + \psi_0\psi_2 r^2 + ... \quad \text{with} \quad \nabla^2\psi_e = \psi_2 + ... \tag{4.38}$$

And at $r \to \infty$ all the fields vanish. We proceed as follows: in the algorithm, $\hat{\alpha}$ is fixed by the choice of the mass of the soliton profile we want to compute. Next, we try a value of ψ_0 at the origin. Then, we define the vector $y(r) = \left(\psi_e, \psi_e', \hat{\Phi}_{\rm N}, \hat{\Phi}_{\rm N}'\right)$ and we move forward in r to compute $y(r)$ using a fourth-order Runge-Kutta algorithm to solve the coupled profile equations. So, the initial condition at $r = 0$ is described by $y(0) = \left(\psi_0, \psi_0' = 0, \hat{\Phi}_{\rm N,0} = 0, \hat{\Phi}_{\rm N,0} = 0\right)$. If we find that $\psi_e < 0$ as we move towards r, then we stop since we have started from a value for ψ_0 that is too low. On the other hand, if we find that $\psi' > 0$, we have started from a high value of ψ_0 and we stop. Therefore, we have to update our choice of ψ_0 accordingly to the case in which we are.

One other different situation is if ϵ is too small. In this case, the Runge-Kutta algorithm fails to solve the profile. In this scenario, the Thomas Fermi approximation is used directly.

4.5 Finite difference scheme

Before building 3D the pseudo-spectral method presented in Section 4.2, the preliminary stages consisted of first developing the method in 1D, using both the pseudo-spectral and finite difference methods. However, in this initial numerical study, we decided not to further develop the finite difference method because it became obsolete for the following reasons. First, the computational time of the spectral method was much faster, secondly, it avoided the noise caused by the computation of the spatial derivatives and thirdly as mentioned before, were able to parallelize it.

4.5.1 Dynamical evolution in 1D: Finite difference scheme

To simulate the dark matter scalar field dynamics in 1D we implement a FORTRAN90 code which solves the SP system discretizing the equations (4.4) and (4.6) (Madarassy & Toth, 2013, 2015).

We represent $\psi(x,t)$ by its values at a set grid of points. The values of the scalar field at the grid points will be abbreviated by $\psi(x,t) = \psi_j^n$. We can write the evolution of the system as follows:

$$i\frac{\partial\psi}{\partial t} = -iH\psi, \quad H = -\frac{\epsilon}{2}\frac{\partial^2}{\partial x^2} + \frac{1}{\epsilon}(\Phi_{\rm N} + \Phi_{\rm I}) \tag{4.39}$$

So, the time evolution of the system is defined by:

$$\psi_i^{n+1} = \exp^{-iH\Delta t}\,\psi_i^n = \hat{U}(\Delta t)\psi_i^n. \tag{4.40}$$

Therefore, splitting $\hat{U}(\Delta t)$ as follows, we derive a unitary approximation :

$$\psi_i^{n+1} = \exp^{\frac{-iH\Delta t}{2}} \exp^{\frac{-iH\Delta t}{2}}\,\psi_i^n \tag{4.41}$$

$$\left(1 + \frac{1}{2}iH\Delta t\right)\psi_i^{n+1} = \left(1 - \frac{1}{2}iH\Delta t\right)\psi_i^n \tag{4.42}$$

By replacing H by its finite-difference approximation in x, we have a complex tridiagonal system to solve. The method is stable, unitary, and second-order accurate in space and time. In fact, it is simply the Crank-Nicholson method. By using the finite-difference representation for the x derivative, equation (4.42) reads,

$$\psi_i^{n+1} - \frac{i\Delta t}{2}\left[\epsilon\frac{\psi_{i+1}^{n+1} - 2\psi_i^{n+1} + \psi_{i-1}^{n+1}}{2(\Delta x)^2} - \frac{1}{\epsilon}\Phi_i\psi_i^{n+1}\right] = \psi_i^n + \frac{i\Delta t}{2}\left[\epsilon\frac{\psi_{i+1}^{n} - 2\psi_i^{n} + \psi_{i-1}^{n}}{2(\Delta x)^2} - \frac{1}{\epsilon}\Phi_i\psi_i^{n}\right], \tag{4.43}$$

which can it be written (4.43) as a matrix equation:

$$U_1\psi_i^{n+1} = U_2\psi_i^n. \tag{4.44}$$

Where

$$U_1 = \begin{pmatrix} \beta_0 & -\alpha & . & . & . \\ -\alpha & \beta_1 & -\alpha & . & . \\ . & -\alpha & \beta_3 & -\alpha & . \\ . & . & . & . & . \\ . & . & . & . & . \\ . & . & . & -\alpha & \beta_i \end{pmatrix} \quad \text{and} \quad U_2 = \begin{pmatrix} \gamma_0 & \alpha & . & . & . \\ \alpha & \gamma_1 & \alpha & . & . \\ . & \alpha & \gamma_3 & \alpha & . \\ . & . & . & . & . \\ . & . & . & . & . \\ . & . & . & \alpha & \gamma_i \end{pmatrix} \tag{4.45}$$

with

$$\alpha_i = \frac{i\Delta t\epsilon}{4(\Delta x)^2} \quad \beta_i = 1 + \frac{i\Delta t}{2}\left(\epsilon\frac{1}{(\Delta x)^2} + \frac{1}{\epsilon}\Phi_i\right) \quad \gamma_i = 1 - \frac{i\Delta t}{2}\left(\epsilon\frac{1}{(\Delta x)^2} + \frac{1}{\epsilon}\Phi_i\right) \tag{4.46}$$

Where Δx is the grid space size and Δt the time step. In our code, Δx will be fixed meanwhile Δt will be variable inspired by (Edwards et al., 2018). The contribution of the

gravitational and the self-interaction potential is included in $\Phi_i = \Phi_{N_i} + \Phi_{I_i}$. In 1D the gravitational potential reads:

$$\Phi_{\rm N}(x) = 2\pi \int dx' |\psi|^2 |x - x'| \tag{4.47}$$

For the cases studied in the 1D collisions we considered the following scenarios: FDM $\Phi_{\rm I} = 0$ and for qthe uartic self-interaction, whose potential is: $\Phi_{\rm I} = \lambda |\psi|^2$.

As Φ^{n+1} is not known in advance, we proceed by iterations: we start with Φ^n and then we compute ψ^{n+1}, from which we can deduce Φ^{n+1}. Then we recalculate ψ^{n+1}, followed by Φ^{n+1}, and we keep iterating until ψ^{n+1} does not differ by more than 0.1% between 2 iterations.

Chapter 5

Solitons and halos for self-interacting scalar dark matter

In this chapter, our focus is on the formation of self-interacting solitons within a larger dark matter halo (Galazo García et al., 2023). We assume that the halo is formed through Jeans' instability (Alcubierre et al., 2002; Chavanis, 2018; Harko, 2019; Brax et al., 2019a) and investigate whether solitons can dynamically emerge from the evolution of dark matter within the halo. Specifically, we demonstrate that due to initial density fluctuations around the initial halo profile, self-interacting solitons always emerge and absorb a significant portion of the halo mass. This occurs regardless of whether a small soliton already exists or if no soliton is initially present. We also compare the scenarios of a flat or cuspy halo profile. In the case of cuspy profiles, we find that soliton formation from no initial soliton occurs rapidly within a few dynamical times. In all cases, a soliton forms, grows, and reaches a substantial size relative to the initial halo. This behavior differs from fuzzy dark matter, where solitons are only stable if they are initially present and have a sufficient mass (Schive et al., 2014b,c; Veltmaat et al., 2018; Chan et al., 2022). In the case of self-interacting dark matter, the solitons are spontaneously created.

To validate these findings, we derive a kinetic equation from the nonlinear Schrödinger equation, which is applicable even to a non-homogeneous background. By incorporating a simple energy-cutoff assumption for the occupation numbers of excited states in the halo, we determine that the growth rate of solitons is positive but decreases rapidly as the soliton mass increases.

These results could have significant implications for astrophysical scenarios, suggesting that if dark matter were a scalar with self-interactions, dark matter halos would consist of a combination of a diffuse halo and a smaller soliton, the size of which depends on the halo's formation history. This could have observable effects on the dynamics of stars within dark matter halos, which we leave for future investigations.

This chapter is organized as follows: In the first part, Section 5.1, we remind the model and the initial conditions, specifically the halo from which a soliton will emerge. In the subsequent Section 5.2, we discuss the emergence of solitons in flat halos, followed by Section 5.3, where we explore cuspy halos. Finally, Section 5.4, we develop a kinetic theory to analyze the growth rate of solitons. We conclude with a summary of our findings.

5.1 Equations of motion and initial conditions

As we have presented in Section 2.7, in the nonrelativistic limit (Brax et al., 2019a), the wavefunction satisfies the nonlinear Schrödinger equation Eq.(2.83). The Newtonian gravitational potential Φ_N is given by the Poisson equation Eq. (2.39) This system is characterized by the coupling of the non-linear Schrödinger equation with the Poisson equation. This can also be reduced to a single integro-differential equation, which will be analysed in Section 5.4,

$$i\frac{\partial\psi}{\partial t} = -\frac{\nabla^2\psi}{2m} + m^2\psi\left(4\pi\mathcal{G}_N\nabla^{-2} + \frac{1}{\rho_a}\right)|\psi|^2, \tag{5.1}$$

with

$$\rho_a = \frac{4m^4}{3\lambda_4}. \tag{5.2}$$

5.1.1 Hydrostatic equilibrium and Thomas-Fermi limit

In the Thomas-Fermi regime that we will consider in this chapter, this soliton is governed by the balance between gravity and the repulsive force associated with the self-interactions (for $\lambda_4 > 0$). As a reminder, the soliton profile is,

$$\rho_{\rm sol}(r) = \rho_{0\rm sol}\frac{\sin(\pi r/R_{\rm sol})}{\pi r/R_{\rm sol}}, \tag{5.3}$$

with the radius

$$R_{\rm sol} = \pi r_a, \quad \text{with} \quad r_a^2 = \frac{3\lambda_4}{16\pi\mathcal{G}_N m^4} = \frac{1}{4\pi\mathcal{G}_N\rho_a}. \tag{5.4}$$

As a reminder, outside of the radius r_a where Eq.(5.3) would give a zero density we can no longer neglect Φ_Q and the exact solution develops an exponential tail at large radii. The approximation (5.3) is valid up to $r \lesssim R_{\rm sol}$ for

$$\Phi_Q \ll \Phi_I : \quad \frac{\rho_{0\rm sol}}{\rho_a} \gg \frac{1}{r_a^2 m^2}. \tag{5.5}$$

5.1.2 Outer halo and semi-classical limit

In this chapter, we will study the emergence and the evolution of these solitons within a larger halo of radius $R_{\rm halo} > R_{\rm sol}$. As seen above, the self-interactions can only support an hydrostatic equilibrium within the radius $R_{\rm sol}$ of Eq.(5.4), independently of the soliton mass. Therefore, while inside $R_{\rm sol}$ the self-interactions can balance gravity and build a flat core when the condition (5.5) is satisfied, outside of $R_{\rm sol}$ the self-interactions are negligible. There, as for FDM and CDM models, gravity is balanced by the velocity dispersion or the angular momentum of the system. Thus, in cosmological numerical simulations of FDM halos, one finds a flat core governed by the quantum pressure inside an NFW halo that is similar to the halos found in CDM simulations (Navarro et al., 1996b). The halo is made of granules that are stochastic fluctuations with a size of the order of the de Broglie wavelength. A similar configuration would then apply to our case, except that the flat core is now supported by the self-interactions instead of the quantum pressure.

We will consider the semi-classical limit (i.e., large scalar mass m), where the de Broglie wavelength is much smaller than both the core and halo radii. Then, the granules also correspond to temporary wave packets that play the role of particules (Hui et al., 2017) with a velocity dispersion or an angular momentum that balances gravity and supports a virialized halo. This means that $\Phi_Q \ll \Phi_N$. For a system of size $L_\star$ and density $\rho_\star$, this gives

$$\Phi_Q \ll \Phi_N : \quad \epsilon \ll 1 \ \text{ with } \ \epsilon = \frac{1}{\sqrt{\mathcal{G}_N \rho_\star} m L_\star^2}. \tag{5.6}$$

For a virialized system governed by gravity, the gravitational dynamical time $t_\star$ and the virial velocity are

$$t_\star = \frac{1}{\sqrt{\mathcal{G}_N \rho_\star}} \ \text{ and } \ v_\star = \frac{L_\star}{t_\star}. \tag{5.7}$$

Therefore, the de Broglie wavelength $\lambda_{\rm dB}$ reads

$$\lambda_{\rm dB} = \frac{2\pi}{m v_\star} = \frac{2\pi t_\star}{m L_\star} = \frac{2\pi}{\sqrt{\mathcal{G}_N \rho_\star} m L_\star} = \epsilon 2\pi L_\star. \tag{5.8}$$

Thus, the limit $\epsilon \to 0$ corresponds to the semiclassical limit, where the de Broglie wavelength is much smaller than the size of the system. In this chapter, we focus on the semiclassical regime $\epsilon = 0.01 \ll 1$. Then, the halo is composed of incoherent stochastic fluctuations of size $\lambda_{\rm dB}$, with a velocity dispersion set by the virial velocity, whereas a coherent static soliton can appear at the center.

5.1.3 Dimensionless variables

Going back to the Schrödinger equation, it is convenient to work with dimensionless quantities denoted with a tilde,

$$\psi = \psi_\star \tilde{\psi}, \quad t = t_\star \tilde{t}, \quad \vec{x} = L_\star \tilde{\vec{x}}, \quad \Phi = \frac{L_\star^2}{t_*^2} \tilde{\Phi}, \tag{5.9}$$

where $t_\star$ and $L_\star$ are the characteristic time and length scales of the system (in our case the halo that may contain a smaller soliton at the center). Then, the self-interaction potential reads

$$\tilde{\Phi}_I = \lambda \tilde{\rho}, \ \text{ with } \ \lambda = \frac{4\pi r_a^2}{L_\star^2} = \frac{1}{\mathcal{G}_N \rho_a L_\star^2} = \frac{6\pi \lambda_4 M_{\rm Pl}^2}{m^4 L_\star^2}. \tag{5.10}$$

In the following, we remove the tildes for simplicity, as we always work with the dimensionless variables. We will choose $L_\star$ as the radius of our initial spherical halo, so that in dimensionless coordinates we have $R_{\rm halo} = 1$.

5.1.4 Initial conditions and central soliton

In this chapter, we study the evolution of solitons inside self-gravitating halos. As initial conditions of our numerical simulations, we write the wavefunction as

$$\psi_{\rm initial} = \psi_{\rm sol} + \psi_{\rm halo}. \tag{5.11}$$

The first term $\psi_{\rm sol}$ corresponds to a solitonic core, where gravity is balanced by the self-interactions, whereas the second term $\psi_{\rm halo}$ corresponds to the halo that makes up most of the volume and mass of the object, where quantum pressure and self-interactions are negligible and the scalar field behaves like cold dark matter.

As seen in Sec. 5.1.1, in the Thomas-Fermi limit the spherically symmetric soliton is given by the hydrostatic equilibrium

$$\Phi_N(r) + \Phi_I(r) = E_{\rm sol}, \tag{5.12}$$

where we used the dimensionless variables and $E_{\rm sol}$ is a constant with

$$\psi_{\rm sol}(\vec{x}, t) = e^{-iE_{\rm sol}t/\epsilon}\hat{\psi}_{\rm sol}(r). \tag{5.13}$$

For a quartic self-interaction $\lambda_4\phi^4$, which gives $\Phi_I = \lambda\rho$, this yields a linear Helmholtz equation in ρ, with the solution

$$\rho_{\rm sol}(r) = \rho_{0\rm sol}\frac{\sin(\pi r/R_{\rm sol})}{\pi r/R_{\rm sol}}, \quad \hat{\psi}_{\rm sol}(r) = \sqrt{\rho_{\rm sol}(r)}, \tag{5.14}$$

over $r \leq R_{\rm sol}$, and $\rho_{\rm sol} = 0$ for $r > R_{\rm sol}$, as in Eq.(5.3). This is a compact object of dimensionless radius and mass

$$R_{\rm sol} = \frac{\sqrt{\lambda\pi}}{2}, \quad M_{\rm sol} = \frac{4}{\pi}\rho_{0\rm sol}R_{\rm sol}^3. \tag{5.15}$$

In practice, we define our system by $R_{\rm sol}$, and the self-interaction coupling λ follows from Eq.(5.15) as $\lambda = 4R_{\rm sol}^2/\pi$. As the size of the halo is $R_{\rm halo} = 1$, we consider cases with $R_{\rm sol} \lesssim 1$, hence $\lambda \lesssim 1$.

In our numerical computations, we focus on the semiclassical regime $\epsilon = 0.01 \ll 1$. The central soliton is governed by the balance between gravity and self-interactions if the condition (5.5) is satisfied. This reads

$$\rho_{0\rm sol} \gg \frac{4\pi\epsilon^2}{\lambda^2}, \quad \rho_{0\rm sol} \gg \frac{\pi^3\epsilon^2}{4R_{\rm sol}^4}. \tag{5.16}$$

We will consider the cases $R_{\rm sol} = 0.5$ and 0.1. In the former case the soliton is always dominated by the self-interactions as $\rho \gtrsim 1$, whereas in the latter case the self-interactions dominate over the quantum pressure for $\rho \gtrsim 10$.

5.1.5 Decomposition of the halo in eigenfunctions

5.1.5.1 Eigenmodes

For a given time-independent potential $\Phi_N + \Phi_I = \bar{\Phi}$, Eq.(3.5) takes the form of the usual linear Schrödinger equation, which can be solved in terms of the energy eigenmodes $e^{-iEt/\epsilon}\hat{\psi}_E(\vec{x})$ that obey

$$-\frac{\epsilon^2}{2}\nabla^2\hat{\psi}_E + \bar{\Phi}\hat{\psi}_E = E\hat{\psi}_E. \tag{5.17}$$

For a spherically symmetric potential $\bar{\Phi}$, we can expand these eigenmodes in spherical harmonics,

$$\hat{\psi}_{n\ell m}(\vec{x}) = \mathcal{R}_{n\ell}(r)Y_\ell^m(\theta, \varphi), \tag{5.18}$$

where the radial parts obey the usual radial time-independent Schrödinger equation

$$\left[-\frac{\epsilon^2}{2}\frac{1}{r^2}\frac{d}{dr}\left(r^2\frac{d}{dr}\right)+\frac{\epsilon^2}{2}\frac{\ell(\ell+1)}{r^2}+\bar{\Phi}\right]\mathcal{R}_{n\ell}=E_{n\ell}\mathcal{R}_{n\ell} \tag{5.19}$$

and form an orthonormal basis

$$\int dr\, r^2\, \mathcal{R}_{n_1\ell}\mathcal{R}_{n_2\ell}=\delta_{n_1,n_2}\ . \tag{5.20}$$

The energy levels $E_{n\ell}$ depend on the radial and orbital quantum numbers n and ℓ and are independent of the azimuthal number m. As initial condition for the halo, we take a semiclassical equilibrium solution defined by a target spherical density profile $\bar{\rho}(r)$, and hence the associated target gravitational potential $\bar{\Phi}_N(r)$, where we neglect the self-interactions and the central soliton,

$$\bar{\Phi}(r)=\bar{\Phi}_N(r),\quad \nabla^2\bar{\Phi}_N=4\pi\bar{\rho}. \tag{5.21}$$

More precisely, in a fashion similar to Lin et al. (2018); Yavetz et al. (2022), we take for the initial halo wavefunction

$$\psi_{\rm halo}(\vec{x},t)=\sum_{n\ell m}a_{n\ell m}\hat{\psi}_{n\ell m}(\vec{x})e^{-iE_{n\ell}t/\epsilon}, \tag{5.22}$$

where we choose the coefficients $a_{n\ell m}$ of the eigenmodes as

$$a_{n\ell m}=a(E_{n\ell})e^{i\Theta_{n\ell m}}, \tag{5.23}$$

where the amplitude $|a_{n\ell m}|=a(E_{n\ell})\geq 0$ is a deterministic function $a(E)$ of the energy while the phases $\Theta_{n\ell m}$ are uncorrelated random variables with a uniform distribution over $0\leq\Theta<2\pi$.

This gives a stochastic halo density $\rho_{\rm halo}=|\psi_{\rm halo}|^2$, which fluctuates between different realizations of the phases $\Theta_{n\ell m}$. Defining the average $\langle\dots\rangle$ over these random realizations, that is, over the uncorrelated phases $\Theta_{n\ell m}$, we obtain the averaged density

$$\langle\rho_{\rm halo}\rangle=\sum_{n\ell m}a(E_{n\ell})^2|\hat{\psi}_{n\ell m}|^2=\sum_{n\ell}\frac{2\ell+1}{4\pi}a(E_{n\ell})^2\,\mathcal{R}_{n\ell}^2, \tag{5.24}$$

where we used $\sum_m|Y_\ell^m|^2=(2\ell+1)/(4\pi)$. Then, the function $a(E_{n\ell})$ that determines the occupation numbers is chosen so that $\langle\rho_{\rm halo}\rangle=\bar{\rho}$, i.e. we recover the target density profile $\bar{\rho}(r)$ as the averaged profile over the random realizations. In the classical case of discrete particles, this corresponds to the construction of the phase space distribution function $f(\vec{x},\vec{v})$ from the density profile, and the choice (5.23) corresponds to an isotropic distribution $f(E)$.

5.1.5.2 WKB approximation

As we consider the semiclassical regime $\epsilon\ll 1$, we can expect the Wentzel-Kramers-Brillouin (WKB) approximation (Landau & Lifshitz, 1977; Merzbacher, 1998; Yavetz et al., 2022) to be valid. This gives for the radial part $\mathcal{R}_{n\ell}(r)$ the form

$$r_1<r<r_2:\ \mathcal{R}_{n\ell}(r)\simeq\frac{N_{n\ell}}{r\sqrt{k_{n\ell}(r)}}\sin\left[\frac{1}{\epsilon}\int_{r_1}^{r}dr'k_{n\ell}(r')+\frac{\pi}{4}\right] \tag{5.25}$$

where $N_{n\ell}$ is the normalization factor, $k_{n\ell}(r)$ is defined by

$$k_{n\ell}(r) = \sqrt{2\left(E_{n\ell} - \bar{\Phi}_N(r) - \frac{\epsilon^2}{2}\frac{\ell(\ell+1)}{r^2}\right)}, \tag{5.26}$$

and $r_1 < r_2$ are the two turning points of the classical trajectory, where $k_{n\ell}(r) = 0$. The lower bound r_1 is due to the centrifugal barrier and the upper bound r_2 to the confining gravitational potential $\bar{\Phi}_N$. For radial trajectories, associated with $\ell = 0$, we have $r_1 = 0$. Outside of the interval $[r_1, r_2]$ the wavefunction shows a fast decrease as this corresponds to the forbidden region in the classical limit and we consider the semiclassical regime $\epsilon \ll 1$. The normalization condition (5.20) gives

$$N_{n\ell} = \left(\int_{r_1}^{r_2} \frac{dr}{2k_{n\ell}(r)}\right)^{-1/2}, \tag{5.27}$$

where we neglected the contributions from the classically forbidden regions and took the average over the fast oscillations of the wavefunction. Finally, the quantization condition of the energy levels is given in this WKB approximation by

$$\frac{1}{\epsilon}\int_{r_1}^{r_2} dr\, k_{n\ell}(r) = \left(n + \frac{1}{2}\right)\pi, \tag{5.28}$$

where $n = 0, 1, 2, \ldots$ is a non-negative integer. We can see that in the semiclassical regime, $\epsilon \ll 1$, the quantum numbers become large as

$$n \sim 1/\epsilon, \quad \ell \sim 1/\epsilon, \tag{5.29}$$

and the difference between energy levels decreases as $\Delta E \sim \epsilon$. In particular, at fixed ℓ we obtain from Eq.(5.28)

$$\frac{\partial n}{\partial E} = \frac{1}{\pi\epsilon}\int_{r_1}^{r_2} \frac{dr}{k_{n\ell}(r)}. \tag{5.30}$$

In this continuum limit, we can replace the sums in Eq.(5.24) by integrals and we obtain

$$\langle\rho_{\rm halo}(r)\rangle = \frac{1}{2\pi^2\epsilon^3}\int dE\, a(E)^2\sqrt{2[E - \bar{\Phi}_N(r)]}, \tag{5.31}$$

where we used the WKB approximation (5.25). Comparing this expression with the classical result that expresses the density in terms of the particle phase-space distribution (Binney & Tremaine, 2008),

$$\rho_{\rm classical}(r) = 4\pi\int_{\bar{\Phi}_N(r)}^{0} dE\, f(E)\sqrt{2[E - \bar{\Phi}_N(r)]}, \tag{5.32}$$

where we normalized the potential so that bound orbits correspond to $E < 0$, we obtain

$$a(E)^2 = (2\pi\epsilon)^3 f(E). \tag{5.33}$$

The classical phase-space distribution can be obtained from the density by Eddington's formula (Binney & Tremaine, 2008),

$$f(E) = \frac{1}{2\sqrt{2}\pi^2}\frac{d}{dE}\int_E^0 \frac{d\Phi_N}{\sqrt{\Phi_N - E}}\frac{d\rho_{\rm classical}}{d\Phi_N}. \tag{5.34}$$

In practice, choosing a target halo density profile $\bar{\rho}(r)$, we obtain the classical phase-space distribution $f(E)$ from Eddington's formula (5.34), the eigenmode coefficients $a_{n\ell m}$ from Eqs.(5.23) and (5.33), and the initial halo wavefunction from Eq.(5.22). However, to avoid the singularity of the WKB approximation at the turning points, we do not use the WKB expression (5.25) for the eigenmodes. Instead, we explicitly solve the linear eigenmode problem associated with the radial Schrödinger equation (5.19). Therefore, the WKB approximation is only used for the determination of the initial coefficients $a_{n\ell m}$. This is sufficient for our purpose, which is to build random initial conditions with a target radial density profile.

5.2 Halo with a flat-core density profile

5.2.1 Halo eigenmodes

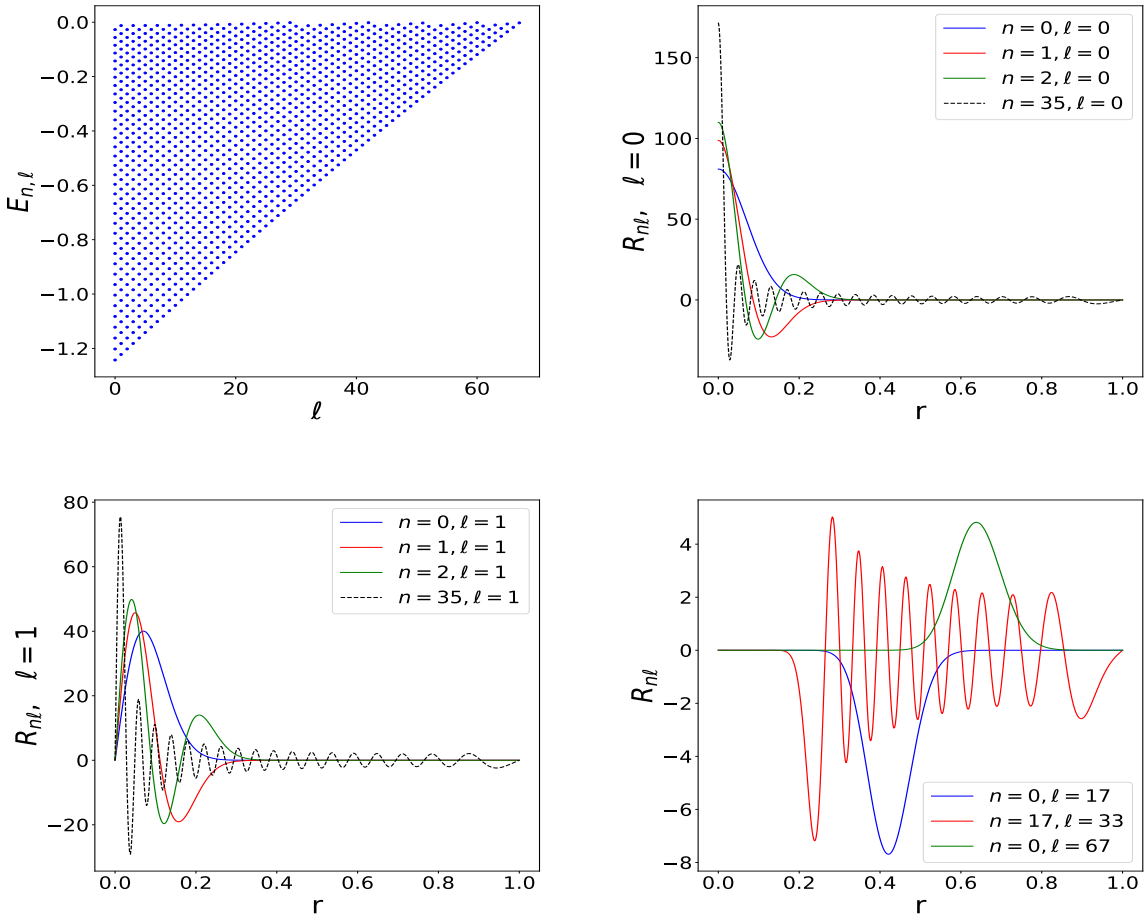

Figure 5.1. Energy levels $E_{n\ell}$ in the $(\ell, E_{n\ell})$ plane (*upper left panel*), for the gravitational potential (5.35). Eigenmodes $\mathcal{R}_{n\ell}(r)$ for $\ell = 0$ (*upper right panel*), $\ell = 1$ (*lower left panel*) and some large values of n or ℓ (*lower right panel*).

We first investigate the dynamics of systems with a flat halo density core. Thus, we

consider a Lane-Emden profile with a polytropic index $n = 1$,

$$0 \leq r \leq 1 : \ \bar{\rho}(r) = \rho_0 \frac{\sin(\pi r)}{\pi r}, \ \bar{\Phi}_N(r) = -\frac{4\rho_0 \sin(\pi r)}{\pi^2 r}, \tag{5.35}$$

which corresponds to the phase-space distribution

$$-\frac{4\rho_0}{\pi} < E < 0 : \quad f(E) = \frac{1}{8\pi\sqrt{-2E}}. \tag{5.36}$$

Although this halo profile happens to take the same form as the hydrostatic soliton (5.14), its physics is quite different. Indeed, here gravity is not balanced by self-interactions but by the velocity dispersion, as for collisionless particles. With $\rho_0 = 1$, this is a simple model for a halo with a flat-core density profile and $\rho_{\rm halo} \sim 1$ within the radius $R_{\rm halo} = 1$.

We solve the eigenvalue problem (5.19) with a numerical spectral method. For each orbital quantum number ℓ, we expand the radial wavefunctions $\mathcal{R}_{n\ell}$ on the basis defined by the eigenvectors of the spherical flat potential well with infinite walls at $r = 1$ (they are given by the spherical Bessel functions $j_\ell(k_n r)$ where k_n is a zero of j_ℓ). This automatically satisfies the boundary condition at $r = 0$, $\mathcal{R}_{n\ell} \propto r^\ell$. This also gives $\mathcal{R}_{n\ell}(r = 1) = 0$, which is a good approximation in the semiclassical regime $\epsilon \ll 1$, as we only include bound eigenmodes with $E < 0$ that are classically forbidden beyond $r = 1$. Truncating the basis at the first 100 eigenvectors, we obtain a finite linear eigenvalue problem associated with a real symmetric matrix of size 100×100. Then, we obtain the $n_{\rm max}(\ell)$ energy levels with $E < 0$ and their associated bound-state eigenvector. Starting from $\ell = 0$ we increase ℓ with unit step until there are no more negative eigenvalues.

We show in Fig. 5.1 the energy levels and some radial eigenmodes associated with the gravitational potential (5.35), with $\epsilon = 0.01$. We find that there exist bound states until $\ell_{\rm max} = 67$. The number n of bound radial modes decreases as ℓ increases and we find $n_{\rm max} = 35$ at $\ell = 0$. In agreement with (5.29), because $\epsilon \ll 1$ there are many eigenmodes inside the potential well Φ_N, which has a depth of the order of unity. As seen in Fig. 5.1, high-energy modes with large n can probe small scales, down to $\Delta r \sim \epsilon = 0.01$, while high orbital momentum modes with large ℓ probe large radii. The modes $\ell = 0$ correspond to radial trajectories in the classical limit.

5.2.2 Large soliton radius, $R_{\rm sol} = 0.5$

We first consider cases where the radius r_a associated with the self-interactions is of the order of the halo radius. Thus, in this section we take $R_{\rm sol} = 0.5$. In the cosmological context, this corresponds to the first overdensities that can collapse just above the Jeans length $\sim r_a$, as gravity can overcome the pressure associated with the repulsive ϕ^4 self-interaction.

5.2.2.1 Halo without initial soliton

We first investigate the dynamics when there is no initial soliton inside the halo, $\rho_{0\rm sol} = 0$. To compute the evolution of the system, we employ the dynamical method presented in Chapter 4. We show in the left column in Fig. 5.2 our initial condition for one realization of the random phases $\Theta_{m\ell m}$ in Eq.(5.23). As seen in the upper left panel, the averaged density $\langle \rho_{\rm halo} \rangle$, defined by Eq.(5.24) where the interferences between the different modes

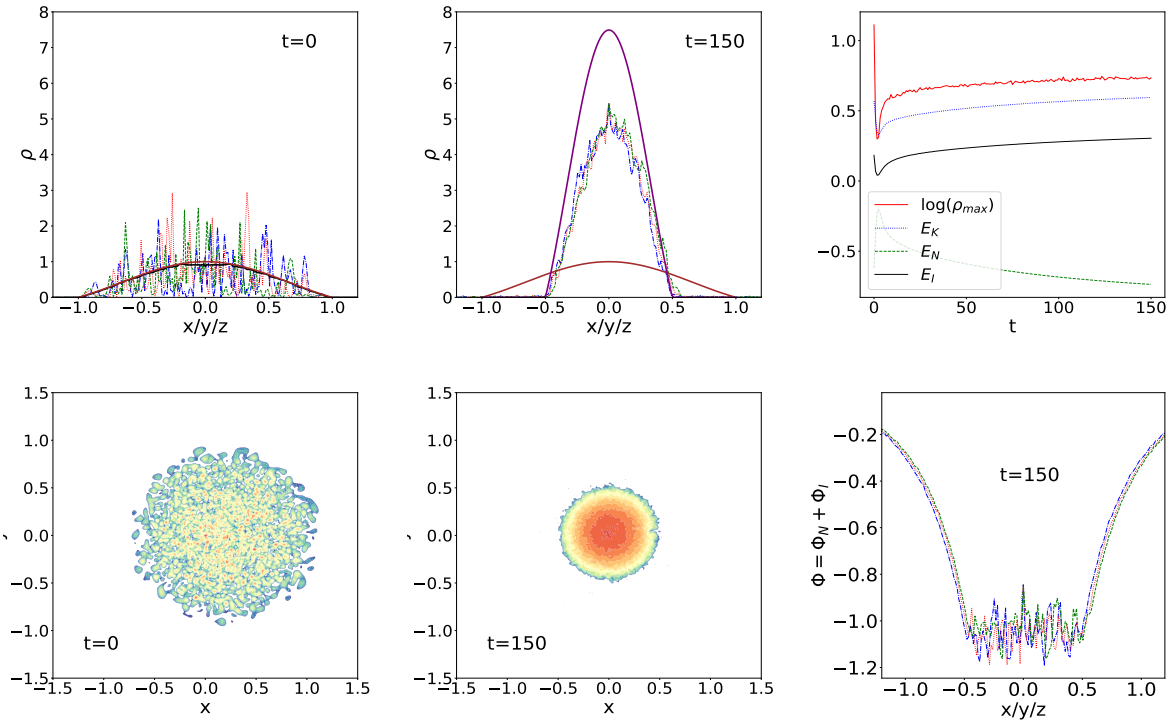

Figure 5.2. [$R_{\rm sol} = 0.5$, $\rho_{0\rm sol} = 0.$] *Upper left panel:* Initial density ρ along the x (blue dash-dot line), y (red dotted line) and z (green dashed line) axis running through the center of the halo. The smooth brown solid line is the target density profile (5.35) and the black wiggly solid line is the averaged density $\langle\rho_{\rm halo}\rangle$ of Eq.(5.24) (they can hardly be distinguished in the figure). There is no central soliton in this initial condition. *Upper middle panel:* density profile along the x, y and z axis that run through the point $\vec{r}_{\rm max}$ where the density is maximum, at time $t = 150$. The lower brown solid line is the initial target density profile as in the upper left panel, while the upper purple solid line is the density profile of a soliton (5.14) that would contain all the mass of the system. *Upper right panel:* evolution with time of the maximum density and of the kinetic, gravitational and self-interaction energies. *Lower left panel:* initial density profile on the 2D (x, y) plane at $z = 0$. *Lower middle panel:* density profile at time $t = 150$ on the 2D (x, y) plane centered on $\vec{r}_{\rm max}$. *Lower right panel:* total potential $\Phi = \Phi_N + \Phi_I$ at $t = 150$, along the x, y and z axis passing through $\vec{r}_{\rm max}$.

$\hat{\psi}_{n\ell m}$ vanish, provides a good approximation of the target density (5.35). Moreover, $\langle\rho_{\rm halo}\rangle$ is identical along any axis that runs through the origin as there is no angular dependence left in Eq.(5.24), which is consistent with the spherical symmetry of the target profile (5.35). Thus, for $\epsilon = 0.01$ the WKB approximation (5.33) for the amplitude of the coefficients $a_{n\ell m}$ is already rather good. As expected, it fares somewhat less well at the center of the halo, dominated by low (n, ℓ) modes. On the other hand, the exact random initial density $\rho_{\rm halo} = |\sum a_{n\ell m}\hat{\psi}_{n\ell m}|^2$ shows strong fluctuations around $\langle\rho_{\rm halo}\rangle$ and depends on the chosen axis running through the center. In agreement with Eq.(5.8), these spikes have a width $\Delta x \sim \epsilon$ that decreases in the semiclassical regime but their amplitude remains of order unity. Thus, $\rho_{\rm halo}$ only converges in a weak sense to the target classical density profile, after coarse-graining over a finite-size window. Note that for a classical system of discrete particles the density field is also very noisy, as it is a sum of Dirac peaks in the point-mass limit. Here the width of the spikes is set by the de Broglie wavelength (5.8). More precisely, from Eqs.(5.24) and (5.33), we can see that the number N of eigenmodes $\hat{\psi}_{n\ell m}$ that contribute to the density at a given point $\vec{x}$ grows as $1/\epsilon^3$.

We can also write powers of the exact random halo density, $\rho_{\rm halo} = \psi\psi^\star \geq 0$, as

$$\rho_{\rm halo}^p = \sum_{i_1,..,i_p=1}^{N} \sum_{j_1,..,i_p=1}^{N} a_{i_1}..a_{i_p} a^\star_{j_1}..a^\star_{j_p} \psi_{i_1}..\psi_{i_p} \psi^\star_{j_1}..\psi^\star_{j_p}, \tag{5.37}$$

where the indices i or j denote $\{n, \ell, m\}$. Taking the average over the random phases Θ_i of Eq.(5.23), the only terms that contribute are those where each a_{i_k} can be paired with a coefficient $a^\star_{j_{k'}}$ with $j_{k'} = i_k$. This gives $p!$ possible permutations,

$$\langle \rho_{\rm halo}^p \rangle = p! \, \langle \rho_{\rm halo} \rangle^p, \tag{5.38}$$

and we obtain the probability distribution

$$\rho_{\rm halo} \geq 0 : \quad \mathcal{P}(\rho_{\rm halo}) = \frac{1}{\langle \rho_{\rm halo} \rangle} e^{-\rho_{\rm halo}/\langle \rho_{\rm halo} \rangle}, \tag{5.39}$$

which does not depend on N nor ϵ. In particular, the standard deviation is $\sqrt{\langle \rho^2_{\rm halo} \rangle_c} = \langle \rho_{\rm halo} \rangle$, in agreement with the relative fluctuations of order unity seen in the upper left panel in Fig. 5.2. Thus, the initial density shows strong relative fluctuations of order unity throughout the halo.

We show the evolution with time of the system in the other panels in Fig. 5.2. Because the soliton moves somewhat around the center of the halo, at the last time $t = 150$ we show the profiles along the $x/y/z$ axis or on the 2D (x, y) plane that run through the point $\vec{r}_{\rm max}$ where ρ is maximum and reaches the value $\rho_{\rm max}$ shown in the upper right panel, as a function of time. We show the final density profiles in the middle column and the final total potential $\Phi = \Phi_N + \Phi_I$ in the lower right panel. The upper right panel shows the evolution with time of the maximum density $\rho_{\rm max}(t)$ of the system, and of the kinetic, gravitational and self-interaction energies. In our dimensionless units, they are given by

$$\begin{aligned} E_K &= \frac{\epsilon^2}{2} \int d\vec{x} \, \nabla\psi \cdot \nabla\psi^*, \quad E_N = \frac{1}{2} \int d\vec{x} \, \rho \Phi_N, \\ E_I &= \int d\vec{x} \, \mathcal{V}_I = \frac{\lambda}{2} \int d\vec{x} \, \rho^2. \end{aligned} \tag{5.40}$$

The total energy $E = E_K + E_N + E_I$ is conserved by the equation of motion (3.5), as well as the total mass M. We checked that M and E are conserved in the numerical simulations until the final time shown in the figures. The kinetic energy E_K comes with a prefactor ϵ^2 in Eq.(5.40). This means that in the semiclassical limit, $\epsilon \to 0$, it is negligible for smooth static configurations such as the equilibrium soliton (5.12), which is thus governed by the balance between gravity and self-interactions. However, this is not the case for the halo for two reasons. First, nonzero orbital velocities $\vec{v}$ of order unity (i.e., of the order of the virial velocity) correspond locally to a phase $e^{i\vec{v}\cdot\vec{x}/\epsilon}$ in the wavefunction (i.e., orbital quantum number $\ell \sim 1/\epsilon$). This implies that ψ shows large gradients that grow as $1/\epsilon$ and balance the prefactor ϵ^2 in Eq.(5.40). Second, as seen above the halo also shows strong density fluctuations on a spatial width $\Delta x \sim \epsilon$, which again lead to large gradients that balance the prefactor ϵ^2. Therefore, even for small ϵ the wavelike nature of the system, governed by the Schrödinger equation rather than by the hydrodynamical Euler equation, remains important.

We can see that within a few dynamical times, $t \lesssim 8$, the system reaches a quasi-stationnary state where half of the mass is contained in a central soliton that follows the profile (5.14). Afterwards, the maximum density, which is a proxy for the soliton peak density, and the energies only show a slow evolution. The central equilibrium soliton is clearly seen on the density profiles shown in the middle column, with its radius $R_{\rm sol} = 0.5$. Superimposed on this soliton, there remains a depleted halo, with the remaining half of the initial mass, with again relative fluctuations of order unity as in in Eq.(5.39). The fluctuations are somewhat lower than in the initial state as the halo mass has been decreased by half. The hydrostatic equilibrium (5.12) is also clearly shown in the lower right panel by the constant plateau of the total potential $\Phi = \Phi_N + \Phi_I$ over the extent of the soliton, $r \leq 0.5$ (with small wiggles associated with the excited halo modes that cross the central region). Beyond the soliton radius, the rapid decrease of the density means that Φ_I becomes small as compared with Φ_N and Φ is dominated by the smooth $-1/r$ shape of the gravitational potential. This collapse of the initial halo onto the half-radius soliton is also clearly seen by the comparison between the left and middle columns. This shows the depletion of the strongly fluctuating halo and the rise of a smooth central soliton with a high density.

5.2.2.2 Initial soliton $\rho_{0\rm sol} = 5$

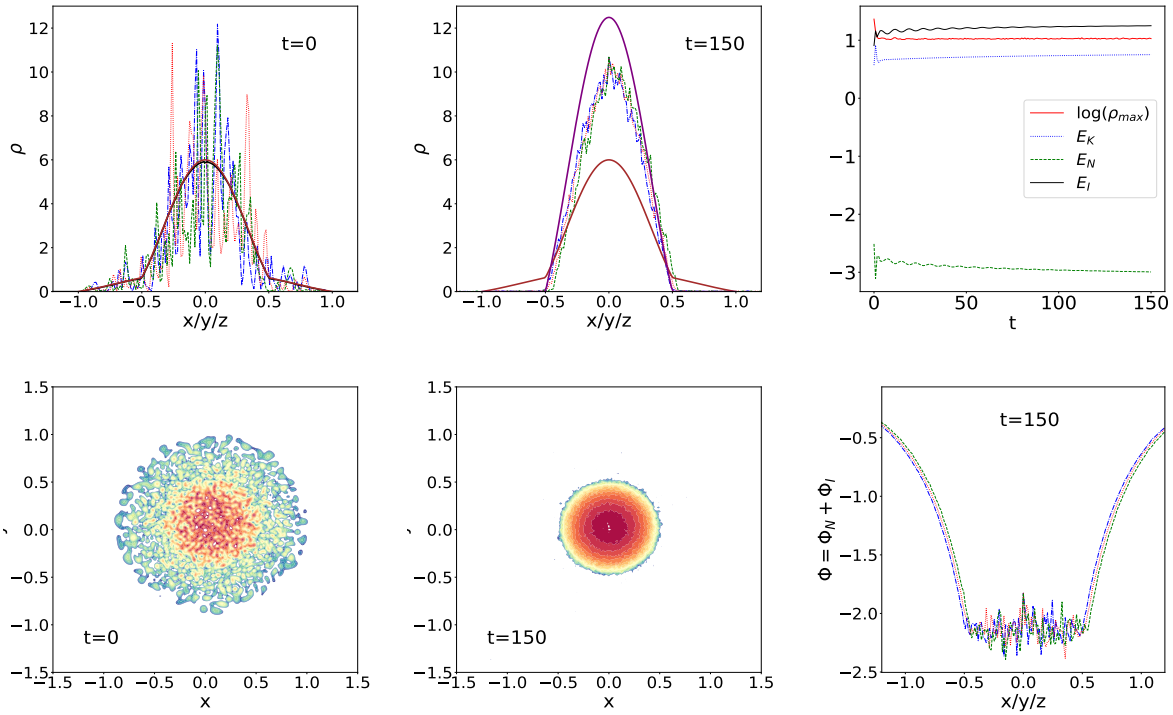

Figure 5.3. Same as Fig. 5.2 but for the case where there is an initial soliton of density $\rho_{0\rm sol} = 5$ and again $R_{\rm sol} = 0.5$.

We now consider the case where there is an initial soliton of density $\rho_{0\rm sol} = 5$ on top of the halo profile. This initial condition is shown in the left column in Fig. 5.3. We can see that very quickly, in a few dynamical times $t \lesssim 2$, the mass of the soliton grows to about 75% of the total mass and seems to remain stable thereafter. This decreases the

halo density and the amplitude of the density fluctuations, as compared with the initial state. Again, this process is clearly apparent in the shape of the potential Φ and the 2D density maps shown in the lower row.

Together with the results of Fig. 5.2, this shows that the soliton is to some degree an attractor of the dynamics, when $R_{\rm sol}$ is not much below the size of the system. It appears from a random initial state to make up 50% of the total mass, as in Fig. 5.2, or can grow to larger values if it is already present with a significant mass, as in Fig. 5.3. The latter results also suggest that the soliton does not grow to capture all the mass of the system. However, this numerical simulation cannot rule out secular effects that would become manifest on timescales that are much greater than the dynamical time and the time of our simulations.

5.2.3 Small soliton radius, $R_{\rm sol} = 0.1$

We now consider cases where the radius r_a associated with the self-interactions is much smaller than the halo radius. Thus, in this section we take $R_{\rm sol} = 0.1$. In the cosmological context, this would correspond to late-time structures that collapse on a scale that is much greater than the characteristic length r_a associated with the self-interactions. We also take the mass of the system to be constant, $M_{\rm sol}+M_{\rm halo} = 4/\pi$, so that all simulations have about the same mass (up to the random fluctuations associated with the stochastic initial conditions). To compute the evolution of the system, we employ the dynamical method presented in Chapter 4

5.2.3.1 Halo without initial soliton

We first study in Fig. 5.4 the dynamics of a halo without initial soliton, $\rho_{0\rm sol} = 0$.

We can see that no soliton dominated by the self-interactions appears until $t \sim 200$. As seen in the middle column, at $t = 180$ the halo is still dominated by strong fluctuations, associated with the superposition of incoherent modes, and a few rare high-density spikes that appear randomly. Their spatial width is not set by the radius $R_{\rm sol} = 0.1$ associated with hydrostatic equilibria governed by the balance between the self-interaction and gravity. Instead, it is of the order of $\Delta x \sim \epsilon = 0.01$ and as in FDM scenarios it is governed by the quantum pressure, that is, by wave effects that appear on the de Broglie scale. One of these high density peaks grows sufficiently to dominate over all other peaks and becomes stable, forming a soliton governed by the quantum pressure rather than the self-interactions. This is also seen in the lower middle panel, where there is no flat region, associated with an hydrostatic equilibria governed by the self-interaction, and $\Phi \simeq \Phi_N$. The small peak associated with the highest density peak is also off-center in the smooth gravitational potential well and this offset is not the same in the three $x/y/z$ directions, as this peaks wanders around within the extend $r \sim 1$ of the system.

The oscillations seen in the lower left panel for the maximum density and the integrated energies until $t \lesssim 100$ are due to global modes, associated with a pulsation of the halo radius, whence of its characteristic densities and energies. These modes appear to be damped after $t \gtrsim 100$. Thus, by $t \sim 100$, the halo relaxes to a quasi-stationary state close to the initial conditions obtained from the WKB approximation. The radius is not significantly modified but it appears that small-scale density fluctuations have grown in the central region, with the appearance of a long-lived high-density peak governed by the

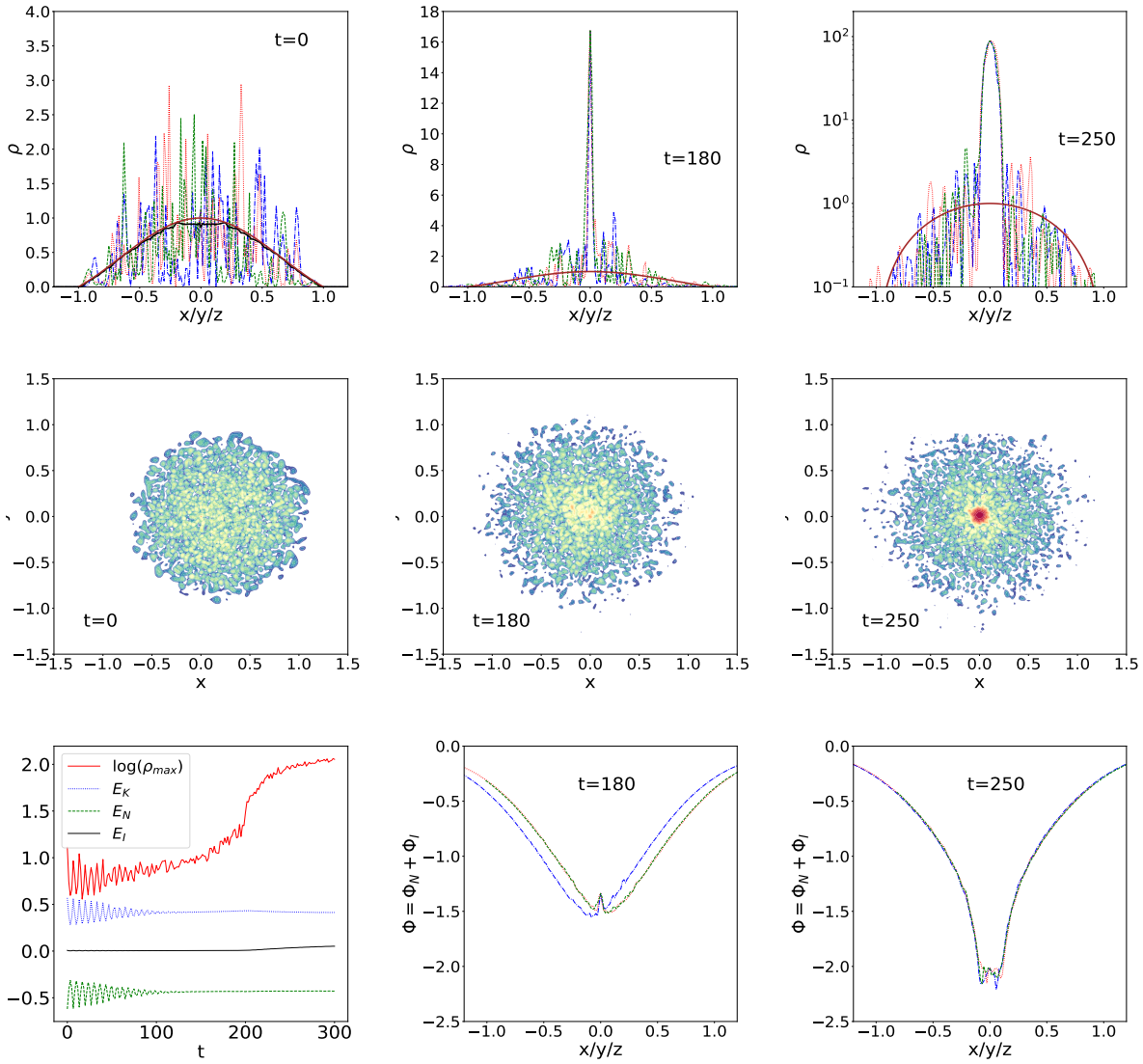

Figure 5.4. Evolution of a flat system with $R_{\rm sol} = 0.1$, $\rho_{0\rm sol} = 0$.

quantum pressure. The halo appears off-center in the box in the central panel because the coordinates are centered on the point $\vec{r}_{\rm max}$, which wanders within the half radius of the halo.

However, the configuration shown at $t = 180$ is not the final state of the system and after the density of the highest spike has kept slowly increasing it reaches a threshold at $t \sim 200$, where it shows a sudden sharp increase. This corresponds to a change of the physics of the system, with the formation of a new soliton that is no longer of the FDM type (balance between gravity and quantum pressure) but of the self-interaction type (balance between gravity and self-interactions), as given by Eq.(5.12). This is clearly seen in the right column at $t = 250$, where we can see the characteristic radius $R_{\rm sol} = 0.1$ of such hydrostatic equilibria and the plateau in the total potential Φ over the soliton extent. In agreement with the condition (5.16), it is only after one of the narrow high density peaks has grown sufficiently to reach a density threshold $\rho \gtrsim 15$ that this transition takes place and a soliton supported by the self-interactions can appear.

Thus, in this case we find that while the system remains dominated by FDM spikes

for a long time and seems almost stationary, the secular evolution eventually makes such a spike to slowly grow until the self-interactions come into play and lead to the formation of a broad soliton governed by these self-interactions. There is thus a transition in the system from a FDM phase to a self-interacting phase, embedded in the FDM halo. This transition may only happen after a long time, much greater than the dynamical time of the system, as the growth of the central density peaks is very slow until one of them reaches this threshold and suddenly builds a unique massive soliton.

5.2.3.2 Small initial soliton $\rho_{0\mathrm{sol}} = 5$

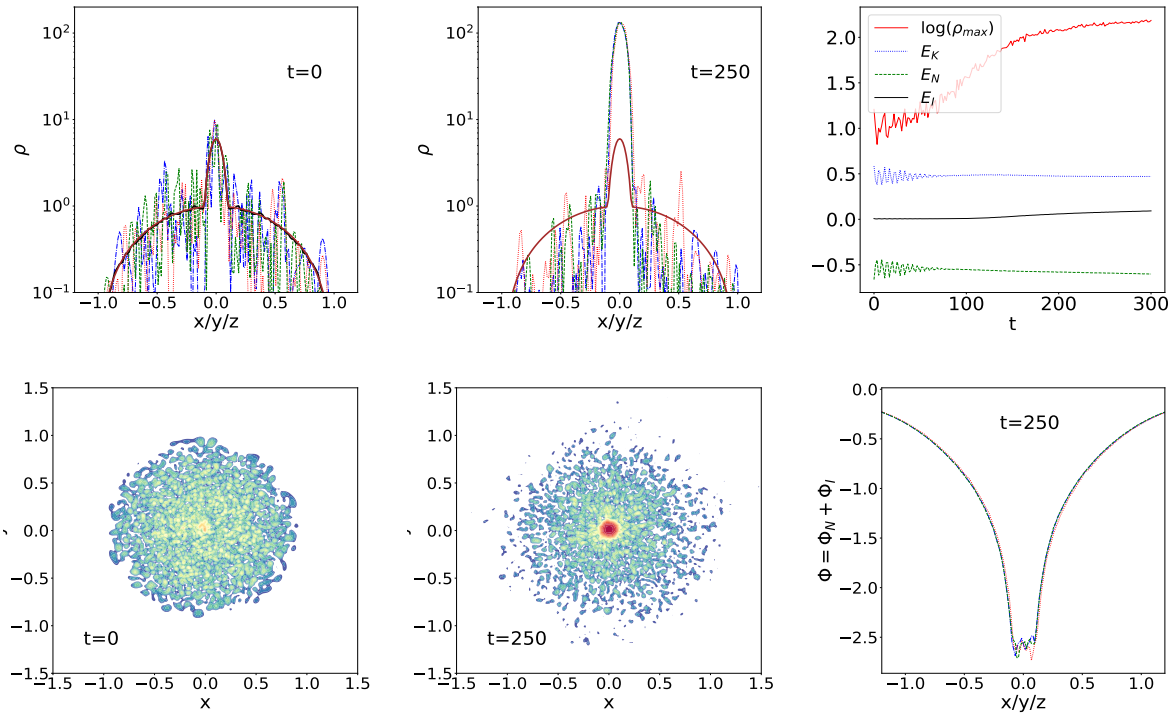

Figure 5.5. Evolution of a flat system with $R_{\mathrm{sol}} = 0.1$, $\rho_{0\mathrm{sol}} = 5$.

We study in Fig. 5.5 the dynamics of a halo with a small initial soliton, $\rho_{0\mathrm{sol}} = 5$. In agreement with Eq.(5.16), it is initially strongly perturbed by the wave packets from the halo as it is close to this density threshold, but we can see that its density slowly grows with time. Until $t \sim 50$, the soliton cannot be clearly seen as it wanders inside the half-radius of the halo and is somewhat masked by the overlying fluctuations associated with higher-energy modes. However, as its density slowly grows it becomes less affected by these perturbations and by $t = 100$ we can clearly see the characteristic size $R_{\mathrm{sol}} = 0.1$ of the central overdensity, much greater than the size $\sim \epsilon = 0.01$ of the incoherent fluctuations. This is also apparent in the potential Φ, which shows a flat plateau at the center perturbed by the wiggles due to the higher-energy modes. The density is still growing at $t = 300$. Therefore, even reasonably small solitons, with a density a few times greater than the halo background, survive and grow with time. This is despite their energy and potential Φ is much smaller than the halo counterparts. This is of course consistent with the fact that initial conditions without a soliton eventually form one, as found in the previous section and in Fig. 5.4. Therefore, solitons governed by the self-interactions appear to

be robust attractor. We checked with numerical simulations that initial solitons with a higher density follow the same pattern, they are not destroyed and slowly grow with time.

5.3 Halo with a cuspy density profile

5.3.1 Halo eigenmodes

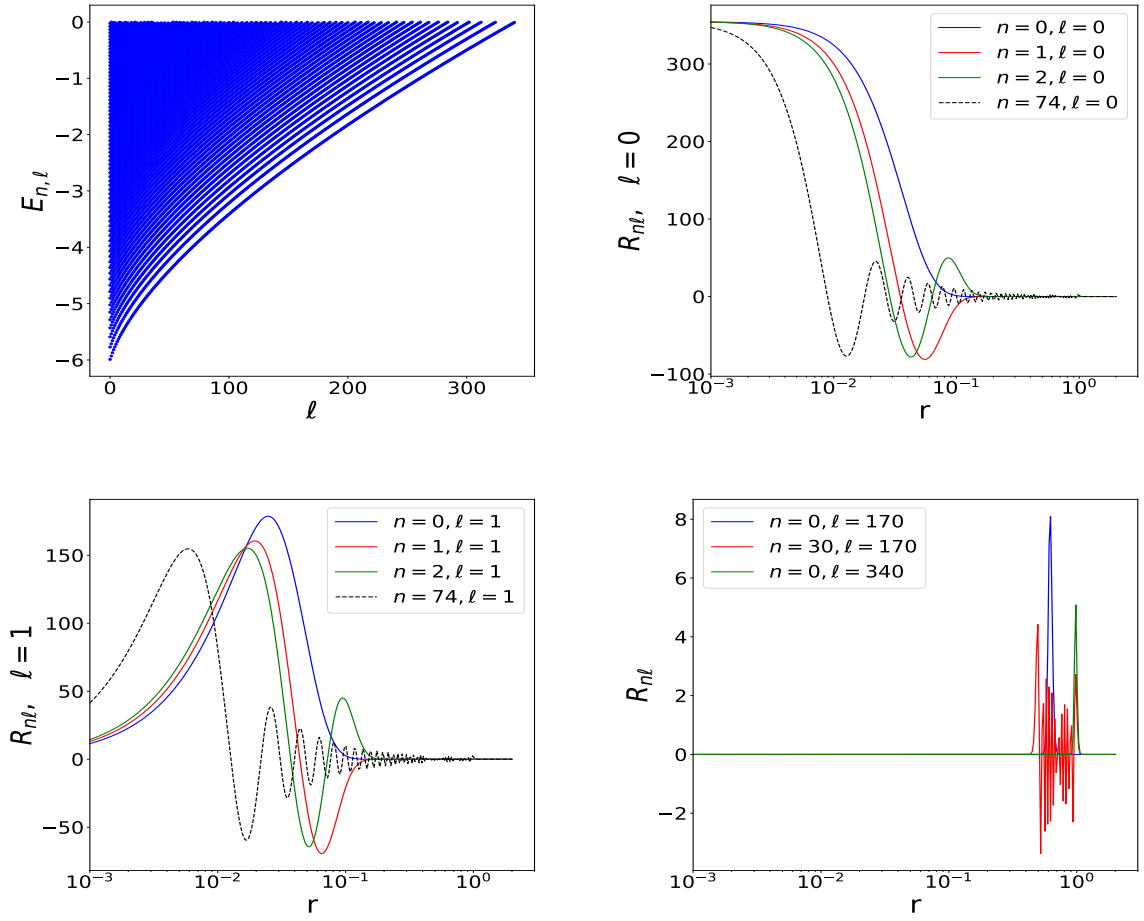

Figure 5.6. Energy levels $(\ell, E_{n\ell})$ and eigenmodes $\mathcal{R}_{n\ell}$ for the gravitational potential (5.41).

We now study the dynamics of cuspy halos, as found in cosmological numerical simulations of both CDM and FDM models. For simplicity, we consider an initial target density profile $\rho \propto 1/r$, which corresponds to the inner regions of both NFW and Hernquist profiles,

$$0 \leq r \leq 1 : \bar{\rho}(r) = \frac{\rho_0}{r}, \quad \bar{\Phi}_N(r) = 2\pi\rho_0(r-1), \tag{5.41}$$

with the phase-space distribution over $-2\pi\rho_0 < E < 0$

$$f(E) = \frac{3\rho_0^2}{2\pi(E+2\pi\rho_0)^2\sqrt{-2E}} - \frac{\rho_0}{4\pi^2(E+2\pi\rho_0)\sqrt{-2E}} + \frac{3\rho_0^2 \mathrm{Arccos}\sqrt{1+E/(2\pi\rho_0)}}{2\sqrt{2}\pi(E+2\pi\rho_0)^{5/2}} . \tag{5.42}$$

Because of the divergent density at the center, the gravitational potential well is deeper than for the flat core profile studied in Section 5.2.1. This leads to a greater number of bound states, as can be seen by comparing the energy levels in Figs. 5.1 and 5.6. This higher number of eigenmodes and their near degeneracy makes the numerical computation of the matrix eigenvalue problem associated with the radial Schrödinger equation (5.19) more difficult. Therefore, we use another method and instead of such a numerical computation we derive approximate but explicit analytical expressions of the eigenmodes. As described in more details in Appendix A, this corresponds to neglecting the centrifugal barrier at large radii and the gravitational potential at small radii (i.e., we only keep the dominant contribution among them). This is exact for $\ell = 0$, where there is no centrifugal barrier at all. For $\ell \geq 1$, the asymptotic behaviors at small and large radii are automatically recovered, up to a possible phase shift and a small error in the energy eigenvalues that are not important for our purposes. This provides explicit expressions for the eigenmodes, avoiding the diagonalization of a large matrix with many close eigenvalues.

We show the energy levels and some radial eigenmodes in Fig. 5.6. As announced above, because of the cuspy density profile, associated with a deeper potential well, there are many more bound states than for the flat profile shown in Fig. 5.1. There are 75 energy levels for $\ell = 0$ and we find bound states until $\ell_{\rm max} = 340$. Again, high-n modes probe small scales, down to $\Delta r \sim \epsilon = 0.01$, while high-$\ell$ modes probe large radii.

5.3.2 Large soliton radius, $R_{\rm sol} = 0.5$

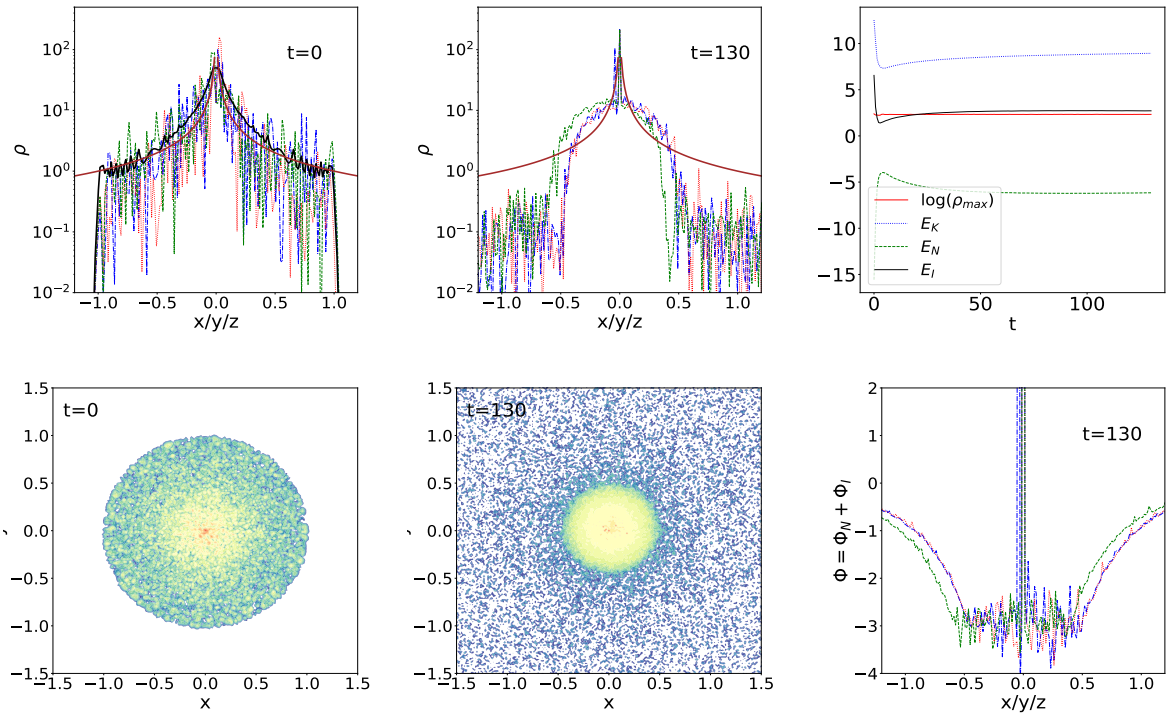

Figure 5.7. Evolution of a cuspy system with $R_{\rm sol} = 0.5$, $\rho_{0\rm sol} = 0$.

We show in Fig. 5.7 the dynamics of a cuspy halo (5.41) in the case $R_{\rm sol} = 0.5$ without initial soliton. As for the flat halo shown in Fig. 5.2, we can see in the upper left

panel that the WKB approximation for the coefficients $a_{n\ell m}$ provides a reasonably good agreement between the averaged density $\langle\rho_{\rm halo}\rangle$ and the target density (5.41), although it overestimates somewhat the density at the center. Again, the interferences between the different modes $\psi_{n\ell m}$ lead to strong relative density fluctuations of order unity, in agreement with (5.39).

As in the flat halo case of Fig. 5.2, we can see that in a few dynamical times, $t \lesssim 4$, a central solition of radius $R_{\rm sol} = 0.5$ forms and contains about 33% of the total mass. This relaxation depletes the halo that also diffuses beyond its initial unit radius, as the process occurs in a rather fast and violent manner. The shape and size of this soliton, governed by the self-interactions, can be clearly seen in the final density profiles and in the final total potential Φ, which is flat over the extent of the soliton. However, in addition to the small wiggles associated with high-energy modes that run across the center of the system, there are a few very high-density spikes on top of the soliton. Their width $\Delta x \sim \epsilon$ shows that these are not solitons supported by the self-interactions, but small-scale peaks on the de Broglie wavelength that wander over the extent of the former soliton. Thus, in the central region there is a co-existence of the two types of features, a large smooth soliton where gravity is balanced by the self-interactions, and a few high-density spikes on the de Broglie wavelength that are far from hydrostatic equilibrium. This is embedded within a halo of fluctuating high-energy modes.

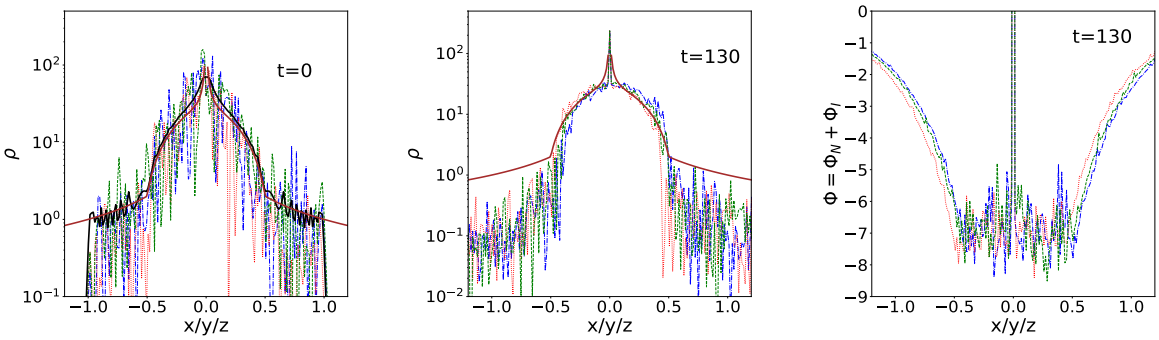

Figure 5.8. Evolution of a cuspy system with $R_{\rm sol} = 0.5$, $\rho_{0\rm sol} = 20$.

We show in Fig. 5.8 the initial and final density profiles when we start with a soliton of density $\rho_{0\rm sol} = 20$ on top of the halo. As for the case of a flat halo shown in Fig. 5.3, the system quickly reaches an equilibrium close to the initial state, where the soliton has slightly increased its mass and depleted the halo. The most striking result is that, as for the flat case shown in Fig. 5.3, the random fluctuations inside this soliton have been significantly damped. Thus, the soliton appears to be an attractor, damping stochastic perturbations. However, as in the case without initial soliton shown in Fig. 5.7, there remain a few very high-density spikes of width $\sim \epsilon$.

5.3.3 Small soliton radius, $R_{\rm sol} = 0.1$

We now consider cases where the radius r_a associated with the self-interactions is much smaller than the halo radius, taking again $R_{\rm sol} = 0.1$ as for the flat case.

5.3.3.1 No initial soliton

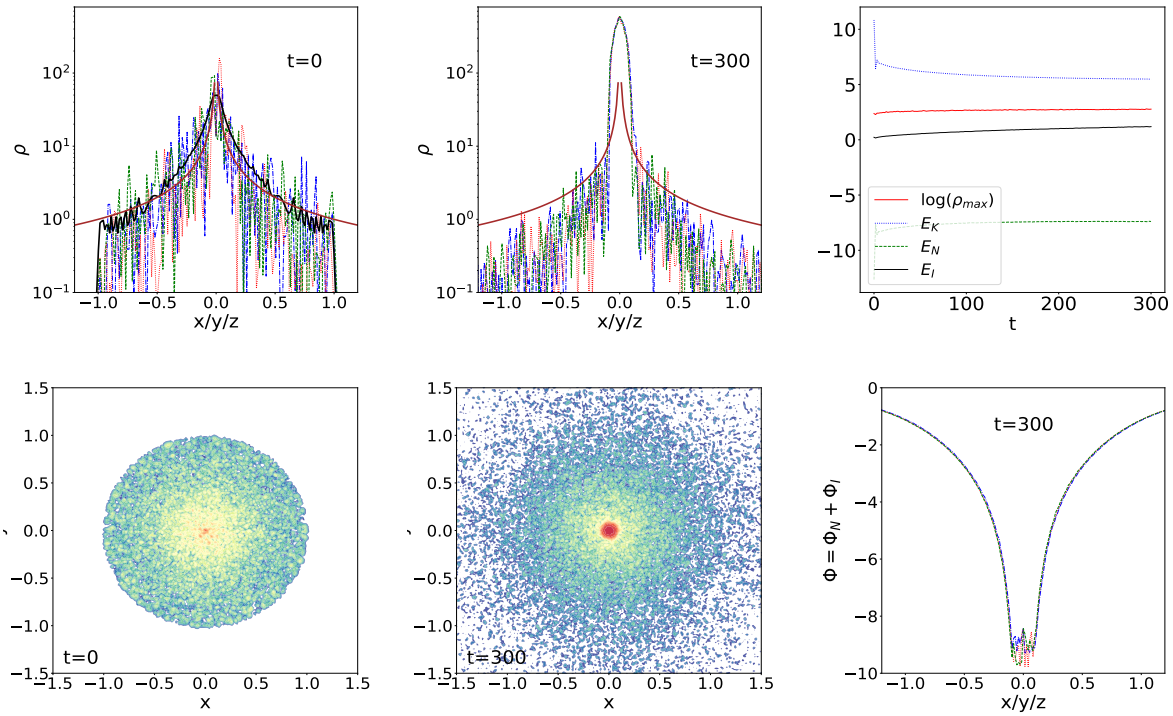

Figure 5.9. Evolution of a cuspy system with $R_{\rm sol} = 0.1$, $\rho_{0\rm sol} = 0$.

We first consider an initial profile without soliton, shown in Fig. 5.9. Because of the high density at the center, $\rho_{\rm halo} \propto 1/r$, the self-interaction $\Phi_I = \lambda\rho$ is large in the central region. This leads to the formation of a central soliton supported by the self-interaction in a few dynamical times, $t \lesssim 2$. This again depletes somewhat the halo, which diffuses slightly beyond its initial radius, while the fluctuations inside the soliton are damped. In contrast with Figs. 5.7 and 5.8 there are no narrow density spikes, supported by the quantum pressure, inside this soliton. This is presumably because the hierarchy of scale between the de Broglie wavelength and the self-interaction soliton is not so large, only a factor ten instead of fifty.

5.3.3.2 Small initial soliton

We show in Fig. 5.10 the case where there is an initial soliton of density $\rho_{0\rm sol} = 100$. Again, the central soliton density grows somewhat with time and damps the central fluctuations, while the halo diffuses slightly beyond its initial radius. Thus, as for the case of a flat halo, we find that the solitons governed by the balance between gravity and the self-interactions are robust and always form, either in a few dynamical times if the initial density is high enough, or after small-scale density fluctuations are grown large enough by a slow secular process to trigger an instability and a fast soliton formation.

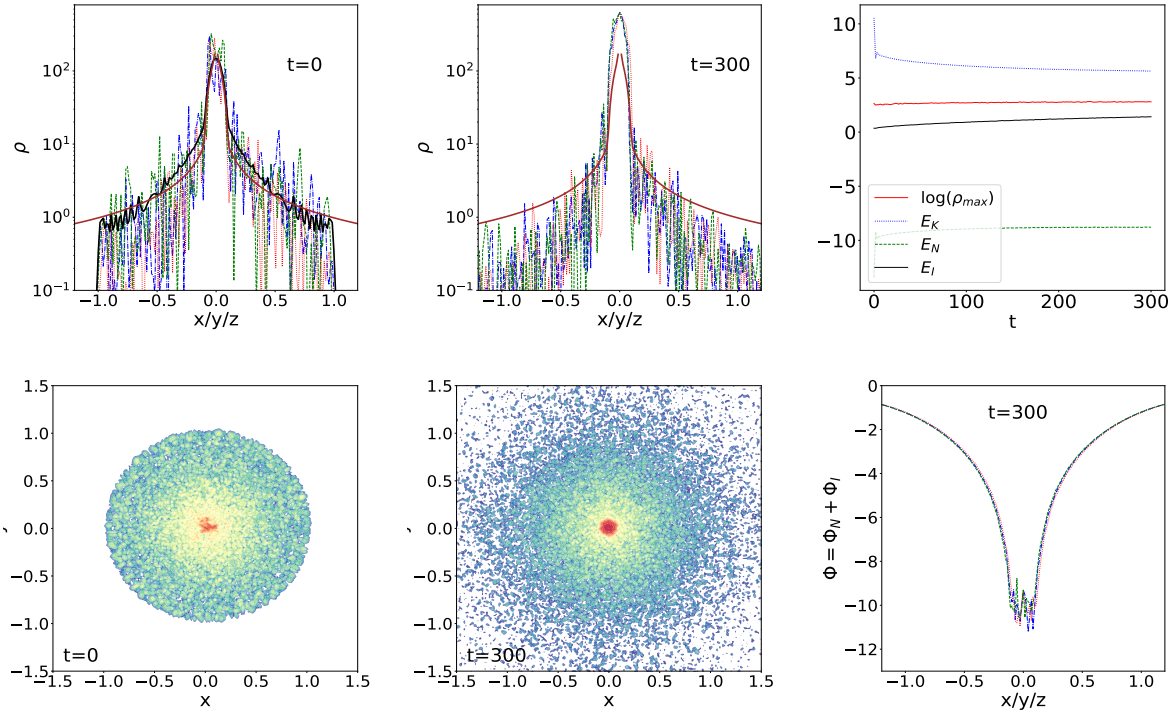

Figure 5.10. Evolution of a cuspy system with $R_{\rm sol} = 0.1$, $\rho_{0\rm sol} = 100$.

5.4 Kinetic theory

5.4.1 Kinetic equation

In the following analysis, we will derive a kinetic equation that describes the time evolution of the system, specifically focusing on the occupation numbers of the central soliton and the halo eigenstates. Previous studies, such as those by Chan et al. (2022); Jain et al. (2023), have explored similar approaches for the formation of FDM solitons within a homogeneous background that can be decomposed into plane waves.

However, in our investigation, we extend these results by considering the effects of self-interactions and a non-homogeneous background. The non-homogeneous background cannot be decomposed into plane waves, which means we cannot rely on Fourier analysis as before. Instead, we introduce a different approach by decomposing the background into eigenmodes of a reference potential, similar to how we described the halo in Section 5.1.5.1.

Furthermore, as we study the time-dependent background, it becomes crucial to distinguish the smooth background from the stochastic fluctuations that drive the dynamics. These fluctuations introduce randomness into the system and play a significant role in its evolution.

By considering these factors, we aim to develop simple kinetic equations that capture the behaviour of the system and shed light on the interplay between the smooth background and the stochastic fluctuations.

The equation of motion (3.5) is the Schrödinger equation in a self-force potential $\Phi = \Phi_N + \Phi_I$, sourced by the system self-gravity and self-interaction. For the quartic

scalar-field model considered in this chapter, Φ is quadratic over the wavefunction ψ, and the equations of motion read

$$i\epsilon\frac{\partial\psi}{\partial t} = -\frac{\epsilon^2}{2}\nabla^2\psi + \Phi\psi, \tag{5.43}$$

with

$$\Phi = (4\pi\nabla^{-2} + \lambda)\psi^\star\psi. \tag{5.44}$$

If the potential Φ is fixed, $\psi(\vec{x},t)$ can be decomposed as usual in energy eigenmodes with the simple time dependence $e^{-iEt/\epsilon}$. In the semiclassical limit, the system behaves like a collection of classical particules and the Husimi phase-space distribution $f_H(\vec{x},\vec{v},t)$ (Husimi, 1940) defined from $\psi(\vec{x},t)$ approximately follows the Vlasov equation that governs the dynamics of the classical distribution $f(\vec{x},\vec{v},t)$ (Uhlemann et al., 2014; Mocz et al., 2018). As described in Section 5.1.5, in this limit $\epsilon \ll 1$, we can build approximate equilibrium configurations by choosing the eigenmode coefficients $a_{n\ell m}$ in correspondance with a classical phase-space equilibrium solution, as in Eqs.(5.23) and (5.33). This procedure would give true equilibria if the potential Φ were only sourced by the average density $\langle\rho\rangle$, which neglects interferences between different eigenmodes as in Eq.(5.24). However, as shown in Eq.(5.39) and in the plots of the initial conditions displayed in the previous sections, the interference terms lead to significant fluctuations of the density profile. They have a relative magnitude of order unity but a spatial width that decreases as ϵ. Hence they only become small in a coarse-graining sense. These random fluctuations mean that even if we start with an equilibrium configuration in this averaged sense, the system will not be exactly stationary as the potential Φ deviates from $\langle\Phi\rangle$. To describe this system, we therefore split the potential Φ in an average spherically symmetric part $\bar{\Phi}$ and a fluctuating part $\delta\Phi$,

$$\bar{\Phi}(\vec{x},t) = \bar{\Phi}(r) + \delta\Phi(\vec{x},t). \tag{5.45}$$

Within an adiabatic approximation, we have in mind that the smooth potential $\bar{\Phi}$ slowly evolves on long time scales whereas the incoherent stochastic fluctuations $\delta\Phi$ evolve on short times and drive the averaged dynamics, as would do an external noise for instance. The potential $\bar{\Phi}$ defines the energy eigenmodes ψ_j,

$$\psi_j(\vec{x},t) = e^{-iE_jt/\epsilon}\hat{\psi}_j(\vec{x}), \quad \hat{\psi}_{n\ell m}(\vec{x}) = \mathcal{R}_{n\ell}(r)Y_{\ell m}(\theta,\varphi), \tag{5.46}$$

where the index j denotes $\{n,\ell,m\}$ and for future convenience we use the real spherical harmonics $Y_{\ell m}$ (also called tesseral spherical harmonics) instead of the more usual complex harmonics,

$$\begin{aligned} m<0: &\quad Y_{\ell m} = \sqrt{2}\,\mathrm{Im}Y_\ell^{|m|}, \quad Y_{\ell 0} = Y_\ell^0, \\ m>0: &\quad Y_{\ell m} = \sqrt{2}\,\mathrm{Re}Y_\ell^m. \end{aligned} \tag{5.47}$$

Therefore, the functions $\hat{\psi}_j(\vec{x})$ are real and form a complete orthonormal basis. We can then expand the wavefunction ψ over this basis as

$$\psi(\vec{x},t) = \sum_j \sqrt{M_j(t)}e^{-i\theta_j(t)/\epsilon}\hat{\psi}_j(\vec{x}), \tag{5.48}$$

where $M_j \geq 0$ and θ_j are real. The squared amplitude M_j is the mass contained in the eigenmode j, if we neglect interferences. Substituting this expansion into the equation of

motion (5.43) we obtain

$$i\epsilon\dot{M}_j + 2M_j\dot{\theta}_j = 2M_jE_j + \sum_{j'} 2\sqrt{M_jM_{j'}}e^{i(\theta_j-\theta_{j'})/\epsilon} \times \int d\vec{x}\,\hat{\psi}_j\,\delta\Phi\,\hat{\psi}_{j'} \tag{5.49}$$

where the dots denote the derivatives with respect to time. We define the reference potential $\bar{\Phi}$ as the sum of the diagonal terms,

$$\bar{\Phi} = (4\pi\nabla^{-2} + \lambda)\sum_j M_j\hat{\psi}_j^2, \tag{5.50}$$

while the remainder $\delta\Phi$ is given by the off-diagonal interference terms,

$$\delta\Phi = (4\pi\nabla^{-2} + \lambda)\sum_{j\neq j'} \sqrt{M_jM_{j'}}e^{i(\theta_j-\theta_{j'})/\epsilon}\hat{\psi}_j\hat{\psi}_{j'}. \tag{5.51}$$

Next, we make the assumption that the background field $\bar{\Phi}$ evolves slowly over time, allowing us to neglect its time dependence in the equation of motion (5.49). The evolution of the system is primarily influenced by small fluctuations $\delta\Phi$, which arise from interferences. These fluctuations perturb the occupation numbers M_j of different energy levels, and in turn, they affect the reference potential $\bar{\Phi}$ as the density profile gradually changes.

In the adiabatic approximation, the slow variation of $\bar{\Phi}$ only causes a change in the phase of the eigenmodes (and energy levels), while leaving their occupation numbers unchanged. Consequently, our main focus lies in understanding the driving mechanism associated with $\delta\Phi$.

Therefore, we can express the equation of motion (5.49) as

$$i\epsilon\dot{M}_1+2M_1\dot{\theta}_1 = 2M_1E_1+\sum_{234}^{2\neq4} 2\sqrt{M_1M_2M_3M_4} \times e^{i(\theta_1+\theta_2-\theta_3-\theta_4)/\epsilon}\int d\vec{x}\,\hat{\psi}_1\hat{\psi}_3(4\pi\nabla^{-2}+\lambda)\hat{\psi}_2\hat{\psi}_4, \tag{5.52}$$

where the indices $\{1,2,3,4\}$ denote $\{j_1,j_2,j_3,j_4\}$. Let us define the vertices $V_{13;24}$ as

$$V_{13;24} = \int d\vec{x}\,\hat{\psi}_1\hat{\psi}_3(4\pi\nabla^{-2}+\lambda)\hat{\psi}_2\hat{\psi}_4, \tag{5.53}$$

which are real and symmetric over $\{1\leftrightarrow3\}$, $\{2\leftrightarrow4\}$ and $\{(13)\leftrightarrow(24)\}$. Then, separating the real and imaginary parts of Eq.(5.52) gives

$$\begin{aligned}
\epsilon\dot{M}_1 &= 2\sum_{234}^{2\neq4}\sqrt{M_1M_2M_3M_4}V_{13;24}\sin\left(\frac{\theta_1+\theta_2-\theta_3-\theta_4}{\epsilon}\right),\\
\dot{\theta}_1 &= E_1 + \sum_{234}^{2\neq4}\sqrt{\frac{M_2M_3M_4}{M_1}}V_{13;24}\cos\left(\frac{\theta_1+\theta_2-\theta_3-\theta_4}{\epsilon}\right).
\end{aligned} \tag{5.54}$$

To avoid secular effects, associated with trivial resonances between products of identical oscillatory terms (Nazarenko, 2011), we define the renormalized frequencies ω_j as

$$\omega_1 = E_1 + \sum_{2}^{2\neq1} M_2\,V_{12;21}. \tag{5.55}$$

Then, the system (5.54) also reads

$$\dot{M}_1 = \frac{2\gamma}{\epsilon} \sum_{234} \sqrt{M_1 M_2 M_3 M_4}\, \hat{V}_{13;24}\, \sin\!\big(\theta_{12}^{34}/\epsilon\big),$$
$$\dot{\theta}_1 = \omega_1 + \gamma \sum_{234} \sqrt{\frac{M_2 M_3 M_4}{M_1}}\, \hat{V}_{13;24}\, \cos\!\big(\theta_{12}^{34}/\epsilon\big), \tag{5.56}$$

where we introduced the notation

$$\theta_{12}^{34} = \theta_1 + \theta_2 - \theta_3 - \theta_4 \tag{5.57}$$

and the new vertices $\hat{V}_{13;24}$ defined as

$$\hat{V}_{13;24} = V_{13;24} \;\text{ except }\; \hat{V}_{13;22} = 0, \;\; \hat{V}_{12;21} = 0. \tag{5.58}$$

We also introduced a book-keeping parameter $\gamma = 1$ that multiplies the vertices $\hat{V}$, i.e. the potential $\delta\Phi$. We have in mind that the fluctuating part $\delta\Phi$ leads to a slow drift of the system as compared with the orbital motions in the mean potential $\bar{\Phi}$. Therefore, we will develop a perturbation theory in $\delta\Phi$, which corresponds to a perturbation theory in powers of γ (taking $\gamma = 1$ at the end).

The system (5.56) is similar to those encountered in four-wave systems (Nazarenko, 2011; Onorato & Dematteis, 2020). However, the vertices $\hat{V}$ are no longer fully symmetric and do not contain Krönecker symbols δ_{12}^{34} in wavenumbers. This is because we expand around a non-homogeneous equilibrium $\bar{\Phi}$, with a peculiar radial density profile $\bar{\rho}(r)$. This breaks the invariance over translations obeyed by wave systems over a uniform background.

We now look for the perturbative expansion of the squared amplitudes M_j and the phases θ_j in powers of γ,

$$M_j = M_j^{(0)} + \gamma\, M_j^{(1)} + \gamma^2 M_j^{(2)} + \dots \tag{5.59}$$

At zeroth order we obtain

$$M_1^{(0)}(t) = \bar{M}_1, \quad \theta_1^{(0)}(t) = \bar{\theta}_1 + \bar{\omega}_1 t, \tag{5.60}$$

with $\bar{M}_1 = M_1(0)$, $\bar{\theta}_1 = \theta_1(0)$, setting the initial conditions of the system at the time $t = 0$. At first order we obtain

$$\dot{M}_1^{(1)} = \frac{2}{\epsilon} \sum_{234} \sqrt{\bar{M}_1 \bar{M}_2 \bar{M}_3 \bar{M}_4}\, \hat{V}_{13;24}\, \sin[(\bar{\theta}_{12}^{34} + \bar{\omega}_{12}^{34} t)/\epsilon], \tag{5.61}$$

and

$$M_1^{(1)}(t) = 2 \sum_{234} \sqrt{\bar{M}_1 \bar{M}_2 \bar{M}_3 \bar{M}_4}\, \frac{\hat{V}_{13;24}}{\bar{\omega}_{12}^{34}} \left[\cos\!\big(\bar{\theta}_{12}^{34}/\epsilon\big) - \cos[(\bar{\theta}_{12}^{34} + \bar{\omega}_{12}^{34} t)/\epsilon]\right], \tag{5.62}$$

$$\theta_1^{(1)}(t) = \epsilon \sum_{234} \sqrt{\frac{\bar{M}_2 \bar{M}_3 \bar{M}_4}{\bar{M}_1}}\, \frac{\hat{V}_{13;24}}{\bar{\omega}_{12}^{34}} \left[\sin[(\bar{\theta}_{12}^{34} + \bar{\omega}_{12}^{34} t)/\epsilon] - \sin\!\big(\bar{\theta}_{12}^{34}/\epsilon\big)\right]. \tag{5.63}$$

At second order, using trigonometric identities we obtain

$$\dot{M}_1^{(2)} = \sum_{234} \hat{V}_{13;24} \sum_{m=1}^{4} \sum_{567} \frac{\hat{V}_{m6,57}}{\bar{\omega}_{m5}^{67}} \sqrt{\frac{\bar{M}_1\bar{M}_2\bar{M}_3\bar{M}_4\bar{M}_5\bar{M}_6\bar{M}_7}{\bar{M}_m}}$$
$$\times \frac{2}{\epsilon} \left[\sin[(\bar{\theta}_{12}^{34} + \bar{\omega}_{12}^{34} t - \sigma_m \bar{\theta}_{m5}^{67})/\epsilon] \right.$$
$$\left. - \sin[(\bar{\theta}_{12}^{34} + \bar{\omega}_{12}^{34} t - \sigma_m \bar{\theta}_{m5}^{67} - \sigma_m \bar{\omega}_{m5}^{67} t)/\epsilon] \right], \tag{5.64}$$

where we introduced $\sigma_1 = \sigma_2 = 1$, $\sigma_3 = \sigma_4 = -1$.
At zeroth order we have $\dot{M}_1^{(0)} = 0$. At first order we obtain from Eq.(5.61)

$$\langle \dot{M}_1^{(1)} \rangle = 0, \tag{5.65}$$

assuming that the initial phases $\bar{\theta}_j$ are uncorrelated and uniformly distributed over $[0, 2\pi]$, as in (5.23). Here we used the properties (5.58) of the non-symmetric vertex $\hat{V}$. At second order we obtain from Eq.(5.64)

$$\langle \dot{M}_1^{(2)} \rangle = \frac{2}{\epsilon} \sum_{234} \bar{M}_1\bar{M}_2\bar{M}_3\bar{M}_4 \left\{ \frac{\sin(\bar{\omega}_{12}^{34} t/\epsilon)}{\bar{\omega}_{12}^{34}} \hat{V}_{13;24} \right.$$
$$\times \left[\frac{\hat{V}_{13;24} + \hat{V}_{14;23}}{\bar{M}_1} + \frac{\hat{V}_{23;14} + \hat{V}_{24;13}}{\bar{M}_2} - \frac{\hat{V}_{31;42} + \hat{V}_{32;41}}{\bar{M}_3} \right.$$
$$\left. - \frac{\hat{V}_{41;32} + \hat{V}_{42;31}}{\bar{M}_4} \right] + \frac{\sin(\bar{\omega}_1^3 t/\epsilon)}{\bar{\omega}_1^3} \hat{V}_{12;23} \left[\frac{\hat{V}_{14;43}}{\bar{M}_1} - \frac{\hat{V}_{34;41}}{\bar{M}_3} \right]$$
$$\left. + \frac{\sin(\bar{\omega}_2^4 t/\epsilon)}{\bar{\omega}_2^4} \hat{V}_{23;34} \frac{\hat{V}_{14;21} - \hat{V}_{12;41}}{\bar{M}_2} \right\}, \tag{5.66}$$

where we used the properties and symmetries of the vertices $\hat{V}$ and V. In usual four-wave systems over an homogeneous background, with a symmetric vertex $\hat{V}$, the last two terms vanish and the first term simplifies as $\sin(\bar{\omega}_{12}^{34} t/\epsilon)(2\hat{V}_{1234}^2/\bar{\omega}_{12}^{34})(1/\bar{M}_1 + 1/\bar{M}_2 - 1/\bar{M}_3 - 1/\bar{M}_4)$. In our case, the inhomogeneous background leads to the more complicated expression (5.66).

5.4.2 Soliton ground state and halo excited states

We are interested in hydrostatic solitons embedded within a halo formed by a quasi-continuum of excited states, as described in Section 5.1.5. As shown in the figures in the previous sections, in the limit $\epsilon \ll 1$ the central soliton follows the density profile (5.14) with a flat potential $\Phi = E_{\rm sol}$ over its extent, determined by the hydrostatic equilibrium (5.12). This is the ground state $j = 0$ of the system. Higher-energy states correspond in the classical limit to particles that orbit up to a radius $r_j^{\rm max} > R_{\rm sol}$, with a higher energy $E_j = \frac{v^2}{2} + \Phi \geq \Phi(r_j^{\rm max}) > \Phi(R_{\rm sol})$. The soliton contains a macroscopic mass, that can make up a significant fraction of the system, whereas the higher-energy states that build the halo form a quasi continuum, with a mass of the order of $\epsilon^3 \ll 1$ as in Eq.(5.33) and energy levels separation $\Delta E \sim \epsilon$ as in (5.28).

Therefore, we look for the evolution of $M_{\rm sol} = M_0$ and we separate the contributions of the soliton from those of the halo quasi-continuum in the sums in the right-hand side in Eq.(5.66). We also consider times much longer than the orbital periods, using

$$\lim_{t\to\infty} \frac{\sin(tx)}{x} = \pi\, \delta_D(x). \tag{5.67}$$

This gives

$$\begin{aligned}
\dot{M}_0 = \frac{2\pi}{\epsilon} \sum_{12} M_0^2 M_1 M_2 \Big\{ & \delta_D(\omega_{00}^{12}) 4 V_{01;02}^2 \left(\frac{1}{M_0} - \frac{1}{M_1} \right) \\
& + \delta_D(\omega_0^1) \frac{V_{02;21} V_{00,01}}{M_0} \Big\} + \frac{2\pi}{\epsilon} \sum_{123} M_0 M_1 M_2 M_3 \Big\{ \delta_D(\omega_{01}^{23}) \\
& \times \frac{1}{2} (V_{02;13} + V_{03;12})^2 \left(\frac{1}{M_0} + \frac{1}{M_1} - \frac{1}{M_2} - \frac{1}{M_3} \right) \\
& + \delta_D(\omega_0^1) V_{02;21} V_{03;31} \left(\frac{1}{M_0} - \frac{1}{M_1} \right) \Big\},
\end{aligned} \tag{5.68}$$

where the sums only run over the halo excited states $j \neq 0$ (and at least one is transformed into an integral in the continuum limit). Here we dropped the overbars for simplicity and we replaced $\hat{V}$ by V as we discarded the constraints (5.58) in the sums over the halo excited states, as each of them only contains a mass of the order of ϵ^3.

5.4.3 Renormalized frequencies ω_j

We also separate the soliton from the quasi-continuum of halo excited states in the expression (5.55) of the renormalized frequencies ω_j. Thus, we write $\omega_j = E_j + \Delta E_j$ with

$$\Delta E_0 = \sum_1 V_{01;10} M_1, \quad \Delta E_1 = V_{10;01} M_0 + \sum_2 V_{12;21} M_2, \tag{5.69}$$

where the indices 1 and 2 stand for halo excited states. As in Eq.(5.33) for the initial halo configuration, we assume that the squared amplitudes M_j only depend on the energy E_j, and hence on the quantum numbers n and ℓ, and are independent of the azimuthal number m,

$$M_j = a_j^2 = (2\pi\epsilon)^3 f(E_{n,\ell}). \tag{5.70}$$

In particular, as in Eq.(5.24), we obtain from (5.48) the averaged halo density as

$$\langle \rho_{\rm halo} \rangle = \sum_j M_j \hat{\psi}_j^2 = \sum_{n\ell} \frac{2\ell+1}{4\pi} M_{n\ell}\, \mathcal{R}_{n\ell}^2, \tag{5.71}$$

where we used again the assumption that the initial phases $\bar{\theta}_j$ are uncorrelated.

The vertices $V_{13;24}$ defined in Eq.(5.53) can be decomposed over their self-interaction and gravitational parts

$$V_{13;24} = V_{13;24}^{\lambda} + V_{13;24}^{N}, \tag{5.72}$$

with

$$V_{13;24}^{\lambda} = \lambda \int d\vec{x}\, \hat{\psi}_1 \hat{\psi}_3 \hat{\psi}_2 \hat{\psi}_4, \tag{5.73}$$

and

$$V^N_{13;24} = -\int \frac{d\vec{x}\, d\vec{x}\,'}{|\vec{x}-\vec{x}\,'|}\, \hat{\psi}_1(\vec{x})\hat{\psi}_3(\vec{x})\, \hat{\psi}_2(\vec{x}\,')\hat{\psi}_4(\vec{x}\,'). \tag{5.74}$$

Then, we obtain for the self-interaction contribution to the frequency shifts

$$\begin{aligned} \Delta E^\lambda_0 &= \lambda \int dr\, r^2 \mathcal{R}_0^2 \langle \rho_{\rm halo}\rangle, \\ \Delta E^\lambda_1 &= V^\lambda_{1001} M_0 + \lambda \int dr\, r^2 \mathcal{R}_1^2 \langle \rho_{\rm halo}\rangle. \end{aligned} \tag{5.75}$$

This gives the order of magnitude estimates $\Delta E^\lambda_0 \sim \lambda \langle \rho_{\rm halo}\rangle_{R_{\rm sol}} = \Phi_{I{\rm halo}}(R_{\rm sol})$ and $\Delta E^\lambda_1 \sim \lambda M_{\rm sol}\mathcal{R}_1^2(R_{\rm sol}) + \Phi_{I{\rm halo}}(R_1)$, where R_1 is the radial extent of the eigenmode $\mathcal{R}_1$. By definition, we consider systems where the self-interaction is negligible in the halo, which is governed by gravity and the velocity dispersion. We also have $\lambda \ll 1$ and $M_{\rm sol} \ll 1$. Therefore, the shifts $\Delta E^\lambda_j \ll 1$ are negligible as compared with the energies $E_j \sim 1$, except for low-energy modes that are confined within the soliton radius.

The gravitational contribution reads as

$$\begin{aligned} \Delta E^N_0 &= -\sum_1 M_1 \int \frac{d\vec{x}\, d\vec{x}\,'}{|\vec{x}-\vec{x}\,'|}\, \hat{\psi}_0\hat{\psi}_1\hat{\psi}'_1\hat{\psi}'_0 \\ \Delta E^N_1 &= V^N_{10;01} M_0 - \sum_2 M_2 \int \frac{d\vec{x}\, d\vec{x}\,'}{|\vec{x}-\vec{x}\,'|}\, \hat{\psi}_1\hat{\psi}_2\hat{\psi}'_2\hat{\psi}'_1. \end{aligned} \tag{5.76}$$

A crude estimate, where we would replace the mixed product $\hat{\psi}_1\hat{\psi}_2\hat{\psi}'_2\hat{\psi}'_1$ by $\hat{\psi}_1^2\hat{\psi}_2'^2$, would give $\Delta E^N_j \sim \Phi_{N{\rm halo}}(R_j)$. This is much smaller than E_0 for the ground state $j=0$, while for halo excited states this would give $\Delta E^N_j \sim E_j$. However, this is a significant overestimate because the mixed product $\hat{\psi}_1\hat{\psi}_2\hat{\psi}'_2\hat{\psi}'_1$ means that we have significant interferences between the two eigenmodes in the integrals over both $\vec{x}$ and $\vec{x}\,'$. Then, for halo excited states we also have $\Delta E^N_j \ll E_j$.

Thus, we find that the frequency shifts are small, $\omega_j \simeq E_j$, except for the low energy modes that are confined within the soliton radius where $\Delta E^\lambda_j \geq 0$ can be significant. The soliton frequency shift is smaller than that of these low-energy halo states, because it does not contain the term $V^\lambda_{1001}M_0$ in Eq.(5.75). Therefore, as we checked numerically, the soliton ground state keeps the lowest frequency,

$$\omega_j > \omega_0 \quad \text{for} \quad j \neq 0. \tag{5.77}$$

Some of the renormalized frequencies ω_j are shown in Figs. 5.11 and 5.13 below.

5.4.4 Evolution of the soliton mass

We are interested in the evolution with time of the mass of the soliton, given by Eq.(5.68) Because the halo excited states have $\omega_j > \omega_0$ from (5.77), the Dirac factors $\delta_D(\omega^{12}_{00})$ and $\delta_D(\omega^1_0)$ vanish and Eq.(5.68) simplifies as

$$\dot{M}_0 = \frac{\pi}{\epsilon} \sum_{123} M_0 M_1 M_2 M_3\, \delta_D(\omega^{23}_{01})\, (V_{02;13} + V_{03;12})^2 \times \left(\frac{1}{M_0} + \frac{1}{M_1} - \frac{1}{M_2} - \frac{1}{M_3} \right). \tag{5.78}$$

This is actually similar to the usual kinetic equation of four-wave systems (Nazarenko, 2011; Onorato & Dematteis, 2020), but as seen above for excited states the kinetic equation would take the more complicated form (5.68).

The kinetic equation (5.78) shows at once that if we start without a central soliton, it will be generated by the nonlinear dynamics, as we have

$$\dot{M}_0 = \frac{2\pi}{\epsilon}\sum_{123} M_1 M_2 M_3\, \delta_D(\omega_{01}^{23})\, (V_{02;13} + V_{03;12})^2 > 0 \tag{5.79}$$

for $M_0 = 0$.

Nevertheless, this expression becomes less informative when dealing with small values of M_0. In such cases, it becomes challenging to distinguish the soliton from the random fluctuations present in the central region. In fact, the constraint (5.5) demonstrates that solitons with low mass, meaning low density, cannot be supported solely by self-interactions. Initially, low-mass density peaks are sustained by the quantum pressure, and they must surpass a specific density threshold to transition into solitons supported by the self-interaction pressure. This was discussed in detail in Section 5.2.3.1, particularly in reference to the simulation depicted in Figure 5.4.

Using the fact that the occupation numbers M_j and the renormalized frequencies ω_j do not depend on the azimuthal numbers m_j, we can perform the sums over $\{m_1, m_2, m_3\}$ in Eq.(5.78). Using the expressions (5.73)-(5.74) of the vertices V we obtain

$$\begin{aligned}
\dot{M}_0 = {} & \frac{1}{2\epsilon}\widehat{\sum}_{123} M_0 M_1 M_2 M_3\, \delta_D(\omega_{01}^{23}) \begin{pmatrix} \ell_1 & \ell_2 & \ell_3 \\ 0 & 0 & 0 \end{pmatrix}^2 \\
& \times (2\ell_1+1)(2\ell_2+1)(2\ell_3+1) \left(\frac{1}{M_0}+\frac{1}{M_1}-\frac{1}{M_2}-\frac{1}{M_3}\right) \\
& \times \left[\frac{\lambda}{2\pi}\int dr\, r^2 R_0 R_1 R_2 R_3 - \int dx\, x^2 \frac{R_0 R_2}{2\ell_2+1}\int dx'\, x'^2 \right. \\
& \left. \times R_1' R_3' \frac{x_<^{\ell_2}}{x_>^{\ell_2+1}} - \int dx\, x^2 \frac{R_0 R_3}{2\ell_3+1}\int dx'\, x'^2 R_1' R_2' \frac{x_<^{\ell_3}}{x_>^{\ell_3+1}}\right]^2
\end{aligned} \tag{5.80}$$

where $\widehat{\sum}$ denotes that we only sum over the quantum numbers n_j and ℓ_j, $x_< = \min(x, x')$, $x_> = \max(x, x')$, R_j' denotes $R_j(x')$, and we used the expansion

$$\frac{1}{|\vec{x} - \vec{x}\,'|} = \sum_{\ell,m} \frac{4\pi}{2\ell+1}\frac{x_<^\ell}{x_>^{\ell+1}} Y_\ell^m(\vec{x})^* Y_\ell^m(\vec{x}\,'). \tag{5.81}$$

5.4.5 Halo with a flat density profile

We consider in this section the growth of the central soliton inside the flat halo studied in Section 5.2

5.4.5.1 Modified potential and approximate energy cutoff

As the central soliton grows, it modifies the shape of the potential Φ. Indeed, as seen in the previous sections, inside the soliton Φ is roughly constant, in agreement with

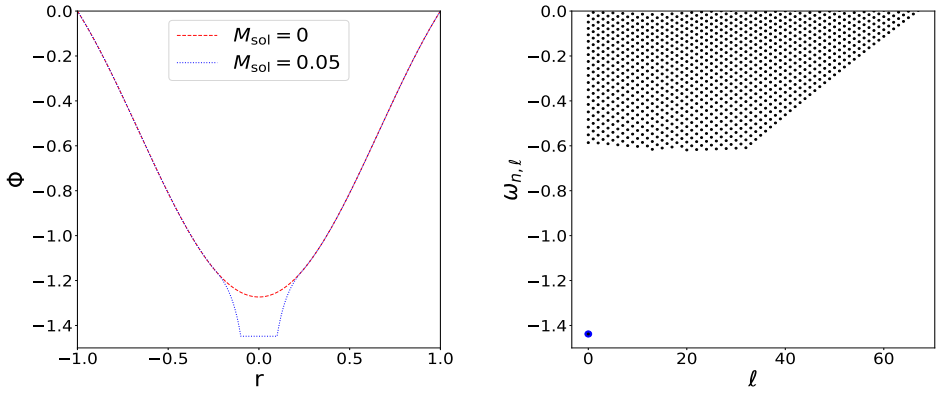

Figure 5.11. *Left panel:* potential $\bar{\Phi}$ without a soliton (red dashed line) and with a soliton of mass $M_{\rm sol} = 0.05$ (blue dotted line). *Right panel:* renormalized frequencies ω_j such that $E_j > E_{\rm coll}$. The soliton ground state frequency ω_0 is shown by the lower left blue point.

the hydrostatic equilibrium (5.12). At radii slightly beyond the soliton radius $R_{\rm sol}$, Φ is dominated by the gravitational potential $\Phi_{N\rm sol} = -M_{\rm sol}/r$ of the soliton. Finally, at large radii Φ is dominated by the gravitational potential $\Phi_{N\rm halo}$ of the halo. In principle, we should follow simultaneously the evolution with time of the potential $\bar{\Phi}$, the halo occupation numbers M_j, and the soliton mass M_0. However, in this article we investigate a simplified approach where we only use the kinetic equation (5.80) to follow the soliton growth rate and use instead approximate explicit models for the potential $\bar{\Phi}$ and the halo occupation numbers M_j.

We approximate the potential $\bar{\Phi}(r)$ by

$$\begin{aligned} &r > R_{\rm coll} : \bar{\Phi}(r) = \Phi_{N\rm halo}(r), \\ &R_{\rm sol} < r < R_{\rm coll} : \bar{\Phi}(r) = -\frac{M_{\rm sol}}{r} + \frac{M_{\rm sol}}{R_{\rm coll}} + \Phi_{N\rm halo}(R_{\rm coll}), \\ &r < R_{\rm sol} : \quad \bar{\Phi}(r) = -\frac{M_{\rm sol}}{R_{\rm sol}} + \frac{M_{\rm sol}}{R_{\rm coll}} + \Phi_{N\rm halo}(R_{\rm coll}), \end{aligned} \tag{5.82}$$

where $\Phi_{N\rm halo}$ is the initial gravitational potential (5.35) of the halo and $R_{\rm coll}$ is the radius where the initial enclosed mass is equal to the soliton mass, $M_{\rm halo}(< R_{\rm coll}) = M_{\rm sol}$. This simple approximation provides a reasonably good description of the potential Φ displayed in Figs. 5.4 and 5.5, except in the outer parts as it does not capture the diffusion of the halo somewhat beyon its initial radius. This potential $\bar{\Phi}$ defines in turns the eigenmodes ψ_j.

Instead of using the kinetic equations (5.66) to follow the occupation numbers of the halo excited states, we assume an adiabatic evolution with $M_j = M_j(t = 0)$, where $M_j(0) = (2\pi\epsilon)^3 f[E_j(0)]$ are the initial halo occupation numbers as in Eq.(5.33). Then, to take into account the transfer of mass from the halo to the central soliton, we assume that the soliton mostly builds from the lowest energy modes. Therefore, we take $M_j = 0$ for all modes with $E_j < E_{\rm coll}$, where the threshold $E_{\rm coll}$ is such that the mass associated with all these modes is equal to the increase of the soliton mass,

$$\sum_j^{E_j < E_{\rm coll}} (2\ell + 1) M_{n\ell}(0) = M_{\rm sol} - M_{\rm sol}(0), \tag{5.83}$$

where $M_{\rm sol}(0)$ is the initial soliton mass at time $t = 0$.

We show in Fig. 5.11 the potential $\bar{\Phi}$ given by the approximation (5.82) and the renormalized frequencies ω_j for the case of a small soliton $M_{\rm sol} = 0.05$. The soliton creates a flat potential over $R_{\rm sol}$, which is deeper than the initial halo potential because of the central overdensity. The new energy levels E_j are close to the initial energy levels $E_j(0)$ of the unperturbed halo for $E > E_{\rm coll}$ but are significantly lowered for $E < E_{\rm coll}$, because of the increased depth of $\bar{\Phi}$ in the central region. This is why the ground state (soliton) level $E_0 = \bar{\Phi}(0) \simeq -1.4$ is below the initial energy level $E_0 \simeq -1.2$ shown in Fig. 5.1. In agreement with the analysis in Section 5.4.3, the shifts ΔE_j that give the renormalized frequencies ω_j are small, except for the low-energy states that are confined within the soliton radius. However, these states do not appear in the right panel in Fig. 5.11, because they are removed by the energy cutoff (5.83). Nevertheless, the small but nonzero shifts ΔE_j for higher energy levels explain why the constant-energy cutoff $E_{\rm coll}$ gives a cutoff for $\omega_{n\ell}$ that is not completely constant with ℓ, as seen in Fig. 5.11.

We can see in the figure that for the small mass $M_{\rm sol} = 0.05$ there is already a large gap between ω_0 and the remaining halo frequencies ω_j. In fact, we have $|\omega_j| < |\omega_0|/2$ for all halo modes with $E_j > E_{\rm coll}$. This means that the Dirac factor $\delta_D(\omega_{01}^{23})$ in Eq.(5.80) is always zero. Therefore, the soliton growth rate $\Gamma_{\rm sol}$, defined by

$$\Gamma_{\rm sol} = \frac{\dot{M}_0}{M_0}, \tag{5.84}$$

vanishes within the approximation (5.83). This means that this approximation is not sufficient to predict the soliton growth rate in this configuration. We need to follow more precisely the evolution with time of the low-energy occupation numbers $M_j(t)$ as the growth rate $\Gamma_{\rm sol}$ is very sensitive to the distribution at low energies, for halo modes that have a significant overlap with the soliton central region so that the kernal $V_{02;13}$ are not negligible.

5.4.5.2 Growth of the soliton mass

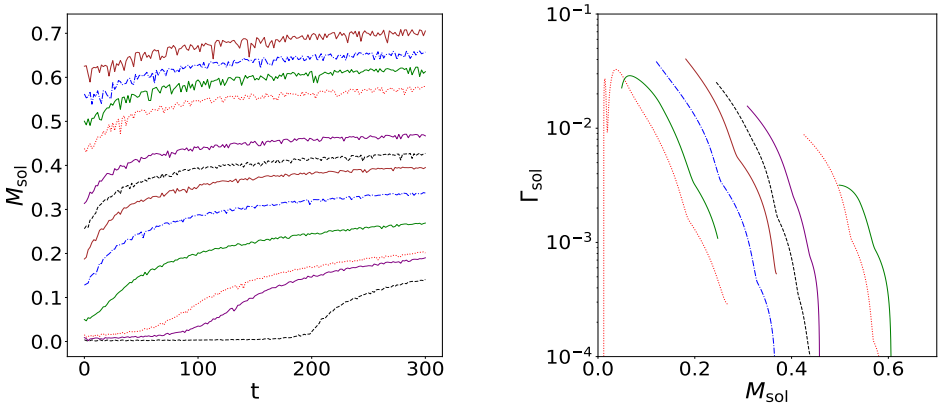

Figure 5.12. *Left panel:* growth with time of the soliton mass $M_{\rm sol}(t)$, for a set of simulations with different initial conditions. *Right panel:* growth rate $\Gamma_{\rm sol}$ from these simulations shown as a function of $M_{\rm sol}$.

We show in Fig. 5.12 the growth with time of the soliton mass $M_{\rm sol}(t)$, for numerical simulations of the Schrödinger equation (3.5) with different initial soliton density $\rho_{0\rm sol}$. We measure $M_{\rm sol}(t)$ by counting the total mass within the radius $R_{\rm sol}$ from the highest density peak in the system. This provides a good proxy for $M_{\rm sol}$ as soon as a well-characterized soliton forms at the center of the halo.

We can see in the right panel that, when we start with an initial soliton $M_{\rm sol}(0) \gtrsim 0.05$, $M_{\rm sol}(t)$ typically shows an early fast growth over a few dynamical times and next grows at a much slower rate. The initial stage presumably corresponds to a violent relaxation, where the low-energy levels of the halo are depleted as they mostly merge with the soliton, while the late stage corresponds to a slow accretion limited by the low occupation numbers of these low halo energy levels. The three bottom curves, where there is no initial soliton or a very small overdensity at the center, show the behavior found in Fig. 5.4. Until a long time, $t \sim 200$ in the case without initial central overdensity, there is no soliton supported by the self-interaction but only narrow stochastic peaks. However, they slowly grow and when one peak reaches the density threshold (5.16) a broad soliton supported by the self-interaction appears and next follows a similar evolution to that displayed by the other cases.

We show in the right panel the growth rate $\Gamma_{\rm sol}(t)$ as a function of the soliton mass. To compute $\Gamma_{\rm sol}$ we first fit the simulation curve $M_{\rm sol}(t)$ with splines and next we compute the time derivative (5.84) from this smooth curve. We plot the result as a function of $M_{\rm sol}(t)$, to see whether the dynamics reach a scaling regime where the growth rate only depends on the soliton mass (which also defines the halo mass as $M_{\rm halo} = M_{\rm tot} - M_{\rm sol}$). We can see that this is not the case and the growth rate at late times still depends on the initial conditions. This is thus different from the scaling regime found in numerical simulations Chan et al. (2022) for FDM (i.e. without self-interactions). Another difference is that the solitons displayed in Fig. 5.12 always grow, whereas in Chan et al. (2022) small solitons evaporate. Note that in our simulations the self-interactions indeed dominate in the central region. However, all cases follow the same pattern. The growth rate steadily decreases with time (while $M_{\rm sol}$ grows increasingly slowly). This falloff may be understood from the increasingly large gap between the soliton frequency ω_0 and the halo frequencies ω_j above the increasingly large cutoff $E_{\rm coll}$, shown in Fig. 5.11, and the low occupation numbers of the lower energy states where resonances with the soliton are possible. The leftmost red-dotted curve, which starts with the lowest central overdensity and mass, starts with a very low growth rate and oscillations, before reaching the same pattern as the other cases. As explained above, this is because before the threshold (5.16) is reached there is no self-interaction supported soliton and the central region is dominated for a long time by narrow stochastic peaks, with a size set by the de Broglie wavelength.

5.4.6 Halo with a cuspy density profile

We now consider the growth of the central soliton in the case of the cuspy halo studied in Section 5.3. We use the same approximation (5.82) for the potential $\bar{\Phi}$ and the energy cutoff (5.83) for the removal of the low energy levels.

As seen in Fig. 5.13, we recover the flat potential $\bar{\Phi}$ over the extent of the soliton, somewhat deeper than the initial halo potential. The gap between the ground-state frequency ω_0 and the lowest levels ω_j above the threshold $E_{\rm coll}$ is not as large as in Fig. 5.11, even though the ratio $M_{\rm sol}/M_{\rm halo} \simeq 0.05$ is about the same. This is because

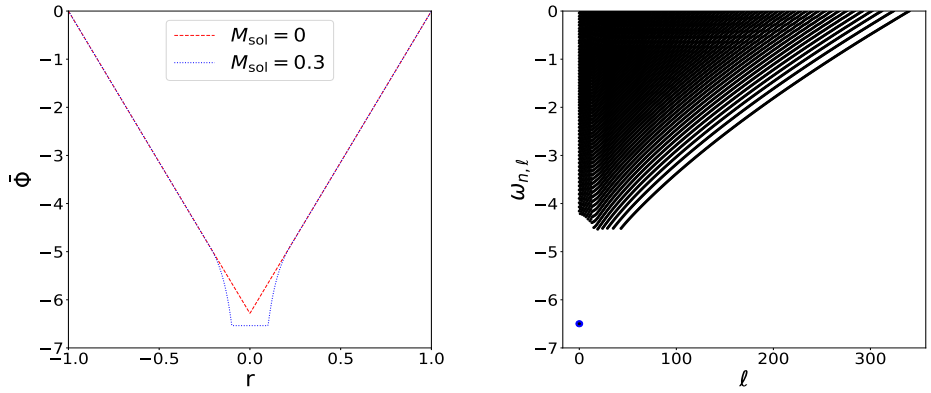

Figure 5.13. Potential $\bar{\Phi}$ and renormalized frequencies ω_j as in Fig. 5.11, but for a cuspy halo and a soliton mass $M_{\rm sol} = 0.3$.

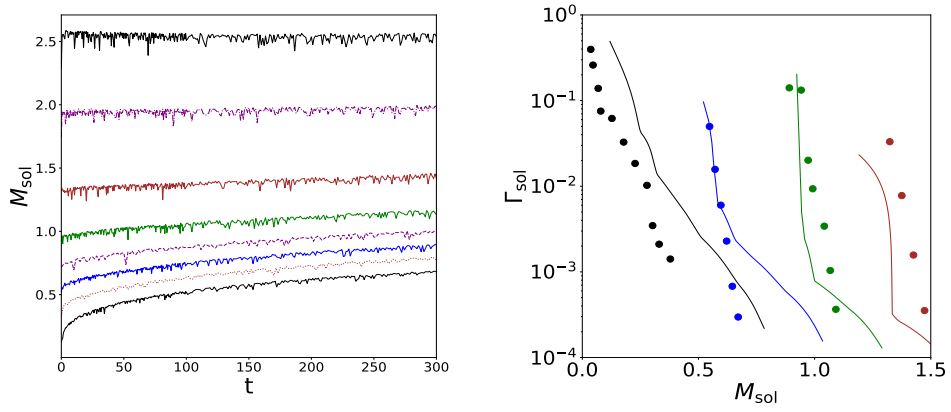

Figure 5.14. Growth with time of the soliton mass $M_{\rm sol}(t)$ (left panel) and growth rate $\Gamma_{\rm sol}$ as a function of $M_{\rm sol}$ (right panel), as in Fig. 5.12 but for a cuspy halo. The dots are the theoretical predictions.

the cuspy initial density profile means that low-energy levels initially contain a greater relative fraction of the total mass of the system. Therefore, a smaller fraction of them is needed to make up the growing soliton mass. As seen in Fig. 5.13, the lowest energy levels above the threshold $E_{\rm coll}$ now have $|\omega_j| > |\omega_0|/2$. Therefore, the Dirac factor $\delta_D(\omega_{01}^{23})$ in Eq.(5.80) is no longer always zero. The soliton mass can grow through the interaction with two low-energy levels $-4.5 \lesssim \omega_2, \omega_3 \lesssim -3.5$ and a high energy level $\omega_1 \simeq 0$. However, for higher solition mass E_0 decreases while more low-energy levels are depleted, within the approximation (5.83), so that the gap increases and eventually the Dirac factor $\delta_D(\omega_{01}^{23})$ always vanishes.

We show in Fig. 5.14 the growth with time of the soliton mass. As for the flat-core halos displayed in Fig. 5.12, except for this highest-mass case, the soliton always grows, with a growth rate that decreases with time. The total mass of the system is $2\pi \simeq 6$, so that the upper curve corresponds to a central soliton that makes about 40% of the total mass. In this case, the soliton mass seems to slightly decrease over the course of the simulation. Therefore, the numerical simulations suggest that the central soliton can slowly grow until it makes a large fraction of the total mass of the system, of the order of 40%.

We show in the right panel the growth rate as a function of the soliton mass. As for the flat-core halos displayed in Fig. 5.12, there is no clear sign of a scaling regime, as the growth rate still depends on the initial conditions at late times. The dots are the theoretical predictions from Eqs.(5.80) and (5.83), for the different initial conditions. In agreement with the lower panel in Fig. 5.13, at early times when the soliton has not grown too much, the gap between the renormalized soliton and halo frequencies ω_0 and ω_j is not too large and the simple energy-cutoff ansatz (5.83) allows for some resonances in the theoretical prediction (5.80). This gives a positive growth rate that shows a fast decrease with $M_{\rm sol}$ and vanishes beyond some mass threshold as the frequency gap becomes too large to allow for resonances. This provides a reasonably good agreement with the results from the numerical simulations, except close to this mass threshold and beyond. There, our ansatz underestimates the growth rate, which remains positive but steadily decreasing in the numerical simulations. As for the flat-core halos displayed in Fig. 5.12, this means that the halo low-energy levels are partially refilled by the interactions between higher-energy states. This cannot be captured by the simple ansatz (5.83) and is beyond the scope of this study. We leave a detailed study of this regime, where one needs to simultaneously follow the evolution of all halo excited states, to future works.

5.5 Conclusion

In this chapter we have discussed the emergence of solitons in self-interacting scalar dark matter models. In doing so, we have first chosen specific initial conditions for the initial halo in the form of a decomposition in eigenmodes of the Schrödinger equation in the presence of the Newtonian gravity due to the halo. This allows us to solve for the eigenmodes in the WKB approximation and then construct an initial state whose projection on this basis depends on random phases. The modulus of the coefficients of the decomposition reproduce the halo profile whilst the random phases create strong fluctuations in the initial wavefunction. We then let the system evolve under the influence of gravity and the self-interaction and solve the nonlinear Schrödinger equation.

The WKB approximation for the coefficients $a_{n\ell m}$ of the eigenmodes of the halo provides a reasonably good approximation of the target density profile by the averaged density $\langle\rho_{\rm halo}\rangle$. This could be expected as we focus on the semiclassical limit $\epsilon \ll 1$. However, the actual density profile $\rho_{\rm halo}$ always shows strong density fluctuations, of the same order as the mean density $\langle\rho_{\rm halo}\rangle$, because of the interferences between the different eigenmodes. The amplitude of these fluctuations does not decrease with ϵ, but their spatial width decreases as $\Delta x \propto \epsilon$.

When halos form on a scale of the order of the length r_a associated with the self-interactions (the cases $R_{\rm sol} = 0.5$ in our units), without initial soliton, a unique central soliton supported by the self-interactions quickly forms in a few dynamical times. It contains $30-50\%$ of the total mass. It also damps the initial density fluctuations, associated with interferences, within its radius. This holds whether we start with a flat or a cuspy halo profile. However, in the cuspy case, we find that a few narrow and very high-density spikes survive and wander inside the large central soliton.

If there is an initial soliton, it grows in a few dynamical times to reach a quasi-stationary state where initial fluctuations are also damped. Again, in the cuspy case a few narrow quantum-pressure supported spikes survive and wander inside this central

soliton.

Next, we considered halos with a size much greater than the self-interaction scale ($R_{\rm sol} = 0.1$ in our units). If the halo has a flat density profile, with density fluctuations of order unity, it takes a long time for a central soliton supported by the self-interactions to appear, until the small-scale spikes on sizes of the order of the de Broglie wavelength grow and reach densities that are high enough to trigger the self-interactions. In contrast, if the halo has a cuspy density profile, the high density at the center leads at once to significant self interactions. This gives rise in a few dynamical times to a central soliton supported by the self-interactions. Again, the fluctuations are damped within this soliton. If there is an initial soliton, it slowly grows for many dynamical times.

We developed a kinetic theory to follow the evolution with time of the system for arbitrary profile (i.e., going beyond plane waves in an homogeneous system). For the quartic self-interaction $\lambda_4\phi^4$ that we consider in this chapter, which leads to an effective quadratic pressure $P \propto \rho^2$ in the nonrelativistic limit, we obtain a kinetic equation that is similar to the kinetic equation of four-wave systems. To estimate the soliton growth rate, we further simplify the theory by taking a simple ansatz for the halo excited modes, assuming that they keep their initial occupation numbers in an adiabatic fashion, except for the low-energy levels that are depleted below a threshold $E_{\rm coll}$ to build the soliton. This allows us to compute the soliton growth rate at once, for a given soliton and halo mass, without following the precise evolution with time of all occupation numbers. For a cuspy halo, this provides a reasonably good prediction for the growth rate $\Gamma_{\rm sol}$ at early times. This simple ansatz breaks down for large $M_{\rm sol}$, and for a flat halo, because it does not follow the replenishing of the low-energy excited states and predicts an abrupt end of the soliton growth as there are no more possible resonances.

To improve this theoretical prediction, we would need to go beyond the energy-threshold ansatz and use the kinetic theory to follow the simultaneous evolution of all occupation numbers. We leave such a task to future works.

All solitons that are lighter than 40% of the total mass of the system keep slowly growing until the end of our numerical simulations, albeit at an increasingly slow rate. Therefore, our results suggest that the soliton mass observed at a given time depends on the past history of the system and can make up a significant fraction of the total mass of the system.

In a cosmological context, these results suggest that, in scalar-field dark matter scenarios with repulsive self-interactions, a soliton with about half of the total mass forms when overdense regions first collapse just above the Jeans mass. These solitons should then survive as the halos grow by accretion or mergings. The solitons should also grow in the process by accretion or direct mergings of solitons. The absence of clear relation between the halo and soliton masses suggests that the complex hierarchical formation process of cosmological halos will lead to a large scatter for the mass of the soliton at fixed halo mass, depending on the assembly history of the system. We leave a detailed investigation of this point to future works, using cosmological simulations.

Chapter 6

Solitons and halos for truncated self-interacting scalar dark matter

This chapter explores the formation and evolution of solitons within extended halos. Our investiagation centers around a bounded potential described by the cosine model, which is introduced in Section 2.8 supplemented by the opposite case, an unbound potential. Similar to the preceding Chapter 5, our analysis focuses mainly on the semiclassical regime. In this limit, the quantum pressure is significantly smaller in comparison to the self-interactions. To carry out our study, we follow exactly the same procedure described in Chapter 5. Therefore, we use initial conditions derived from the WKB approximation for the eigenfunction coefficients of the halo and we employ the numerical method described in Chapter 4. For a comprehensive understanding of the WKB approximation and the details of the procedure, please refer to Chapter 5 and for detailed explanations and further information of the numerical procedure to Chapter 4.

The primary reasons for exploring these scenario are:

1. The cosine model: The simulations conducted in this chapter are aimed at exploring the characteristics of the cosine model. While we will make an approximation of this model and supplement the study with an incorporation a truncated potential, the simulations will provide valuable insights and clues regarding the behaviour and phenomenology of solving the actual potential. By studying the simplified cosine model, we can gain a better understanding of the underlying dynamics and potentially apply this knowledge to the more complex real potential.

2. Explore new phenomena: This scenario presents an opportunity to study new phenomena that give rise to novel equilibria and dynamics. This opens up possibilities to study soliton transitions and how they manifest in this model. These findings may have significant implications for understanding astrophysical systems. Specifically, in the context of galaxies, very massive ones can be linked to the FDM regime, while below a certain threshold, the balance between self-interactions and gravity becomes applicable to satellite galaxies. On the other hand, smaller galaxies exhibit a balance between quantum pressure and gravity. These simulations could shed light on the mechanisms that govern their equilibrium and dynamics.

3. Comparisons with other dark matter models: By considering this potential, we aim to extend our understanding beyond the quartic model and Fuzzy dark matter. Doing so, we can establish a connection and facilitate comparisons between them.

This chapter is organized as follows: In the first part, Section 6.1, we provide a recap of the cosine model and the initial conditions of the numerical simulations. Subsequently in Section 6.2, we discuss the emergence of solitons in flat halos in the proxy Model A, followed by Section 6.3, where we explore flat halos in the second potential, Model B. Finally, in Section 6.4 we conclude the chapter by summarizing our findings.

6.1 The cosine scenario

Axions have been extensively studied as potential candidates for dark matter. In the case of the QCD axion, which arises from the breaking of the Peccei-Quinn symmetry, the associated potential term is non-perturbative and exhibits periodicity. This periodicity is a fundamental characteristic of axions and axion-like particles, where the axion field can be understood as a Goldstone mode originating from a globally broken symmetry. The potential terms for these scalar or pseudo-scalar fields retain a discrete U(1) symmetry and arise either from non-perturbative effects related to the symmetry or from soft breaking terms prior to the symmetry-breaking phase. In most cases, these give rise to cosine-like potentials in the same spirit of the scenarios that we consider in this chapter.

6.1.1 Equations of motion

Our direction is to investigate the formation of solitons within extended halos. These small-scale structures are subjected to the dynamics governed by the Schrödinger–Poisson system (2.38)-(2.39), as we have discussed in Section 2.5.1. Similar to our approach in Chapter 5, we use the dimensionless quantities (5.9). This gives the dimensionless Schrödinger - Poisson equations,

$$i\epsilon\frac{\partial\tilde{\psi}}{\partial\tilde{t}} = -\frac{\epsilon^2}{2}\tilde{\nabla}^2\tilde{\psi} + (\tilde{\Phi}_{\rm N} + \tilde{\Phi}_{\rm I})\tilde{\psi}, \tag{6.1}$$

$$\tilde{\nabla}^2\tilde{\Phi}_{\rm N} = 4\pi\tilde{\rho}, \tag{6.2}$$

with the now familiar ϵ parameter Eq.(5.6). We recall that these parameters measure the relevance of wave effects in the system, such as interferences or the effect of the quantum pressure. As usual, $\tilde{\Phi}_{\rm N}$ denotes the dimensionless gravitational potential and $\tilde{\Phi}_{\rm I}$ is the dimensionless non-relativistic cosine potential given by,

$$\tilde{\Phi}_{\rm I}(\tilde{\rho}) = \frac{8\lambda}{\gamma}\left(1 - \frac{2J_1\left(\sqrt{\tilde{\rho}\gamma}\right)}{\sqrt{\tilde{\rho}\gamma}}\right), \quad \text{with} \quad \lambda = \frac{1}{\mathcal{G}_N\rho_a L_\star^2} \quad \text{and} \quad \gamma = \rho_\star/\rho_b \tag{6.3}$$

As explained in Section 2.8 the potential (2.94) exhibits different behaviours at low and high densities. At low densities, it follows a linear relationship with ρ (2.96), resembling the quartic potential (2.86). Conversely, at high densities, the self-interaction potential approaches a finite value (2.97).

To accommodate these distinct characteristics, we simplify the model and we represent the potential as a piecewise function defined in two parts. This allows us to incorporate a linear portion in ρ and a constant portion. Therefore, to explore all the possibilities, we will examine two distinct models.

6.1.1.1 Model A

The first model is formulated straightforwardly, featuring initially linear in ρ followed by a second part where the potential assumes a finite value defined by $\lambda\tilde{\rho}_c$. Thus, the Model A reads,

$$\tilde{\Phi}_{\mathrm{I,A}}(\tilde{\rho}) = \begin{cases} \lambda\tilde{\rho} & \text{if,} \quad \tilde{\rho} < \tilde{\rho}_c \\ \lambda\tilde{\rho}_c & \text{if,} \quad \tilde{\rho} > \tilde{\rho}_c \end{cases} \tag{6.4}$$

with the critical density, $\tilde{\rho}_c$, where the potential changes is,

$$\tilde{\rho}_c = \frac{8}{\gamma} \tag{6.5}$$

In Appendix B we provide a variational approach to explore solutions with the Gaussian ansatz in this potential.

6.1.1.2 Model B

The second model, on the other hand, represents the opposite scenario. It begins with a constant value of 0, resembling to FDM, and then undergoes a change in its behaviour at the critical density $\tilde{\rho}_c$, transitioning to behave similar to the quartic model. The Model B is formulated as follows,

$$\tilde{\Phi}_{\mathrm{I,B}}(\tilde{\rho}) = \begin{cases} 0 & \text{if,} \quad \tilde{\rho} < \tilde{\rho}_c \\ \lambda(\tilde{\rho} - \tilde{\rho}_c) & \text{if,} \quad \tilde{\rho} > \tilde{\rho}_c \end{cases} \tag{6.6}$$

For convenience, we remove the tilde from the variables in the following discussion.

6.1.2 Initial conditions and simulation set up

To initiate our numerical study, we focus solely on the halo component and consider the initial wavefunction as ψ_{halo}. In this chapter, we exclude the soliton as an initial condition.

We follow the same procedure as in Section 5.1.5. Initially, we select specific initial conditions for the halo by decomposing it into eigenmodes of the Schrödinger equation, considering the influence of Newtonian gravity induced by the halo. Our desired target halo density profile in this chapter is the flat-core density profile. This is a reminder of the steps we follow to determine the initial conditions:

1. Using Eddington's formula (5.34), we derive the classical phase-space distribution $f(E)$.
2. The eigenmode coefficients $a_{n\ell m}$ are calculated using Equations (5.23) and (5.33).
3. The initial halo wavefunction is obtained from Equation (5.22).

The WKB approximation is utilized solely to determine the initial coefficients $a_{n\ell m}$, allowing us to establish random initial conditions that align with the desired target radial density profile. Subsequently, we allow the system to evolve by considering the effects of gravity and self-interaction, and we solve the nonlinear Schrödinger equation using the symmetrized split-step Fourier technique as described in Section 4.2.

In this study, we maintain the same parametrization as in Chapter 5. This ensures consistency and allows us to compare our results with the previous study. Consequently, we keep the size of the halo fixed at $R_{\rm halo} = 1$, and we choose $\epsilon = 0.01$ to focus on the semi-classical regime.

To determine the first parameter of the potential, λ, we follow the same approach as described in Section 5.1.4. We use the dimensionless radius $R_{\rm sol}$ to calculate the self-interaction coupling λ using the relation $\lambda = 4R_{\rm sol}^2/\pi$. This allows us to set the strength of the self-interactions in the model. In this study, we consider the same two cases for $R_{\rm sol}$: $R_{\rm sol} = 0.5$ and $R_{\rm sol} = 0.1$. The second parameter, ρ_c represents critical the density at which the self-interaction potential undergoes a transition. By exploring different values of ρ_c, we can investigate its impact on the formation and evolution of solitons within extended halos. Specifically, we consider three scenarios for ρ_c: one with a small value of $\rho_c = 0.5$, one with an intermediate value of $\rho_c = 3$, and one with a large value of $\rho_c = 100$. These different choices for ρ_c allow us to examine how changes in the density where the potential undergoes a change affect the dynamics.

We examine these set of parameters in the two models, Model A and Model B, that we have defined previously. By systematically varying the parameters $R_{\rm sol}$ and ρ_c in our study, we aim to understand how these choices influence the formation and evolution of solitons within extended halos. This analysis will provide valuable insights into the role of these parameters in shaping the properties of solitons and their interaction with the surrounding environment.

6.2 Halo with a flat-core density profile in Model A

In this section, we explore the effects of the self-interacting potential $\tilde{\Phi}_{\rm I,A}$, presented in Section 6.1.1.1, on the dynamics of the system. Thus, initial part of the self-interacting potential is linear with $\tilde{\rho}$ upto the critical density ρ_c where it takes a fixed value.

6.2.1 Large soliton radius, $R_{\rm sol} = 0.5$

As we have discussed in Section 5.1.4, when is $R_{\rm sol} = 0.5$, the scale of the self-interactions set by λ is of the order of the halo radius. In the context of cosmology, this choice represents the initial overdensities that are capable of collapsing slightly above the Jeans length.

6.2.1.1 Large critical density, $\rho_c = 100$

We first set $\rho_c = 100$ in Eq. (6.4). In this case, we put the threshold far away, at high density, which means that given the initial conditions of the cloud, it will primarily reside in the first part of the potential, characterized by its linear dependence on ρ. As a result, this set-up mimics the quartic potential and we observe that we get the same outcome as in Section 5.2.2.1. Specifically, Figure 6.1 presents the same features as in Figure 5.2.

We check that again within a few dynamical times, typically when $t \lesssim 8$, the system reaches a quasi-stationary state and the halo collapses in a soliton.This soliton remains relatively stable over time, with only slow changes in the maximum density and energy. The presence of the central equilibrium soliton is clearly evident in the density profiles

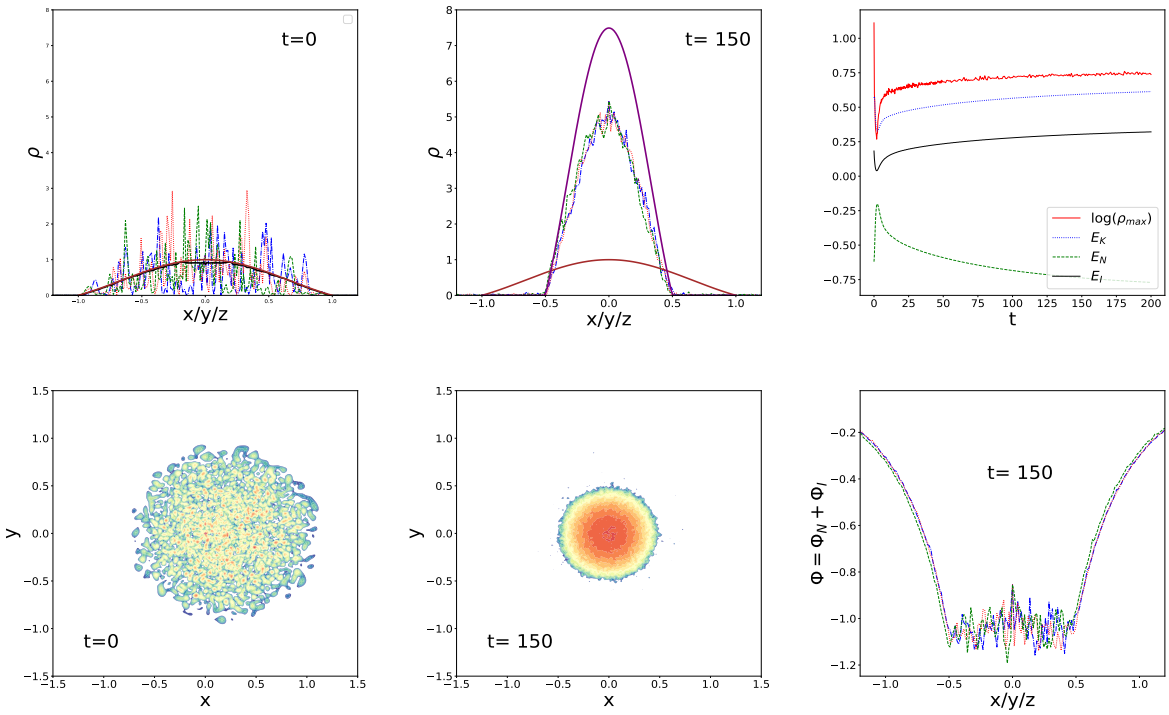

Figure 6.1. [Model A, $R_{\rm sol} = 0.5$, $\rho_{0\rm sol} = 0$, $\rho_{\rm c} = 100$.] *Upper left panel:* Initial density ρ along the x (blue dash-dot line), y (red dotted line) and z (green dashed line) axis running through the center of the halo. The smooth brown solid line is the target density profile (5.35) and the black wiggly solid line is the averaged density $\langle\rho_{\rm halo}\rangle$ of Eq.(5.24) (they can hardly be distinguished in the figure). There is no central soliton in this initial condition. *Upper middle panel:* density profile along the x, y and z axis that run through the point $\vec{r}_{\rm max}$ where the density is maximum, at time $t = 150$. The lower brown solid line is the initial target density profile as in the upper left panel, while the upper purple solid line is the density profile of a soliton (5.14) that would contain all the mass of the system. *Upper right panel:* evolution with time of the maximum density and of the kinetic, gravitational and self-interaction energies. *Lower left panel:* initial density profile on the 2D (x, y) plane at $z = 0$. *Lower middle panel:* density profile at time $t = 150$ on the 2D (x, y) plane centered on $\vec{r}_{\rm max}$. *Lower right panel:* total potential $\Phi = \Phi_N + \Phi_I$ at $t = 150$, along the x, y and z axis passing through $\vec{r}_{\rm max}$.

shown in the middle column. Its radius is fixed at $R_{\rm sol} = 0.5$. The lower right panel provides a visual representation of hydrostatic equilibrium, as expressed by equation (5.12). This equilibrium is evident from the constant plateau observed in the total potential, $\Phi = \Phi_N + \Phi_I$. However, small oscillations may occur due to the presence of excited halo modes crossing the central region. Beyond the soliton radius, the density rapidly decreases, resulting in a diminished influence of Φ_I compared to Φ_N. As a result, the smooth gravitational potential characterized by a $-1/r$ shape dominates in this region.

By comparing the left and middle columns, we can clearly observe the collapse of the initial halo onto the soliton with half the original radius. This comparison highlights the depletion of the highly fluctuating halo and the emergence of a central soliton characterized by a high density.

6.2.1.2 Intermediate critical density, $\rho_c = 3$

We now discuss the intermediate case, where $\rho_c = 3$ in the Model A given by Eq.(6.4). Figure 6.2 presents the results obtained for this simulation. In this set-up, the halo initially

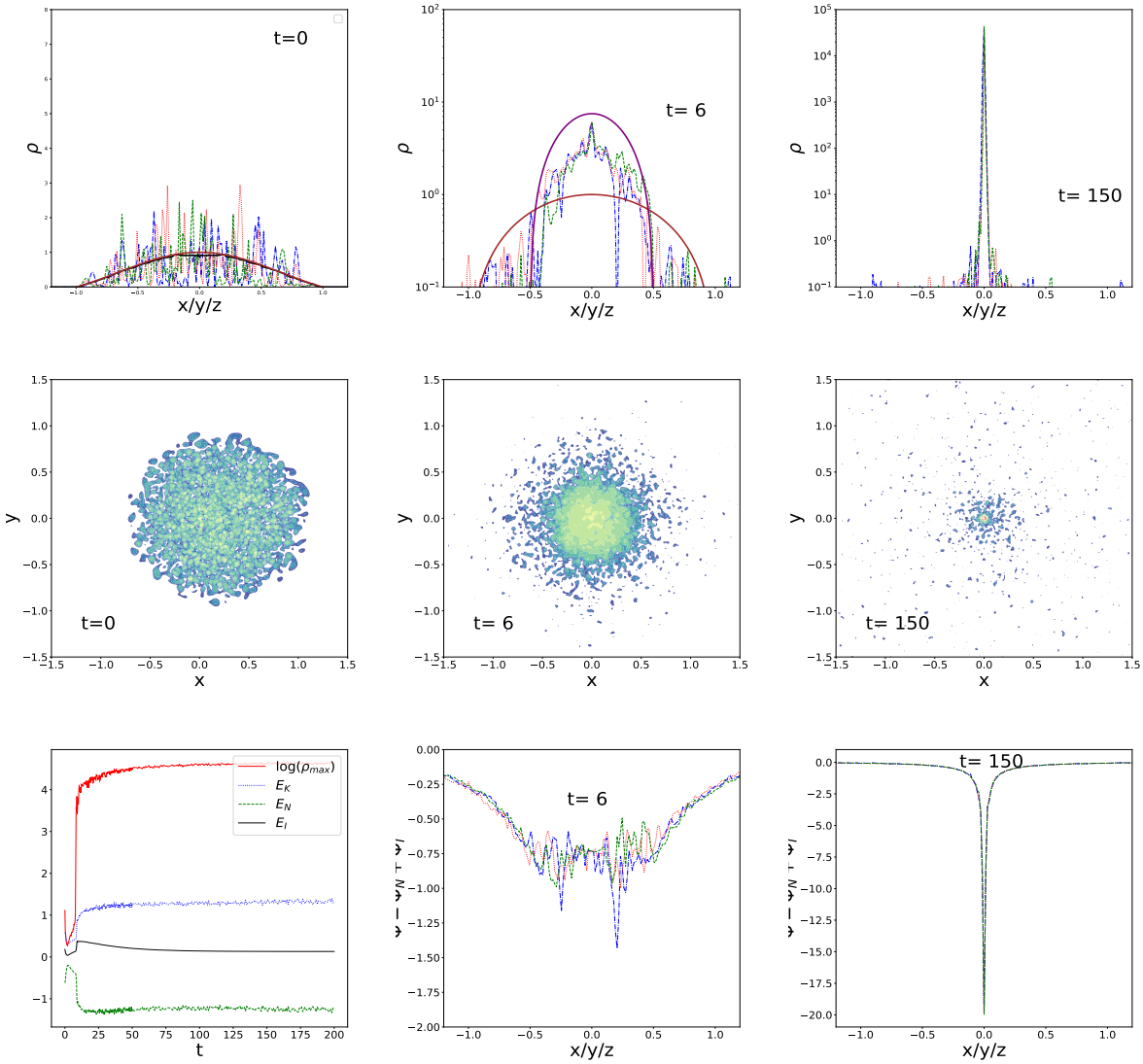

Figure 6.2. Same labels as Figure 6.1 but for Model A with $R_{\rm sol} = 0.5$ and $\rho_{\rm c} = 3$.

resides in the linear part of the potential, similar to the quartic potential. However, the threshold at which the potential changes its shape is now closer compared to the previous case. This proximity has significant implications.

As shown in Figure 6.2, the halo initially appears with strong fluctuations, associated with the superposition of incoherent modes, similar to what we have observed before. However, at $t = 6$, something interesting happens. We can observe the fast emergence of self-interacting soliton within the halo leading to a coherent state. This occurrence is not surprising since under these conditions, the halo has the potential to form self-interacting solitons.

Later, specifically at $t = 20$, the halo reaches densities where the self-interaction potential is a constant value. As a consequence, the self-interacting soliton collapses leading to a formation of a unique FDM spike. The size of this spike is determined by the value of ϵ, which is set at $\epsilon = 0.01$ in this case. This simulation shows a rapid evolution from the self-interacting regime to the FDM-like regime. The rapidity of this transition can be attributed to the fact that FDM peak originates from a coherent state. Unlike

other scenarios where the peak may emerge gradually from fluctuations, the presence of a coherent state accelerates the transition process. The coherent state serves as a well-defined starting point for the formation of the FDM peak, allowing it to quickly manifest and establish its dominance within the system.

6.2.1.3 Small critical density, $\rho_c = 0.5$

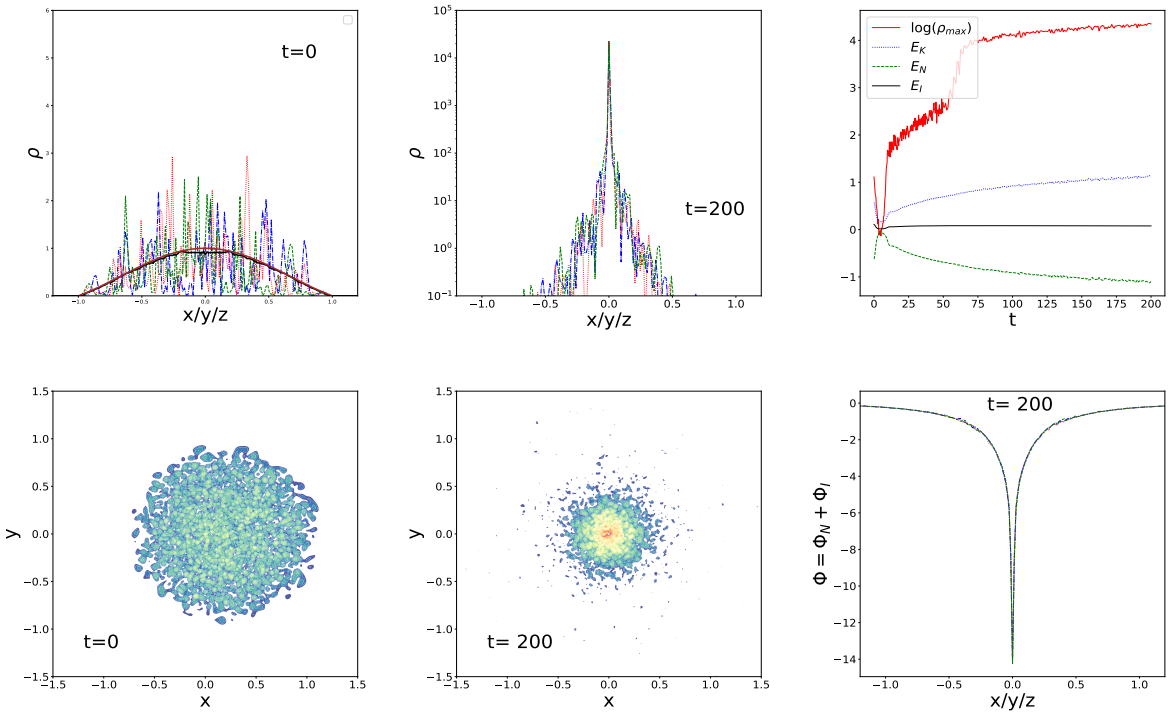

Figure 6.3. Evolution of a flat system in Model A with $R_{sol} = 0.5$ and $\rho_c = 0.5$. (Same labels as Fig.6.1)

In this particular case, the critical density is set at $\rho = 0.5$ in Eq.(6.4). Consequently, almost the entire self-interacting potential domain assumes a constant value. Despite this uniformity, we can observe a fascinating dynamic unfolding.

As seen in Figure 6.3, the final outcome of this simulation is a dominant FDM-like peak that reaches a quasi-stationary state around $t \sim 75$ dynamical times. Unlike the previous case discussed in Section 6.2.1.2, no self-interacting soliton is formed here due to the constant nature of the self-interacting potential. Consequently, the rapid formation of the FDM peak, as observed in the previously, does not occur. Instead, the growth of the maximum halo density is characterized by a noisy competition between different peaks associated with incoherent modes of the halo. Note that the width of the FDM peak at lower densities looks wider in this simulation because it is surrounded by other small peaks within a halo-like envelope (like NFW).

6.2.2 Small soliton radius, $R_{sol} = 0.1$

We explore in this section scenarios where the scale of self-interactions is significantly smaller than the halo radius. For this purpose, we set $R_{sol} = 0.1$. In the cosmological

context, this choice corresponds to structures that form at later times, collapsing on a much larger scale than the characteristic length associated with the λ self-interactions. We continue investigating the three different thresholds for ρ_c, as we have done in the previous Section 6.2.1.

6.2.2.1 Large critical density, $\rho_c = 100$

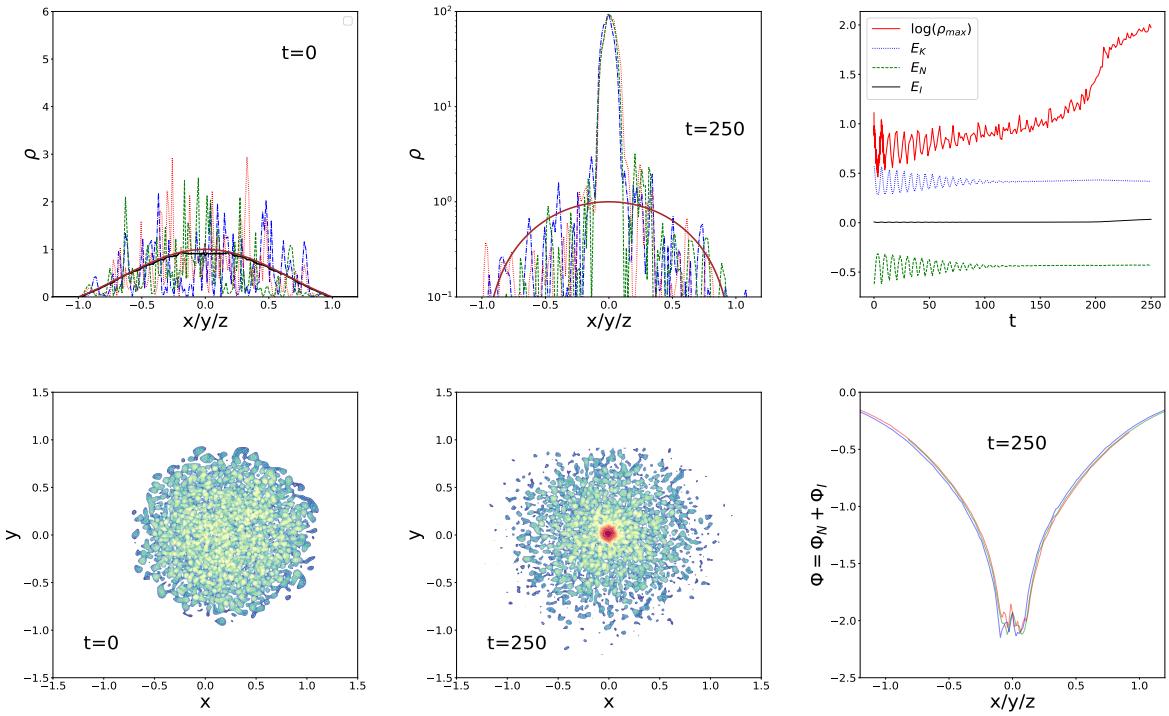

Figure 6.4. Evolution of a flat system in Model A with $R_{\rm sol} = 0.1$ and $\rho_c = 100$. (Same labels as Fig.6.1)

In this case, we set the threshold at high densities which leads to a configuration where the initial part of the self-interacting potential given by Eq.(6.4), linear with ρ is sufficiently large. This configuration prevents the system from reaching densities where the potential is constant. Therefore, the system will behave as in Section 5.2.3.1. If we examine the dynamics of this system, illustrated in Figure 6.4 , we find that it has similar characteristics to the case presented in the previous Section 5.2.3.1, as shown in Figure 5.4.

We observe that while the system remains dominated by FDM spikes for an extended period and appears nearly stationary, the slow evolution eventually leads one of these spikes to gradually grow. This growth persists until self-interactions come into play, resulting in the formation of a broad soliton of the size of $R_{sol} = 0.1$ governed by these interactions at $t \sim 200$. Consequently, there is a transition in the system from the FDM phase to a self-interacting phase embedded within the FDM halo. This transition may only occur after a considerable duration, far exceeding the dynamical time of the system, as the growth of central density peaks is very gradual until one of them surpasses the threshold and suddenly forms a distinct massive soliton.

6.2.2.2 Intermediate critical density, $\rho_c = 3$

Here, the critical density parameter of the self-interaction potential $\tilde{\Phi}_{\mathrm{I,A}}$ given by (6.4) is set at $\rho_c = 3$. Thus, densities above this critical value will experience a constant potential, preventing the formation of a self-interacting soliton governed by self-interactions. As illustrated in Figure 6.5, the dynamics of this system is characterized by the presence of a FDM peak that grows with fluctuations. As shown in the bottom left panel, the ρ_{max} during the simulation constantly grows, reaching the value of $\rho_{max} \sim 30$. This fluctuating halo has a FDM behaviour.

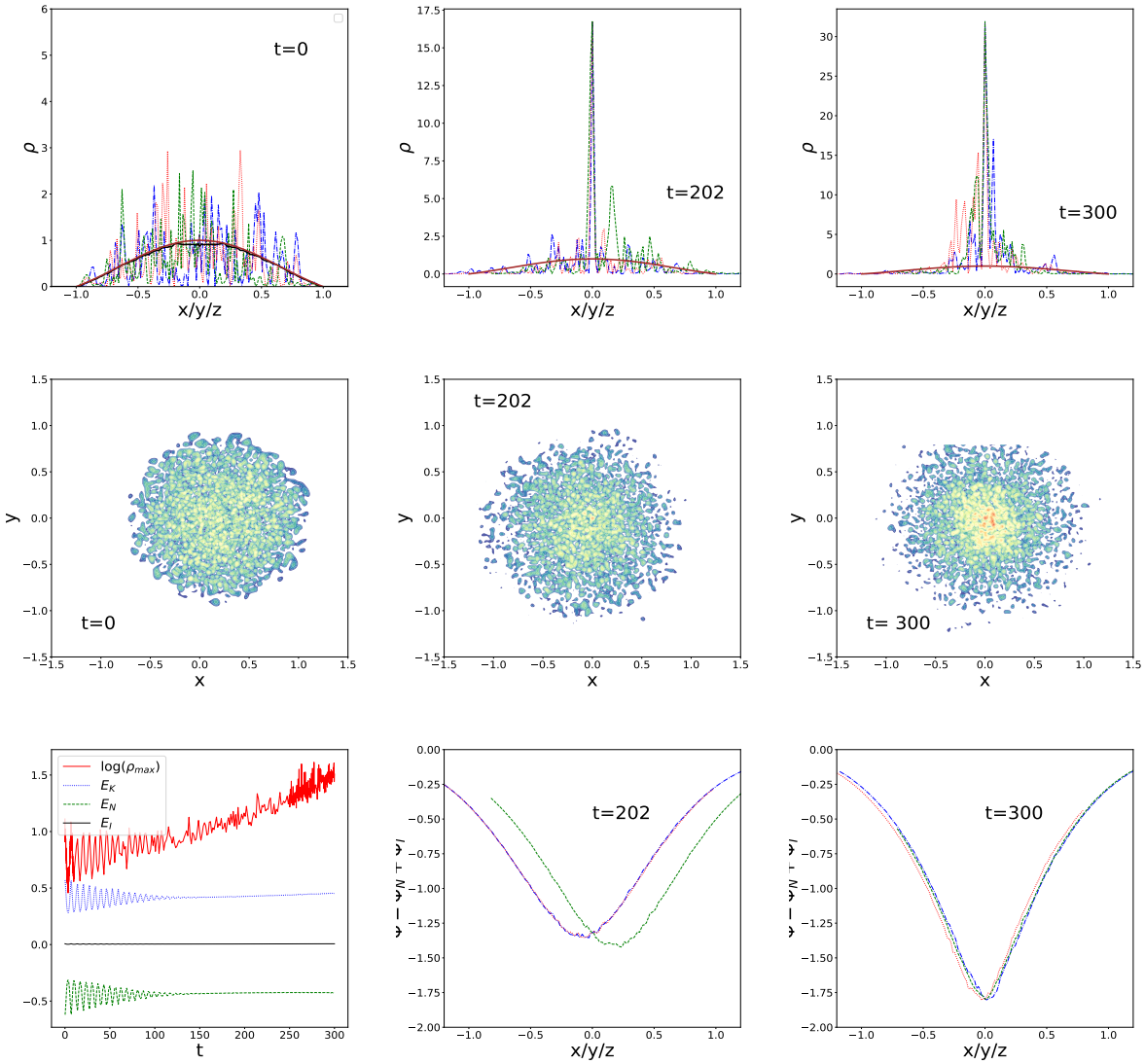

Figure 6.5. Evolution of a flat system in Model A with $R_{\mathrm{sol}} = 0.1$ and $\rho_c = 3$. (Same labels as Fig.6.1)

6.2.2.3 Small critical density, $\rho_c = 0.5$

In this case, the critical density for the change in the self-interaction potential $\tilde{\Phi}_{\mathrm{I,A}}$ given by Eq.(6.4) is set very low, at $\rho_c = 0.5$. Consequently, most of the domain of the potential takes a constant value fixed by $\lambda\rho_c$. As depicted in Figure 6.6, the halo fluctuates and the

dynamics of this system is characterized by the presence of an FDM peak that oscillates around $\rho_{max} = 8$. There is no hint of the dynamics being anything but FDM. This is in agreement with Chan et al. (2022).

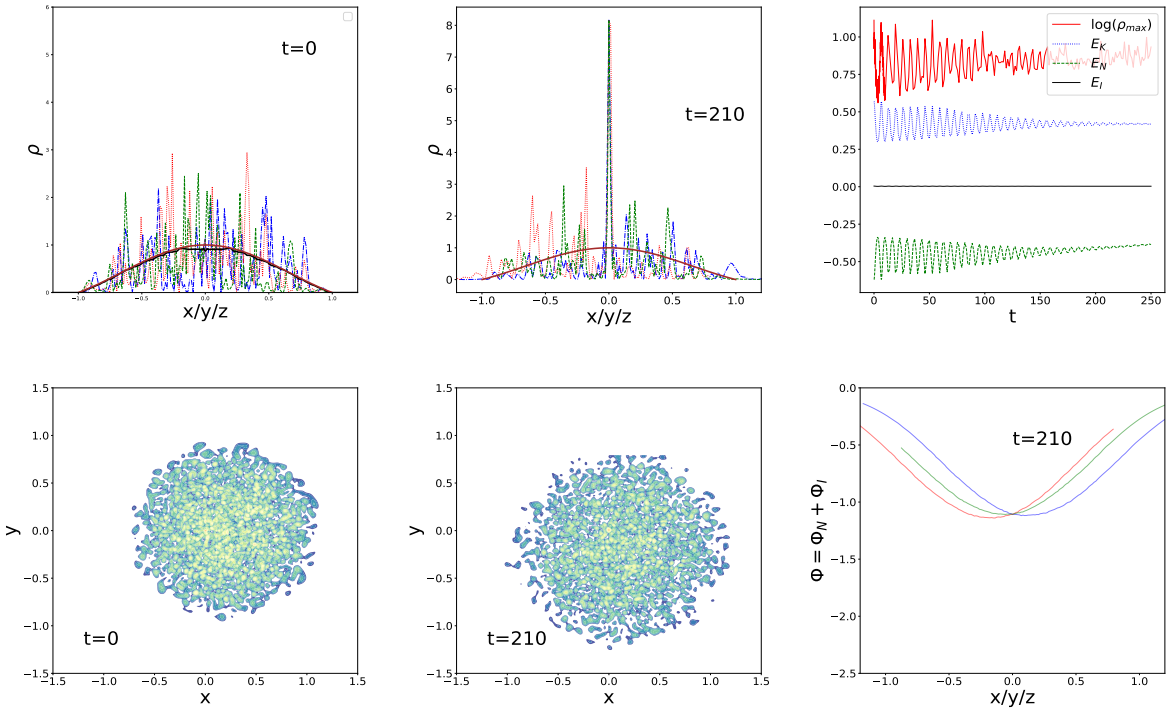

Figure 6.6. Evolution of a flat system in Model A with $R_{\rm sol} = 0.1$ and $\rho_{\rm c} = 0.5$. (Same labels as Fig.6.1)

6.3 Halo with a flat-core density profile in Model B

In this section, we investigate the impact of the self-interacting potential formulated in Section 6.1.1.2. Thus, the first part of $\Phi_{\rm I,B}$ given by Eq.(6.6) is set to zero, resulting in a FDM scenario. However, beyond the density threshold ρ_c, the potential grows, resembling the behaviour of the quartic model. We remark that this potential is no longer bounded and that we study this scenario to compare. We explore the same set of parameters as we did for Section 6.3.

6.3.1 Large soliton radius, $R_{\rm sol} = 0.5$

In this section we focus on scenarios where the scale associated with the λ self-interaction is of the size of the system. Thus, we keep the value $R_{\rm sol} = 0.5$, as in previous simulations.

6.3.1.1 Large critical density, $\rho_c = 100$

In this case, the self-interaction potential $\Phi_{\rm I,B}$ defined in Eq.(6.6) is zero up to $\rho_{\rm c} = 100$, where it recovers the behaviour of the quartic model. We illustrate in Figure 6.7, the outcome of the numerical simulation. Initially, the halo is dominated by strong fluctuations, associated with the superposition of incoherent modes, and a few rare high-density spikes

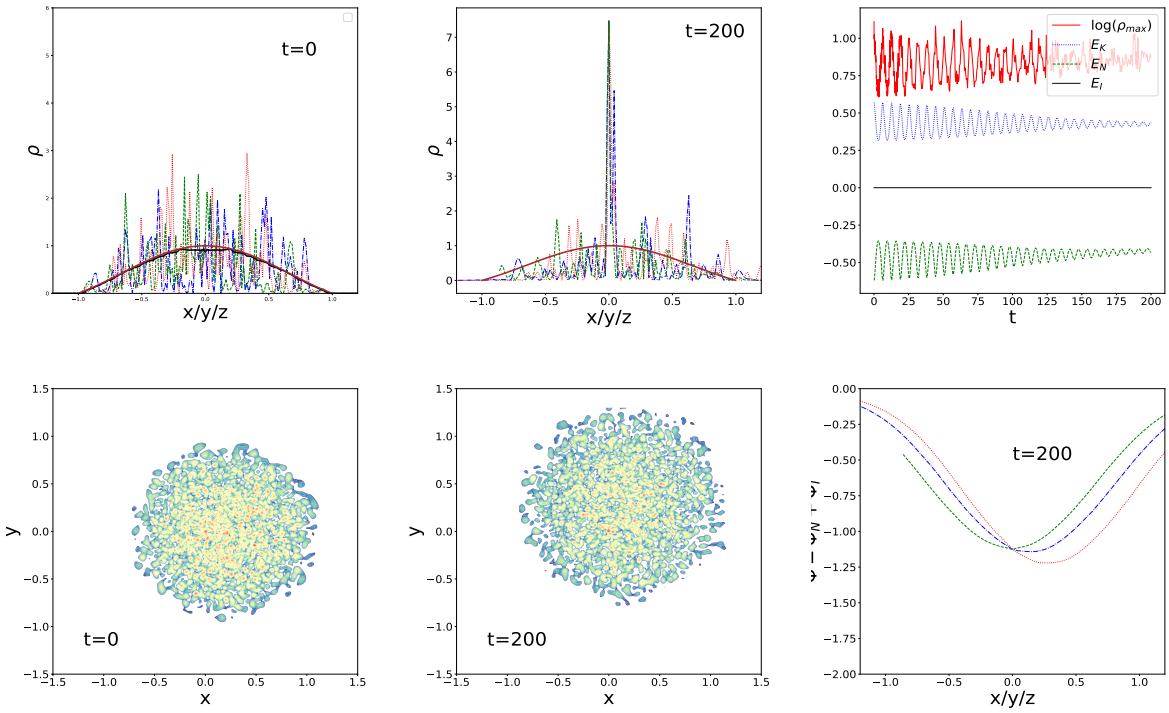

Figure 6.7. Evolution of a flat system in Model B with $R_{\rm sol} = 0.5$ and $\rho_{\rm c} = 100$. (Same labels as Fig.6.1)

that appear randomly. However, we observe that one of these high density peaks grows sufficiently to dominate over all other peaks and becomes stable, forming a "soliton" governed by the quantum pressure rather than the self-interactions. The size of the peak is of the order of $\Delta x \sim \epsilon = 0.01$. This is not surprising since, in this set-up the system is goberned by the quantum pressure, that is, by wave effects that appear on the de Broglie scale.

6.3.1.2 Intermediate critical density, $\rho_c = 3$

In this simulation, the function $\Phi_{\rm I,B}$ in Eq.(6.6) takes the critical density $\rho_{\rm c} = 3$. Therefore, the potential remains at zero in the first part, and beyond this threshold, it resembles to the quartic model. The results are illustrated in Figure 6.8. Initially, the halo displays strong fluctuations caused by the superposition of incoherent modes. Around $t \sim 25$, the center the halo experiences the second part of the self-interacting potential. At this point, the self-interactions are strong and come into play and initiate the formation of a soliton. Subsequently, the soliton remains approximately stationary. However, it is important to note that the shape of this soliton differs from previously observed ones. In this configuration, when $\rho < 3$, the value of $\Phi_{\rm I,B}$ is 0, meaning that no force is acting. Consequently, the soliton profile drops faster, resulting in a slightly smaller soliton.

6.3.1.3 Small critical density, $\rho_c = 0.5$

Here, we explore the behaviour of a system governed by the inverse potential given by Eq.(6.6). Specifically, when the critical density is set at $\rho_c = 0.5$. Thus, the potential takes on a shape similar to the quartic model throughout almost its entire domain. As

a consequence of this configuration, we witness the rapid formation of a self-interacting soliton as we can observe in Figure 6.9. This outcome aligns with our previous findings in Section 5.2.2.1, and Section 6.2.1.1. Specifically in Fig.6.1 and Fig.5.2.

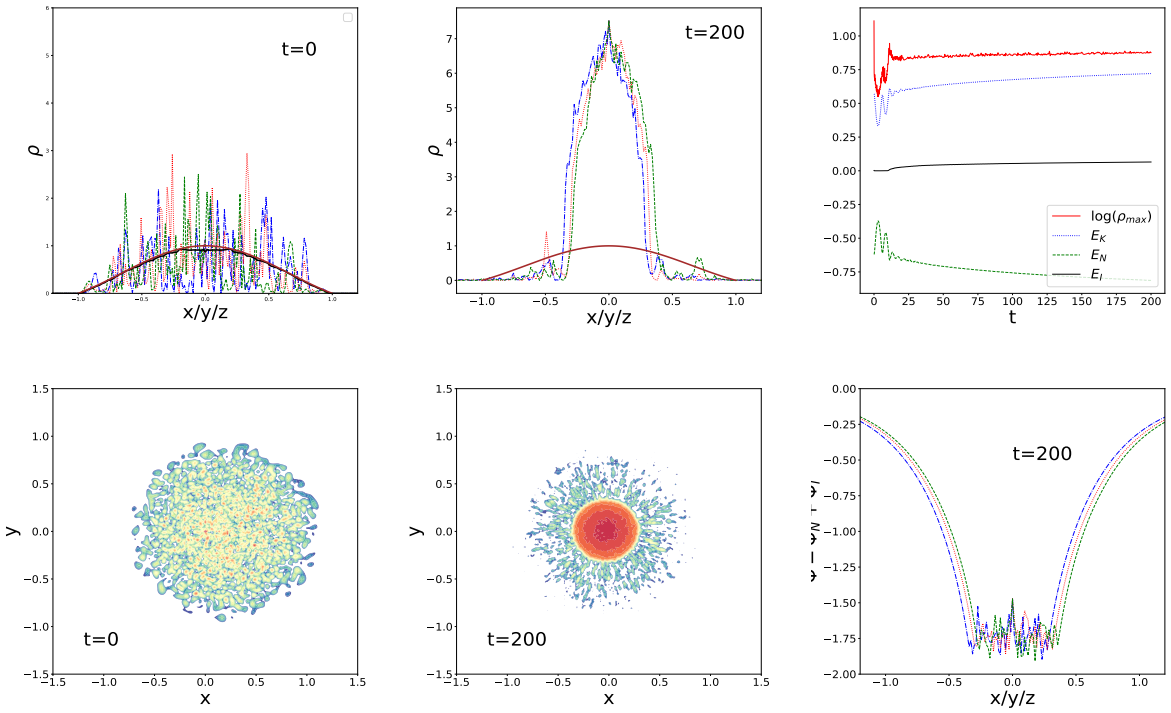

Figure 6.8. Evolution of a flat system in Model B with $R_{\rm sol} = 0.5$ and $\rho_{\rm c} = 3$. (Same labels as Fig.6.1)

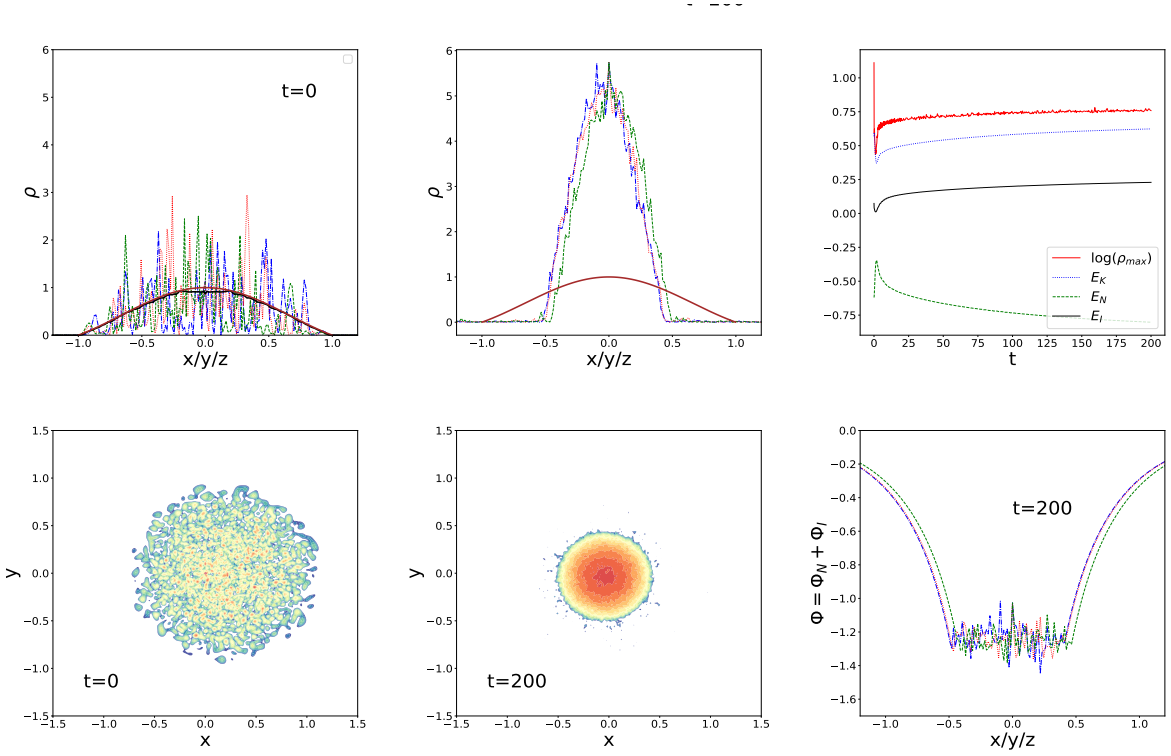

Figure 6.9. Evolution of a flat system in Model B with $R_{\rm sol} = 0.5$ and $\rho_{\rm c} = 0.5$. (Same labels as Fig.6.1)

6.3.2 Small soliton radius, $R_{\rm sol} = 0.1$

In this part, we shift our focus to scenarios where the radius associated with the self-interactions is significantly smaller than the radius of the halo. Thus, we take the value $R_{\rm sol} = 0.1$.

6.3.2.1 Large critical density, $\rho_c = 100$

In this case, we study a system that follows the inverse potential described by Equation (6.6), where the critical density is set to a high values, $\rho_c = 100$. The results depicted in Figure 6.10 reveal that initially, the halo displays significant fluctuations due to the combination of incoherent modes. However, as the simulation progresses, no distinct peak corresponding to FDM is formed up to the end of the simulation. Instead, during this time, the halo fluctuates and changes smoothly its shape by shrinking and stretching within the simulation box. These findings align with the conclusions of a study by Chan et al. (2022), who also investigated the evolution of FDM clouds and found that light solitons do not form under similar conditions.

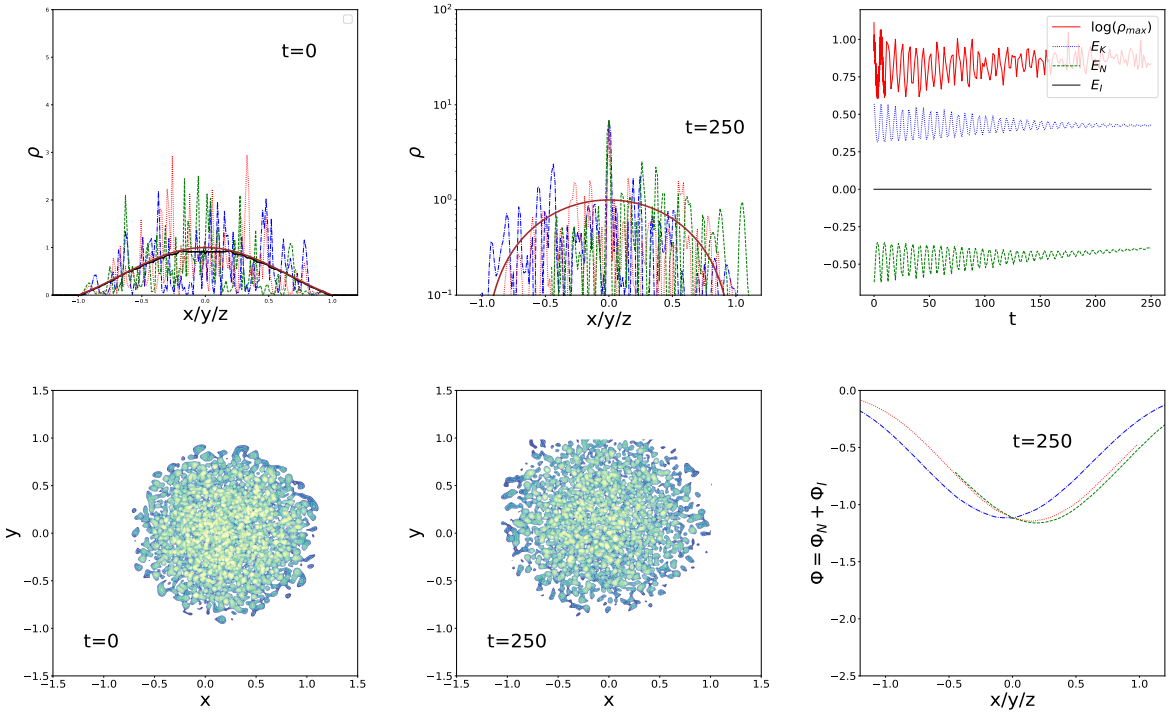

Figure 6.10. Evolution of a flat system in Model B with $R_{\rm sol} = 0.1$ and $\rho_{\rm c} = 100$. (Same labels as Fig.6.1)

6.3.2.2 Intermediate critical density, $\rho_c = 3$

In this specific simulation, we explore the behaviour of a system governed by the inverse potential described in Equation (6.6), with a critical density set to an intermediate value of $\rho_c = 3$. As shown in Figure 6.11, we find that the halo initially displays strong fluctuations due to the superposition of incoherent modes. However, as the evolution progresses, no

FDM peak forms. The halo instead continues to exhibit oscillatory dynamics, similar to the behaviour observed in the case with $\rho_c = 100$, presented in Figure 6.10. This finding is simply like the previous case, in agreement with Chan et al. (2022).

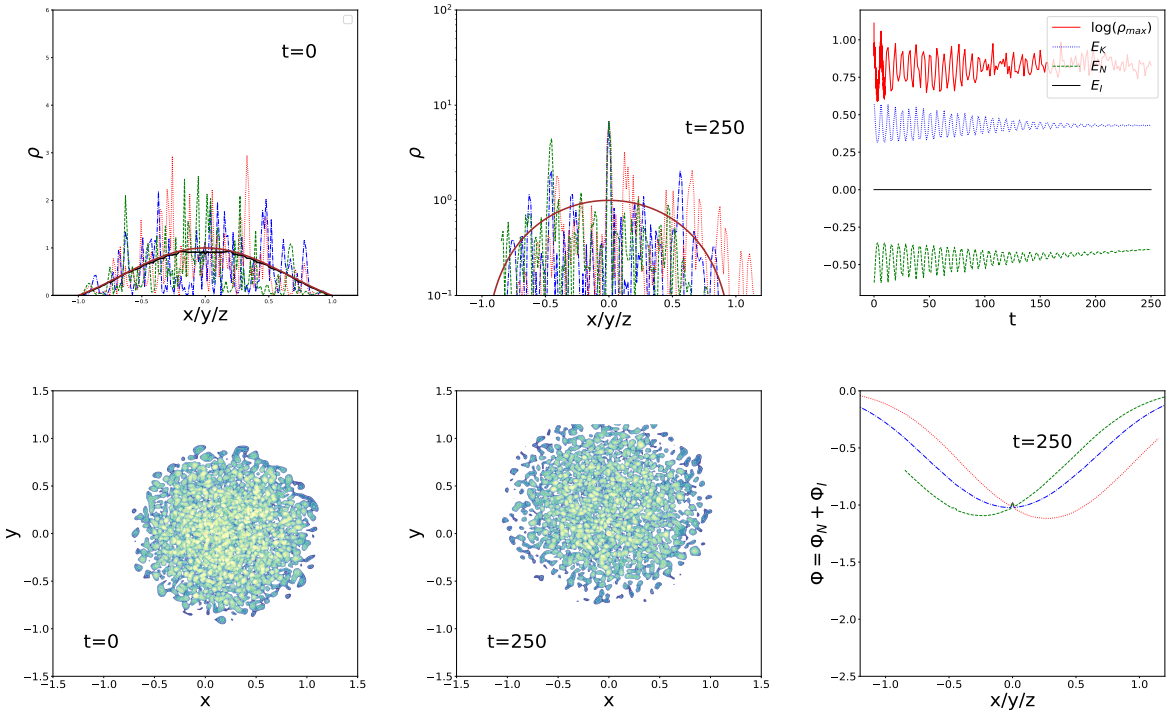

Figure 6.11. Evolution of a flat system in Model B with $R_{\rm sol} = 0.1$ and $\rho_{\rm c} = 3$. (Same labels as Fig.6.1)

6.3.2.3 Small critical density, $\rho_c = 0.5$

In this case, we investigate a system governed by the inverse potential described in Equation (6.6). We specifically focus on the scenario where the critical density is set to $\rho_c = 0.5$. This choice results in the self-interacting potential adopting a shape that closely resembles the quartic model across its entire range.

As a consequence of this potential configuration, we observe a prolonged dominance of FDM spikes in the system, giving the appearance of almost stationary behaviour. However, the slow evolution eventually leads one of these spikes to gradually grow, enabling the influence of self-interactions and resulting in the formation of a small soliton of radius $R_{\rm sol} = 0.1$ governed by these interactions. This transition from the FDM phase to the self-interacting phase, embedded within the FDM halo, occurs after a considerable duration that exceeds the dynamical time of the system. The growth of central density peaks is slow until one of them reaches the threshold and abruptly forms a distinct and massive soliton. The characteristics and behaviour of this soliton can be observed in Figure 6.12. This finding aligns with our previous observations which are illustrated in Figure 6.4 and Figure 5.4.

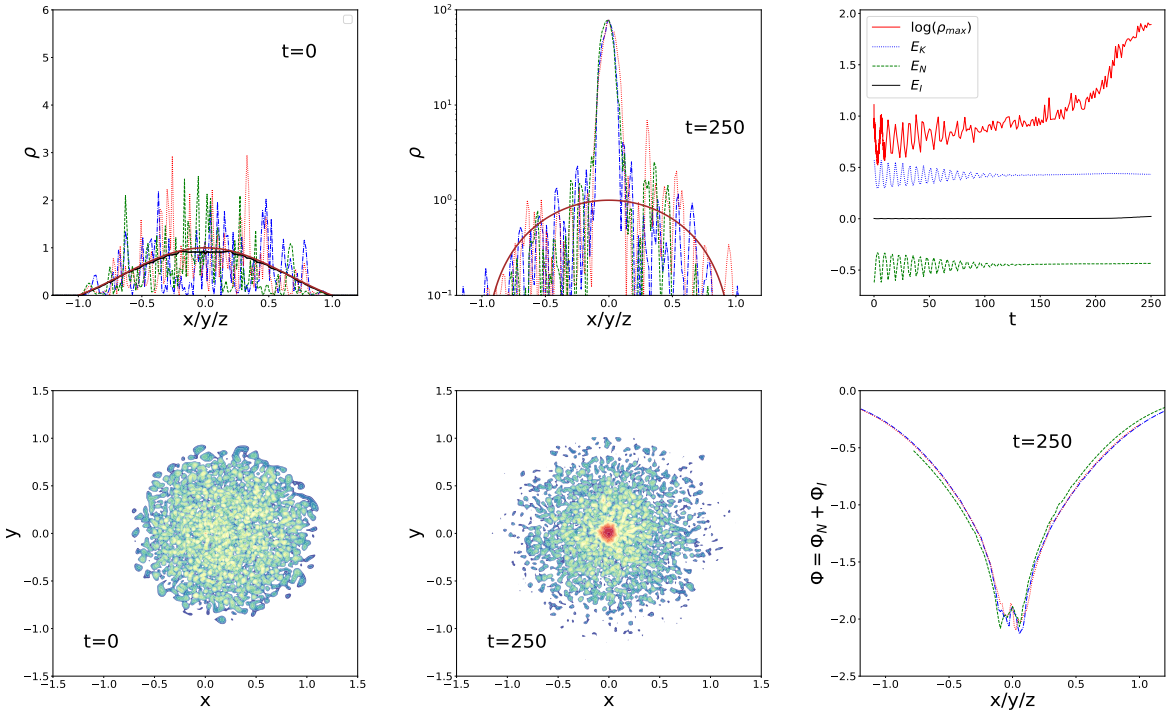

Figure 6.12. Evolution of a flat system in Model B with $R_{\rm sol} = 0.1$ and $\rho_{\rm c} = 0.5$. (Same labels as Fig.6.1)

6.4 Conclusion

In this chapter, our focus was on investigating the formation and evolution of solitons in two distinct truncated scalar dark matter models. The first model, referred to as Model A, discussed in Section 6.1.1.1, was based on an approximation of the bounded cosine potential. Additionally, in order to provide a comprehensive analysis, we also explored the contrasting scenario, which involved an unbounded potential, named as Model B, presented in Section 6.1.1.2.

As we did for Chapter 5, we started by selecting specific initial conditions for the halo, which involved decomposing it into eigenmodes of the Schrödinger equation in the presence of Newtonian gravity. This decomposition allowed us to construct an initial state with random phases, resulting in strong fluctuations in the wavefunction. The system was then allowed to evolve under the influence of gravity and self-interactions, following the nonlinear Schrödinger equation.

In Model A, we observed that when halos formed on a scale similar to the length associated with self-interactions, a central soliton supported by the self-interactions quickly emerged if the critical density had a high value as presented in Fig.6.1. The central soliton in this case accounted for a significant fraction of the total mass and reduced the initial density fluctuations within its region. This finding aligns with the results obtained in the previous Chapter 5 in Fig.5.2.

Additionally, when the critical density was at an intermediate level, we observed a fast transition from a soliton dominated by self-interactions to FDM peak as shown in Fig.6.2. The new phenomena that we observed is the collapse of the halo into a soliton

and subsequently into an FDM peak which was the final state of the simulation. Similarly, the final outcome when the critical density was at small values, a FDM peak was also observed in Fig.6.3. However, in this later case, the FDM peak took longer to form. This suggests that the formation of the FDM peak is more efficient when the initial condition is a coherent state, as to the soliton state. So the soliton governed by self-interactions played a role in triggering the formation of the FDM peak, collapsing onto it.

In Model B, we observed that when halos formed on a scale similar to the length associated with self-interactions, a central soliton supported by the self-interactions rapidly emerged, particularly when the critical density was small as shown Fig.6.9. This finding is consistent with the results obtained in the precedent Chapter in Fig.5.2 as well as in Model A in Fig.6.1. However, when the critical density was at intermediate levels, a soliton governed by self-interactions still formed, as presented in Fig.6.8, but its shape exhibited slight variations compared to the previous cases. In particular, the tail profile of the soliton exhibited a faster drop-off. This can be attributed to the absence of a self-interacting potential, which means that no force is acting in that region. As a result, the soliton profile decreases more rapidly and sharply in this scenario. This can lead to relevant consequences in astrophysics. When the critical density in Model B was very high, no soliton formation was found, Fig.6.7. This aligns with the results founds in Chan et al. (2022) where FDM halos were studied and light solitons evaportate, which means that other mechanisms are needed to form them.

We also explored halos with sizes significantly larger than the scale of self-interactions. In the case of Model A, when a large critical density was considered, we observed that it took a substantial amount of time for a central soliton supported by self-interactions to form as seen in Fig.6.4. Initially, the halo exhibited a flat density profile with fluctuations of order unity. However, over time, the small-scale spikes within the halo gradually grew and reached densities high enough to trigger self-interactions. This led to the emergence of a self-interacting soliton.

For the cases with intermediate, Fig.6.5, and small critical densities, Fig.6.6, we observed a continuous flat density profile within the halo, accompanied by noisy fluctuations that oscillated. Additionally, a FDM peak appeared in the center of the halo, exhibiting oscillatory behaviour. Notably, in the case of the small critical density, the simulations reached a quasi-stationary state, as evident from the maximum density fluctuations and overall potential. However, in the intermediate case, there was an hint that the maximum density was still increasing, suggesting ongoing dynamics in the system.

Moving on to Model B, we found that for both large, Fig.6.10, and intermediate critical densities, Fig.6.11, the halo exhibited fluctuations of the order of unity and it did not collapse into a fuzzy dark matter peak. This observation aligns with the findings of Chan et al. (2022). Furthermore, when the critical density was too small, Fig.6.12, we observed similar dynamics in Fig.5.4 and Fig.6.4, where the initial flat density profile with fluctuations took a considerable amount of time for a central soliton supported by self-interactions to form. This occurred when the small-scale spikes reached sufficiently high densities due to their growth and triggered self-interactions.

Chapter 7

Conclusions

In this thesis, we have conducted both numerical and analytical investigations on different scalar field dark matter models within the non-relativistic regime. This regime is relevant for large-scale structure and astrophysical structures. Therefore, the dynamics are described by the Schrödinger–Poisson equations.

In Chapter 2 we provide a comprehensive overview of the derivation of the Schrödinger-Poisson equations, and we present the fundamental equations that govern the theory.

In Chapter 3, we employed semi-analytical techniques to compute self-similar solutions for Fuzzy Dark Matter (FDM). Our findings highlighted the different nature of these FDM self-similar solutions compared to their Cold Dark Matter (CDM) counterparts. The self-similar solutions for CDM in a perturbed Einstein-de Sitter universe described gravitational collapse, with the density contrast growing in the linear regime and transitioning to the non-linear regime where the profile shape in the inner regions was altered by non-linear effects. However, the self-similar solutions for FDM exhibited significant differences. They did not display gravitational collapse; instead, matter was expelled from central peaks through successive clumps, resembling gravitational cooling. This behaviour was attributed to the quantum pressure and wavelike properties of the Schrödinger equation. In contrast to CDM, outer shells in FDM did not follow the trajectory of free-fall spherical collapse. The dominance of quantum pressure over gravity led to acoustic-like oscillations, facilitating the coupling between small and large scales.

Furthermore, when comparing the soliton profile with the self-similar solution profile in the high-density asymptotic limit, we observed that the central peak of the self-similar profile did not converge to the equilibrium state of the soliton profile, despite the increase in central density. This discrepancy could be attributed to the influence of kinetic effects near the boundary of the central peak.

In terms of the semiclassical limit, we discovered that FDM self-similar solutions disappeared as the limit approached, becoming confined to an increasingly small radius. This indicated that the semiclassical limit did not recover the dynamics of CDM in the case of FDM. It emphasized the need for caution and careful consideration when dealing with the semiclassical limit, as the standard CDM self-similar solutions were only precisely recovered at $\epsilon = 0$.

In Chapter 4, we introduced the pseudo-spectral code that we designed for simulating the dynamical evolution of the Schrödinger-Poisson system. The code employed a combination of Fourier domain operations and position space evaluations to handle linear and

non-linear terms, respectively. This approach eliminated the noise typically associated with finite-difference methods for computing spatial derivatives. Although the code incurred computational costs due to Fourier and inverse Fourier transforms, we optimized these transforms using the efficient FFTW3 and along with the parallelization capabilities offered by OpenMP.

In Chapter 5 we have explored the formation and evolution of solitons in the quartic model both analytical and numerically.

By considering specific initial conditions and solving the nonlinear Schrödinger equation, we observed the rapid emergence of central solitons supported by self-interactions within halos on the scale of self-interaction length. These solitons dampened initial density fluctuations and accounted for a significant fraction of the total mass. The behaviour held for both flat and cuspy halo profiles, with cuspy halos exhibiting additional high-density spikes within the soliton.

For halos larger than the scale of the self-interactions, it took longer for solitons to form, with flat density profiles requiring substantial time until small-scale spikes grew to trigger self-interactions. Cuspy halos, on the other hand, quickly led to soliton formation. We developed a kinetic theory and simplified ansatz to estimate soliton growth rates, which showed reasonable agreement with early-time growth for cuspy halos but had limitations for large soliton masses and flat halo profiles. Overall, our findings suggest that solitons play a crucial role in scalar-field dark matter scenarios with self-interactions. They can form within collapsing overdense regions and persist as halos grow, gradually increasing in mass through accretion and mergers. The relationship between halo and soliton masses is complex, depending on the assembly history of the system and potentially leading to a wide scatter in soliton masses at a given halo mass.

Finally, in Chapter 6 we studied numerically the emergence and evolution of solitons in two truncated scalar field dark matter models. Model A was based on a bounded cosine potential, while Model B was the opposite potential. We examined halos formed on a scale comparable to the self-interaction length. In Model A, a central soliton supported by self-interactions quickly formed, when the critical density was high. This soliton accounted for a significant fraction of the total mass and reduced initial density fluctuations. When the critical density was intermediate, a new phenomenon appears. There was a transition from a soliton dominated by self-interactions collapsing to a fuzzy dark matter peak. At small critical densities, the FDM peak formation was delayed but still occurred, indicating that the formation of the FDM peak is more efficient when the initial condition is a coherent state. In Model B, solitons formed rapidly when the critical density was small and intermediate. However, the soliton shape exhibited in the latter case showed slight variations compared to the other cases. It showed a faster drop-off. This can be attributed to the absence of a self-interacting potential, which means that no force is acting in that region. At large critical density the system did not lead to soliton formation. The absence of soliton formation at large critical densities aligns with previous studies indicating the evaporation of light solitons in FDM halos. We also investigated halos with sizes much larger than the self-interaction scale and found that soliton formation took a considerable amount of time in flat density profiles for both Model A and B, when the potential resembled the quartic model. In other cases, a fuzzy dark matter nature regime was observed with the signature of a fluctuating halo. Overall, these findings provide

insights into soliton formation and evolution in scalar dark matter models, highlighting the influence of self-interactions and initial conditions on the emergence of solitons and FDM peaks.

Thanks to these studies, we have extended the knowledge frontier in the different scalar dark matter models, in particular for the FDM model, for the quartic model and for the cosine model. We have been able to better understand the semiclassical boundary between the CDM and FDM models through self-similar solutions, as well as the formation and evolution of solitons in halos in the quartic and truncated models. These results are novel and answer open questions in the field of SFDM models.

Future research

In future research, one important goal is to parallelize the numerical method presented in Section 4.2 using MPI (Message Passing Interface). In this way, it would significantly enhance its performance and enable the exploration of larger and more complex systems. This parallelization will facilitate more efficient and faster calculations, allowing for more extensive investigations.

Another area for future investigation is the refinement of the kinetic theory developed in Section 5.4 and the study of hierarchical halo formation through cosmological simulations. By improving the understanding of the underlying kinetic processes and their impact on structure formation, we can gain deeper insights into the formation and evolution of cosmological halos.

To comprehensively explore these phenomena, future investigations should also incorporate baryonic physics and consider mixtures of different dark matter components in the numerical simulations. This will provide a more realistic representation of the Universe and enable a more accurate analysis of the interplay between different physical processes.

In addition, a thorough numerical analysis of the cosine model Section 6.1, including the oscillations in the Bessel function, is an important avenue for future research. These simulations will provide a comprehensive understanding of the behaviour and properties of the cosine model and its implications for dark matter dynamics.

Appendix A

Eigenvectors in the linear 3D gravitational potential

We describe in this appendix how we obtain approximate analytical expressions for the eigenmodes of the linear gravitational potential (5.41). We first define $r_\star$ as the radius where the centrifugal term $\epsilon^2\ell(\ell+1)/(2r^2)$ is equal to the linear potential term $2\pi\rho_0 r$ in the radial Schrödinger equation (5.19),

$$r_\star = \left[\frac{\epsilon^2\ell(\ell+1)}{4\pi\rho_0}\right]^{1/3}. \tag{A.1}$$

Then, on the left of $r_\star$ we only keep the centrifugal term, giving the radial Schrödinger equation for $r < r_\star$,

$$-\frac{\epsilon^2}{2}\frac{1}{r^2}\frac{d}{dr}\left(r^2\frac{d\mathcal{R}_{n\ell}}{dr}\right) + \frac{\epsilon^2}{2}\frac{\ell(\ell+1)}{r^2}\mathcal{R}_{n\ell} = (E+2\pi\rho_0)\mathcal{R}_{n\ell}, \tag{A.2}$$

whereas on the right of $r_\star$ we only keep the linear potential term, giving for $r > r_\star$,

$$-\frac{\epsilon^2}{2}\frac{1}{r^2}\frac{d}{dr}\left(r^2\frac{d\mathcal{R}_{n\ell}}{dr}\right) + 2\pi\rho_0 r\mathcal{R}_{n\ell} = (E+2\pi\rho_0)\mathcal{R}_{n\ell}. \tag{A.3}$$

This approximation is actually exact for $\ell = 0$. Then, below $r_\star$ the eigenmodes read as

$$r < r_\star : \quad \mathcal{R}_{n\ell}(r) = N j_\ell(\lambda r), \quad \lambda^2 = \frac{2(E+2\pi\rho_0)}{\epsilon^2}, \tag{A.4}$$

while above $r_\star$ they read as

$$\begin{aligned} r > r_\star : \ \mathcal{R}_{n\ell}(r) &= \frac{N'}{r}\mathrm{Ai}(\alpha r - \omega), \quad \text{with} \\ \alpha = \left(\frac{4\pi\rho_0}{\epsilon^2}\right)^{1/3}, &\quad \omega = \alpha\frac{E+2\pi\rho_0}{2\pi\rho_0}, \end{aligned} \tag{A.5}$$

where N and N' are normalization factors. For $\ell = 0$, the expression (A.5) extends down to $r = 0$, as $r_\star = 0$. Then, the regularity condition at the center $r = 0$ directly gives the quantization condition

$$\ell = 0 : \quad \omega = \omega_n, \quad E_{n0} = -2\pi\rho_0 + 2\pi\rho_0\omega_n/\alpha, \tag{A.6}$$

where $0 > -\omega_0 > -\omega_1 > -\omega_2 > \dots$ are the zeros of the Airy function $\mathrm{Ai}(x)$. For $\ell \geq 1$, the quantization condition is given by the continuity of $\mathcal{R}_{n\ell}$ and $\mathcal{R}'_{n\ell}$ at the junction radius $r_\star$. These two constraints give one equation for the ratio N'/N and one nonlinear equation for the energy E. The roots of this latter condition provide the the discrete energy levels $E_{n\ell}$, which we compute with a numerical root solver algorithm.

Appendix B

Gaussian ansatz for the radial profile

In this appendix we describe how we can study analytically solitons transitions in the bounded potential (2.94) using the Gaussian ansatz. As we have discussed, solitons are equilibrium configurations of the non-relativistic Schrödinger–Poisson equations. Therefore, they represent static solutions that minimize the energy functional of the system.

The total energy of the system is given by (2.60). Thus, the energy functional as a function of ρ reads,

$$E = \int d^3x \left(\frac{\rho}{2}\Phi_N + \mathcal{V}_I(\rho) + \frac{(\nabla\sqrt{\rho})^2}{2m^2} \right). \tag{B.1}$$

Since they are static configurations, solitons satisfy the following Euler equation,

$$\nabla(\Phi_{\rm N} + \Phi_{\rm I} + \Phi_{\rm Q}) = 0 \tag{B.2}$$

B.1 Solitons

Obtaining an explicit solution for equation (B.2) is not feasible. Hence, we will employ a variational approach and explore solutions characterized by a static Gaussian spherical density profile with a constant mass M given by,

$$\rho(r) = \rho_c\, e^{-(r/R)^2}, \quad \text{with} \quad \rho_c = \frac{M}{\pi^{3/2}R^3}. \tag{B.3}$$

Using this ansatz in (B.1), we obtain the following energy contributions: the gravitational energy,

$$E_G = -\frac{\mathcal{G}_{\mathcal{N}}\pi^{5/2}R^5\rho_c^2}{\sqrt{2}}, \tag{B.4}$$

the quantum energy,

$$E_Q = \frac{3\pi M^{1/3}\rho_c^{2/3}}{4m^2}, \tag{B.5}$$

and, after one integration by parts, the energy due to the self-interactions is given by,

$$E_I = \frac{8\pi}{3}\rho_c R^3 \int_0^\infty dx\; x^4 e^{-x^2}\Phi_I(\rho_c e^{-x^2}), \quad \text{with} \quad x = r/R. \tag{B.6}$$

To simplify the problem, we take the asymptotic limit of the self-interacting potential $\Phi_{\rm I}$, (2.94), at low (2.96) and large (2.97) densities. Thus, the self-interaction energy for $\rho < 8\rho_b$ is,

$$E_I = \frac{M\rho_c}{4\sqrt{2}\rho_a} \tag{B.7}$$

and for $\rho > 8\rho_b$,

$$\begin{aligned} E_I \;=\; & \frac{M}{24\sqrt{\pi}\rho_a\rho_c}\Big(192\sqrt{\pi}\rho_b\rho_c \mathrm{Erf}\left(\sqrt{-\log(8\rho_b/\rho_c)}\right) + 3\sqrt{2\pi}\rho_c^2 \mathrm{Erfc}\left(\sqrt{2}\sqrt{-\log(8\rho_b/\rho_c)}\right) \\ & +256\rho_b^2\sqrt{-\log(8\rho_b/\rho_c)}\,(-9+4\log(8\rho_b/\rho_c))\Big) \end{aligned} \tag{B.8}$$

B.1.1 Dimensionless quantities

To simplify the calculations, we employ the rescaling described in expression (3.4). By applying this rescaling, we establish the connection between the dimensional energy and the dimensionless energy, represented by the tilde symbol. The relationship between them reads,

$$E = \rho_\star \frac{L_\star^5}{T_\star^2}\tilde{E} = E_\star \tilde{E}. \tag{B.9}$$

We define the characteristic scale of the density, denoted as $\rho_\star$, at which the potential exhibits a change in behaviour. Consequently, the characteristic scales of the system can be specified as follows:

$$\rho_\star = 8\rho_b, \quad L_\star = \frac{1}{\sqrt{\mathcal{G}_{\rm N}\rho_a}}, \quad T_\star = \frac{1}{\sqrt{\mathcal{G}_{\rm N}\rho_\star}}. \tag{B.10}$$

Therefore, the dimensionless gravitational energy reads,

$$\tilde{E}_G = -\frac{\tilde{M}^{5/3}\tilde{\rho}^{1/3}}{\sqrt{2}} \tag{B.11}$$

the quantum energy,

$$\tilde{E}_Q = \frac{3\pi}{4}\,\epsilon\,\tilde{M}^{1/3}\tilde{\rho}^{2/3} \tag{B.12}$$

and for the self-interaction we have, when $\tilde{\rho} < 1$,

$$\tilde{E}_I = \frac{\tilde{M}\tilde{\rho}}{4\sqrt{2}} \tag{B.13}$$

and when $\tilde{\rho} > 1$,

$$\tilde{E}_I = \frac{\tilde{M}}{24\sqrt{\pi}\tilde{\rho}}\Big(24\sqrt{\pi}\,\tilde{\rho}\,\mathrm{Erf}\left(\sqrt{\log\tilde{\rho}}\right) + 3\sqrt{2\pi}\tilde{\rho}^2\,\mathrm{Erfc}\left(\sqrt{2}\sqrt{\log\tilde{\rho}}\right) + 4(-9-4\log\tilde{\rho})\sqrt{\log\tilde{\rho}}\Big) \tag{B.14}$$

B.2 Low density solitons: Gravity and Self-interactions

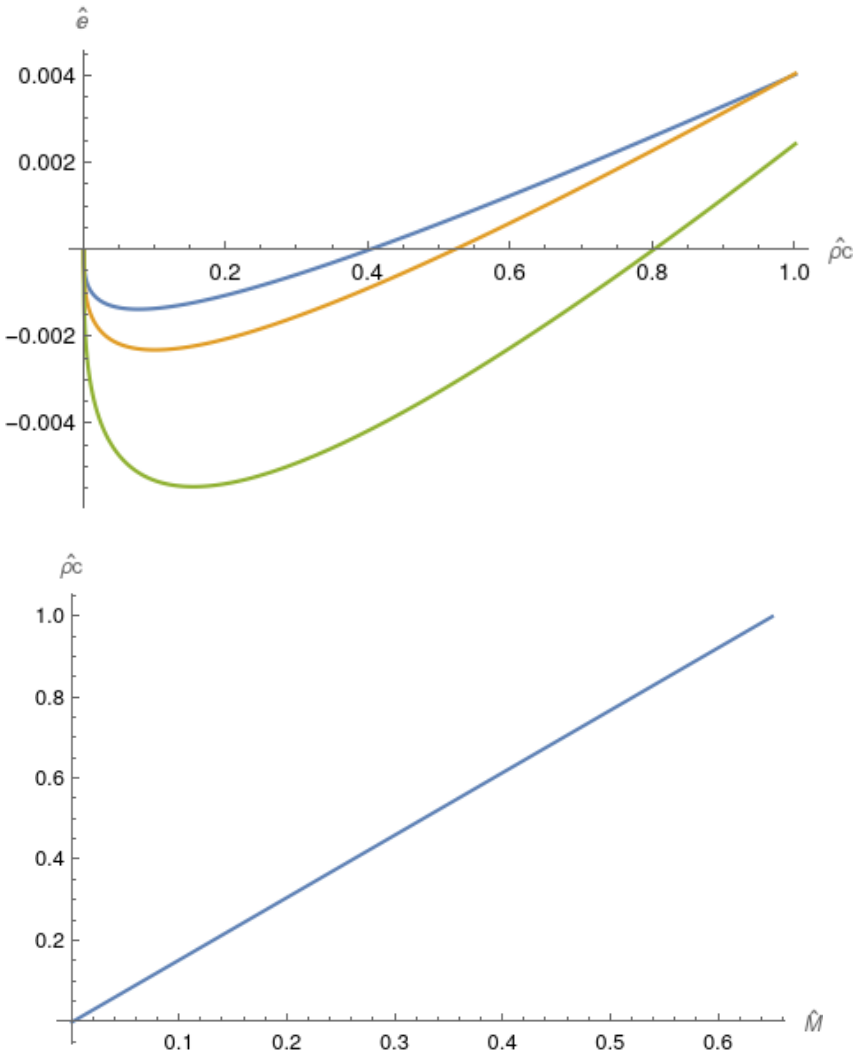

Figure B.1. *Upper panel:* Energy as a function of the density for different solitons. In blue when the soliton mass is $\tilde{M}$=0.05, in orange, $\tilde{M}$=0.06 and in green, $\tilde{M}$=0.1 *Bottom panel:* Mass-density relation.

In this case, the equilibrium configuration arises from the equilibrium between attractive gravity and repulsive self-interactions. In the regime where the soliton density is low, we can disregard the contribution of the repulsive quantum pressure. The energy functional that describes this scenario is:

$$E = -\frac{\tilde{M}^{5/3}\tilde{\rho}^{1/3}}{\sqrt{2}} + \frac{\tilde{M}\tilde{\rho}}{4\sqrt{2}} \tag{B.15}$$

If we take the derivative respect to $\tilde{\rho}$, we have,

$$\frac{dE}{d\tilde{\rho}} = \frac{\tilde{M}}{4\sqrt{2}} - \frac{\tilde{M}^{5/3}}{3\sqrt{2}\tilde{\rho}^{2/3}} \tag{B.16}$$

By setting this quantity equal to zero, we obtain the mass-density relation of the solitons in this set-up,

$$\tilde{\rho} = \frac{8\tilde{M}}{3\sqrt{3}} \tag{B.17}$$

As anticipated, we consistently observe a minimum in the energy functional for a given mass within this regime. This minimum corresponds to the soliton formed in the Thomas-Fermi regime, since the quantum pressure contribution is negligible in the functional.

B.3 Mid-density solitons: Gravity and self-interactions

In this section we explore configurations where the central density of the soliton is approximately around the critical density.Therefore, the two parts of the potential Φ_I play a role. The soliton arises when there is an equilibrium between an attractive and a repulsive force. Specifically, the soliton can only form when its central density resides in the first part of the self-interaction potential, as the second part is unable to counteract the gravitational effects. Consequently, within this regime, the more masive soliton that can be formed has a mass of $\tilde{M} = 0.84$.

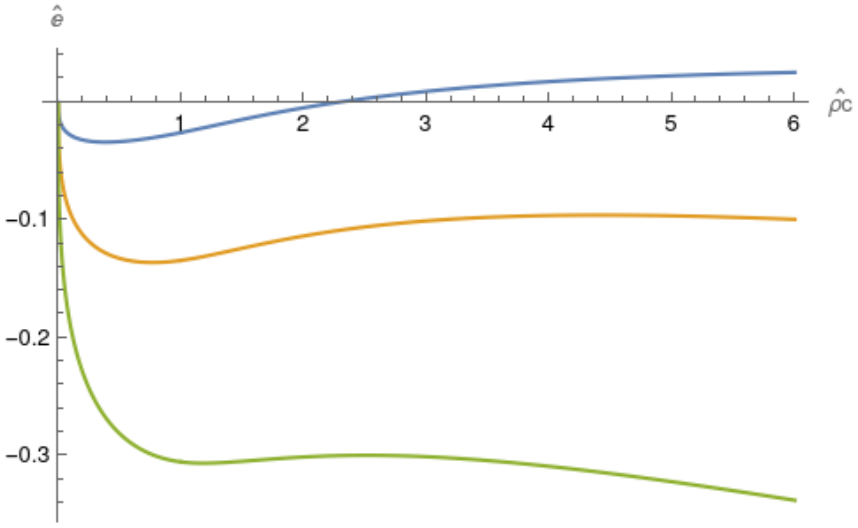

Figure B.2. Energy as a function of the density for different solitons. In blue when the soliton mass is $\tilde{M}$=0.25, in orange, $\tilde{M}$= 0.5 and in green, $\tilde{M}$=0.75.

B.4 Low density solitons: Gravity, Self-interactions and Quantum pressure

In this section, unlike Section B.2, we also consider the influence of quantum pressure in the soliton configuration. Consequently, the total energy functional we have is as follows:

$$\tilde{E} = -\frac{\tilde{M}^{5/3}\tilde{\rho}^{1/3}}{\sqrt{2}} + \frac{3}{4}\tilde{M}^{1/3}\pi\epsilon^2\tilde{\rho}^{2/3} + \frac{\tilde{M}\tilde{\rho}}{4\sqrt{2}} \tag{B.18}$$

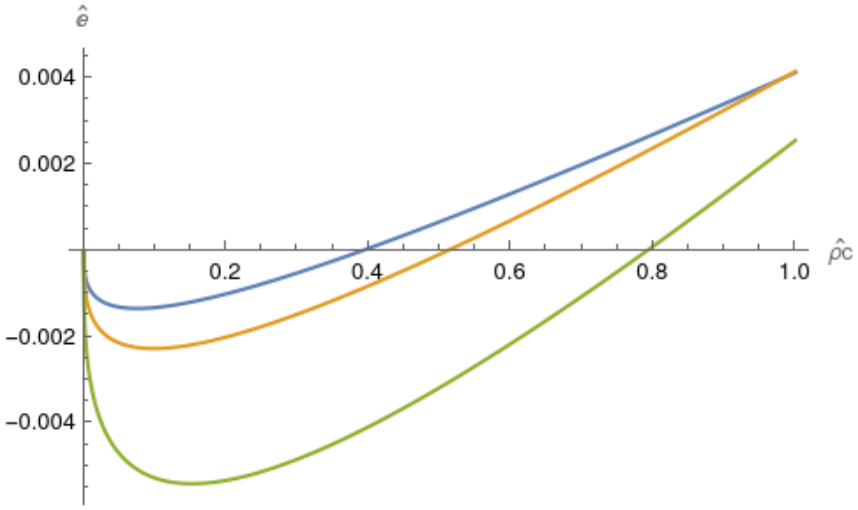

Figure B.3. Energy as a function of the density for different solitons. In blue when the soliton mass is $\tilde{M}$=0.05, in orange, $\tilde{M}$=0.06 and in green, $\tilde{M}$=0.1

As we can see, the incorporation of quantum pressure does not substantially modify the dynamics. We find ourselves again with a single minimum.

B.5 Mid-density solitons: Gravity, Self-interactions and Quantum pressure

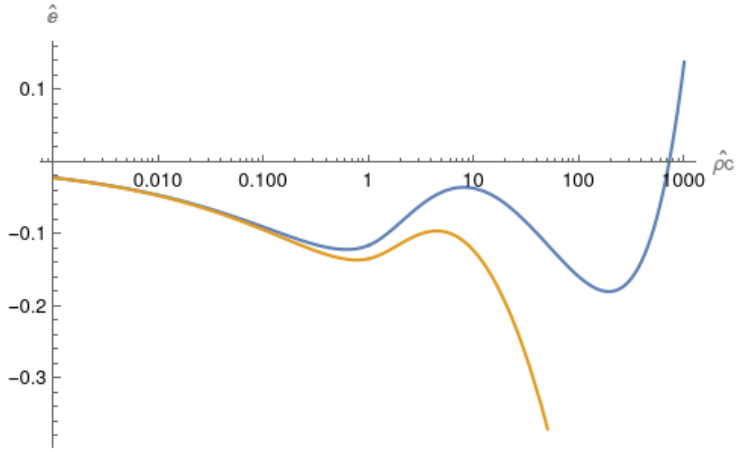

Figure B.4. Energy as a function of the density for the soliton with $\tilde{M} = 0.5$ and $\epsilon = 0.1$. Blue line: energy with the contribution of the quantum pressuere (Cases 3 & 4). Orange line, energy functional without quantum pressure (Cases 1 & 2).

In this case, we investigate the model that incorporates all contributions, including the attractive gravity, the repulsive self-interactions, and the repulsive quantum pressure. So the total energy has the three contributions.

In Figure B.4, we compare the energy functional in two configurations: one considering the quantum pressure and the other without it. The orange curve represents the case where quantum pressure is neglected, and it shows a single minimum corresponding to

the Thomas-Fermi soliton. We can verify that neglecting the quantum pressure at low densities is a valid approximation because both curves exhibit the same behaviour in this regime. We show in Fig.B.5 the time evolution of the first minima. Since it is an equilibrium configuration, we can observe oscillations around 0 in the virial quantity. The mass and the total energy of the system is conserved and matches with the analytical predictions.

However, in the case we are currently examining, we observe a different behaviour. A second minimum appears in the energy functional at much higher densities. This new minimum corresponds to the soliton formation when the quantum pressure is taken into account. It is important to note that there are energy levels that can explore both minimas. This implies that there is a possibility of transitioning from the original self-interaction regime to a fuzzy dark matter regime by crossing the potential barrier and settling into the global minimum of the functional. This scenario is reminiscent of the findings from numerical simulation in Fig.6.2, where a similar transition was observed.

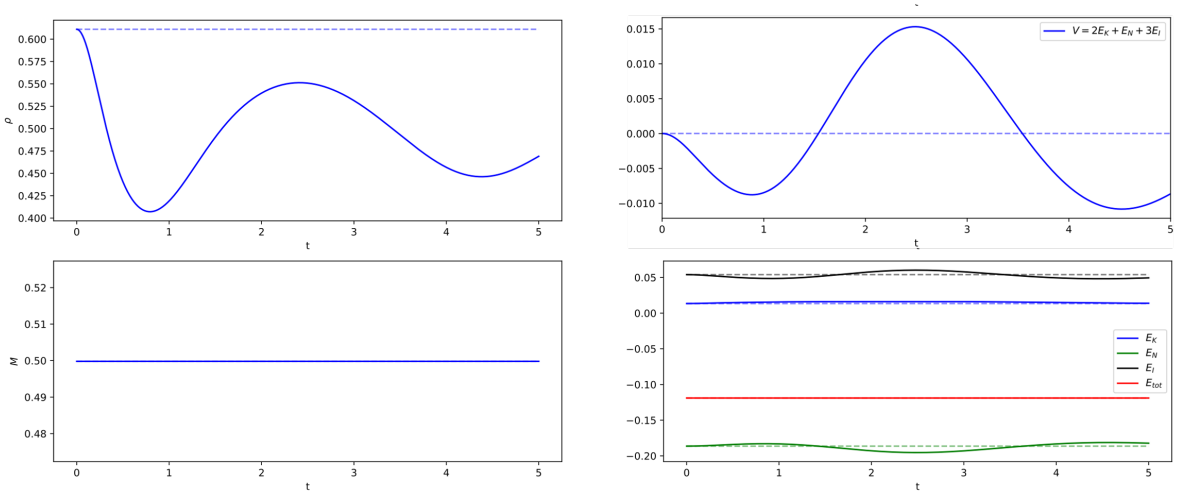

Figure B.5. Evolution of the soliton $\rho_c = 0.61$ $\tilde{M} = 0.5$, $\epsilon = 0.1$. *Upper left panel*: Density at the center. *Upper right panel*:Virial quantity. *Lower left panel:* Total mass. *Lower right panel:* Energies.

Bibliography

Alcock, C., Akerlof, C. W., Allsman, R. A., et al. 1993, Nature, 365, 621, doi: 10.1038/365621a0

Alcubierre, M., Guzmán, F. S., Matos, T., et al. 2002, in Dark Matter in Astro- and Particle Physics (Springer Berlin Heidelberg), 356–364, doi: 10.1007/978-3-642-55739-2_35

Arcadi, G., Dutra, M., Ghosh, P., et al. 2018, European Physical Journal C, 78, 203, doi: 10.1140/epjc/s10052-018-5662-y

Bachlechner, T. C., Eckerle, K., Janssen, O., & Kleban, M. 2019, J. Cosmology Astropart. Phys., 2019, 062, doi: 10.1088/1475-7516/2019/09/062

Bednyakov, V. A., Klapdor-Kleingrothaus, H. V., & Kovalenko, S. G. 1997, Phys. Rev. D, 55, 503, doi: 10.1103/PhysRevD.55.503

Bennett, C. L., Larson, D., Weiland, J. L., et al. 2013, ApJS, 208, 20, doi: 10.1088/0067-0049/208/2/20

Bertschinger, E. 1985, Astrophys. J. Suppl., 58, 39, doi: 10.1086/191028

Binney, J., & Tremaine, S. 2008, Galactic Dynamics: Second Edition, rev - revised, 2 edn. (Princeton University Press)

Bird, S., Cholis, I., Muñoz, J. B., et al. 2016, Phys. Rev. Lett., 116, 201301, doi: 10.1103/PhysRevLett.116.201301

Bond, J. R., Szalay, A. S., & Turner, M. S. 1982, Phys. Rev. Lett., 48, 1636, doi: 10.1103/PhysRevLett.48.1636

Boylan-Kolchin, M., Bullock, J. S., & Kaplinghat, M. 2011, Monthly Notices of the Royal Astronomical Society: Letters, 415, doi: 10.1111/j.1745-3933.2011.01074.x

Brax, P., Cembranos, J. A. R., & Valageas, P. 2019a, Phys. Rev. D, 100, 023526, doi: 10.1103/PhysRevD.100.023526

Brax, P., Valageas, P., & Cembranos, J. A. 2019b, Physical Review D, 100, doi: 10.1103/PhysRevD.100.023526

Brooks, A. M., Kuhlen, M., Zolotov, A., & Hooper, D. 2013, ApJ, 765, 22, doi: 10.1088/0004-637X/765/1/22

Bullock, J. S., & Boylan-Kolchin, M. 2017, ARA&A, 55, 343, doi: 10.1146/annurev-astro-091916-055313

Cartwright, N. D. 1976, Physica A: Statistical Mechanics and its Applications, 83, 210, doi: 10.1016/0378-4371(76)90145-X

Chan, J. H.-H., Sibiryakov, S., & Xue, W. 2022. https://arxiv.org/abs/2207.04057

Chan, T. K., Kereš, D., Oñorbe, J., et al. 2015, Monthly Notices of the Royal Astronomical Society, 454, 2981, doi: 10.1093/mnras/stv2165

Chavanis, P.-H. 2011, Phys. Rev. D, 84, 043531, doi: 10.1103/PhysRevD.84.043531

—. 2018, Physical Review D, 100, doi: 10.1103/PhysRevD.100.083022

Chluba, J., & Grin, D. 2013, Mon. Not. Roy. Astron. Soc., 434, 1619, doi: 10.1093/mnras/stt1129

Chwolson, O. 1924, Astronomische Nachrichten, 221, 329, doi: 10.1002/asna.19242212003

Clowe, D., Bradač, M., Gonzalez, A. H., et al. 2006, ApJ, 648, L109, doi: 10.1086/508162

Coil, A. L. 2013, in Planets, Stars and Stellar Systems. Volume 6: Extragalactic Astronomy and Cosmology, ed. T. D. Oswalt & W. C. Keel, Vol. 6, 387, doi: 10.1007/978-94-007-5609-0_8

Colless, M., Dalton, G., Maddox, S., et al. 2001, MNRAS, 328, 1039, doi: 10.1046/j.1365-8711.2001.04902.x

Conrad, J. 2014, arXiv e-prints, arXiv:1411.1925, doi: 10.48550/arXiv.1411.1925

Dashyan, G., Silk, J., Mamon, G. A., Dubois, Y., & Hartwig, T. 2018, Monthly Notices of the Royal Astronomical Society, 473, 5698, doi: 10.1093/MNRAS/STX2716

Del Popolo, A. 2014, International Journal of Modern Physics D, 23, 1430005, doi: 10.1142/S0218271814300055

Del Popolo, A., & Delliou, M. L. 2016, Galaxies, 5, doi: 10.3390/galaxies5010017

Dent, J. B., Easson, D. A., & Tashiro, H. 2012, Phys. Rev. D, 86, 023514, doi: 10.1103/PhysRevD.86.023514

Di Luzio, L., Giannotti, M., Nardi, E., & Visinelli, L. 2020, Physics Reports, 870, 1, doi: 10.1016/j.physrep.2020.06.002

Dodelson, S., & Widrow, L. M. 1994, Phys. Rev. Lett., 72, 17, doi: 10.1103/PhysRevLett.72.17

Drees, M., Godbole, R., & Roy, P. 2004, Theory and phenomenology of sparticles: An account of four-dimensional N=1 supersymmetry in high energy physics

Drlica-Wagner, A., Bechtol, K., Rykoff, E. S., et al. 2015, ApJ, 813, 109, doi: 10.1088/0004-637X/813/2/109

Edwards, F., Kendall, E., Hotchkiss, S., & Easther, R. 2018, J. Cosmology Astropart. Phys., 2018, 027, doi: 10.1088/1475-7516/2018/10/027

Edwards, F., Kendall, E., Hotchkiss, S., & Easther, R. 2018, Journal of Cosmology and Astroparticle Physics, doi: 10.1088/1475-7516/2018/10/027

Einstein, A. 1936, Science, 84, 506, doi: 10.1126/science.84.2188.506

Einstein, A. 1986, in Cosmological Constants, ed. J. Bernstein & G. Feinberg, 16

Ferreira, E. G. M. 2020. https://arxiv.org/abs/2005.03254

Fillmore, J. A., & Goldreich, P. 1984, Astrophys. J., 281, 1, doi: 10.1086/162070

Flores, R. A., & Primack, J. R. 1994, The Astrophysical Journal, 427, L1, doi: 10.1086/187350

Frigo, M., & Johnson, S. G. 2005, Proceedings of the IEEE, 93, 216

Funk, S. 2015, Proceedings of the National Academy of Science, 112, 12264, doi: 10.1073/pnas.1308728111

Galazo-García, R., Brax, P., & Valageas, P. 2022, Phys. Rev. D, 105, 123528, doi: 10.1103/PhysRevD.105.123528

Galazo García, R., Brax, P., & Valageas, P. 2023, arXiv e-prints, arXiv:2304.10221, doi: 10.48550/arXiv.2304.10221

Galli, S., Iocco, F., Bertone, G., & Melchiorri, A. 2009, Phys. Rev. D, 80, 023505, doi: 10.1103/PhysRevD.80.023505

—. 2011, Phys. Rev. D, 84, 027302, doi: 10.1103/PhysRevD.84.027302

García-Bellido, J., & Ruiz Morales, E. 2017, Physics of the Dark Universe, 18, 47, doi: 10.1016/j.dark.2017.09.007

Garny, M., Konstandin, T., & Rubira, H. 2020, Journal of Cosmology and Astroparticle Physics, 2020, 003, doi: 10.1088/1475-7516/2020/04/003

Garrison-Kimmel, S., Boylan-Kolchin, M., Bullock, J. S., & Kirby, E. N. 2014, Monthly Notices of the Royal Astronomical Society, 444, 222, doi: 10.1093/mnras/stu1477

Geller, M. J., & Huchra, J. P. 1989, Mapping the universe, Science, doi: 10.1126/science.246.4932.897

Giagu, S. 2019, Frontiers in Physics, 7, 75, doi: 10.3389/fphy.2019.00075

Goodman, J. 2000, New A, 5, 103, doi: 10.1016/S1384-1076(00)00015-4

Gott, J. R., Jurić, M., Schlegel, D., et al. 2003, The Astrophysical Journal, 624, 463, doi: 10.1086/428890

Graham, P. W., Irastorza, I. G., Lamoreaux, S. K., Lindner, A., & van Bibber, K. A. 2015, Annual Review of Nuclear and Particle Science, 65, 485, doi: 10.1146/annurev-nucl-102014-022120

Griest, K. 1996, in Dark Matter in the Universe, ed. S. Bonometto, J. R. Primack, & A. Provenzale, 343, doi: 10.48550/arXiv.astro-ph/9510089

Guth, A. H., Hertzberg, M. P., & Prescod-Weinstein, C. 2015, Phys. Rev. D, 92, 103513, doi: 10.1103/PhysRevD.92.103513

Guzman, F. S., & Urena-Lopez, L. A. 2003, Phys. Rev. D, 68, 024023, doi: 10.1103/PhysRevD.68.024023

Guzman, F. S., & Urena-Lopez, L. A. 2006, The Astrophysical Journal, 645, 814, doi: 10.1086/504508/FULLTEXT/

Hanany, S., Ade, P., Balbi, A., et al. 2000, ApJ, 545, L5, doi: 10.1086/317322

Harko, T. 2011, Mon. Not. Roy. Astron. Soc., 413, 3095, doi: 10.1111/j.1365-2966.2011.18386.x

—. 2019, European Physical Journal C, 79, doi: 10.1140/epjc/s10052-019-7285-3

Hinshaw, G., Larson, D., Komatsu, E., et al. 2013, Astrophysical Journal, Supplement Series, 208, 19, doi: 10.1088/0067-0049/208/2/19

Hu, W., Barkana, R., & Gruzinov, A. 2000, Phys. Rev. Lett., 85, 1158, doi: 10.1103/PhysRevLett.85.1158

Hu, W., Barkana, R., & Gruzinov, A. 2000, Phys. Rev. Lett., 85, 1158, doi: 10.1103/PhysRevLett.85.1158

Hui, L. 2021, Annual Review of Astronomy and Astrophysics, 59, 247, doi: 10.1146/annurev-astro-120920-010024

Hui, L., Ostriker, J. P., Tremaine, S., & Witten, E. 2017, Phys. Rev. D, 95, 043541, doi: 10.1103/PhysRevD.95.043541

Hui, L., Ostriker, J. P., Tremaine, S., & Witten, E. 2017, Physical Review D, 95, 043541, doi: 10.1103/PhysRevD.95.043541

Husimi, K. 1940, Proceedings of the Physico-Mathematical Society of Japan. 3rd Series, 22, 264, doi: 10.11429/PPMSJ1919.22.4_264

Jain, M., Amin, M. A., Thomas, J., & Wanichwecharungruang, W. 2023. https://arxiv.org/abs/2304.01985

Jin, S., Markowich, P., & Sparber, C. 2011, Acta Numerica, 20, 121, doi: 10.1017/S0962492911000031

Jing, Y. P., Mo, H. J., & Börner, G. 1998, ApJ, 494, 1, doi: 10.1086/305209

Jungman, G., Kamionkowski, M., & Griest, K. 1996, Phys. Rep., 267, 195, doi: 10.1016/0370-1573(95)00058-5

Kaiser, N., & Squires, G. 1993, ApJ, 404, 441, doi: 10.1086/172297

Kennicutt, R. C., Oh, S. H., De Blok, W. J., Brinks, E., & Walter, F. 2011, Astronomical Journal, 141, 193, doi: 10.1088/0004-6256/141/6/193

Kim, J. E. 1979, Phys. Rev. Lett., 43, 103, doi: 10.1103/PhysRevLett.43.103

Klypin, A., Kravtsov, A. V., Valenzuela, O., & Prada, F. 1999, The Astrophysical Journal, 522, 82, doi: 10.1086/307643

Kopp, J. 2021, arXiv e-prints, arXiv:2109.00767, doi: 10.48550/arXiv.2109.00767

Kuhlen, M., Diemand, J., Madau, P., & Zemp, M. 2008, in Journal of Physics Conference Series, Vol. 125, Journal of Physics Conference Series, 012008, doi: 10.1088/1742-6596/125/1/012008

Landau, L. D., & Lifshitz, E. M. 1977, Quantum mechanics: non-relativistic theory, 3rd edn. (Pergamon Press)

Lee, T. D., & Pang, Y. 1992, Phys. Rept., 221, 251, doi: 10.1016/0370-1573(92)90064-7

Limousin, M., Beauchesne, B., & Jullo, E. 2022, A&A, 664, A90, doi: 10.1051/0004-6361/202243278

Lin, S., Schive, H., Wong, S., & Chiueh, T. 2018, Physical Review D, 97, 103523, doi: 10.1103/PHYSREVD.97.103523/FIGURES/7/MEDIUM

Madarassy, E. J., & Toth, V. T. 2013, Computer Physics Communications, 184, 1339, doi: 10.1016/j.cpc.2012.12.024

Madarassy, E. J. M., & Toth, V. T. 2015, Physical Review D - Particles, Fields, Gravitation and Cosmology, 91, 1, doi: 10.1103/PhysRevD.91.044041

Madau, P., Shen, S., & Governato, F. 2014, Astrophysical Journal Letters, 789, L17, doi: 10.1088/2041-8205/789/1/L17

Madelung, E. 1926, Ann. d. Phys, 79

Marsh, D. 2015, Physical Review D, 91, doi: 10.1103/PhysRevD.91.123520

Marsh, D. J. E. 2016, Phys. Rep., 643, 1, doi: 10.1016/j.physrep.2016.06.005

Massey, R., Kitching, T., & Richard, J. 2010, Reports on Progress in Physics, 73, 086901, doi: 10.1088/0034-4885/73/8/086901

Mauskopf, P. D., Ade, P. A. R., de Bernardis, P., et al. 2000, ApJ, 536, L59, doi: 10.1086/312743

Merzbacher, E. 1998, Quantum mechanics, 3rd edn. (Wiley)

Miguel Hermanns. 1997, OpenMP Fortran API v1.0, Tech. rep., Universidad Politécnica de Madrid. https://www.openmp.org/wp-content/uploads/F95_OpenMPv1_v2.pdf

Mo, H., van den Bosch, F., & White, S. 2010, Galaxy Formation and Evolution (Cambridge University Press), doi: 10.1017/CBO9780511807244

Mocz, P., Lancaster, L., Fialkov, A., Becerra, F., & Chavanis, P. H. 2018, Physical Review D, 97, 083519, doi: 10.1103/PhysRevD.97.083519

Mocz, P., Vogelsberger, M., Robles, V. H., et al. 2017, Monthly Notices of the Royal Astronomical Society, 471, 4559, doi: 10.1093/mnras/stx1887

Moore, B. 1994, Nature, 370, 629, doi: 10.1038/370629a0

Moore, B., Ghigna, S., Governato, F., et al. 1999a, The Astrophysical Journal, 524, L19, doi: 10.1086/312287

Moore, B., Quinn, T., Governato, F., Stadel, J., & Lake, G. 1999b, Monthly Notices of the Royal Astronomical Society, 310, 1147, doi: 10.1046/j.1365-8711.1999.03039.x

Nakama, T., Chluba, J., & Kamionkowski, M. 2017, Physical Review D, 95, 121302, doi: 10.1103/PhysRevD.95.121302

Navarro, J. F., Frenk, C. S., & White, S. D. M. 1996a, The Astrophysical Journal, 462, 563, doi: 10.1086/177173

—. 1996b, Astrophys. J., 462, 563, doi: 10.1086/177173

Nazarenko, S. 2011, Wave turbulence (Springer Berlin, Heidelberg)

Oh, S. H., Hunter, D. A., Brinks, E., et al. 2015, Astronomical Journal, 149, doi: 10.1088/0004-6256/149/6/180

Onorato, M., & Dematteis, G. 2020, Journal of Physics Communications, 4, 095016, doi: 10.1088/2399-6528/abb4b7

OpenMP Architecture Review Board. 2005–*present*, OpenMP. https://www.openmp.org/

Ostriker, J. P., Choi, E., Chow, A., & Guha, K. 2019, The Astrophysical Journal, 885, 97, doi: 10.3847/1538-4357/ab3288

Ostriker, J. P., & Peebles, P. J. E. 1973, ApJ, 186, 467, doi: 10.1086/152513

Pathria, D., & Morris, J. L. 1990, Journal of Computational Physics, 87, 108, doi: 10.1016/0021-9991(90)90228-S

Peacock, J. A. 1998, Cosmological Physics (Cambridge University Press), doi: 10.1017/CBO9780511804533

Peccei, R. D., & Quinn, H. R. 1977, Phys. Rev. Lett., 38, 1440, doi: 10.1103/PhysRevLett.38.1440

Peebles, P. 1980, The large-scale structure of the universe (Princeton University Press)

Peebles, P. J. E. 1982, ApJ, 263, L1, doi: 10.1086/183911

Penzias, A. A., & Wilson, R. W. 1965, ApJ, 142, 419, doi: 10.1086/148307

Planck Collaboration, Ade, P. A. R., Aghanim, N., et al. 2014, A&A, 571, A15, doi: 10.1051/0004-6361/201321573

Planck Collaboration, Aghanim, N., Akrami, Y., et al. 2020a, A&A, 641, A6, doi: 10.1051/0004-6361/201833910

—. 2020b, A&A, 641, A6, doi: 10.1051/0004-6361/201833910

Planck Collaboration, Akrami, Y., Ashdown, M., et al. 2020c, A&A, 641, A7, doi: 10.1051/0004-6361/201935201

Press, W. H., Flannery, B. P., Teukolsky, S. A., & Vetterling, W. T. 1992, Numerical Recipes in FORTRAN 77: The Art of Scientific Computing, 2nd edn. (Cambridge University Press). http://www.worldcat.org/isbn/052143064X

Read, J. I., Agertz, O., & Collins, M. L. 2016, Monthly Notices of the Royal Astronomical Society, 459, 2573, doi: 10.1093/mnras/stw713

Rubin, V. C., & Ford, W. Kent, J. 1970, ApJ, 159, 379, doi: 10.1086/150317

Rubin, V. C., Thonnard, N., & Ford, W. K., J. 1978, The Astrophysical Journal, 225, L107, doi: 10.1086/182804

Sasaki, M., Suyama, T., Tanaka, T., & Yokoyama, S. 2018, Classical and Quantum Gravity, 35, 063001, doi: 10.1088/1361-6382/aaa7b4

Schive, H. Y., Chiueh, T., & Broadhurst, T. 2014a, Nature Physics, 10, 496, doi: 10.1038/nphys2996

—. 2014b, Nature Physics 2014 10:7, 10, 496, doi: 10.1038/nphys2996

Schive, H. Y., Liao, M. H., Woo, T. P., et al. 2014c, Physical Review Letters, 113, 1, doi: 10.1103/PhysRevLett.113.261302

Schumann, M. 2019, Journal of Physics G Nuclear Physics, 46, 103003, doi: 10.1088/1361-6471/ab2ea5

Schwabe, B., Niemeyer, J. C., & Engels, J. F. 2016, Physical Review D, 94, 043513, doi: 10.1103/PHYSREVD.94.043513/FIGURES/9/MEDIUM

Seidel, E., & Suen, W. M. 1994, Physical Review Letters, 72, 2516, doi: 10.1103/PhysRevLett.72.2516

Shapiro, P. R., Dawoodbhoy, T., & Rindler-Daller, T. 2022, MNRAS, 509, 145, doi: 10.1093/mnras/stab2884

Shi, X., & Fuller, G. M. 1999, Phys. Rev. Lett., 82, 2832, doi: 10.1103/PhysRevLett.82.2832

Sikivie, P., & Yang, Q. 2009, Phys. Rev. Lett., 103, 111301, doi: 10.1103/PhysRevLett.103.111301

Skodje, R. T., Rohrs, H. W., & VanBuskirk, J. 1989, Phys. Rev. A, 40, 2894, doi: 10.1103/PhysRevA.40.2894

Smith, S. 1936, The Astrophysical Journal, 83, 23, doi: 10.1086/143697

Smoot, G. F., Bennett, C. L., Kogut, A., et al. 1992, ApJ, 396, L1, doi: 10.1086/186504

Spiegel, E. A. 1980, Physica D: Nonlinear Phenomena, 1, 236, doi: 10.1016/0167-2789(80)90015-9

Springel, V., Frenk, C. S., & White, S. D. M. 2006, Nature, 440, 1137, doi: 10.1038/nature04805

Springel, V., Wang, J., Vogelsberger, M., et al. 2008, MNRAS, 391, 1685, doi: 10.1111/j.1365-2966.2008.14066.x

Stadel, J., Potter, D., Moore, B., et al. 2009, MNRAS, 398, L21, doi: 10.1111/j.1745-3933.2009.00699.x

Steffen, F. D. 2006, J. Cosmology Astropart. Phys., 2006, 001, doi: 10.1088/1475-7516/2006/09/001

Steigman, G., & Turner, M. S. 1985, Nuclear Physics B, 253, 375, doi: 10.1016/0550-3213(85)90537-1

Svrcek, P., & Witten, E. 2006, Journal of High Energy Physics, 2006, 051, doi: 10.1088/1126-6708/2006/06/051

Teyssier, R., Chièze, J.-P., & Alimi, J.-M. 1997, The Astrophysical Journal, 480, 36, doi: 10.1086/303965

Tisserand, P., Le Guillou, L., Afonso, C., et al. 2007, A&A, 469, 387, doi: 10.1051/0004-6361:20066017

Uhlemann, C., Kopp, M., & Haugg, T. 2014, Physical Review D, 90, 023517, doi: 10.1103/PhysRevD.90.023517

Veltmaat, J., Niemeyer, J. C., & Schwabe, B. 2018, Phys. Rev. D, 98, 043509, doi: 10.1103/PhysRevD.98.043509

Wallstrom, T. C. 1994, Physical Review A, 49, 1613, doi: 10.1103/PhysRevA.49.1613

Weinberg, D. H., Bullock, J. S., Governato, F., De Naray, R. K., & Peter, A. H. 2015, Proceedings of the National Academy of Sciences of the United States of America, 112, 12249, doi: 10.1073/pnas.1308716112

Weinberg, S. 2008, Cosmology

Widrow, L. M., & Kaiser, N. 1993, ApJL, 416, L71, doi: 10.1086/187073

Wigner, E. 1932, Phys. Rev., 40, 749, doi: 10.1103/PhysRev.40.749

Yavetz, T. D., Li, X., & Hui, L. 2022, Phys. Rev. D, 105, 023512, doi: 10.1103/PhysRevD.105.023512

Yoo, J., Chanamé, J., & Gould, A. 2004, ApJ, 601, 311, doi: 10.1086/380562

Zhang, Q., & Hayee, M. I. 2008, Journal of Lightwave Technology, 26, 302, doi: 10.1109/JLT.2007.909861

Zwicky, F. 1933, Helv. Phys. Acta, 6, 110, doi: 10.5169/SEALS-110267